X-Ray diagnostics on corium-sodium interactions during a severe accident scenario

Shifali Singh

NNT: 2019SACLS114

Thèse de doctorat

Radioscopie X pour les interactions corium-sodium lors d'un scénario d'accident grave

Thèse de doctorat de l'Université Paris-Saclay
préparée à l'Université Paris-Sud
au sein du CEA
(CEA, DEN, DTN, SMTA/LEAG)

École doctorale n° 576 Particules, Hadrons, Énergie, Noyau, Instrumentation, Imagerie, Cosmos et Simulation (PHENIICS)
Spécialité de doctorat: Energie nucléaire

Thèse présentée et soutenue à Orsay, le 10 Mai 2019, par

Shifali SINGH

Composition du jury:

Michel GRADECK Université de Lorraine, France	Président du jury
Sevostian BECHTA KTH Stockholm, Suède	Rapporteur
Emmanuel PORCHERON IRSN Saclay, France	Rapporteur
Michael BUCK Université de Stuttgart, Allemagne	Examinateur
Patrice HELLO Université Paris Sud, France	Examinateur
Christophe JOURNEAU CEA DEN, France	Directeur de thèse
Magali ZABIÉGO CEA DEN, France	Encadrante de thèse
Nathalie CASSIAUT-LOUIS Autorité de Sûreté Nucléaire, France	Encadrante de thèse

NNT: 2019SACLS114

Thèse de doctorat

X-Ray diagnostics on corium-sodium interactions during a severe accident scenario

Doctoral thesis of University Paris-Saclay
prepared at the University Paris-Sud
within the CEA
(CEA, DEN, DTN, SMTA/LEAG)

Doctoral School n° 576 Particules, Hadrons, Énergie, Noyau, Instrumentation, Imagerie, Cosmos et Simulation (PHENIICS)
Specialty: Nuclear Energy

Thesis presented and defended at Orsay, on 10 May 2019, by

Shifali SINGH

Composition of jury:

Michel GRADECK University of Lorraine, France	President of the jury
Sevostian BECHTA KTH Stockholm, Sweden	Reviewer
Emmanuel PORCHERON IRSN Saclay, France	Reviewer
Michael BUCK University of Stuttgart, Germany	Examiner
Patrice HELLO University Paris Sud, France	Examiner
Christophe JOURNEAU CEA DEN, France	Thesis Director
Magali ZABIÉGO CEA DEN, France	Thesis Supervisor
Nathalie CASSIAUT-LOUIS Autorité de Sûreté Nucléaire, France	Thesis Supervisor

" *I tried out various experiments described in treatises on physics and chemistry,*
and the results were sometimes unexpected.
At times, I would be encouraged by a little unhoped-for success, at others I would be in the deepest despair because of accidents and failures resulting from my inexperience."

- Marie Curie

Abstract

In Sodium-cooled Fast Reactors (SFR), hypothetical failure of the core cooling system or the plant protection system may lead to a severe accident scenario. In such a scenario, core materials (fuel and cladding) melt down generating a hot molten mixture called corium. This corium may interact with the coolant (liquid sodium) leading to Fuel Coolant Interaction (FCI) which can generate energetic events and hence jeopardize the reactor structures. The yield of these energetic events strongly depends on the state of the corium-sodium mixture prior to the energetic event. Therefore, the knowledge of the features of the mixture composed of three-phases (i.e., corium, liquid sodium, and sodium vapor) is crucial.

The lack of knowledge on the phenomenology of the interaction emphasizes the need to study it with the help of experiments. PLINIUS-2, the future large-mass experimental platform of CEA Cadarache, will be dedicated to experiments aiming at understanding the interaction phenomenology of prototypic corium with coolant (sodium and water). The present research aims to develop a high-energy X-Ray imaging system for this facility, to visualize and better understand the corium-sodium interaction. An image-processing algorithm to analyze the three-phase repartition is also developed to contribute to the improvement of numerical modeling.

This Ph.D. research has been executed in three steps. In the first step, a bibliographic study of the past experiments was carried out to better understand the physics of the interaction and the mechanism of fragmentation during corium-sodium interaction. This bibliographic study, along with a statistical analysis of the particle size distribution data of various experiments conducted in the past, revealed that the particles formed in these tests are extremely fine fragments with characteristic diameters smaller than 1 mm. Due to the small particle size and the detection limitations of corium fragments in sodium with our X-Ray system, clouds of particles were detected instead of individual particles.

In the second phase, the simulation of clouds of corium particles followed by the designing of phantoms (3D mock-ups) representing the 3-phase medium was carried out. Simulations of clouds of corium fragments in liquid sodium and vapor were performed using the CEA Cadarache in-house tool MODHERATO. Based on the results obtained from the simulations, certain phantoms were designed to conduct some physical experiments. These phantoms representative of the FCI interaction zone were manufactured to experimentally evaluate the performance of the radioscopy system and to facilitate the development and calibration of the image processing software.

The third step of this work was dedicated to performing experiments with the phantoms and analyzing the radiographic images by developing an image processing algorithm. Experiments were carried out with phantoms in several configurations with the X-Ray radiography system at the CEA Cadarache KROTOS facility. The radioscopic images obtained were treated by developing a new comprehensive image processing and analysis code called PICSEL to identify the three phases composing the medium. Further verification and validation of the PICSEL software were carried out on a test conducted between corium and water at the KROTOS facility under the Euro-Chinese project “ALISA”.

Thus, in this Ph.D. research, an X-Ray imaging system was qualified to visualize the corium-sodium interaction in the future PLINIUS-2-FR facility. A qualitative analysis of the images produced by this system was also performed using the PICSEL software to better characterize the evolution of the three-phase mixture and understand the FCI phenomenon, knowledge of which is deemed essential to improve the safety and designs of future sodium-cooled fast reactors.

Keywords: Sodium-cooled Fast Reactors, Nuclear Severe Accidents, Fuel-Coolant Interaction, X-Ray radioscopy, image processing.

Résumé

Dans les réacteurs à neutrons rapides refroidis au sodium (RNR-Na), une défaillance dans le système de refroidissement du coeur ou de protection du réacteur peut conduire à un accident grave. Dans un tel scenario, les matériaux du coeur (combustible et acier) fondent pour former un mélange appelé corium susceptible d'interagir avec le réfrigérant (sodium). Une telle interaction (Fuel Coolant Interaction, FCI) peut générer des évènements énergétiques aptes à mettre en danger les structures du réacteur. La violence de l'explosion dépend essentiellement de l'état du mélange corium-sodium. Connaître les caractéristiques des trois phases en présence dans la zone d'interaction (corium, sodium liquide, vapeur de sodium) est donc crucial.

Le manque de connaissances de la phénoménologie de l'interaction conduit à l'étudier au moyen de dispositifs expérimentaux. PLINIUS-2, la future plateforme expérimentale du CEA Cadarache consacrée aux grandes masses, sera dédiée à l'étude de la phénoménologie de l'interaction corium-réfrigérant (eau et sodium). L'objectif du présent travail est de développer, pour cette installation, un système d'imagerie basée sur des radiographies X afin de visualiser et de mieux comprendre l'interaction corium-sodium. Un algorithme de post-traitement de ces images a aussi été écrit afin de les analyser, d'en déduire la répartition des trois phases dans le système et de contribuer ainsi à l'amélioration de la modélisation numérique.

Ce travail de thèse a été conduit en trois étapes. La première était consacrée à une étude bibliographique des expériences passées d'interaction corium-sodium et des mécanismes de fragmentation mis en jeu. Cette étude, complétée d'une analyse statistique des distributions de particules obtenue alors, a montré que les particules générées lors de ces expériences sont extrêmement fines avec des diamètres caractéristiques inférieurs au mm. Ces très petites tailles de particules combinées aux limites de détection de notre système d'imagerie nous ont amenés à travailler plutôt sur la détection de nuages de particules que de particules individuelles.

Dans une deuxième étape, la simulation du nuages de particules de corium suivie de la conception de fantômes (maquettes 3D) représentant les trois phases du milieu ont été réalisées. Les simulations de nuages de fragments dans le sodium liquide et la vapeur ont été réalisées avec le logiciel CEA MODHERATO. Sur la base des résultats de ces calculs, certains fantômes ont été fabriqués afin de générer des images "réelles" à l'aide d'une chaîne d'imagerie existant au CEA. Ces fantômes représentatifs de la zone d'interaction corium-sodium ont été fabriqués pour faciliter le développement et la calibration du logiciel de traitement d'images.

La troisième étape de cette thèse était dédiée à la conduite des expériences avec les fantômes 3D et au développement du logiciel de traitement des images ainsi obtenues. Les radiographies X des fantômes ont été générées à l'aide du système d'imagerie de l'installation KROTOS du CEA Cadarache. Les images ont ensuite été traitées avec le logiciel appelé PICSEL que nous avons développé afin de localiser les trois phases en présence dans la zone d'interaction. PICSEL a ensuite été appliqué à une expérience d'interaction corium-eau réalisée dans l'installation KROTOS dans le cadre du projet ALISA de collaboration Europe-Chine ; ceci a permis une première validation du logiciel.

Ainsi, lors de cette thèse, un système de radioscopie X a été défini pour visualiser l'interaction corium-sodium dans les expériences de la future installation PLINIUS-2 du CEA Cadarache. Une analyse qualitative des images produites par ce système (expériences menées avec des fantômes) est aussi réalisée avec le logiciel PICSEL développé lors de cette thèse afin de mieux caractériser le mélange, de mieux comprendre les mécanismes de l'interaction et de contribuer ainsi à l'amélioration de la sûreté des réacteurs à neutrons rapides.

Mots-clés: Réacteur à neutrons rapides à caloporteur sodium, Accidents graves nucléaires, Interaction corium-sodium, radioscopie X, traitment d'images

Acknowledgments

I would like to thank all the people who contributed to help me achieve this research and accompanied its proper completion. First and foremost, I am thankful to Dominique Pecheur, head of Service "Mesures et modélisation des Transferts et des Accidents graves (SMTA)" service and Christophe Suteau, head of the "Laboratoire d'Etudes et d'expérimentations pour les Accidents Graves (LEAG)" laboratory, respectively, for giving me an opportunity to carry out research at CEA Cadarache.

A huge thanks and appreciation is reserved for Christophe Journeau, my Ph.D. director, without whose contribution, this work would not have been possible. His kind support and motivation throughout this research, drove me to accomplish my task efficiently. Moreover, in addition to being one of the major international experts in his field, I wish to thank him for being such a friendly character at all times.

I would also like to extend my deepest gratitude to my Ph.D. supervisors Magali Zabiégo and Nathalie Cassiaut-Louis, two wonderful persons with whom I enjoyed working. Their supervision and friendly guidance throughout my entire Ph.D. work, especially on the work related to the understanding of FCI both experimentally and theoretically, is to be appraised. Magali, I appreciate all your guidance that helped me improve day-by-day.

Special thanks to Nicolas Estre and Leonie Tamagno for having several discussions throughout this Ph.D. work on the use of the MODHERATO software. The several exchanges we had over meetings and e-mails were fruitful and helped me in the successful completion of this work.

Special thanks to Claude Brayer, Christophe Fochesato and Frederic Payot for their contribution in every possible way out, which allowed the successful completion of this research subject.

I am also grateful to Pascal Fouquart, Marc Valerian, Frederic Compagnon, Emmanuel Payan, Patricia Correggio, Brigitte Valentin for their valuable contribution in the designing, fabrication and successful conduct of the experiments with the phantoms on the KROTOS facility. Without their support, the experiments would not have been possible.

A big thanks to Michel Gradeck, Sevostian Bechta, Emmanuel Porcheron, Michael Buck, Patrice Hello and the entire Ph.D. committee for taking the time out of their busy schedule and providing great comments and suggestions.

A special thanks to Michael Johnson for all his wonderful ideas that helped me improve the manuscript. I would also like to extend my heartily thanks to all my colleagues of LEAG for their welcoming spirit and my smooth integration into the team. In particular, I would like to thank Arthur Denoix for his help throughout my Ph.D. My journey so far would not have been interesting without Héléna Mastori, Louis Viot, Pascal Sauvecane, Hubert Delacroix, Justine Zanini, Kevin Compagnon and Alain Coissieux. Vaishnavi Tiwari, having you around is something I will always cherish, the time that we shared at CEA and the several parties we had together, is something I am going to miss a lot.

I gratefully acknowledge Cecile Dubernet and Laure Dewerdt for helping me with all the French administrative formalities starting from the security clearances to the management of all my missions during the entire duration of my Ph.D.

A warm expression of thanks to all my friends, especially Savneet Kaur, Ronit Panda, Amreen Jan, Saptarshi Mitra, Shambhavi Nandan, Saptarshi Bhattacharjee, Advait Ghate, Zayed Parkar for making my stay in France enjoyable.

Vaibhav, your support is something that kept me motivated in all the difficult times and I can never thank you enough for bearing with me always. Our Ph.D. journey started together, and I will always cherish this phase of my life, forever.

And finally, I would like to thank my mom, dad, brother and my sister-in-law for believing in me and supporting me in every possible manner. *"Aap sabhi ko sadar charan sparsh"* (Seeking for your blessings).

Contents

List of Figures

List of Tables

List of Abbreviations

ASTRID	**A**dvanced **S**odium **T**echnological **R**eactor for **I**ndustrial **D**emonstration
SFR	**S**odium **F**ast **R**eactor
FCI	**F**uel **C**oolant **I**nteraction
ULOF	**U**nprotected **LO**ss Of **F**low
CDA	**C**ore **D**amage **A**ccidents
PWR	**P**ressurized - **W**ater **R**eactor
CWI	**C**orium - **W**ater **I**nteraction
CSI	**C**orium - **S**odium **I**nteraction
SCONE	**S**oftware for **CO**rium-**Na** interaction **E**valuation
KIWI	**K**rotos **I**mage analysis for **W**ater-corium **I**nteraction
MCCI	**M**olten **C**orium **C**oncrete **I**nteraction
JRC	**J**oint **R**esearch **C**enter
NNC/RK	**N**ational **N**uclear **C**enter of the **R**epublic of **K**azakhstan
MISTEE	**M**icro **I**nteractions in **S**team **E**xplosion **E**xperiments
LINAC	**LIN**ear **AC**celerator
GADOX	**GAD**olinium **OX**ysulphide
CMOS	**C**omplementary **M**etal **O**xide **S**emiconductor
CCD	**C**harge **C**oupled **D**evice

OECD	**O**rganization for **E**conomic **C**ooperation and the **D**evelopment
NEA	Nuclear **E**nergy **A**gency)
SERENA	**S**team **E**xplosion **RE**solution for **N**uclear **A**pplication
TROI	**T**est for **R**eal c**O**rium **I**nteraction with water
KAERI	**K**orea **A**tomic **E**nergy **R**esearch **I**nstitute
ANL	**A**rgonne **N**ational **L**ab
MODHERATO	**MO**delling **D**etectors for **H**igh **E**nergies **RA**diography and **TO**mography
MCNP	**M**onte **C**arlo **N**-**P**article
ADCU	**A**nalogue to **D**igital **C**onversion **U**nits
FWHM	**F**ull **W**idth at **H**alf **M**axima
SNR	**S**ignal to **N**oise **R**atio
C/N	**C**ontrast to **N**oise ratio
PIV	**P**article **I**mage **V**elocimetry
PICSEL	**P**LINIUS-2 **I**mage processing for **C**orium **S**odium **E**xperimental **L**ibrary
NCCR	**N**ormalized **C**ross-**C**or**R**elation
ALISA	**A**ccess to **L**arge **I**nfrastructures for **S**evere **A**ccidents)

Dedicated to you mamma and papa ...

Chapter 1

Introduction and Research Objective

> *I truly believe that everything that we do and everyone that we meet is put in our path for a purpose. There are no accidents we're all teachers - if we're willing to pay attention to the lessons we learn, trust our positive instincts and not be afraid to take risks or wait for some miracle to come knocking at our door.*
>
> Marla Gibbs

Research on prototypes, experimental or commercial size Sodium-cooled Fast Reactors (SFRs) started in the early 60s. To name a few facilities that were under operation worldwide: RAPSODIE, PHENIX, SUPERPHENIX (France), FBTR (India), KNK-II (Germany), JOYO, MONJU (Japan), BN-350–600 (Russia), DFR, PFR (UK), EBR II and FFTF (USA). All of these facilities have provided significant knowledge and operating experience of SFRs. Based on this knowledge, the design and development of ASTRID reactor (Advanced Sodium Technological Reactor for Industrial Demonstration), a "Generation IV" SFR, has been carried out by the CEA along with its industrial partners. A pictorial representation of the ASTRID reactor is shown in Fig. 1.1. Among several potential candidates of fuel types in SFR, for instance, oxide, nitride, metal

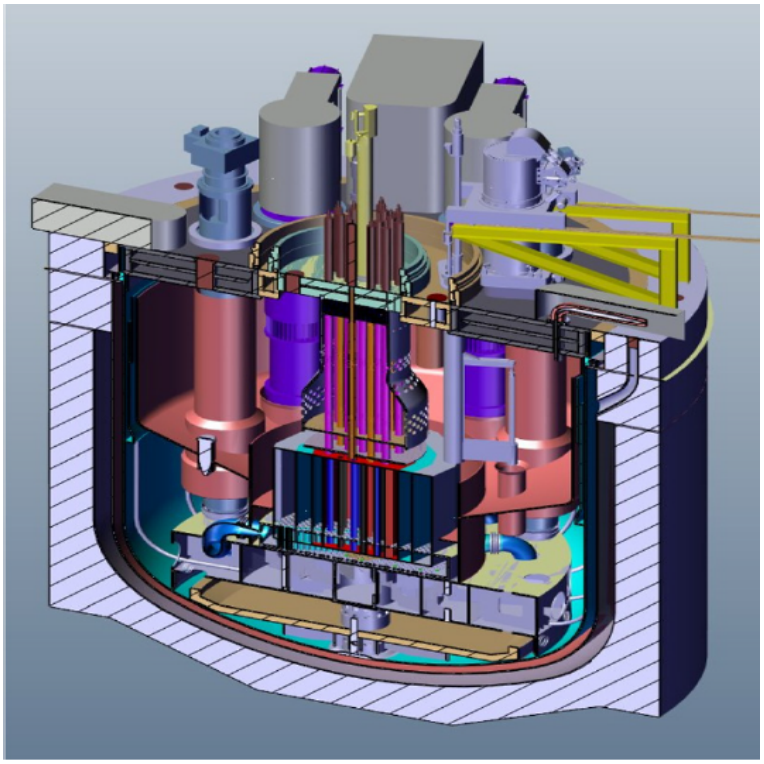

FIGURE 1.1: A pictorial representation of the ASTRID reactor [1].

and carbide fuel, ASTRID reactor is based on mixed oxide fuel $(U, Pu)O_2$. This reactor is a pool type reactor with thermal and electric output of 1500 MW and 600 MW, respectively [1].

The primary objective of the ASTRID project is to demonstrate the safe operation of SFRs and ensure that even in case of an accident there would be a minimal radioactive release and that the reactor can go back to its safe state [1]. Hence, it is essential to perform safety studies not only in the safe state (operating reactor temperature range) but also in case of transients or accidents where the temperature of the reactor might rise abruptly causing the fuel to melt. The next section will introduce reactor transients and severe accidents and the events that trigger such scenarios.

1.1. Severe accidents in SFRs

Accidents are generally classified as design basis accidents or severe accidents depending not only on their probability of occurrence but also based on the severity of the accident that might lead to the release of radioactivity to the environment. Although the possibility of occurrence of such accidents is extremely low, the risk of a large amount of radioactive products release has led to the study of these accidents for a very long time. Accidents such as the one at Chernobyl in Ukraine in 1986 and Fukushima Daiichi in Japan in 2011 had an

immense impact and led the nuclear community to reconsider their safety approaches. This section of transients and accidents have been explained using [2].

It is known that SFR cores are not in the most reactive configuration under a normal operating condition, i.e., the reactor core is highly sensitive to fuel meltdown. Any event of fuel meltdown might lead to prompt criticality conditions with immense mechanical energy released to the reactor structure.

Another safety concern in the case of SFRs is the sodium void effect, i.e., change in reactivity of the core due to the removal of sodium. Generally, in the case of loss of core cooling or boiling of sodium, there can be regions which would be devoid of sodium. If such a situation arises, the reactivity might increase thus leading to power transients with subsequent fuel pin damage. Sodium void effect in SFRs is generally positive (an increase in the reactivity of the core due to the voiding of sodium) and poses significant concerns while designing a reactor. For instance the ASTRID reactor design is based on keeping the sodium void effect close to zero or even negative.

Design basis accidents: It is ensured to maintain radiological release below the permissible limits by carrying out certain stringent design constraints. Certain accidents can be considered as design based accidents, if it is related to the physical design of the system and its acceptable margin limitations. For instance, it is made sure that pin failure should not occur in case of slow power transients during operations, using the emergency shut-down systems. Hence the fuel elements are designed to withstand these transients.

Severe accidents: Also termed as design extension conditions, these are the accidents that occur outside the scope of what reactors are designed to withstand. Accidental conditions more severe than a design basis accident and involving significant core degradation from overheating are termed as severe accidents. These are important to understand in order to plan appropriate prevention and mitigation strategies. Nevertheless, the European Directive, "2014/87/EURATOM" stipulates the objective of *"preventing accidents and, should an accident occur, mitigating its effects"* and, in particular, *"large radioactive releases that would require protective measures that could not be limited in area or time"* [3].

ASTRID is the first reactor for which the possible occurrence of a severe accident leading to fuel melting is considered from its very conception. Mitigation and post-accident management devices are being designed.

Three main transient and accident scenarios can be categorized based on the amount of risk associated with them, i.e. local or generalized core melting.

- **Control-rod withdrawal accident:** Control rods are used to manage the reactor power and in case of an accidental withdrawal (operator's fault or due to hardware dysfunction), power transients can take place

locally. Such an event may lead to an increase in the pin power (of the sub-assemblies surrounding the control rod) that might lead to partial melting of the fuel inside the pins.

- **Local blockage of a sub-assembly:** The coolant flow through the sub-assembly might be hindered in case of a blockage due to an external material. This blockage might lead to pin failure, wall failure, and sub-assembly damage depending on the severity of the blockage. These damages can also propagate to other neighboring sub-assemblies leading to critical events and core meltdown. In fact, the total instantaneous inlet blockage (TIB) of a sub-assembly is supposed to be a major initiator for a core meltdown accident in the European fast reactor studies framework.
- **Unprotected Loss of Flow (ULOF) accident:** Such an event is initiated due to the failure of electric power supply to the primary pump. With the reduced sodium flow rate the reactor power reduces resulting in an increase in the power to flow ratio and hence the temperature of the sodium to the saturation level. Sodium boiling and voiding of the channels occur. This would result in Core Damage Accidents (CDA) due to the positive sodium void effect. Two effects follow:
  - **Primary core power excursion:** On the onset of the primary core power excursion the reactor core starts degrading resulting to either fuel meltdown, clad failure/melting, fuel coolant interaction with mechanical energy release.
  - **Secondary core power excursion:** The primary core power excursion is followed by the formation of large molten pools that leads to the melting of sub-assembly walls causing re-criticality accidents. Significant mechanical energy can be released by the vapor bubble of the fuel or the sodium that might be formed during this process.

In the frame of the ASTRID conception, these accident scenarios and their associated risks are carefully assessed. This will help in implementing design measures to prevent, manage and limit the consequences of the accident which is often termed as "mitigation".

1.2. Fuel-Coolant Interaction (FCI)

The melt down of the reactor core in SFRs would generate a hot (~ 3000 K) mixture which is termed as corium. It is composed of nuclear fuel (UO_2/ PuO_2), cladding (stainless steel), a part of the fission products, control rod and structural material. The hot corium issuing from the degraded core can then come into contact with the

cooling sodium, generating a so-called "Fuel-coolant interaction" (FCI). FCI can take place at different scales within the reactor vessel, depending on the location of interaction. Corium-sodium interaction can occur [4]:

- **At the fuel pin scale:** This can occur due to a power rise in one of the fuel pins causing the pin (composed of fuel and cladding) to melt forming corium which can be ejected into the inter-pin channel. This would generate an FCI with the sodium present in the channel. The FCI can have consequences on the neighboring pins and if sodium is still present in those channels, it can propagate the accident from one pin to the other involving more significant fuel masses. FCI at fuel pin scale cannot threaten the reactor integrity but may have consequences on the accident propagation based on the impact on the neighboring pins [4].
- **At the fuel assembly scale:** Following a loss of coolant flow, the fuel together with the cladding material may vaporize and solidify at the upper part of the core forming a tight plug. If the assembly canister fails, the pressure difference thus created between the inside of the fuel assembly and the outside coolant will govern the direction of flow of sodium which might flow back in the molten assembly. Molten fuel can also be released into the inter-assembly channel, and thus to the neighboring assemblies. Both these contact modes between corium and sodium would lead to FCIs and to pressurization of the medium and might result in energetic FCIs.
- **At the reactor core scale:** The melting of a large number of fuel assemblies would generate a corium pool inside the core with a vault over it. This vault is composed of assemblies that can be damaged or not. This vault can collapse causing a large quantity of corium to come in contact with liquid sodium.
- **When corium is progressing out of the core:** In the ASTRID core, it is planned to insert dedicate guiding tubes to allow the fuel melt to be relocated to the lower plenum as shown in Fig. 1.2. During this relocation, corium will come in contact with lower plenum sodium resulting in an FCI.

The consequences of a corium-sodium interaction depend on the following key parameters:

- the masses of the interacting bodies,
- the thermal conditions of the materials, i.e. their temperature, physical state, physical properties,
- the pressure within the system: the pressure plays an important role in the stabilization/destabilization of the vapor film that can form around the corium particles (see section 1.3).

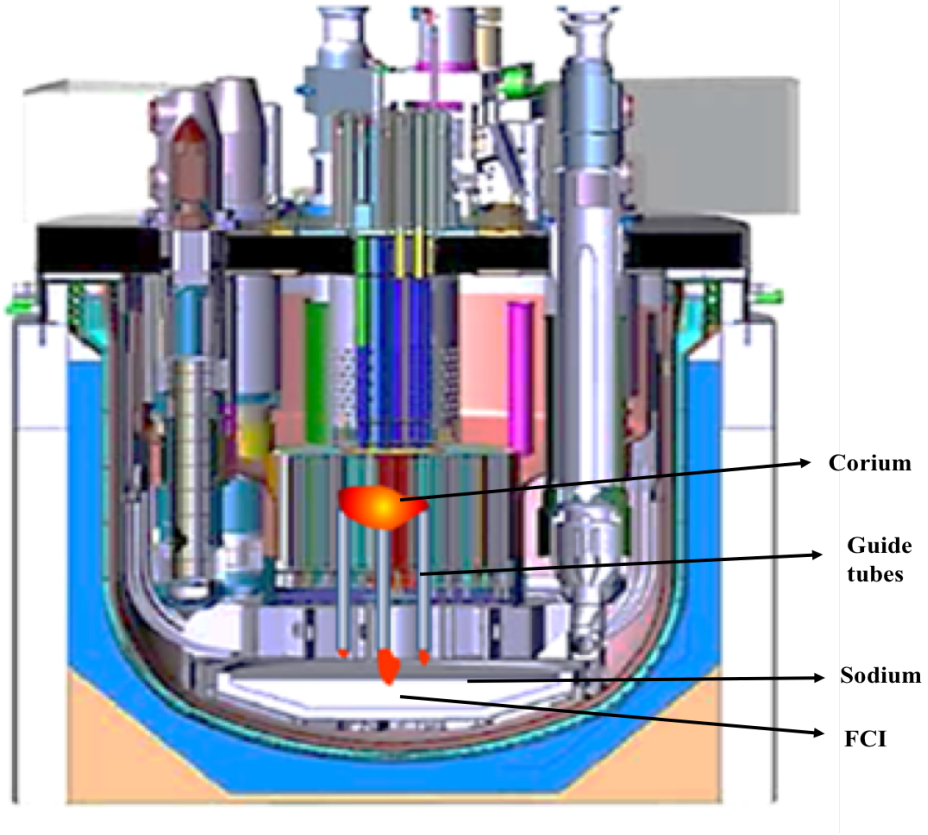

FIGURE 1.2: Accident scenario in ASTRID demonstrator.

- mode of contact: corium falling into sodium, corium ejection into sodium or sodium falling onto corium are the possible modes of contact for an FCI (which will be explained in the next section). These conditions play a major role in the premixing phase.

It was also observed that the nature of confinement of the interaction also plays a significant role in the global heat transfer and pressure build up. It allows the two fluids to separate more or less rapidly after the beginning of the interaction depending on the confinement configuration. CORRECT 2 experiments at CEA-Grenoble illustrated this effect. [5]

FCIs in Sodium-cooled Fast Reactors has become a major concern over the past few years. An important safety aspect of such investigations concerns the possibility of a vapor explosion which can impact the reactor structures especially when large masses are involved [5, 6]. This has long motivated the theoretical and experimental study of such a phenomenon [7, 8]. Research on the consequences of FCI and threat a large amount of mechanical energy release can cause to a reactor system is still ongoing. A second issue lies with the post-accident management in connection to the debris bed coolability. It is foreseen to build a core-catcher in the primary vessel of ASTRID in order to retain the core melt (corium) and enhance the cooling to avoid further re-criticality.

The knowledge of the size distribution of the debris formed during the interaction holds importance since it controls debris behavior in particular its coolability.

The next section discusses the phenomenology of an FCI in sodium-cooled reactors and FCI in water-cooled reactors.

1.3. Phenomenology of an FCI

An interaction between a hot molten fuel and a cold, more volatile liquid coolant, causes a rapid fuel fragmentation and transfer of the internal energy from the fuel to the coolant. Fragmentation increases the heat transfer area between the two. This causes the coolant temperature to increase and generate a lot of vapor in the system resulting in an increased pressurization. "This can lead to the formation of a shock wave and/or the production of missiles at later times, during the expansion of coolant vapor, that may endanger surrounding structures" [9]. This is often termed as "vapor explosions" (and sometimes energetic FCIs).

The general phenomenology of FCI between hot molten fuel (corium, T $\sim$ 3000°C) and water (coolant in PWRs T $\sim$ 70°C) is quite well established. So, we shall first develop an understanding of corium-water interaction (CWI) mechanism and then compare it with the corium-sodium interaction (CSI). A CWI is identified to be occurring in four stages as shown in Fig. 1.3 [6, 9]:

1. **Premixing stage:** when molten fuel (corium) comes in contact with the water, it breaks up into coarse fragments in the order of centimeters. Due to the temperature difference between corium and water, the water evaporates and a stable vapor film is formed around the fragments. This film acts as a barrier for further heat transfers between corium and water. The time scale of the premixing stage is of the order of a few seconds.

2. **Triggering stage:** In this stage, an external event (experimentally represented by a pressure pulse) causes the destabilization of the vapor film. With this destabilized film there is an enhanced contact between corium and water causing further fragmentation of corium like in the previous stage. The overall effect of this stage is an enhanced surface exchange area for heat transfer and vaporization.

3. **Propagation stage:** The fine fragmentation leads to an intense vapor production and a pressure wave that propagates through the medium. The vapor film destabilizes within the whole system and a relative motion

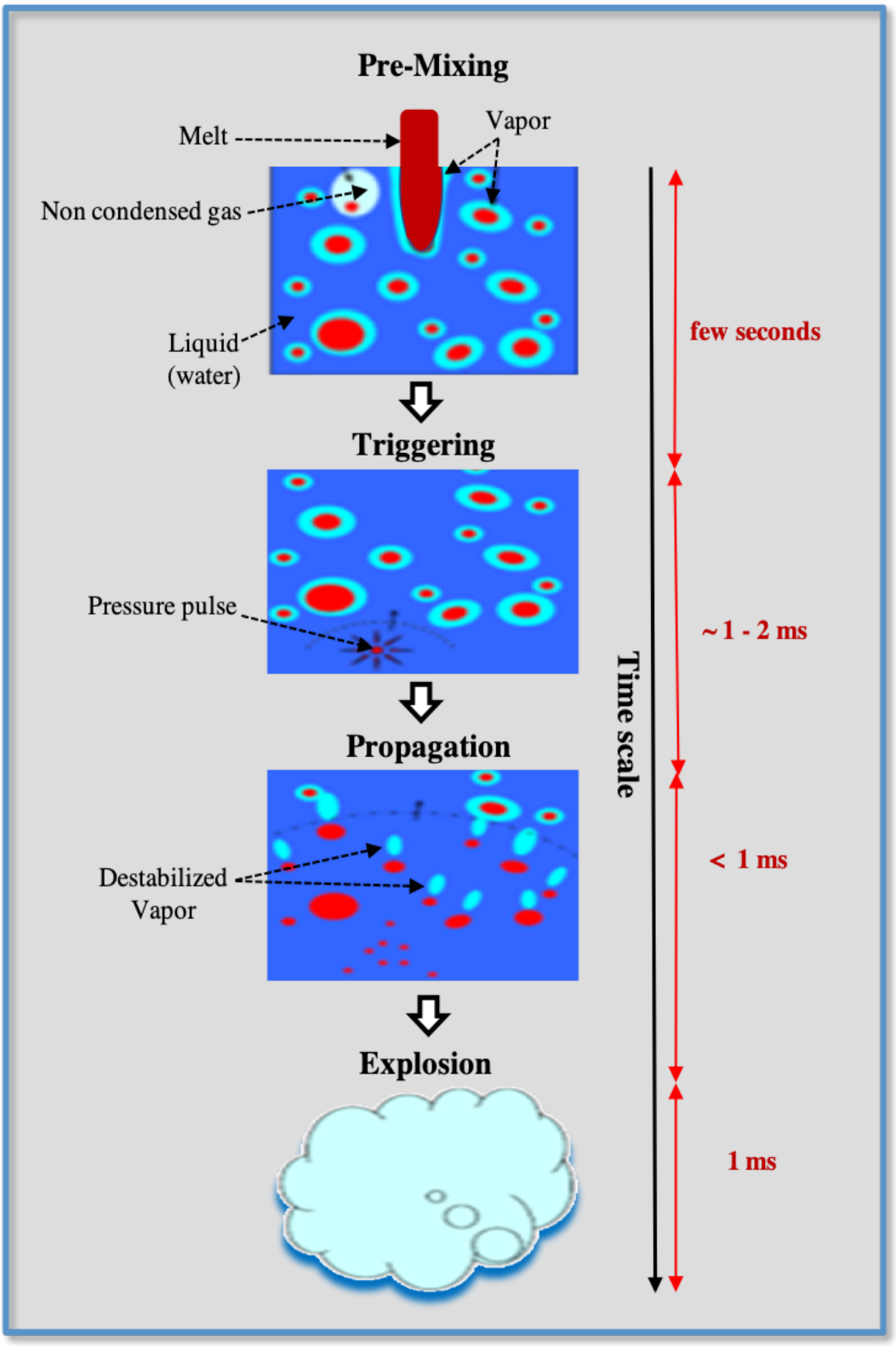

FIGURE 1.3: Interaction mechanism of corium with water.

between corium and the two-phase coolant eventually leads to hydrodynamic fragmentation of the corium fragments. The entire fragmentation process leads to the development of a "vapor bubble"[5, 10].

4. **Explosion stage:** The high-pressure mixture can then result to an expansion of the "vapor bubble" which is often termed as explosion, impacting the surrounding structures and threatening the reactor integrity.

The above explanation of the four stages is based on a considerable amount of experimental evidence and the knowledge gained from them. OECD/CSNI recently issued a report on the Ex-vessel steam explosion risks synthesizing the current consensus view on this topic and unresolved issues [11]. However, there is a lack of substantial information about corium-sodium interaction due to a limited number of experiments. In addition, among the available experiments, simultaneous visualization of the interaction mechanism was performed only in a few experiments. This limits our understanding of corium-sodium interaction and due to this reason, the four stages explained for corium-water interaction may or may not be the same for corium-sodium interaction, especially in terms of timing. Nevertheless, there are some identified notions based on the observations made in the experiments performed in the past and also based on the understanding of an FCI. A few of them will be enlisted herein. When corium comes in contact with sodium, it is coarsely fragmented and a film boiling regime establishes around the fragments. However, unlike with water, in the case of sodium, the vapor film around the corium fragments is very unstable [12, 13]. Stable film boiling might be achievable with nearly saturated sodium, either as an initial condition or because of extended contacts with corium. It has been observed that the CSI with sodium having low sub-cooling (or nearly saturated sodium) exhibits a behavior akin to CWI [5] in terms of pressure rise times and energy release. While in the case of colder sodium, even if these stages exist, it is not easy to separate the premixing phase from the triggering phase. It has also been observed that in case of sodium the size of fragments formed during a corium-sodium interaction is considerably smaller (of sub-millimetric size) than in corium-water interaction (of size ranging from millimeters to centimeters). However, in CSI past experiments, even if no energetic event was detected, the molten material was always heavily fragmented irrespective of the sodium sub-cooling degree. With these incomplete descriptions, it is difficult to predict the entire mechanism in the four stages of corium-sodium interaction, especially when sodium is sub-cooled.

It should be noted that it is very important to accurately model the premixing stage in water as well as sodium, as it will define the amount of fuel which can react violently and identify thermodynamic conditions of the interaction. Presently, there are tools which can do this job but it is only limited to FCI with water [14, 15]. Likewise, CEA is working on the development of a modeling software, SCONE (Software for COrium-Na interaction Evaluation) that aims at simulating FCI with sodium [10]. However, the limited knowledge of the interaction phenomenology of corium-sodium interaction makes it difficult to develop computer models which

could precisely describe all the stages of interaction. The development of SCONE requires significant data from corium-sodium interaction experiments complemented with a good visualization system. This serves as the motivation of this Ph.D. An advanced visualization system which will give valuable information and data about corium-sodium interaction phenomenology is desired. Among others, one of the major interest is to characterize the three-phase mixture formed during the interaction:

- Fuel- molten melt
- 2 phase coolant (sodium): liquid sodium and sodium vapor

Thus, to have a general idea, this Ph.D. aims at developing a visualization instrumentation to provide experimental data on the corium-sodium interaction phenomena. This includes data on the spatial distribution of the multi-phase mixture and also information on the size distribution of corium particles.

In the next section, a comparative study of CSI and CWI will be made to further strengthen the understanding of the two mechanisms.

1.4. Comparison of FCI in sodium with FCI in water

The mechanism of an FCI is generally similar in both sodium and water. But, there are a few discrepancies observed between the two FCIs due to the difference in the physical properties of water and sodium. Table 1.1 enlists a comparison of basic physical properties of water and sodium.

TABLE 1.1: Basic physical properties of water and sodium.

Properties	Water	Sodium
Melting point	273 K	371 K
Boiling point	373 K	1156 K
Density	0.997 g/cm3 at 293 K	0.850 g/cm3 at 673 K
Viscosity	280 Pa.s at 373 K	310 Pa.s at 673 K
Conductivity	0.6 W/m.K at 293 K	76.6 W/m.K at 673 K
Prandtl number	7.56 at 300 K	0.004 at 673 K

Here, we are going to discuss the major differences observed when corium interacts with water and when corium interacts with sodium.

1. One of the major differences concerns the coolant sub-cooling effect. Berthoud [5] discussed the effect of coolant and its sub-cooling degree in detail by comparing the Scale- Urania-Sodium (SUS) tests with Scale-Urania-Water experiments (SUW). The experiments shared the same melt mass, modes of release and system pressure range, but the coolant sub-coolings of 0 to 80K in the case of SUW tests were significantly smaller in comparison to 400K sub-cooling in SUS tests. The principal difference observed between the two tests were the relatively fewer and more vigorous interaction in case of SUW tests. He came up with a possible explanation that "suitable premixing is obstructed and premature local freezing of the melt occurs when a relatively good thermal diffuser like liquid sodium is very deeply sub-cooled (400K)" [5]. The locally frozen melt requires a great amount of energy to fragment, and this may seize the propagation of the interaction, thus leading to relatively weak events recorded in the SUS tests. However, if sodium is lightly sub-cooled or heated upon by multiple interactions with fuel melt, the vaporization of coolant is less inhibited, therefore promoting coarse mixing of melt and liquid coolant to produce more vigorous CSI. Thus, when sodium temperature is close to saturation, the interaction is more akin to FCI with water as stated in [5].

2. As mentioned before, another difference lies in the premixing stages in the two interactions. In corium-water interaction (CWI), the premixing stage is observed to have the three phases defined very distinguishable with corium fragments separated from the coolant with a very stable vapor film around them. However, in the case of corium sodium interaction (CSI), the 3 phases exist but the time scale of the premixing stage is not equal. Moreover, all the past experiments have shown that in CSI an external trigger was not necessary due to very unstable nature of the vapor film surrounding the corium fragments. Premixing state here, might be of very short time duration in comparison to that in CWI but this may evolve with the sodium temperature as explained before.

3. Most of the tests (all performed with sub-cooled Na) with sodium lead to multiple interactions in contrast to relatively fewer interactions with water. Two pressure peaks were observed in CORECT 2 no. 22 [5], seven peaks in SUS 03 [16], two to three peaks in TERMOS tests [17], two interactions in the THINA test [18].

4. It was observed in the Betulla experiment 80 [19] where molten fuel was released into water, that major amount of fuel solidified into a mushroom shape contrary to no mushroom- shaped fragments ever detected in fuel-sodium interaction.

5. Another observation was made on the shape of the UO_2 fragments. Post-test examination of debris in

CORECT 2 and SUS test (test SUS 03) showed an angular appearance unlike very smooth UO_2 fragments in the SUW tests with water [5].

6. A very important difference is in terms of the size of fragments. In the fuel water interaction, the fragments size after the premixing phase ranges from few millimeters to centimeters (after an explosion the size distribution tends to lower sizes). While in the case of sodium-fuel interaction, whatever the level of the energy release, the interactions invariably led to relatively fine fuel fragments of sub-millimetric size. [5] This fact will be discussed in more detail in the following chapters.

1.5. Introduction to the experimental facilities to study FCIs at CEA Cadarche

CEA is interested in carrying out experiments to study FCIs. Two experimental platforms with a few integral facilities are dedicated towards this purpose. This is summarized in the sketch in Fig. 1.4. The existing experimental platform of the CEA, called **PLINIUS** and the forthcoming named **PLINIUS-2**.

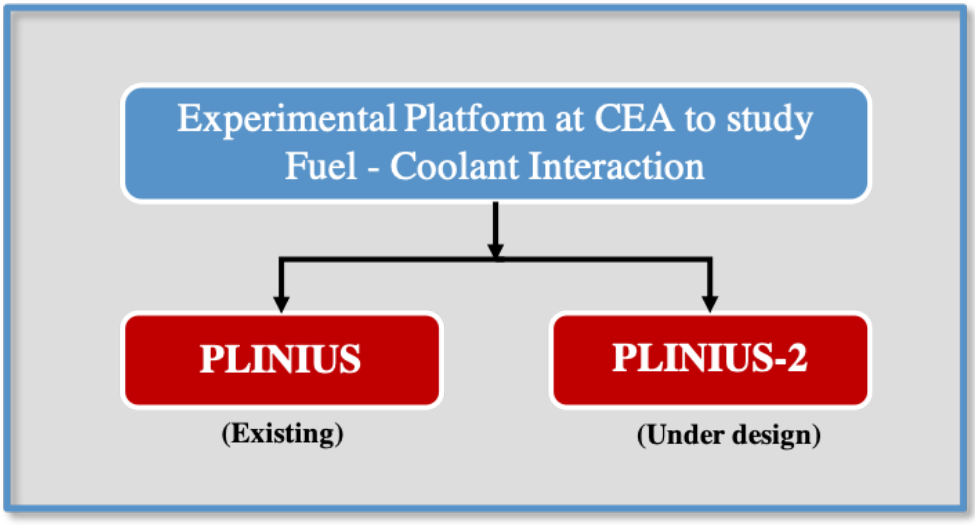

FIGURE 1.4: Experimental platforms at CEA to study Fuel-Coolant Interaction.

1.5.1 Existing platform: PLINIUS

The PLINIUS platform [20] has four facilities to conduct experiments in different domains. A sketch summarizing the three facilities that fall under the umbrella of PLINIUS is shown in the sketch in Fig. 1.5. The KROTOS facility is dedicated to performing Corium-Water interaction experiments. This facility embeds an X-Ray imaging system to visualize the interaction and the images obtained are then analyzed with the CEA in-house

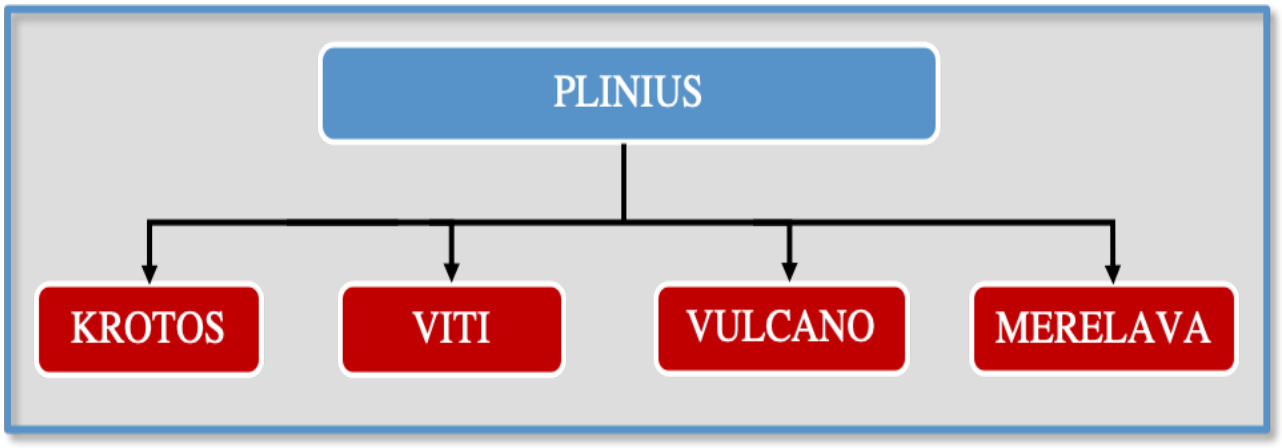

FIGURE 1.5: Experimental facilities at the PLINIUS platform.

code, **KIWI** image processing and analysis software. KIWI stands for **K**rotos **I**mage analysis for **W**ater-corium **I**nteraction. There are three other facilities at the PLINIUS platform, i.e., VITI, VULCANO, and MERELAVA. The former is dedicated to studying physical properties of corium core catcher material properties, whereas the latter two are used to conduct experiments on Molten Corium Concrete Interaction (MCCI).

1.5.2 Future experimental platform: PLINIUS-2

In order to support the safety of Generation II, III and IV reactors, a new experimental platform is under conception at CEA Cadarache, to carry out tests with large masses of prototypic corium. This experimental platform, PLINIUS-2 is foreseen to have three different facilities to conduct tests on Corium-Sodium interaction, Corium-Water interaction and the third one for experiments to study decay heat simulation (material ablation/mitigation). The experimental platform will be composed of three underground halls as illustrated in Fig. 1.6, each devoted to one particular test with sodium, water and material ablation/mitigation [21]. A mobile cold crucible induction furnace designed to melt and pour up to several hundreds of kg of prototypic corium in the test sections will be placed above the three halls on the ground level. A sketch summarizing the experimental facilities in PLINIUS-2 platform is shown in Fig. 1.7. In the facility for Corium-Sodium interaction studies two series of tests will be performed: **PLINIUS-2-FR** dedicated to the study of corium jet fragmentation/premixing stage with corium masses of up to 50 kg and **PLINIUS-2-EXPLO** dedicated to the study of explosion stage of FCI with larger masses of at least 200 kg poured into sodium [21]. The details of this facility will be discussed in the next chapter. The Corium-Water facility and Material ablation facility under PLINIUS-2 platform are not presented here, as it is beyond the scope of this thesis.

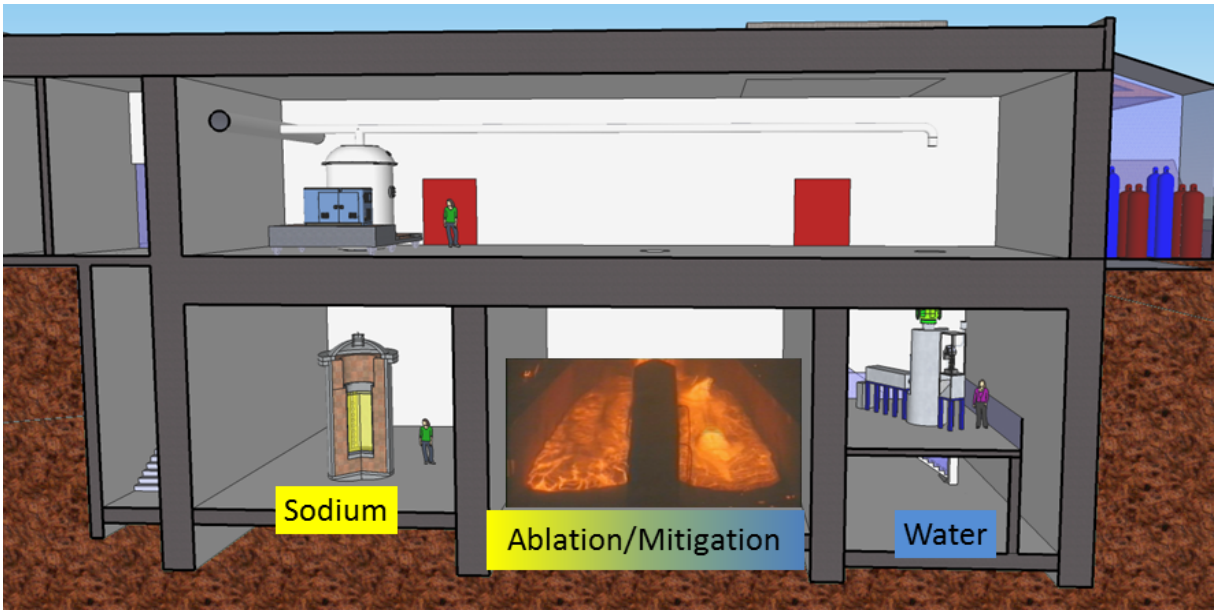

FIGURE 1.6: Schematic view of PLINIUS-2 platform [21].

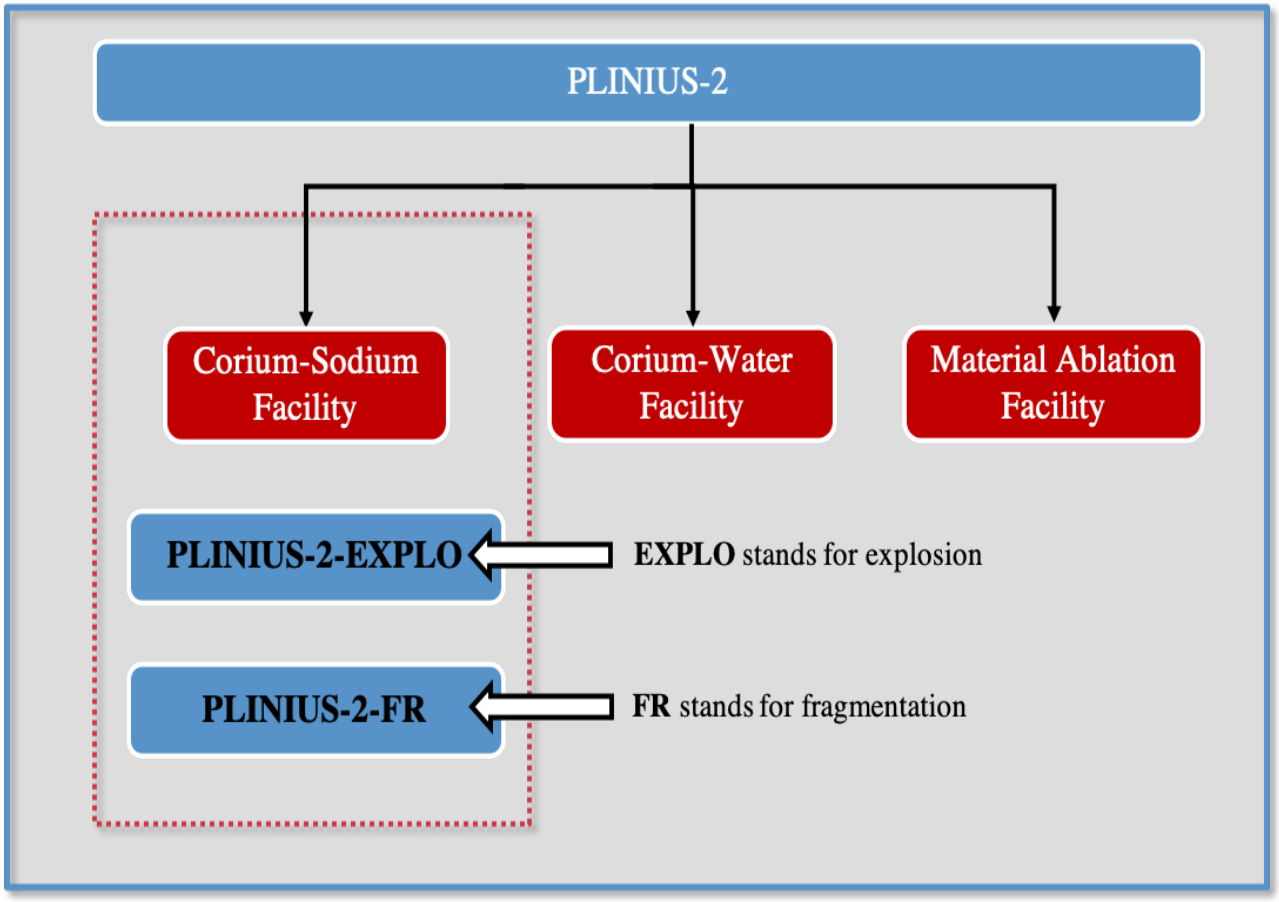

FIGURE 1.7: Experimental facilities at the PLINIUS-2 platform.

It should be noted that like the KROTOS facility which has an X-Ray imaging system to visualize the Corium-Water Interaction and an image processing tool, KIWI, it has been planned to provide PLINIUS-2-FR facility

with an X-Ray imaging system as well as an image processing algorithm to visualize Corium-Sodium interaction. However, due to the complexity and the difference between the two facilities, the same X-Ray imaging system cannot be used.

1.6. Motivation and research objective

Since the 1960s, the understanding of FCI mechanisms in case of SFRs has evolved, but it still remains incomplete. Due to the possibility of occurrence of large scale FCIs in case of a severe accident in a SFR [22], there is a need to investigate the underlying phenomena and develop a clear understanding of the interaction mechanism. To attain a better understanding, CEA is interested in studying FCIs, incorporating, both model development and performing new experiments. Modeling of corium-sodium heat transfer and corium fragmentation is being achieved by developing the SCONE code [10]. Whereas, on the experimentation side, CEA is designing the PLINIUS-2 platform, to carry out tests involving significant masses of prototypic corium with a high-temperature range of sodium (from 400°C to the sodium saturation temperature). Also, CEA is planning to perform small scale experiments, to understand basic phenomena such as sodium film boiling and corium droplet fragmentation [13]. Knowledge from these small scale corium-sodium interaction experiments will help in the development of the software SCONE incorporating all the physics of the interaction. SCONE will thus act as a knowledge repository of corium-sodium interaction. Also, the results from the large scale PLINIUS-2 experiments will help in the validation of such software. Thus, the simultaneous visualization of an interaction phenomenon holds importance.

In order to attain a better understanding of CSIs, experiments have recently been improved by applying X-Rays to study the spatial distribution of the phases present in the interaction zone [23]. However, the X-Ray images need to be processed in order to precisely locate the phases involved. In this research work, we will develop an X-Ray radiography system to visualize the spatial distribution of the three phases:

- Fuel- molten melt
- coolant- liquid sodium
- coolant- sodium vapor

This thesis also reports the experimental radiography performed on models representing certain configurations supposed to occur during FCIs in SFRs. Also, it describes the development of a new image processing algorithm

associated to the qualitative and quantitative analysis of the multi-phase flows. The application of this algorithm to visualize an FCI in sodium will also help further developments and validation of computer models.

The imaging system studied in this research integrates a high energy X-Ray source with high-speed imaging to produce data for configurations including jet fragmentation and explosions.

1.7. Thesis organization

This thesis involves a literature study for FCI and X-Ray image processing, radioscopy system modeling, experimentation and analysis of the X-Ray images from the experiment with mockups. In order to give a brief overview of the progression of the thesis, below is a description of what each chapter has in store.

Chapter 2 reports various experimental facilities worldwide and their X-Ray imaging system (if any) for the simultaneous visualization of molten fuel in sodium. This section also details the FCI test facility for CWI called KROTOS, its measurement X-Ray radiography system and its image processing algorithm. This section also describes in detail the future experimental platform PLINIUS-2 and the X-Ray radiography system that is expected to be utilized for the visualization of the CSI.

Chapter 3 details the relevant past experiments conducted at the facilities worldwide and the statistical analysis of debris bed particles formed, to conclude its characteristic particle shape and size.

Chapter 4 presents the importance of modeling the medium expected in the future test section as a prerequisite step to performing visualization experiments with mock-ups, followed by the description of the X-Ray chain modeling CEA software used, MODHERATO. The need of modeling of fuel particle clouds is presented henceforth, followed by simulations of liquid sodium and its vapor bubbles with this software. It then presents the designs of the mock-ups ("phantoms") representing in a static way some expected medium configurations, their modeling with MODHERATO, issues with the modeling and the need for performing experiments and adapting the KROTOS radiography chain for experiments representing the PLINIUS-2-FR setup.

Chapter 5 describes the experimental apparatus, the configuration description and the way the measurements were made with the phantoms. It also presents the radioscopy images obtained in all the chosen configurations and the comparison of experimental images with MODHERATO modeling.

Chapter 6 details the development of the image processing and analysis software, PICSEL for the analysis of corium-sodium interaction. This software is applied on the experimental images obtained from radiography. The

implemented techniques including filtering techniques and background removal, qualitative analysis including the cloud detection segmentation technique, void (vapor) thresholding techniques and particle motion detection.

Chapter 7 reports a preliminary validation of the PICSEL software on a KROTOS-ALISA test. It also reports the results of the analysis, developments made in the study and describes the improvements that could be applied in the image analyses software for its further development.

This manuscript finally summarizes the conclusions and future perspectives of the research developed during this Ph.D. and suggests strategies to improve the knowledge of FCIs.

Chapter 2

FCI facilities and X-Ray imaging sytems

> *Since human wisdom cannot secure us from accidents, it is the greatest effort of reason to bear them well.*
>
> John Paul Jones

As mentioned in the previous chapter, the Ph.D. thesis aims to help developing the future PLINIUS-2 platform at CEA Cadarache to study corium-sodium interaction and the associated image processing tool. Presently, CEA experimental research is only restricted to corium-water interaction. In order to gain knowledge on corium-sodium interaction, it would be interesting to review all the existing facilities worldwide to develop the concepts, ideas, and principles, the knowledge of which would finally contribute to the development of PLINIUS-2-FR facility.

The following section summarises all the major facilities available worldwide to study FCI along with their X-Ray imaging system if available. It also discusses the principle behind X-ray image formation.

2.1. FCI test facilities worldwide

In the aim of improving nuclear safety, facilities worldwide have thrived between the years, $\sim$ 1980s and $\sim$ 1990s to perform tests to study FCIs in sodium and water and understand how various factors influence an interaction. A brief description of the facilities of interest in connection to our large scale PLINIUS-2-FR facility is discussed below. The results of the relevant experiments conducted in these facilities will be presented in Chapter 3.

1. **FARO-TERMOS (European Commission),** $\sim$ 1990**:**

   The FARO-TERMOS program was defined to contribute to the understanding of the interaction of kilogram-scale of molten fuel with sodium. It consisted of a test section TERMOS connected to the FARO furnace via a release channel as illustrated in Fig. 2.1. In the furnace pure UO_2 melt of 100 kg scales at

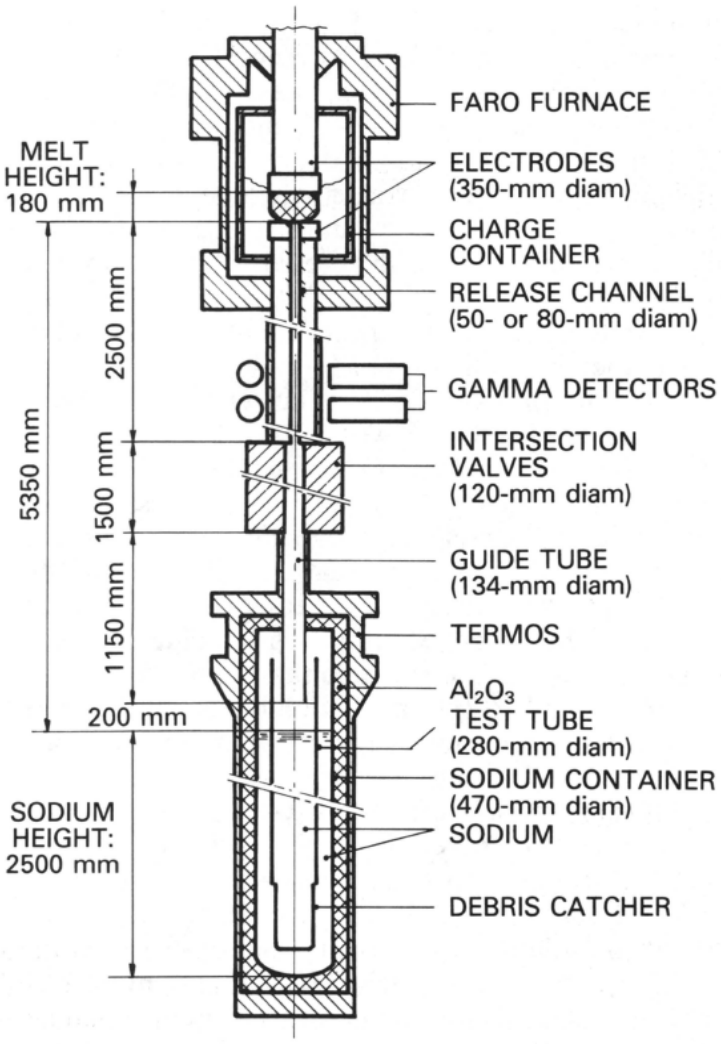

FIGURE 2.1: Experimental sketch of the FARO-TERMOS facility [17].

3000°C is produced and is made to fall into 130 kg of sodium in the TERMOS test section [17].

The initial plan of the experimental program of this facility was to reach low sub-cooling temperatures of sodium, but it was aborted after conducting only two tests of high sodium sub-cooling. However, this facility lacked an associated X-ray imaging system to produce data that could have been very crucial for understanding corium-sodium interaction mechanism. Nevertheless, the results from this experiment remain the most instructive when it comes to mixing large masses of materials.

2. **THINA (Germany),** $\sim$ 1990**:**

A series of experiments were conducted at this facility with an objective to know whether energetic

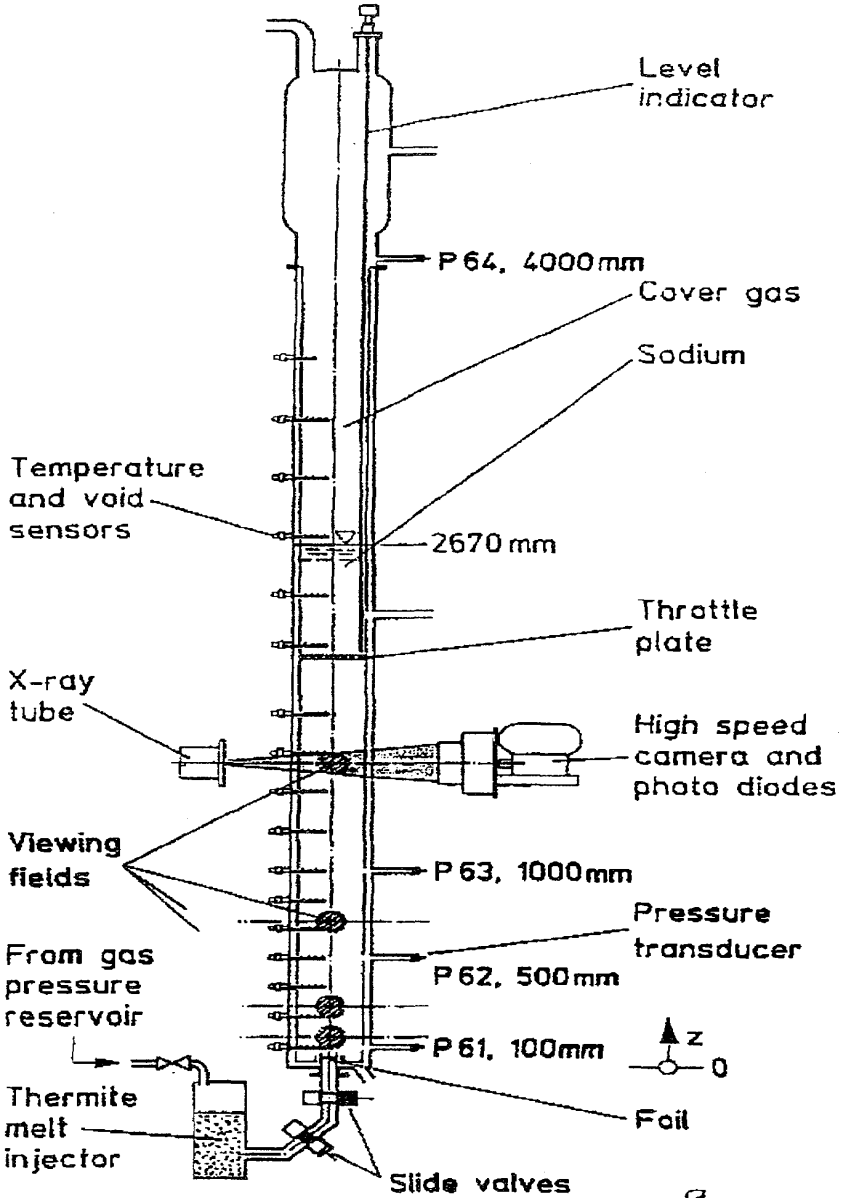

FIGURE 2.2: Experimental sketch of the THINA facility [18].

thermal interactions are possible with sodium. Simulants such as iron-alumina thermite reaction were injected into a sodium filled test vessel from below as shown in Fig. 2.2. The test vessel was equipped with four X-Ray imaging system which was made possible considering the small diameter of the test vessel.

Since alumina is used as a simulant in these tests and due to differences in the behavior of alumina and prototypic corium [24], this puts a limitation on the data being crucial for the PLINIUS-2-FR facility. Also, the injection of the melt from the bottom is different from the ejection mechanism of melt in PLINIUS-2-FR. Thus, this test facility could not be considered significant for our case.

3. **CORECT-2 (France),** $\sim 1980 - 1990$**:**

This facility was aimed to study the fall of sodium in the molten pool that could be generated in a sub-assembly. About 100 litres of sodium contained in column D was dropped onto a 5 kg molten UO_2 pool in the interaction chamber B shown in Fig. 2.3. The contact mode used in this case was not applicable to our

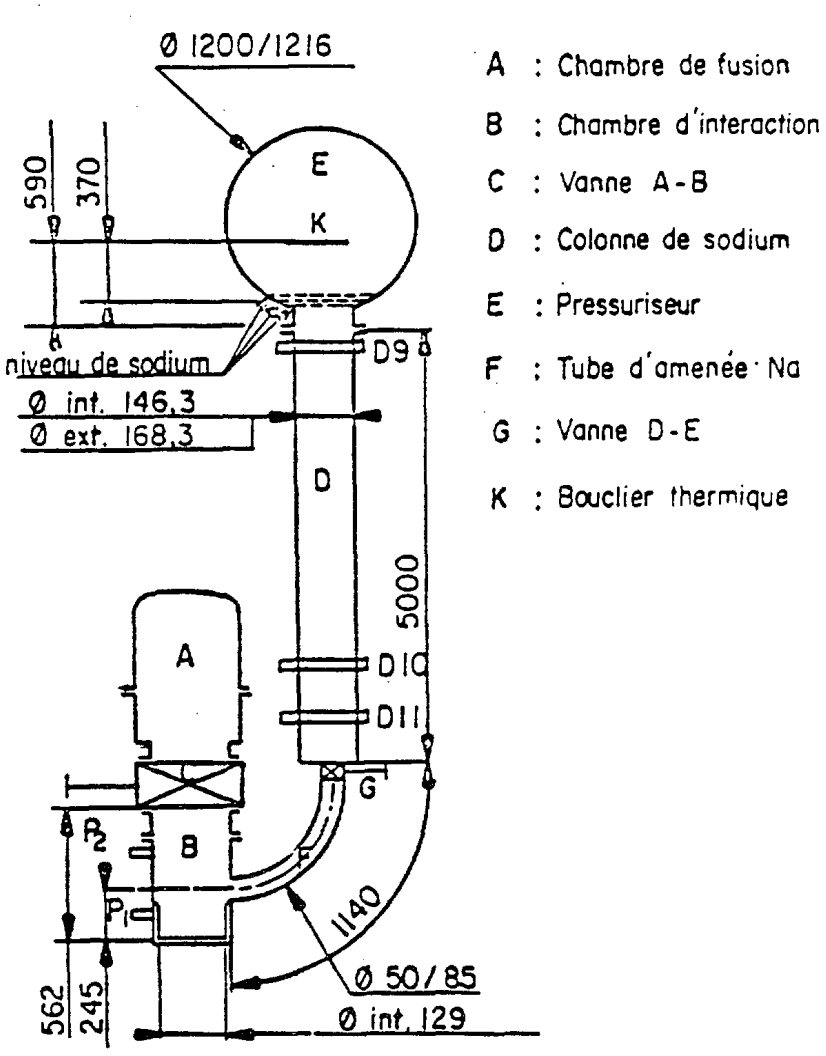

FIGURE 2.3: Experimental sketch of the CORECT 2 facility [5].

case. Also, there was no X-ray imaging that could support and produce significant results. Thus, this test was not considered for study.

4. **BETULLA I (European Commission),** $\sim$ 1980**:**

   Within the context of Nuclear Safety Program, the Joint Research Center (JRC) of Ispra in close collaboration with KfK, Karlsruhe built a facility called Betulla I. Fig 2.4 depicts the schematics of the facility. A crucible containing 4 kg of molten UO_2 at is dropped from the heating furnace above the interaction tank via a tube. Before its arrival the crucible is caught and overturned automatically, and the $UO_2$is spilled

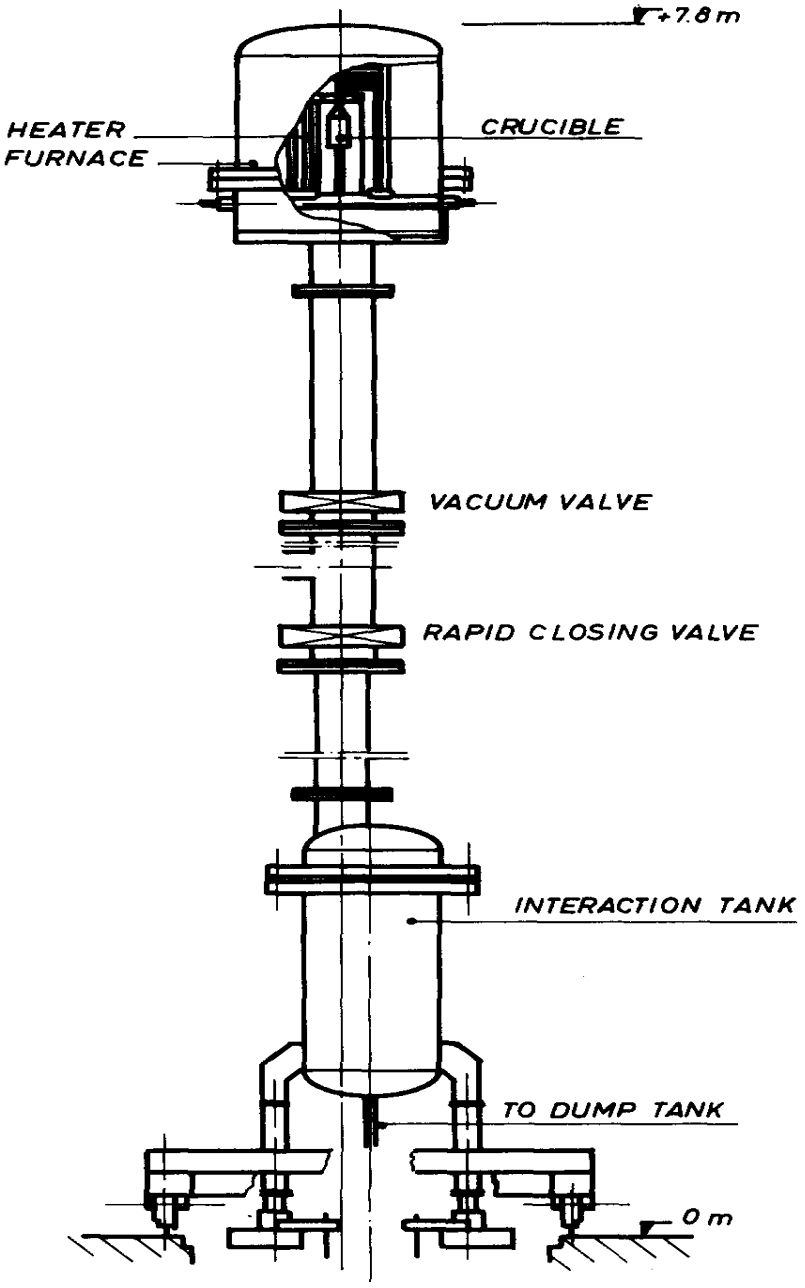

FIGURE 2.4: Experimental sketch of the Betulla I facility [19].

into a pool of liquid sodium between 350°C and 700°C [25].

The use of significant masses of UO_2 fuel to observe its interaction with low sub-cooled sodium (of T= 700°C) produced important results, and thus tests in this facility were considered for our study. However, this facility also lacks an X-Ray imaging system to have a simultaneous visualization of the test.

5. **FRAG series (USA),** $\sim$ 1980**:**

The Frag series experimental program was designed to determine the mode of fuel fragmentation and the characteristics of resulting debris. Experiments in this series utilized 20 kg each of sodium and molten stainless steel-UO_2-ZrO_2 melt. The melt was released by a melt out channel into a sodium crucible assembly [26]. Schematics of the facility used is shown in Fig. 2.5. As none of the constituents of the fuel and the cladding in SFRs include ZrO_2, thus this facility using ($SS-UO_2-ZrO_2$) is not consistent

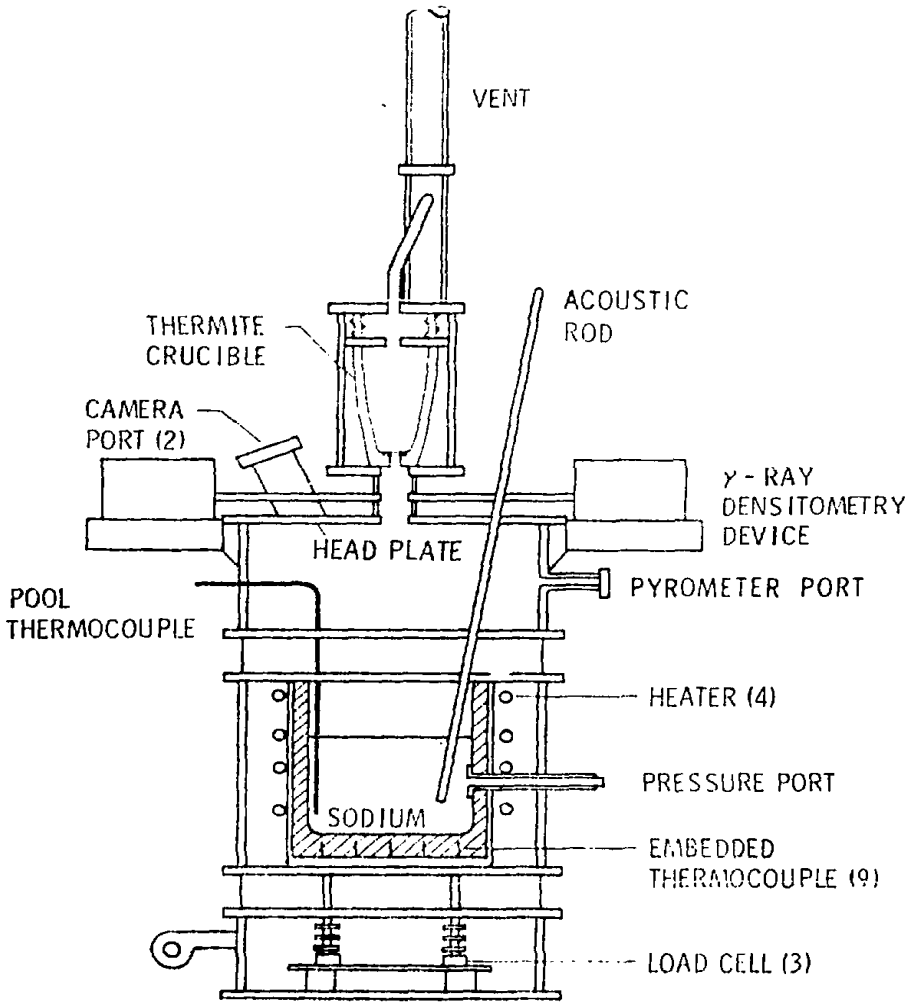

FIGURE 2.5: Experimental sketch of the FRAG facility [26].

with the prototypical composition. However, this facility employing large masses of fuel melt ejected in high-temperature sodium pool represented the case of PLINIUS-2-FR well. Thus, the results from tests in this facility could be exciting and thus was considered for our study. However, in this facility too, no X-Ray imaging system was used.

6. **SOFI facility (India),** $\sim 2010 - operating$**:**

The objective of the facility is to generate data for understanding the various fuels ($U/UO_2/Zr$/steel) melt-solidification and fragmentation, dispersion/relocation of debris, settlement behavior on core catcher, to validate the numerical models for predicting the above mentioned phenomenon. In the first phase

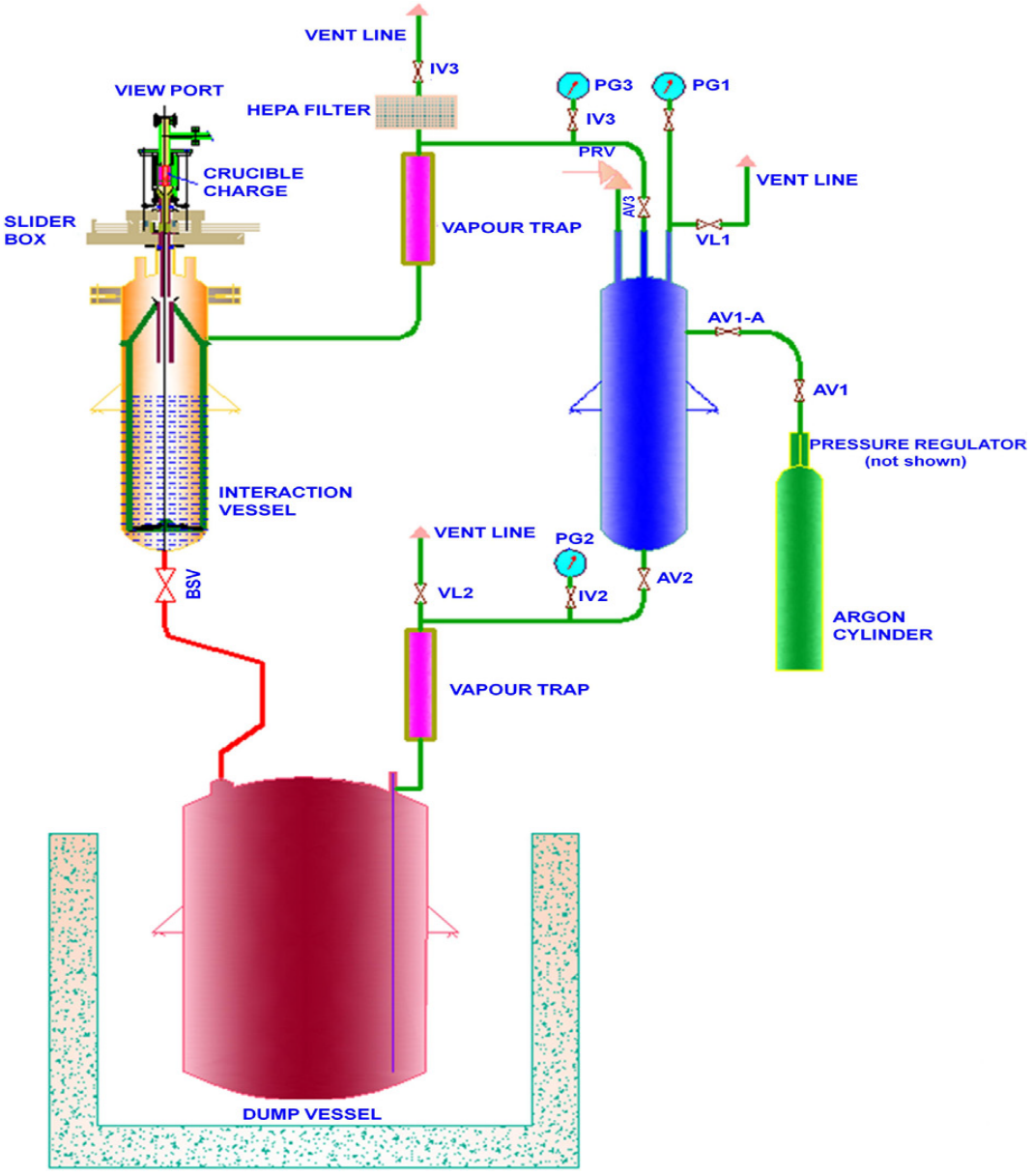

FIGURE 2.6: Schematics of the SOFI facility [27].

simulants like woods metal is being used in the water system. In the second phase, molten SS304L and sodium will be used and in the third phase molten UO_2 and sodium will be used. An X-Ray imaging technique to depict the FCI process following a severe accident scenario in SFRs, is being developed [28]. Schematics of the SOFI facility is shown in Fig. 2.6.

Till date, tests with water have only been conducted in this facility. The interaction process being different for water and sodium, the results from this facility could not be a representative of our case.

7. **EAGLE project (Kazakhstan),** $\sim 1998 - operating$**:**

Within the EAGLE project, an out-of-pile facility at the National Nuclear Center of the Republic of Kazakhstan (NNC/RK) is used with an objective to obtain preliminary data on fuel movements under conditions simulating an accident involving the melt of the core. The work is performed by the NNC/RK together with Japanese organizations [29]. A schematic of the test section is shown in Fig. 2.7.

Alumina (Al_2O_3) was employed as a simulant for molten oxide fuel [30]. However, since large differences in the behavior of alumina and UO_2 with water have been shown [24], the results from this facility will not be considered in our study.

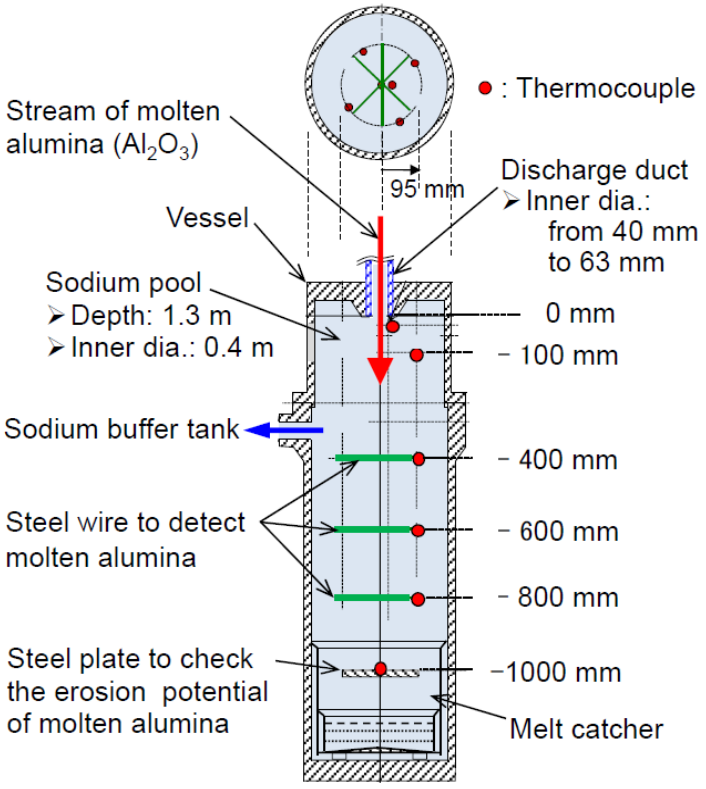

FIGURE 2.7: Schematics of the EAGLE facility [30].

8. **PLUTON (Russia),** $\sim 2014 - operating$**:**

   This facility was designated for investigation of corium simulator (melt ZrO_2 + Fe; Al_2O_3 + Fe; UO_2 + Mo) thermal interaction with sodium and fuel thermal elements cladding damage under ULOF accident conditions. The melts are produced by thermite reactions, initiated using electric heating. The principal unit of the experimental set-up is the reaction chamber, equipped with pressure pulsation sensors. It is supplied by the bypass line with a magnetic flowmeter to measure sodium relocation [31]. However, two of the test fuels in this facility used alumina and ZrO_2 as a simulating material for oxide melt and thus could not be considered for our study. Moreover, since tests with only small masses of around 0.11 kg were conducted in this facility, it could not be considered representative of PLINIUS-2-Fr future tests employing large masses.

9. **MELT (JAEA, Japan),** $\sim 2014 - operating$**:**

   This facility aims at performing out-of-pile experiments related to the molten core material behavior in SFR severe accidents. It basically consists of a melting section and a test section as shown in Fig. 2.8. In the melting section, about 20 *l* of materials such as alumina and stainless steel is melted in the induction heating furnace. The molten materials are poured into the test section through a nozzle by pulling out a plug at the furnace bottom. There are two test sections in this facility, one with liquid sodium and one with water (as a simulant of liquid sodium) [23, 32]. The test section is located in a pit to prevent the external escalation of potential abnormal events accompanying the experiments. An X-Ray imaging system (frame rate: 1000 frames per second) is available for the visualization of transient phenomena in the test section. The MELT facility has been utilized to investigate structure erosion by the melt-jet impingement, fuel-coolant interaction (FCI), etc.

   A recent test, conducted with Aluminium (to simulate metallic component of corium) and sodium (at 400°C) in the MELT facility, simultaneously visualized the test with its X-Ray imaging system [32]. The imaging results could not be analyzed due to the lack of image processing software. Nevertheless, the results from this test are very important for the PLINIUS-2-FR facility.

10. **MISTEE (Stockholm),** $\sim 2010 - operating$**:**

    MISTEE that refers to Micro Interactions in Steam Explosion Experiments is a facility situated at the Royal Institute of Technology (KTH) in Stockholm, Sweden. This facility was designed to study the explosion of a single droplet of molten material [33]. A schematic diagram of MISTEE facility is shown in Fig. 2.9. Approximately 1 g of the simulant melt used in these experiments which is often woods metals

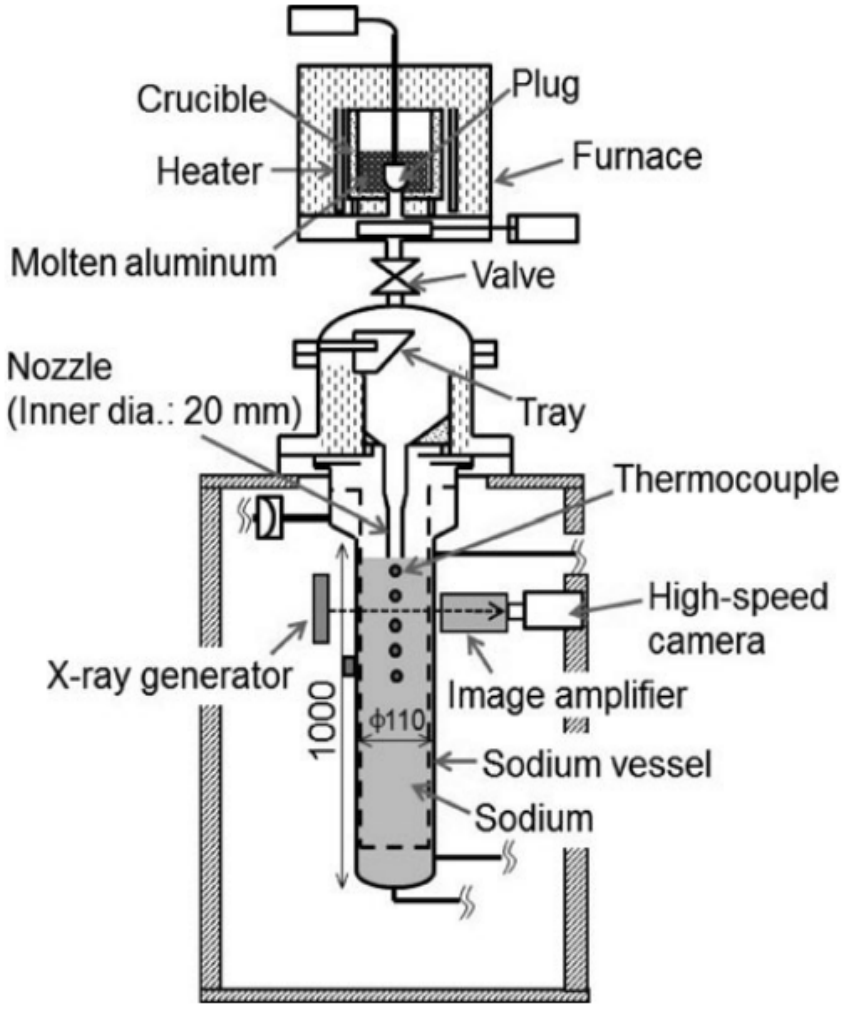

FIGURE 2.8: Schematics of the MELT sodium facility [23].

is prepared in a metal or ceramic crucible. The desired temperature is obtained using an induction furnace and the melt reaches the test section via a hole at the bottom of the test section. It then interacts with water in the test section.

This facility is equipped with the simultaneous high-speed acquisition of X-Ray Radiography and photography (SHARP) shown in Fig. 2.10. The photography part consists of tungsten lighting and a high-speed CMOS digital camera with 20,000 frame rate [33] whereas the radiography part consists of an X-ray source of maximum energy 320 keV, an X-Ray converter and image intensifier. The interaction is captured using a very high frame rate CMOS camera (5000 frames per second) [33].

Recently the facility was modified to conduct experiments using jets of molten material (with jet diameter around 5-10 mm) [34]. With this modification, the facility was renamed to MISTEE-Jet facility. Tests

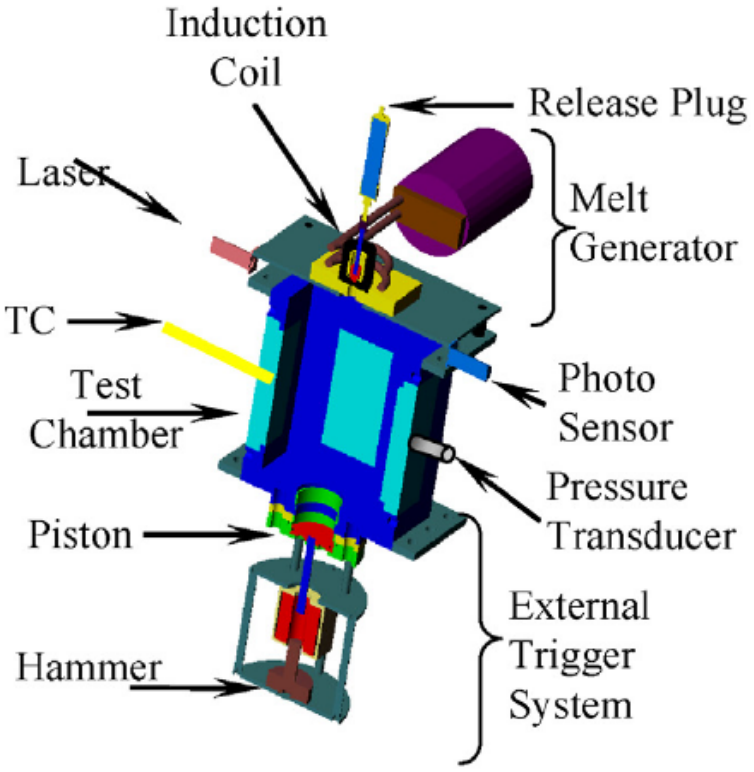

FIGURE 2.9: Schematic of the MISTEE facility [33].

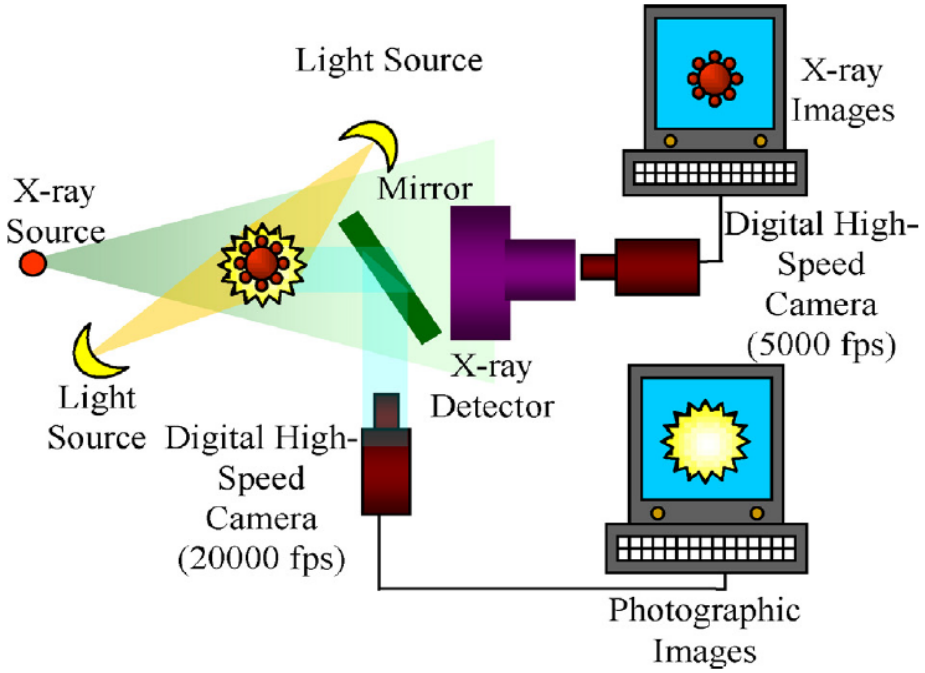

FIGURE 2.10: The SHARP visualization system of the MISTEE facility[33].

are conducted at the MISTEE-Jet facility with woods metal or tin used as a simulant to replicate metallic corium and a mixture of $WO_3-Bi_2O_3$ or WO_3-ZrO_2 used to replicate oxidic fuel. No significant heat

transfer between the woods metal and water takes place as the melting point of woods metal (70°C) is less than the boiling point of water [34]. The experiments were conceived to investigate the effect of thermal and hydrodynamic fragmentation on the jet. The experiments indicated that the melt jet underwent Rayleigh-Taylor instability (surface wave instability) at lower velocities and Kelvin-Helmholtz instability (wave stripping) at higher velocities. However, since this facility employed small masses of melt injected in water, their representativeness to PLINIUS-2-FR was not justifiable.

2.2. FCI facilities of CEA Cadarache and their X-Ray imaging system

As introduced in the Chapter 1, CEA Cadarache has an existing facility, KROTOS, to study corium-water interactions and a new facility PLINIUS-2-FR is being designed to study the corium-sodium interaction. This section will discuss the X-Ray imaging systems of these facilities to investigate the mixing behavior, allowing a clear characterization of the mixture (volume fractions and spatial distribution of melt, liquid coolant and coolant vapor).

2.2.1 KROTOS corium-water interaction facility

The KROTOS facility (Fig. 2.11) at CEA Cadarache, investigates the prototypic corium-water interactions involving energetic events, i.e. steam explosions [35, 36]. Several tests with ∼5-8 kg of corium melt with water at temperatures ∼ 60°C have been performed at this facility. The KROTOS facility consists of two primary parts: the furnace and the test section as shown in Fig. 2.11. The furnace is a water-cooled stainless steel chamber, consisting of a cylindrical tungsten heating element which is enclosed by a crucible containing the melt material. The positioning of the tungsten crucible is maintained by a pneumatically operated release hook. The furnace is connected to a 130 kW transformer which allows reaching melt temperatures up to 2800°C. After having reached the desired melt temperature, the crucible is released from the furnace. At the bottom of the furnace, a rapidly acting ball valve and a tungsten wire are located. The crucible cuts the tungsten wire and provides a trigger signal for activating the data acquisition and also closes the valve immediately after the crucible passes so as to isolate the furnace from the test section during FCI.

Next, the crucible passes through the transfer channel which is a 4 m long vertical tube connecting furnace to the test section. The crucible falls down by gravity until it is impacted by a puncher, located at the top of the

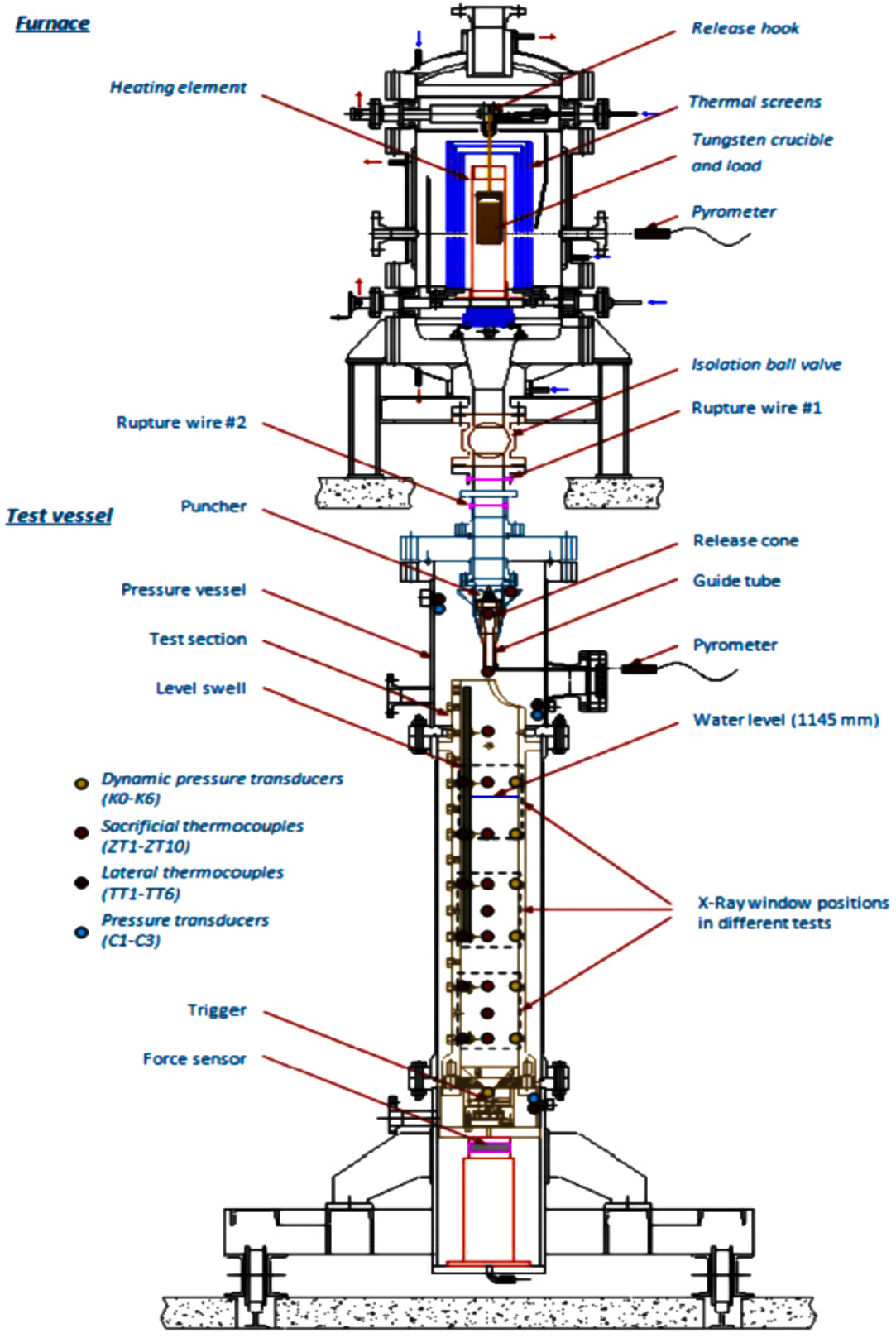

FIGURE 2.11: Principle scheme of the KROTOS installation [37].

test section. The puncher breaks the bottom of the crucible following which the corium flows down to the test section.

The test section consists of a pressure vessel and a test tube placed inside it. Both these components are made up of fortal, an aluminum alloy which allows low attenuation of the X-Ray radiation. The pressure vessel is designed for a pressure of 2.5 MPa at 493K [37]. The test tube is a free-standing cylinder of inner diameter 20 cm and length 160 cm. It can contain water upto variable heights. Several thermocouples (K-type) are used to measure the temperature of the gas atmosphere and of the water in the test tube. At the bottom of the test section, a pressurized (15 MPa) gas trigger device is positioned [38]. It can trigger a steam explosion in the test section once the desired premixing state of FCI is attained.

X-Ray radioscopy system at KROTOS

Various FCI facilities mentioned above, utilize different X-Ray imaging systems and the associated image processing and analysis tools. All the X-Ray imaging systems are based on a common principle that governs the formation of images using an X-ray source. This section describes the interaction of X-Rays with matter and the different processes that can lead to the formation of an image.

Principle of X-Ray image formation

It is imperative to study how X-Ray interacts with a particular material and how does the energy of the X-Ray beam affect the results in the X-Ray radioscopy. There are three major processes that can occur when an X-Ray photon interacts with matter:

- **Photoelectric absorption**: In this process, the energy of the incident X-Ray photon is completely transferred to the atom of the interacting material. As a result, an electron is emitted from the bound shell of the atom. This interaction takes place between the incident X-Ray and the atom as a whole and not with the free electrons [39]. This process is dominant at low energy X-ray photons (typically around 100 keV). Also, a high atomic number Z favors the photoelectric effect. The probability of occurrence of photoelectric absorption is proportional to Z^n / E^3 where n varies between 4 and 5. The choice of the energy of the X-ray source should be greater than 100 keV to avoid photoelectric absorption [39].
- **Compton scattering**: This interaction occurs between the incident X-Ray photon and an electron of the interacting material. In this scattering, the incident X-Ray photon is scattered to a particular angle and a

portion of the energy is transferred to the electron. The angle of scattering of the photon depends on the scattering cross-section of the material. This means that even for the same incident energy of the X-Ray photon, the photons can be scattered differently for different materials. When the photons are scattered to small angles the energy transferred to the electron is low [39]. This feature makes it a favorable choice while deciding X-Ray source that for a small angle of scattering, the scattered energy of the X-Ray will be close to the incident beam. The probability of occurrence of Compton scattering is high in the high energy region (typically around 5-10 MeV) [39]. Since Compton scattering occurs between the incoming X-Ray photon and the electron of the interacting material, the higher the number of electrons, the higher is the probability of Compton scattering. Due to this reason, Compton scattering is linearly proportional to Z and hence less sensitive to the choice of material. Because of all the above favourable reasons, one would choose the energy of X-Ray source that favors Compton scattering..

- **Pair Production**: When the energy of the X-Ray photon is greater than twice the rest mass of an electron (1.02 MeV) pair production takes place. The X-Ray photon is completely absorbed by the nucleus and an electron-positron pair is formed. Any excess energy beyond 1.02 MeV is shared between the positron and the electron. The positron further annihilates into two annihilation photons. The magnitude of the probability of pair production varies as the square of the atomic number of the interacting material [39]. By choosing a very high energy X-Ray source, one would obtain a high energy photon on the detectors.

Due to the interaction processes explained previously, i.e. the photoelectric absorption, Compton scattering and pair production, the incident X-Ray photons on the interacting material are either absorbed (due to photoelectric absorption or pair production) or scattered (due to Compton effect) and might not be able to be detected by a detector (in case it is not scattered in the direction of the detector). The probability of occurrence of each of the interaction process is quantified per unit path length of the interacting material which is called linear attenuation coefficient μ.

Hence, in the case of X-Ray radioscopy when the incident X-Ray photon passes through the interacting material, it undergoes attenuation, i.e. the intensity decreases. This phenomenon of a decrease in the intensity of X-Rays is governed by Beer Lambert's law [39]:

$$I = I_0 \, e^{-\mu \, x} \tag{2.1}$$

here, I_0 is the intensity of the incident X-Ray beam. I is the intensity of the transmitted beam after undergoing attenuation. μ and x denotes the linear attenuation coefficient and the thickness of the matter respectively.

However, for the same material, the linear attenuation coefficient varies with the density of the material, i.e., the linear attenuation coefficient is different for liquid water or water vapor. To avoid this, generally the mass attenuation coefficient μ_m is utilized which is given by:

$$\mu_m = \left(\frac{\mu}{\rho}\right) \tag{2.2}$$

The mass attenuation coefficient is a unique parameter for a given material. For example, steam, water and ice are characterized by a unique mass attenuation coefficient and the difference in their linear attenuation is coming solely from the difference in their density. However, the mass attenuation coefficient is not a constant parameter, it is dependent on the incident beam energy and is determined experimentally.

The incident X-Ray beam is not monochromatic, i.e. the beam is characterized by a certain energy distribution. Now using Eq. 2.1 and 2.2 we obtain:

$$I = \int I_0(E) \cdot \exp(-\mu_m(E)\rho x) dE \tag{2.3}$$

Here, ρx is the mass thickness determining the degree of attenuation. Generally, representation of the thickness by the mass thickness is preferred to quantify X-Ray attenuation with the matter.

Along with all the interaction processes discussed above, in real experiments, there are other phenomena that can also contribute to the X-Ray attenuation ; for instance, scattering from the material. The scattering is medium dependent and difficult to predict. Online measurements of the scattering beam can be performed by blocking the incident light in a series of predefined points and measuring the intensity in the corresponding projections.

The transmitted X-Ray photons fall on a scintillator detector, placed on the other side of the X-Ray beam. This scintillator forms an image which is then captured by a camera.

Simultaneous visualization of FCI in the KROTOS test section is achieved through the use of an X-Ray radioscopy system, the schematics of which is presented in Fig. 2.12.

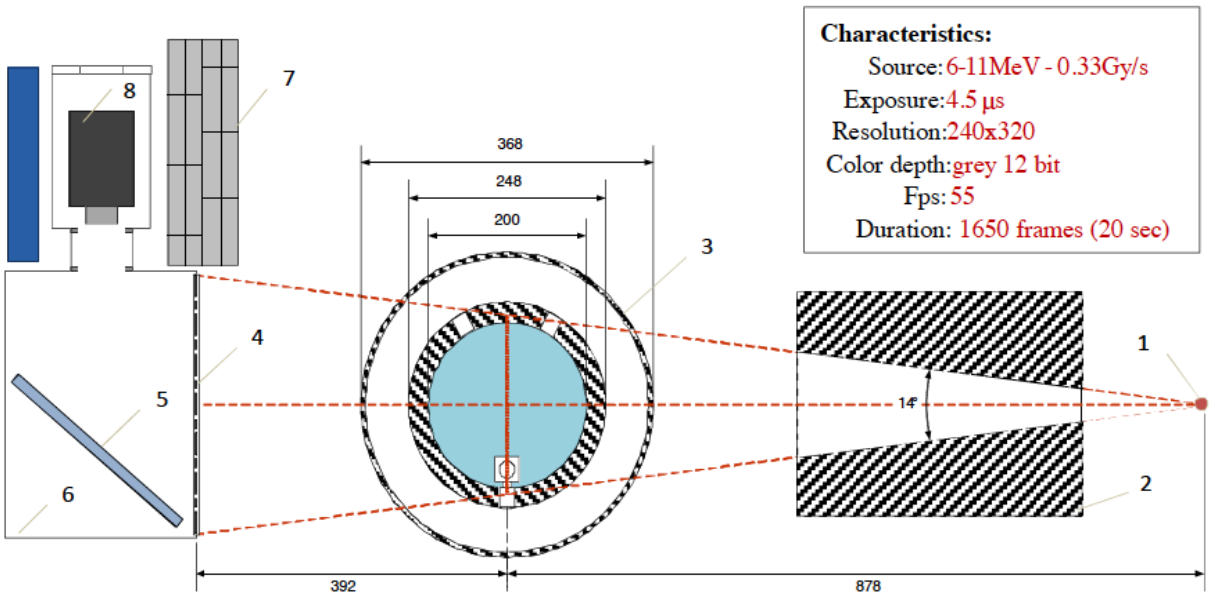

(a) Schematics of the X-Ray radioscopy at the KROTOS facility.

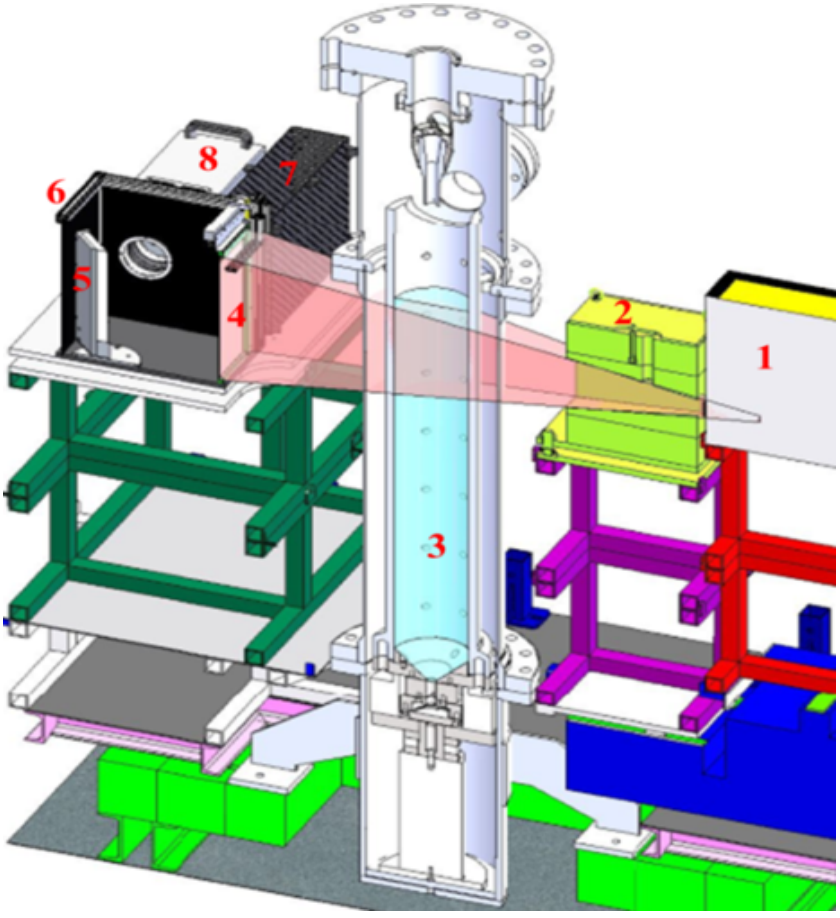

(b) 3D pictorial diagram of the KROTOS radioscopy system.

FIGURE 2.12: Schematics of the X-Ray radioscopy system. 1: X-Ray source; 2: lead collimator; 3: test section; 4: scintillator; 5: mirror; 6: opaque box; 7: lead shields, 8: sCMOS camera [37].

This figure shows both a sketch of the radioscopy system (Fig. 2.12(a)) and a 3D pictorial diagram of the overall facility and its radioscopy system (Fig. 2.12(b)). Component 1 in both the figures of Fig. 2.12 is the high power X-Ray linear accelerator (LINAC). The LINAC model in our facility is a Mini-Linatron as shown in Fig. 2.13. This LINAC emits X-Ray beam of maximum energy 9 MeV [40]. These X-Rays are emitted in the form of pulsed cone-beam of duration 4.5 μs.

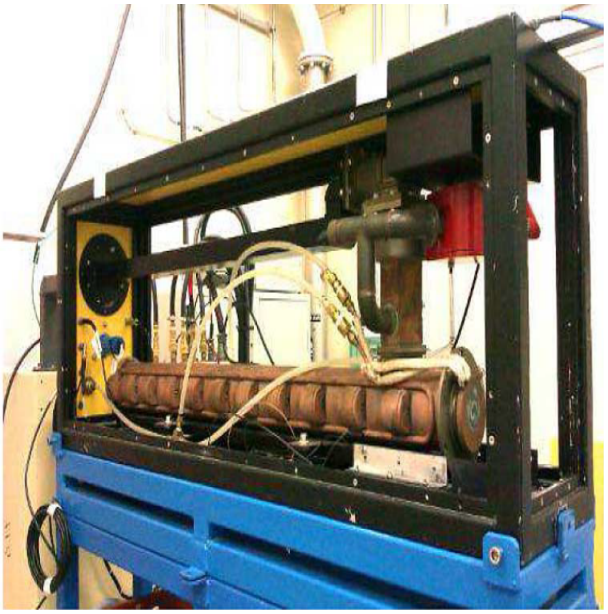

FIGURE 2.13: Linac Mini-Linatron Varian of KROTOS radioscopy system [40].

It passes through the lead collimator represented by 2 in Fig. 2.12 which decreases the noise by suppressing significant amount of scattered radiation [20]. The rays then penetrate the test section (represented by 3 in Fig. 2.12) and the transmitted rays reaches the detection system (represented by 4 in Fig. 2.12). It is important for the detection system to convert the X-Rays to visible light. This is obtained by the use of a scintillator detector. The scintillator utilized in the KROTOS facility is specially designed to be able to perform high-energy imaging, even for large objects. Gadolinium oxysulphide (Gd_2O_2S), often referred as GADOX, has a high density around $7.44\,\mathrm{gm/cm^3}$ [40] and high effective atomic number [41]. This allows a high interaction probability of X-Ray radiation and hence makes it a promising scintillator material in our case [42].

The transmitted X-rays from the test section forms an image on the rear side of the GADOX scintillator screen. These images can be recorded either using CMOS (Complementary Metal Oxide Semiconductor) or a CCD (Charge Coupled Device) [43] camera placed perpendicular to the X-rays (represented by 8 in Fig. 2.12). Currently, in the KROTOS imaging system, a very powerful CMOS camera used for scientific purposes [44] is being employed because of its very low readout noise and high framerate acquisition of 100 frames per second.

It should be noted that the images are not captured directly by the scientific CMOS (often referred as sCMOS) camera, but with a mirror (represented by 5 in Fig. 2.12) placed at 45° to avoid X-rays falling directly on the sCMOS camera and thus damaging it. For an overall protection of the CMOS camera from the scattered radiation, it is protected by a series of lead screens (represented by 7 in Fig. 2.12). Thus, the X-ray radioscopy coupled to the imaging system films the premixing and the explosion stage of the interaction.

The choice of the frequency of the X-Ray source limits the study of the explosion stage of the interaction. For instance, the test performed at the KROTOS facility by Brayer et al. [37], at 55 Hz of the X-ray source was only able to trace the premixing stage but not the explosion stage that occurs at a shorter interval of time.

The field of view of the image formed on the scintillator covers the entire diameter of the test tube (20 cm). However, it cannot cover the entire vertical length of the test tube, i.e., 1.6 m. There are two options to choose the vertical range. One is 31 cm (1/3 of the test tube height) while the other of 64 cm (1/2 to 100% of the pool height depending on the water pool depth) [45]. The radiography system can be easily re-positioned along the vertical direction between the tests; it permits to observe premixing at different levels and to estimate the position of the view with the maximum information to be analyzed.

Image Processing and analysis tool: The KIWI software

OECD/NEA (Organization for Economic Cooperation and the Development/Nuclear Energy Agency) launched a project SERENA (Steam Explosion Resolution for Nuclear Application) to resolve the issues related to steam explosion [36]. SERENA Phase 1 (completed in 2005) concluded that an in-vessel steam explosion would not challenge the integrity of the vessel, but an ex-vessel steam explosion could damage the cavity walls as the calculated loads were in some cases above its load-bearing capacity [11]. However, with no data on the 3 phase distribution (corium, water and steam) in the pre-mixing stage (especially the level of steam) and with an uncertainty in the corium composition effect on the explosion, Phase 1 did not allow for convergence towards a strong understanding [36]. Thus, more research in resolving ex-vessel steam explosion issues were launched with the SERENA Phase 2 project which started in October, 2007 and included new experimental research. With the objective of resolving the 3 phase distribution (especially the level of steam) and the corium effect uncertainty, six experimental tests were performed each at the KROTOS facility of CEA and TROI (Test for Real cOrium Interaction with water) facility of KAERI (Korea Atomic Energy Research Institute). All the experiments conducted at the KROTOS facility, the X-Ray images obtained were difficult to interpret the raw images to get significant information (like the three-phase distribution, the corium volume fraction, void fraction,

size of particles formed in the premixing stage) about the interaction. The raw unprocessed image obtained had to be processed and analyzed. To perform this analysis, a specific software KIWI was developed to perform both image processing/analysis and data computations [37, 46].

The KIWI software and its ability to characterize the distribution of corium, water and steam will be discussed below.

The code has been implemented using MATLAB ver. R2010b, it is compatible with windows graphical user interface and can be executed on Mac, UNIX and Windows platforms within the MATLAB environment. This software is capable of processing the images and extracting the volume fractions of different phases in the pre-mixture.

This is carried out by first pre-processing the images to remove the sparks and lines caused by the X-Ray photons that hit the camera matrix causing its overcharging. After these artifacts are suppressed, the heterogeneous background is removed by dividing the images by its background image. For instance, for the KFC test [37] pre-processing produces an image as shown in Fig. 2.14(b) in comparison to its corresponding raw image shown in Fig. 2.14(a). The pre-processed images are then analyzed qualitatively and quantitatively [37]. For the qualitative analysis, the image is decomposed into the three phases. This is done by first extracting corium particles; afterwards the steam fraction initially hindered by corium is interpolated. Corium particle detection is carried out by image segmentation and edge detection algorithms. The edge detection is performed using Sobel edge detection algorithm [46]. Once the corium particles are extracted, the determination of the interface between steam and water is performed. Instead of steam, an algorithm is developed to detect water regions by simply performing thresholding of the initial image between two values, which are assumed to be the minimum and maximum intensities of the background image. The final qualitatively decomposed image from the KFC test is shown in Fig. 2.14(c) depicting the separating boundaries between corium, steam and water.

Once the images have been decomposed, the quantitative analysis is performed in two steps, one for corium and another for the steam. Quantitative analysis is devoted to the estimation of the steam and corium volumes. The estimation of steam is entirely based on the pixel intensities, while corium computation requires particle boundaries. KIWI performs the corium analysis in two steps: a 3D reconstruction of the corium elements is first performed using the geometrical approach and the method of rolling sphere [46] and in the second step, the volume of the corium droplets is estimated by summation of the corresponding pixels. For more details on these techniques readers are requested to refer to Brayer et al.[37]. The KIWI software computes additional information concerning the corium droplets. Having the volume and the surface area, it can compute their Sauter

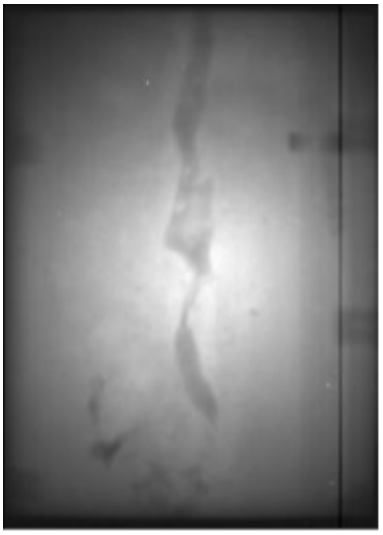

(a) KROTOS KFC test raw image.

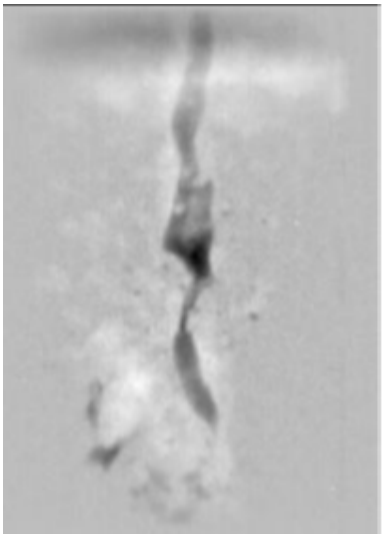

(b) Pre-processed image.

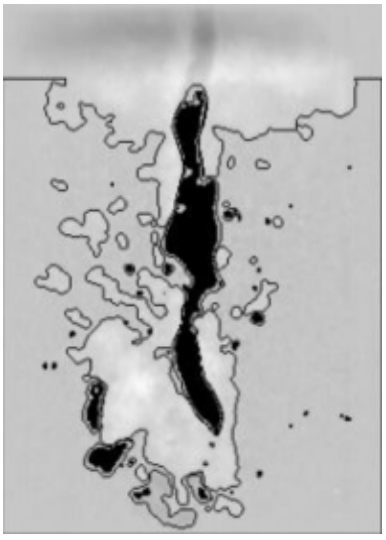

(c) Qualitatively decomposed image.

FIGURE 2.14: Application of KIWI software to process images in KFC test [37].

mean diameter. It can also determine the position of the mass center of each droplet. For instance, data extraction of the KFC test produced the result as shown in Fig. 2.15. The computation of steam depth is performed from steam interpolated images as explained in [37]. The analysis of KFC test depicted in Fig. 2.15, signifies that corium particle size is in the range of millimetres to centimetre during the pre-mixing stage.

2.2.2 Corium-Sodium facility in the future PLINIUS-2 platform

As said in Chapter 1, CEA Cadarache is working on the development of a large mass experimental platform called PLINIUS-2 [21]. This experimental platform will support the ASTRID reactor concept and help to better understand the issues pertaining to severe accidents. This platform will facilitate performing tests with sodium

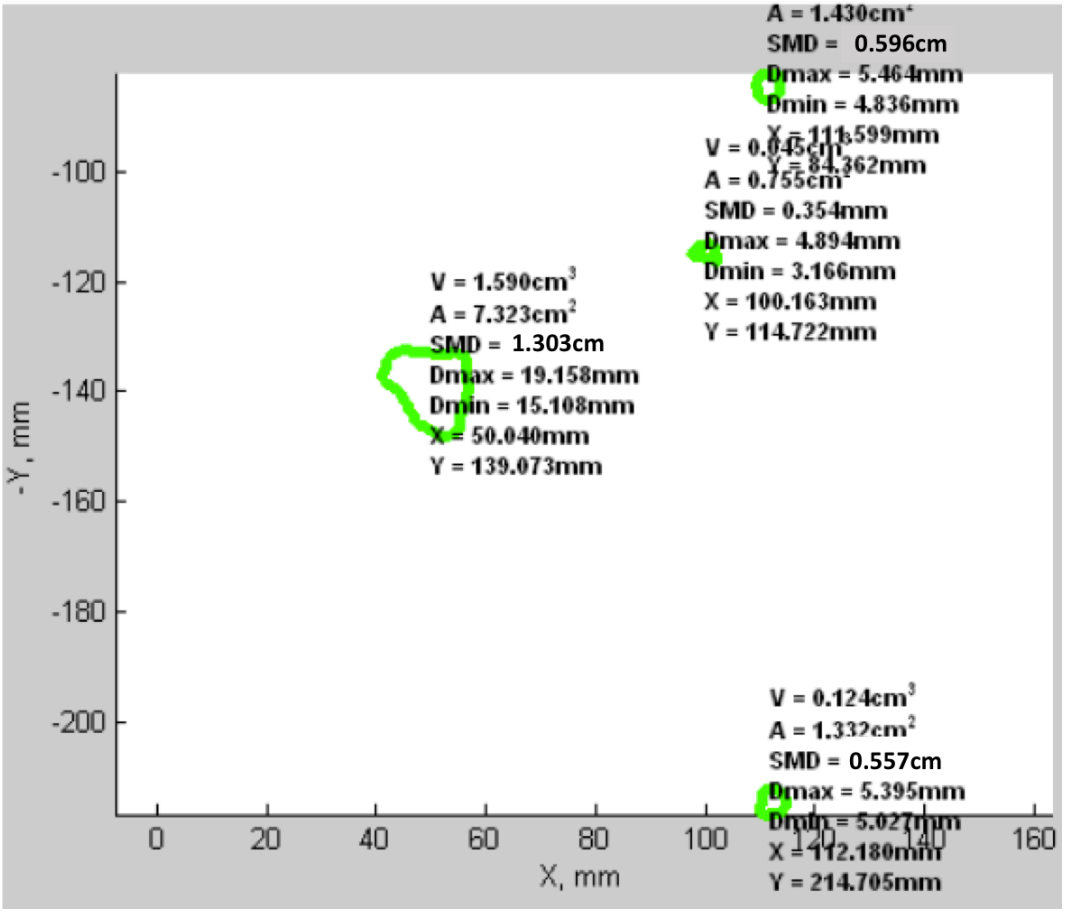

FIGURE 2.15: An example of corium droplet map given by KIWI [37].

and large masses of prototypic corium (up to 500 kg). One of the facilities of this platform will be dedicated to performing corium-sodium interaction test. A pictorial representation of the facility is shown in Fig. 2.16.

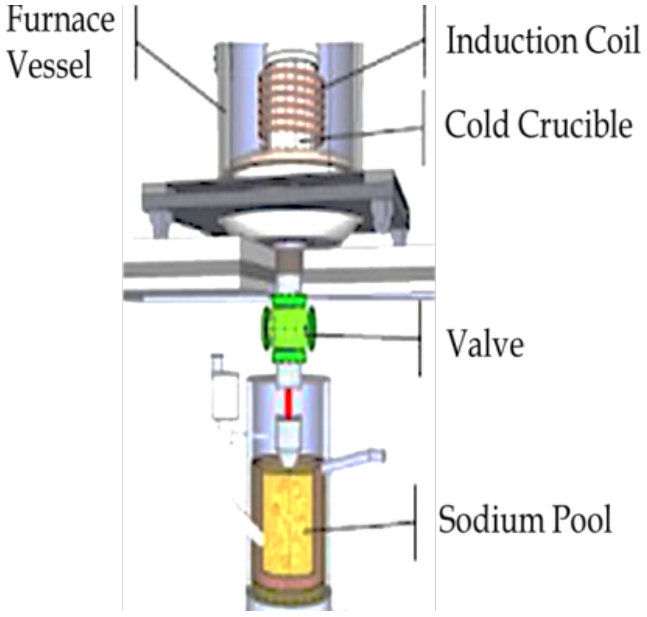

FIGURE 2.16: Schematics of PLINIUS-2 Corium-sodium facility.

The process of the corium ejection from the furnace into the sodium pool will be the same as that in KROTOS. Prototypic corium will be heated to temperatures up to 3000°C in the top furnace vessel. Once the desired corium temperature is reached, the crucible containing the molten corium will be released from the furnace vessel. At the position of the valve, the crucible is pierced at the bottom, to release molten corium into the sodium pool. Two test sections PLINIUS-2-FR and PLINIUS-2-EXPLO have been designed for this facility.

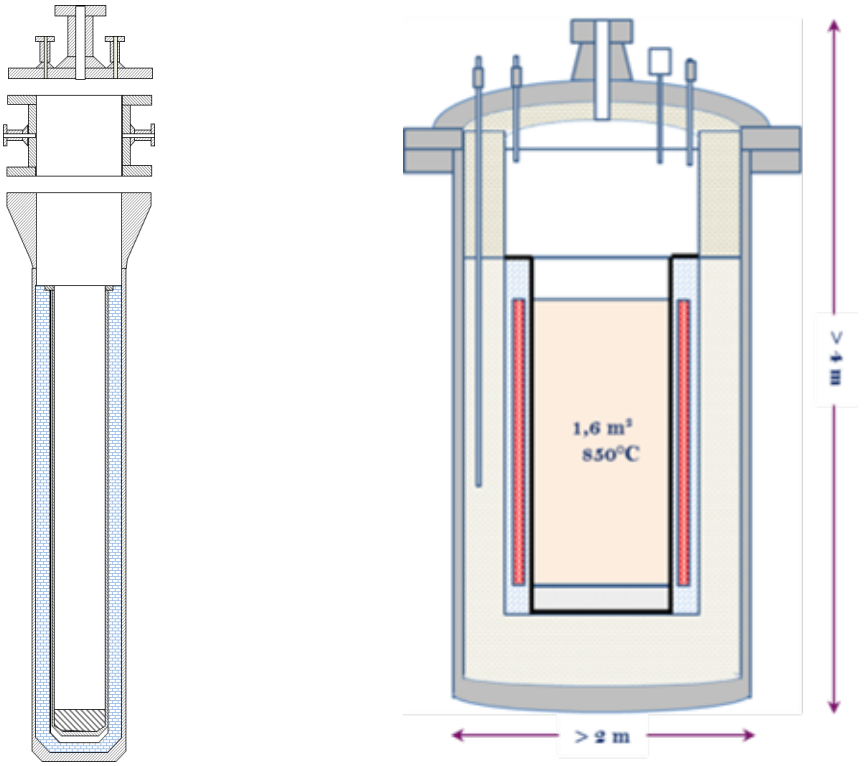

FIGURE 2.17: Sketch of PLINIUS-2-FR (left) and PLINIUS-2-EXPLO (right) test sections [21].

PLINIUS-2-FR test-section (Fig. 2.17) will be dedicated to the study of corium jet fragmentation in sodium. This test section is a ⌀300 mm x 2500 mm sodium filled vessel designed to receive up to 50 kg of corium. It is designed to study the interaction of corium with various sodium initial temperatures (from 400 °C to sodium saturation temperature) thanks to thermal insulation and various experimental conditions (corium inlet diameter and velocity). In order to contribute to the qualification of the SCONE code, this facility will be accompanied by a fine X-Ray radiography system (design of which is studied in the present work) to trace the corium jet from the point of release to its settling down in the debris bed. An explanation of the preliminary design of the foreseen X-Ray instrumentation will be given in the sections to follow.

The **PLINIUS-2-EXPLO** facility (Fig. 2.17) is designed to study the vapor explosion and to validate the SCONE code on the corium fragmentation and the dynamic mechanical loads due to CSI whatever the sodium degree of sub-cooling. As already said, that in low sub-cooling conditions, corium behavior might be closer to that

observed during corium-water interaction, this would result in large mechanical energy release. Also, since the discharge of tons of corium in sodium (in SFR) can significantly increase the local sodium temperature, it is necessary to study these configurations. This test section is being designed for experiments with large masses of corium (at least 200 kg) poured into low ($\sim$ 400°C) to high-temperature sodium ($\sim$ 850°C), it will have an inner diameter of 1000 mm and a length of 2.5 m as in FR experiments. Due to its size and the thickness of its vessel, this test section will not be equipped with an X-Ray system.

PLINIUS-2-FR X-Ray radioscopy system

In order to visualize the fragmentation mechanism of the corium jet in sodium and the three-phase mixture, a high energy X-Ray radioscopy is being developed. This is based on the knowledge and experience gained from the X-Ray radioscopy of the KROTOS facility. The scheme of the foreseen X-ray radioscopy system is presented in Fig. 2.18. Due to the large sodium column and the thick thermal insulation, a more powerful 15 MeV Linear

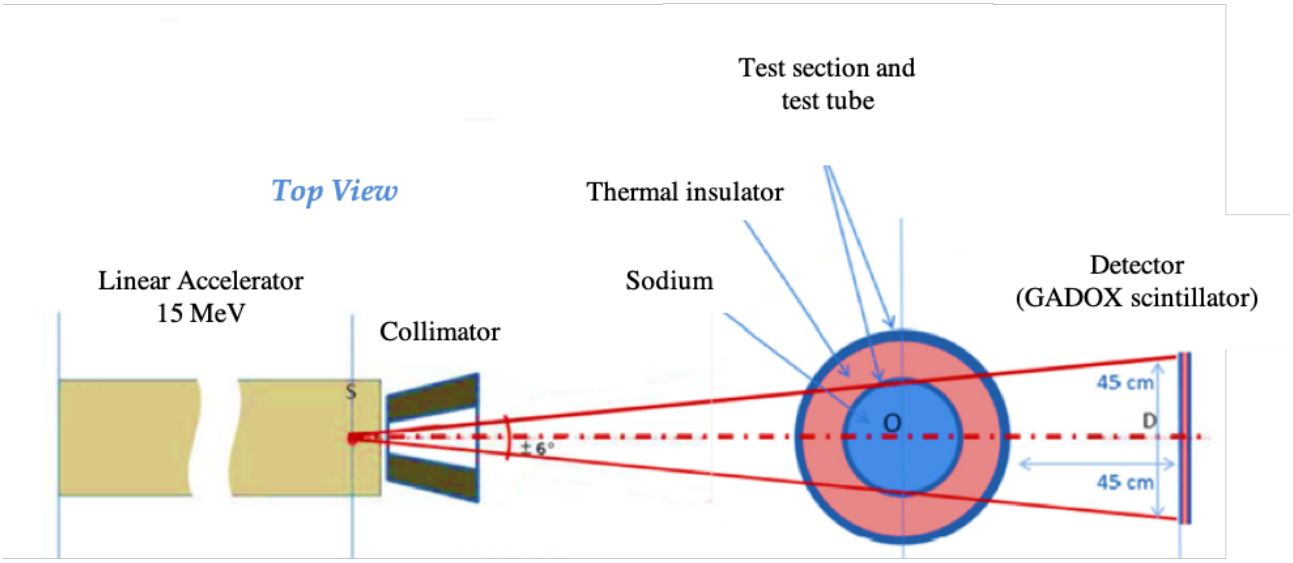

FIGURE 2.18: Foreseen X-Ray radioscopy system for PLINIUS-2-FR test section.

accelerator [42] instead of 9 MeV will be used. The high energy X-Ray flux is attenuated as it passes through the highly dense test section. The transmitted radiation forms a visual spectrum on the GADOX scintillator screen coupled to four scientific CMOS cameras [42].

Image processing and analysis software

The images formed will be analyzed by developing an image processing algorithm similar to KIWI. However, irrespective of the energy released during an FCI, the size of the fragments formed during FCI in sodium is much smaller than that in water. It will be difficult to detect individual particles as performed by the KIWI software for the premixing stage. Instead, it would be ideal to detect them as a cloud of particles. Therefore, there is a need to develop a new image processing software implementing techniques which are capable of detecting clouds of particles. Conclusively, emphasis will be given on detecting clouds of particles rather than each particle in order to understand a corium-sodium interaction.

2.3. Summary

A tabulated review of all the existing facilities dealing with FCI in sodium is important to be performed to help in designing the upcoming future PLINUS-2-FR facility. As has already been discussed in the thesis, we still lack experimental data to visualize and understand corium sodium interaction, this review could show us some insights about the reason behind this. A brief summary of all the FCI facilities mentioned in this chapter has been presented in Table 2.1.

TABLE 2.1: Summary of the experimental facilities studying fuel coolant Interaction .

Facility	Country	Year of operation	Melt used	Coolant	Advantages	Drawbacks
FARO-TERMOS	Italy	1991	UO_2	sodium	high mass fuel	lack of X-Ray imaging system
THINA	Germany	1990	Iron/alumina	sodium	X-Ray imaging possible	alumina not a good simulant
CORECT-2	France	1980-1990	UO_2	sodium	use of UO_2	contact mode, no X-Ray system
BETULLA I	Italy	1980	UO_2 and SS	sodium	significant masses	no X-Ray system
FRAG series	USA	1980	SS-UO_2-ZrO_2	sodium	large mass fuel	no X-Ray system
SOFI	India	Operating	Woods metal	water	X-Ray system	water simulant for sodium
EAGLE	Kazakhstan	Operating	Al_2O_3	sodium	-	alumina (simulant), no X-Ray system
PLUTON	Russia	-	Fe-Al_2O_3	sodium	-	alumina (simulant), no X-Ray system
MELT	Japan	Operating	Al	sodium	X-Ray system	-
MISTEE	Sweden	Operating	woods metal	water	X-Ray system	woods metal,water
KROTOS	France	Operating	UO_2-ZrO_2	water	X-Ray system	water
PLINIUS-2	France	Under conception	$UO_2$and SS	sodium	X-Ray system	-

This table covers the advantages and limitations of each of the facility and thus provides us with a better insight of the present state of the art and throws light on the directions of improvement in designing a new X-ray imaging system as well as a new image processing and analysis tool. The interesting aspect of this table is that it also provides indications to help selecting the parameters for future tests. In the next chapter, a description of the characterization of the clouds of particles as obtained in the tests conducted in the facilities of interest will be discussed. After giving a closer description of the clouds of particles we expect, the following chapters will be dedicated to the step-by-step design of the X-Ray imaging system and the development of the image analysis tool foreseen for PLINIUS-2.

Chapter 3

Past experiments: important conclusions

> *No one undertakes research in physics with the intention of winning a prize. It is the joy of discovering something no one knew before.*
>
> Stephen Hawking

It has been discussed in Chapter 2 that numerous experimental facilities exist, dealing with corium-water and corium-sodium interaction, not only in France but also worldwide. However, experiments dealing with corium-sodium interaction and having an X-Ray visualization system are very limited in number. Thus building a sound knowledge on the phenomenology of corium-sodium interaction and the development of a new X-Ray visualization system is challenging. As mentioned in Chapters 1 and 2, this challenge is coming from the fact that, FCI in sodium acts differently in comparison to FCI in water. In particular, the fragment size formed in the corium-sodium interaction is much smaller as compared to the fragment size formed during corium-water interaction [19]. This small fragment size poses a challenge to be visualized by the X-Ray imaging system and the image processing and analysis tool. This is due to the fact that every image processing tool has a minimum resolution limit, below which the fragments cannot be detected and are difficult to be resolved separately.

The aim of this PhD thesis is to develop an imaging system, additionally, an image processing and analysis tool that can overcome these difficulties and provide resolved images of the real tests. Conducting a real experiment with corium and sodium, and testing an X-ray imaging system on PLINIUS-2-FR is presently not possible as the facility is still under the conception phase. Hence, it was decided to utilize the existing FCI facility at CEA Cadarache, i.e., KROTOS and perform experiments using 3-D phantoms[1] that could mimic corium-sodium interaction. These phantoms should be able to simulate all the three phases of a corium-sodium interaction. The experimental results obtained using these phantoms (i.e. X-Ray images) could then be used to calibrate the upcoming image processing and analysis tool to be able to resolve the three phases separately.

In order to prepare these different phantoms, it is necessary to consider the physical characteristics of each phase of the corium-sodium interaction (CSI). This is taken care of by the proper choice of materials to build the phantoms (which will be discussed in detail in Chapter 4) as well as their size and shape. Generally, the size of the phantom representing liquid sodium is not much of a concern as it depends on how big we want the size of the experimental setup to be (scale of the experiment). Also, it has been introduced in Chapter 1 that the sodium vapor film formed in case of CSI is very unstable. No experimental data or evidence is available that could help to decide the size or the shape of the vapor film formed during the CSI. Hence, all possible sizes of the sodium vapor film thickness have to be considered while designing the sodium vapor 3-D phantom. However, visualization of fine corium fragments formed during a CSI is the most challenging part of the X-Ray image processing and analysis. Among the three-phase mixture that is generally formed during a CSI, the only experimental data we have, is of the size of the corium fragments, collected in the post-test debris beds. In addition, it should be noted that the particles collected on the debris bed might represent the size of the particles formed during the premixing stage. This is due to the fact that no significant energetic explosion has been observed in the past experiments that could lead to further breakdown of the particles.

This chapter studies the assessment of the size of the corium fragments formed in a CSI by a thorough review and analysis of the available experimental data. This review will help us in deciding the size and shape of the phantom that could represent the corium fragments thus enabling the choice of characteristic configurations to be analyzed by the X-Ray imaging system.

[1] static physical models that simplifies the experiment, imitating the significant features of given configurations of the interaction zone

3.1. Review of the past experiments

In the case of SFRs, the molten fuel i.e. corium comprises of nuclear fuel (UO_2, PuO_2), fission products (some may have been released), control rod and structural material comprising mainly of stainless steel (SS). The proportion of UO_2 and SS in the molten fuel/corium depends on the core degradation scenario. FCI experiments performed with UO_2 and SS are thus of more interest to us.

For simplicity, corium is generally classified to be composed of two components, an oxidic component representing the reactor fuel (hereafter referred as **oxide fuel**) and a metallic component representing the clad and other structural materials in the reactor (hereafter referred as **metallic fuel**). It should be noted that, many FCI experiments have been conducted in all the facilities mentioned in Chapter 2. However, only a few experiments have been carried out on prototypic corium (a mixture of UO_2 and SS) with sodium. Few experiments used simulants (instead of prototypic corium) for oxide fuel, such as alumina [30] to simulate corium and aluminium for the metallic fuel [23]. Due to the significant material effect observed between corium and simulant in CWI [24], we remain cautious and prefer to base our analysis on prototypic material experiments. Therefore, only the relevant tests using large masses of prototypic material (UO_2 and SS tests with sodium) will be studied in this chapter even though this choice strongly reduces the available database.

There is a very limited experimental and theoretical information about the fragmentation mechanisms of molten corium in sodium. When liquid corium at high temperature is injected in sodium, it breaks up under hydrodynamic and thermal effects and its fragmentation regime is highly dependent on the melt geometry, the mass being injected, its velocity, its temperature and the temperature of the surrounding coolant [47]. However, there is a lack of considerable research concerning the jet velocity impact and therefore, the study of the impact of velocity has been ruled out. In the FARO-TERMOS experiments, 100 kg of pure UO_2 was poured into sodium at initial temperature $\sim$400°C [17]. A series of vapor explosion occurred that led to an increase in temperature and pressure of the system. Due to an increase in pressure these energetic FCIs limit the quantities of melt penetrating further into the sodium. FARO-TERMOS experiments suggest that in the case of sub-cooled sodium, there are chances of sodium reaching elevated temperatures due to multiple interactions eventually resulting in the penetration of molten corium and to a more energetic interaction. But, if a similar experiment of 100 kg scale of UO_2 is performed with sodium, initially at such elevated temperatures around 800°C, the scenario is unknown. However, past experiments at smaller scale have shown that behaviors similar to water-FCI could be expected, especially in terms of energy release. Chu [48] tried to demonstrate this through FRAG SERIES 6F experiment where 20 kg of UO_2-ZrO_2 (though not prototypic for SFRs), the jet diameter of which was 5.1 cm, was injected

into sodium having initial temperature 690°C. It was observed that the melt stream did not fragment completely and it was able to reach to the bottom of the pool of depth 46 cm. This was confirmed as the particles in the debris bed were observed to be of the order of 5 cm. This behavior is very similar to what is observed in water-FCIs. Thus, the observed behavior is highly dependent on the mass of corium being injected in sodium and is different with sub-cooled sodium and nearly saturated sodium, and thus needs to be studied. Several experiments were carried out to compare the particle size for oxide and metal fuels. Johnson et al. [49] suggested that UO_2 fragments tend to take smaller particle size than the metallic counterpart, i.e. molybdenum. Armstrong et al. [50] also found that molten UO_2 quenched in sodium formed finer particles than molten stainless steel. All the experiments mainly report data of the particle size obtained from the post-test debris bed. It was assumed that particles formed during the fragmentation mechanism would have a similar distribution to the ones retrieved in the debris bed. But, actually these debris bed particles might be smaller than those expected in the premixing stage due to mechanical breaking caused by the stresses during the phase of particles reaching debris bed. This effect has also been reviewed by Manickam et al. [34] and Tyrpekl et al. [35].

The past experiments have also exhibited different interaction behaviors for metallic fuel and oxidic fuel with different temperatures of sodium. In the literature, the highest temperature of sodium where melt mass has been injected into the hot sodium is 725°C [51]. So, we refer here under the experiments with sodium with sub-cooling under 280°C as experiments with "relatively warm sodium". And the experiments with sub-cooling more than 280°C as with "highly sub-cooled sodium". However, ongoing research is being carried out on the thermal modelling of a lower plenum of SFR during corium melt pouring. This will define the maximum initial temperature of the sodium pool to be investigated at the future PLINIUS-2 experimental platform. In addition, large masses of fuel have been observed to have a huge impact on the interaction as it may increase the temperature of sodium from multiple interactions and may thus cause explosions. Thus, experiments utilizing large masses of fuel melt are of particular interest to us.

So, there is a need of sorting the experiments into two groups, one for oxide fuel interaction with sodium at different temperatures,i.e.:

- Oxide fuel interaction with relatively **warm sodium**.
- Oxide fuel interaction with highly **sub-cooled sodium**.

The other one for metal fuel interaction with sodium at different temperatures:

- Metallic fuel interaction with relatively **warm sodium**.

- Metallic fuel interaction with highly **sub-cooled sodium**.

Analysis of the particle size data is carried out on the basis of these four criteria as can be seen in the next section.

3.2. Database concerning fuel debris particle size

3.2.1 Oxide fuel interaction with relatively warm sodium

For oxide fuel (in particular UO_2 melt) interaction with relatively warm sodium, the data of the particle size distribution is limited to ANL-USA M3 test [49], ANL-USA EDT#2 test[51], 2 tests at Betulla-1-JRC tests[25] and FRAG SERIES test [48]. These tests conducted with sodium initial temperature exceeding 600°C are listed below:

1. **Argonne National Laboratory – USA EDT#2 test:** This test is the out-of-pile under surface injection test carried out by Henry [51]. Salient features about this test are:
   - **Test Configuration:** Molten UO_2 (0.5 kg) was injected at approximately 3200°C, underneath the surface of a sodium pool (initial temperature of 750°C).
   - **Main observations:**
     - No explosive phenomenon was observed but UO_2 was heavily fragmented.
     - When the particles were separated out of the slurry solution by a filtration process, they tended to coagulate into larger clumps. It was decided not to attempt to break up these clumps into the original particles. Therefore, the particle distribution would represent the upper bound of the actual weight versus particle size distribution.
   - **Particle size distribution:** The cumulative distribution of the particle size in the debris bed observed is depicted in Fig. 3.1:
2. **Argonne National Laboratory – USA - M3 test:** This test was an "out-of-pile test", carried out by Johnson et al. [52]. Salient features about this test are:
   - **Test configuration:** In this test, ∼3 kg of molten UO_2-Mo-Cr was released into sodium without any mechanical constraints. The melt initial temperature was ranging from 3037°C to 3204°C and the sodium initial temperature was 626°C.

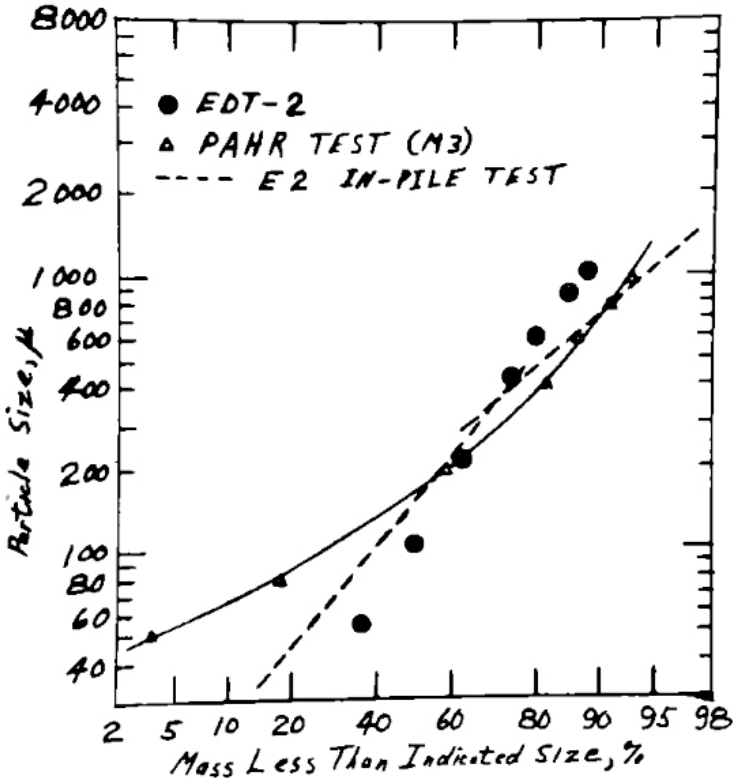

FIGURE 3.1: Particle size distribution of the ANL-USA EDT#2 test [51].

- **Main observations:**
  - Intense fragmentation of the melt was observed. Numerous pressure peaks (maximum ∼7 bars) were observed but the energy release was feeble.
  - The metal particles were observed to be considerably larger than the oxide particles.
  - In all the three runs, the particles of all sizes were primarily angular and irregularly shaped.
- **Particle size distribution:** The cumulative distribution of the particle size in the debris bed observed, is show in Fig. 3.2:

3. **BETULLA I – JRC ISPRA [19, 25]:** Salient features about this test are:
   - **Test configuration:** Crucible containing up to 4 kg of molten UO_2 at 2850°C was dropped in the reaction tank of liquid sodium between 350°C and 700°C.
   - **Main observations:**
     - Several trains of small pressure waves were generated. The entire UO_2 does not enter all at once into sodium and the interaction occurs in repeated events. No coherent violent interaction was

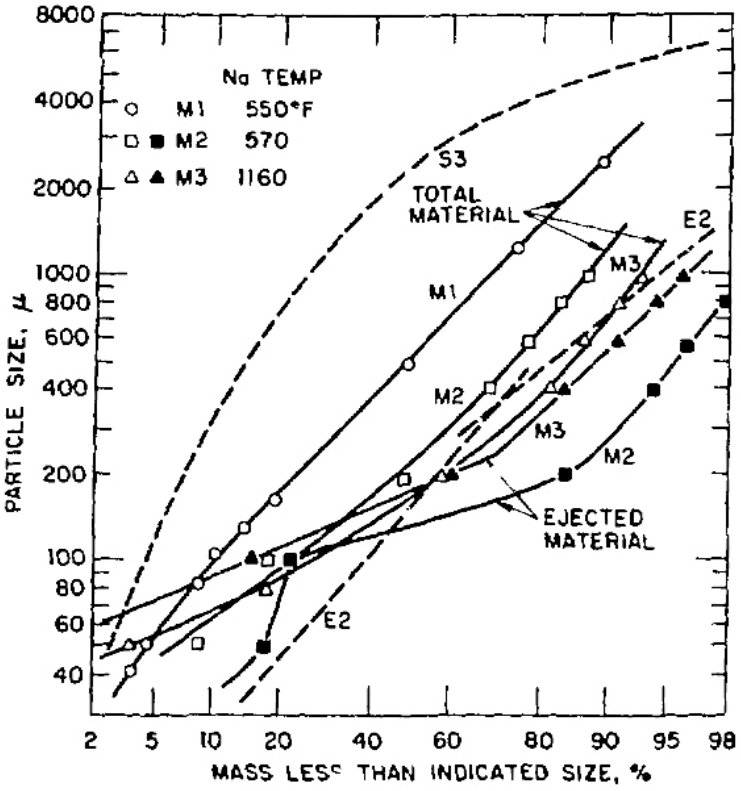

FIGURE 3.2: Particle size distribution of the ANL-USA M3 test [52].

observed in this test. Intense fragmentation occurred and very fine debris was collected with particle size distribution as shown in Fig. 3.3.

– Amongst these series of tests, some tests were performed where molten alumina was released into water. About 80 percent of the debris consisted of fuel solidified into a mushroom shape and the rest into spherical shapes. While for sodium-fuel interactions, it was observed that no mushroom shaped fragments were ever detected in any of the tests and the interactions invariably led to relatively fine fuel fragmentation.

- **Particle size distribution:** The cumulative distribution of the particle size in the debris bed observed in this experiment is shown in Fig. 3.3.

4. **FRAG – Sandia National Laboratory [26, 48]:**

- **Test configuration:** 20 kg of molten stainless steel-UO_2-ZrO_2 melt at temperature ~2600°C. Four tests were performed with four different sodium temperatures: 250°C, 420°C, 500°C, 690°C.

- **Main observation:** Oxide fuel interaction with relatively warm sodium. Several pressure pulses were observed with no coherent energetic event. The maximum pressure that was measured was

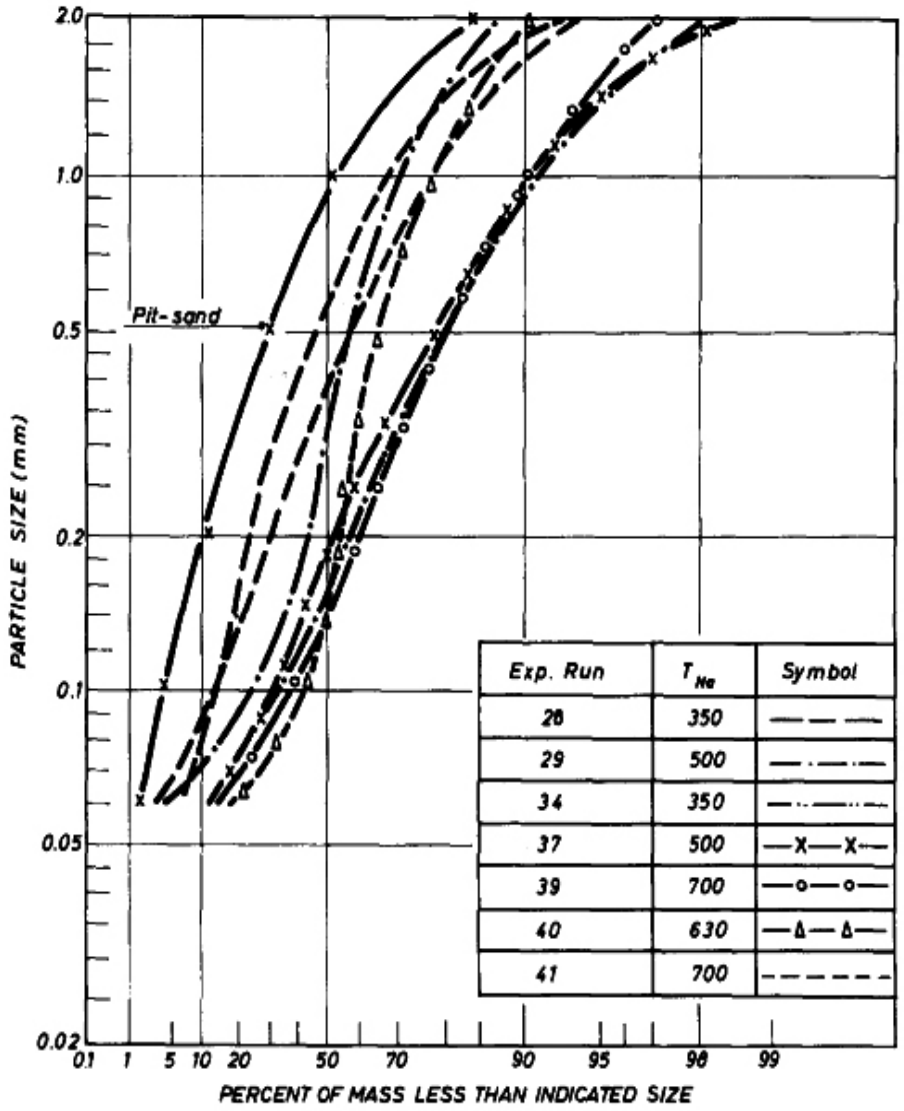

FIGURE 3.3: Particle size distribution of the BETULLA-1-JRC test [19, 25].

around 7 bars. It should be noted that during a test with molten iron instead of corium, 20 bars were reached with damages to the test section. With high-temperature sodium (690°C), "the sodium melt stream was able to reach all the way to the bottom of the pool without fragmenting completely and resulted in some fragments of the order of 5 cm".

- **Particle size distribution:** The cumulative distribution of the particle size observed in this case is depicted by Fig. 3.4.

3.2.2 Oxide fuel interaction with highly sub-cooled sodium

For this case, FARO-TERMOS tests were considered. This experiment is described below briefly:

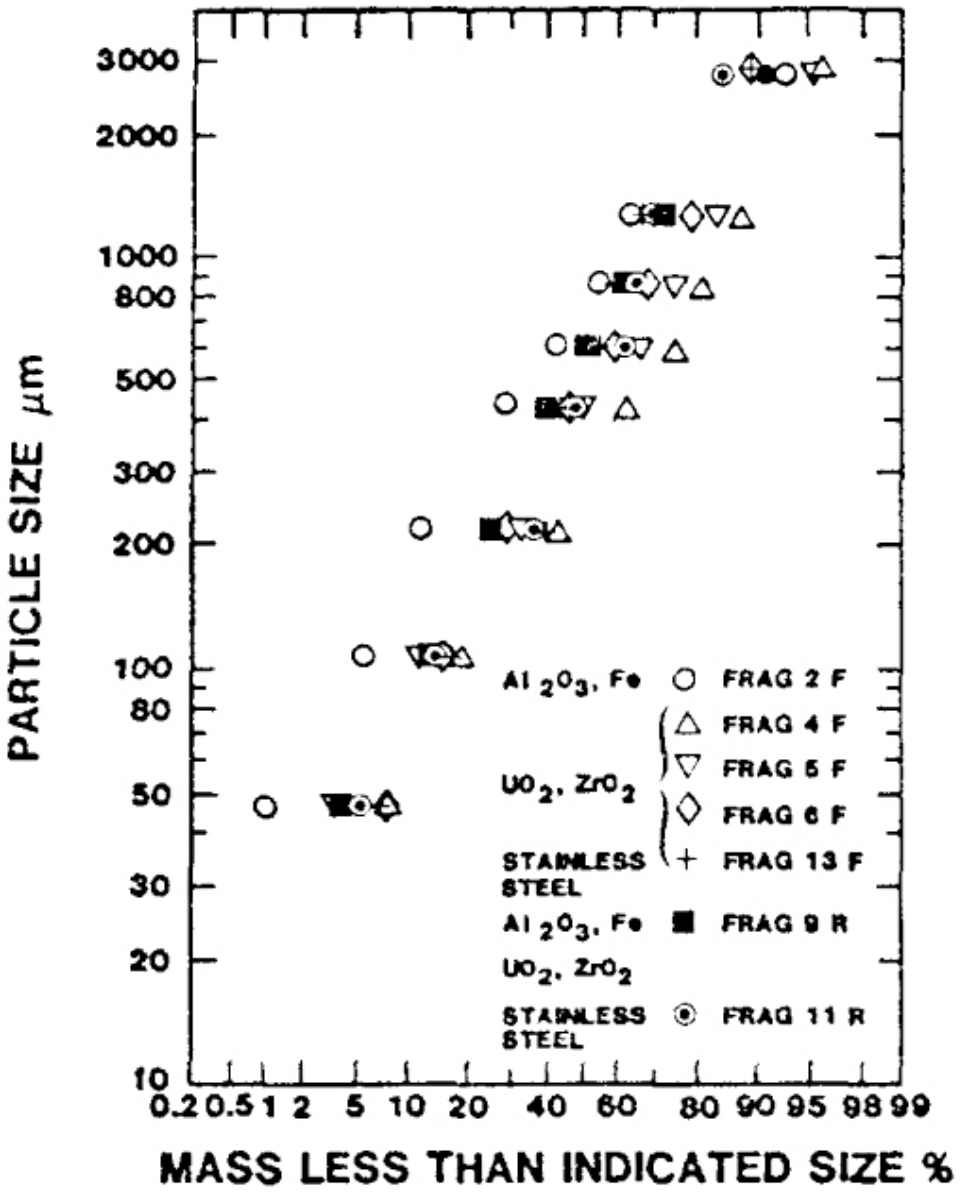

FIGURE 3.4: Particle size distribution of the ANL-USA M3 test [26, 48].

FARO-TERMOS – ISPRA [17]:

- **Test Configuration:** Two tests were performed, T1 and T2, during which, respectively, 110 kg (jet diameter 50 mm) and 140 kg (jet diameter 80 mm) of molten UO_2 ($T_{UO_2} = 3000°C$) were injected into a sodium pool of temperature 400°C.
- **Main observations:** FCIs occur that induced stepwise penetration of the melt into sodium and limitation of the melt quantity that could penetrate into the sodium due to dispersion.

- **Particle size distribution:** The cumulative distribution of the particle size observed in this case is depicted by Fig. 3.5:

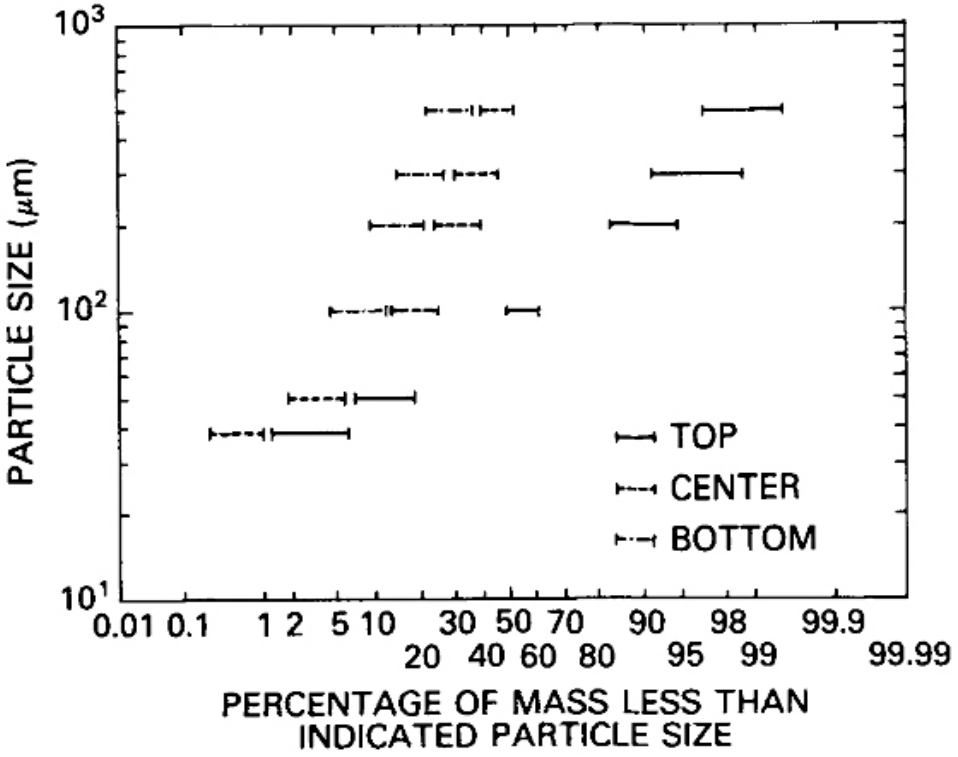

FIGURE 3.5: Particle size distribution of the Faro-Termos test [17].

3.2.3 Metallic fuel interaction with relatively warm sodium

At PLINIUS-2, performing tests with metallic fuel, especially stainless steel is of interest. But, in the literature there are no existing experiments that have been performed between SS and relatively warm sodium. A series of tests with high-temperature sodium were conducted at the Argonne National Lab [53] but with molten uranium, uranium-zirconium alloy and uranium-iron alloys. So, these experiments have been considered for the current case. **ANL T6** [53]:

- **Test Configuration:** These tests were performed to observe the breakup behavior of kilogram quantities of metal melt such as molten uranium, uranium-zirconium alloy and uranium-iron alloys poured into 600°C sodium.
- **Main observations:** No energetic events were observed in any of the tests. A big dispersion of the particles was observed for particles with high injection velocities (10 m/sec).

- **Particle size distribution:** The cumulative particle size distribution for this test was not represented in the form of a graph. Thus, the data of the particle size is referred from [53].

3.2.4 Metallic fuel interaction with highly sub-cooled sodium

In the literature, there are very few tests with stainless steel and highly sub-cooled sodium. Among a few are the NaSS test [54] and BETULLA-1-09 test [19]. For the present analysis, only the Betulla-1-09 test is considered.

Betulla-1-09 [19]:

- **Test Configuration:** In this test, SS was poured in a sodium pool of temperature 400°C.
- **Particle size distribution:** The cumulative distribution of the particle size observed in this case is depicted in Fig. 3.6:

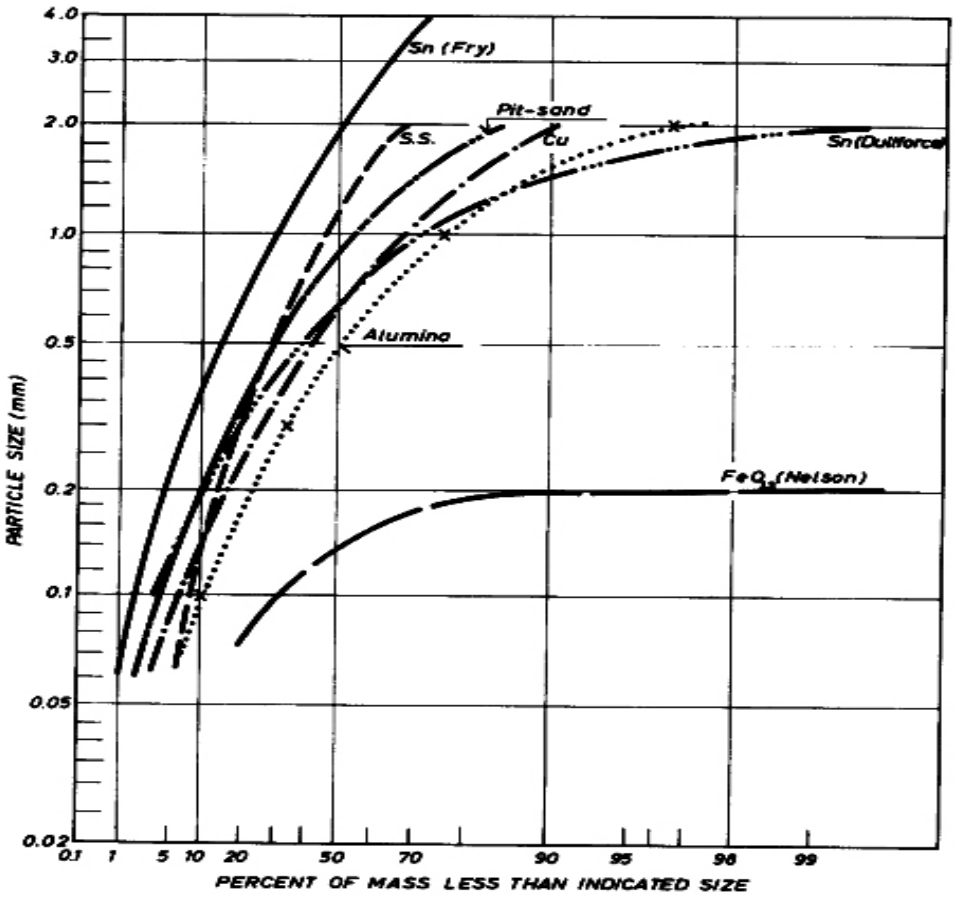

FIGURE 3.6: **Particle size distribution of the Betulla-1-09 test [19].**

3.3. Database concerning fuel debris particle shape

Some tests were performed at the JRC BETULLA 1 and 2 facilities (briefly described in Sec. 3.2), to study the difference in the behavior of oxidic fuel (UO_2) interaction with sodium and that of metallic fuel (SS) interaction with sodium [19]. The study suggested that small fractions of UO_2 debris bed particles tend to take smooth and nearly spherical shapes while most of the oxidic fragments displayed angular geometries as showed in Fig. 3.7. The prompt and rapid fragmentation of the molten fuel due to boiling induces hydrodynamic forces which in turn seems to produce smooth and spherical fuel particles. The angular or the fractured particulate debris is believed to be formed by the delayed thermal stress mechanism. Metallic fragments were mostly found to be smooth. This was attributed to the fact that for metal fuels, the thermal stresses do not exceed the ultimate tensile stress. Thus only the hydrodynamic forces contribute to fuel breakup in case of metal fuel. A similar observation was also made by T.Y. Chu [48].

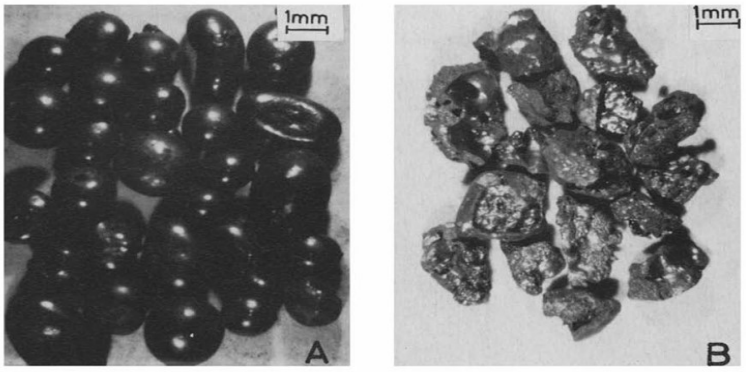

FIGURE 3.7: Smooth (A) and fractured (B) UO_2 particles following sodium quench [19].

3.4. Statistical analysis of debris bed particles

These cumulative distributions of the experiments between oxide and sodium i.e. ANL-USA M3 test, ANL-USA EDT#2 test, 2 tests at Betulla-1-JRC tests and FRAG SERIES test were reduced to mass percentage corresponding to average particle diameters in each range. The particle size distribution (in mass percentage) issuing from these different experiments are plotted in Fig. 3.8. In the statistics presented in Fig.3.8, two bumps were observed for each test. The difference between the particle size distribution in each of the experiment may be due to the difference in the boiling regime of sodium at different temperatures [10]. The two bumps represent what we believe to be two steps of fragmentation. The first step is the fragmentation of the jet of corium, leading

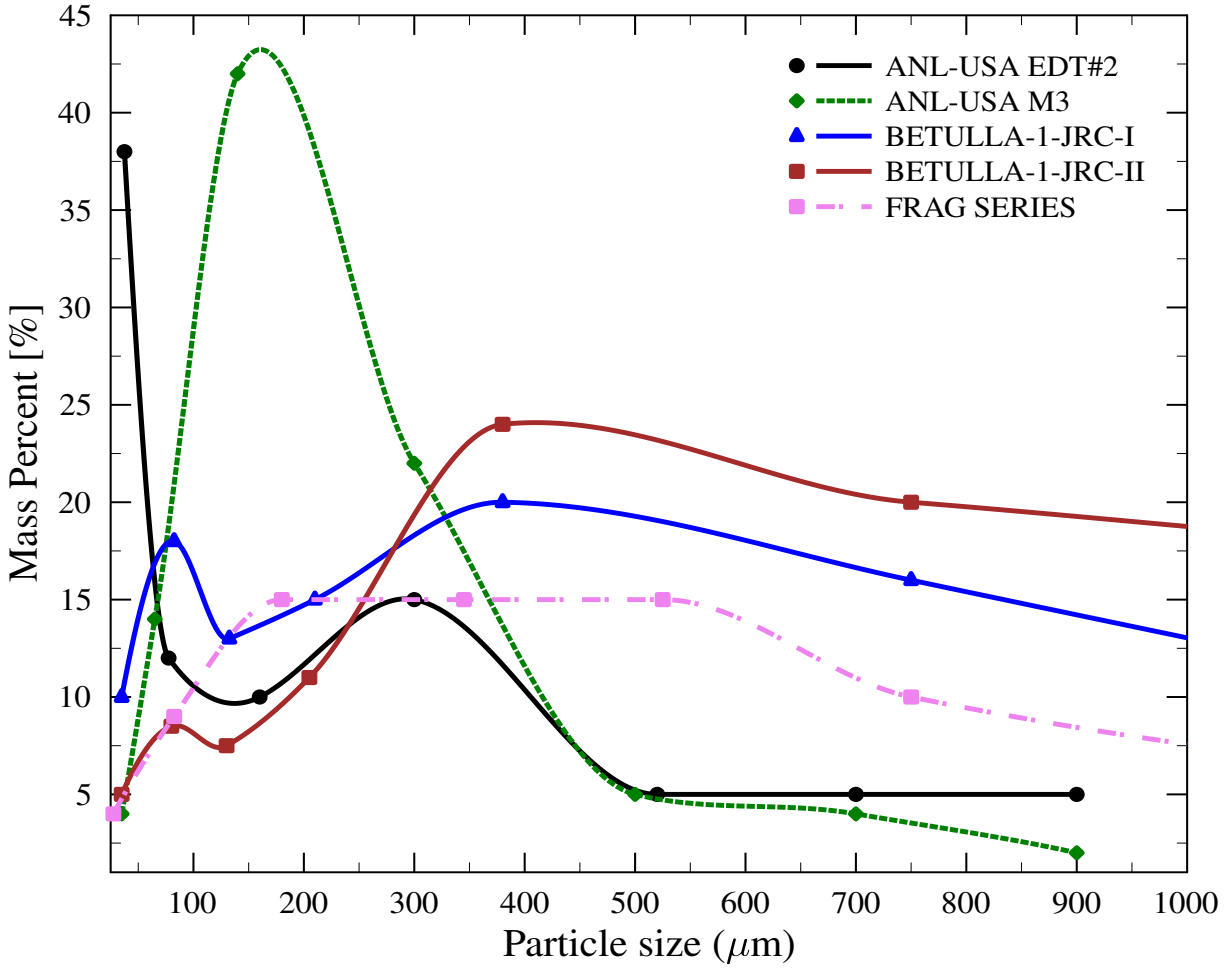

FIGURE 3.8: Statistics of debris particles formed by interaction between UO_2 and relatively warm sodium [55].

to coarse fragmentation. In the second step, thermal and hydrodynamic effects cause finer fragmentation of the corium droplets.

3.4.1 Fragmentation of a jet of corium

A liquid jet of corium when injected into sodium, mainly breaks up under the action of hydrodynamic instabilities. In the case of subcooled sodium, the phenomenology involved with the jet break-up is still unclear and requires new experiments to develop an understanding of its phenomenology. However, when corium interacts with warm or nearly saturated sodium, the phenomenology is believed to be similar to that for corium-water interaction. Under the framework of Light Water Reactors severe accidents, different teams have worked on the jet fragmentation modeling. Among them, the team of the Argonne National Laboratory who developed the THIRMAL code [56] and proposed a modeling of the fragmentation of a corium jet primarily based on the

Kelvin-Helmholtz instability. This occurs when there is velocity shear in a single fluid or at the interface between two fluids travelling at different velocities. The Stuttgart University team proposed the JEMI software [57] where the instabilities within the vapor film are described. Another model was developed by Namiech, at CEA Grenoble [58], quite similar to the Stuttgart University approach, but taking into account the vapor viscosity while calculating the vapor film instabilities and the resulting break-up of the jet. An important factor governing the jet fragmentation is its speed of penetration. If the velocity is less than the inertial forces of water, the jet decelerates with its forehead spreading into a mushroom-like head, thus leading to Rayleigh-Taylor instability (RT instability). RT instability occurs between two fluids of different densities when the lighter fluid is pushing the heavier fluid.

Though corium-water interaction models could be applied to the corium-sodium interactions even for subcooled sodium, more experimental data are required for the understanding of the interaction phenomenology.

3.4.2 Fragmentation of corium droplets

The fragmentation of corium jet gives rise to coarse corium fragments (size between 3 and 10 mm). These fragments and its further fragmentation depend on the material composition and the physical properties and state of the interacting medium.

As stated by Corradini [6], fragmentation mechanisms of the coarse corium fragments can be grouped into two broad classes:

- Based on the thermal effects: Thermal fragmentation.
- Based on the hydrodynamic effects: Hydrodynamic fragmentation.

Though the fragmentation is often considered to be purely arising from the thermal effects or the hydrodynamic effects, the strong coupling between the two effects could not be denied as observed by De Malmazet [59]. These processes produce fine fragmentation that will increase the exchange surface area between the fuel and the coolant. These fine fragments, in turn, will affect the heat transfer and thus the vapor production.

Thermal Fragmentation

Thermal fragmentation may occur due to either the boiling effects, internal pressurization effects, or solidification effects described in detail by Corradini [6]. Several models have been proposed in the literature to describe such

fragmentation. Cronenberg and Chawla [60] proposed a model based on the vapor bubble collapse conditions that can lead to the fine fragmentation of corium droplets. Berthoud and Newmann [61] introduced a solidification-controlled fragmentation model to explain the interaction mechanism in the CORECT II test. These models could be studied and validated for corium-sodium interactions.

Hydrodynamic Fragmentation

Hydrodynamic fragmentation of the corium fragments is caused by the external surface forces of the coolant sufficient to surpass the cohesive forces of the droplets surface tension. This kind of fragmentation occurs in two ways:

- Due to the acceleration of droplet in a coolant: the falling drop meets the coolant and decelerates until it reaches the coolant velocity. The difference in the velocity causes the drop to fragment.
- Due to the impact: This occurs when the inertial forces are high enough to overcome the cohesive forces of the drop surface tension.

For both, the cause of fragmentation can be calculated based on the ratio of inertial to surface tension forces, often referred to as Weber number:

$$We = \frac{\rho_c D_d (|v_d - v_c|)^2}{\sigma_{dc}} \tag{3.1}$$

where, ρ_c is the density of the coolant, D_d is the diameter of the droplet, v_d and v_c are the density of the droplet and the coolant respectively, and σ_{dc} is the interfacial surface tension. If this We number is over a specific critical value, the inertial forces exceed the surface tension, and the droplet undergoes hydrodynamic fragmentation. The fragmentation then occurs in several steps until the droplet Weber number becomes smaller than this critical Weber number.

The effect of viscosity on the droplet fragmentation is associated with the Ohnesorge number (On):

$$On = \frac{\mu_d}{(\rho_d D \sigma)^{0.5}} \tag{3.2}$$

where, μ_d is the dynamic viscosity of the droplet, and ρ_d is its density. Pilch and Erdman [62] have studied the effect of We and On number on the fragmentation mechanism of a liquid droplet in gas or liquid flow. They

introduced five distinct fragmentation mechanisms based on the initial Weber number value. Critical weber number was investigated to be 12 when Ohnesorge number is small (On < 0.1). A Weber number > 350 was observed to produce catastrophic breakup. Hsiang and Faeth [63] introduced a detailed effect of Weber number and Ohnesorge number from the start of deformation to the actual breakup of the droplet. Several liquids were tested in the range of ρ_d/ρ_c of 1.15 - 12,000. The data from this study could be used in the modeling of the fragmentation mechanism.

3.4.3 Corium particle size distribution

The modeling of the fragmentation mechanism is out of scope for this study. This study, will only focus on the particle sizes formed after the two steps of fragmentation. For the FCI safety studies, the density function of the finest particle size distribution holds importance. The particle size distributions in Fig. 3.8 appears to be a bimodal log-normal, i.e. there are two bumps in all the experiments. Instead of visually estimating the parameters of the two log-normals and their respective weights, the Gaussian mixture model available in the mixtools package of the R software [64] was used, to fit the log-transform of the mixture distribution. This tool is based on a maximum likelihood method and the expectation-maximization algorithm. The Gaussian mixture model groups the distributions into two clusters to obtain two fitted Gaussian distributions defined by their respective medians μ_1 and μ_2, standard deviation σ_1 and σ_2, weighted by their estimated probability of occurrence λ_1 and λ_2. Thus, the bimodal mixture probability density distribution f for the particle diameter D is represented by equation 3.3:

$$\begin{aligned} f(lnD) =& \lambda_1 \frac{1}{\sigma_1\sqrt{2\pi}} \exp\left[-\frac{(lnD-\mu_1)^2}{2(\sigma_1)^2}\right] \\ &+ \lambda_2 \frac{1}{\sigma_2\sqrt{2\pi}} \exp\left[-\frac{(lnD-\mu_2)^2}{2(\sigma_2)^2}\right] \end{aligned} \tag{3.3}$$

The above methodology was applied on the experimental data to observe the particle size distribution. To represent the UO_2 interaction tests with relatively warm sodium, the FRAG SERIES 6F test was chosen out of the five tests in Fig. 3.8 as it involves large masses (20 kg) of oxide injected into 690°C sodium [48]. The UO_2 interaction with sub-cooled sodium was represented by FARO-TERMOS test involving 110 kg of UO_2 fuel injected in 400°C sodium. The metallic fuel test with relatively warm by ANL-T6 test (where 3 kg metal fuel was injected in 600°C sodium) and metallic fuel test with sub-cooled sodium by Betulla-1-09 test (where 4 kg metal fuel was injected into 400°C sodium). Appendix A details the code developed in R software to statistically analyse the particle size distribution data.

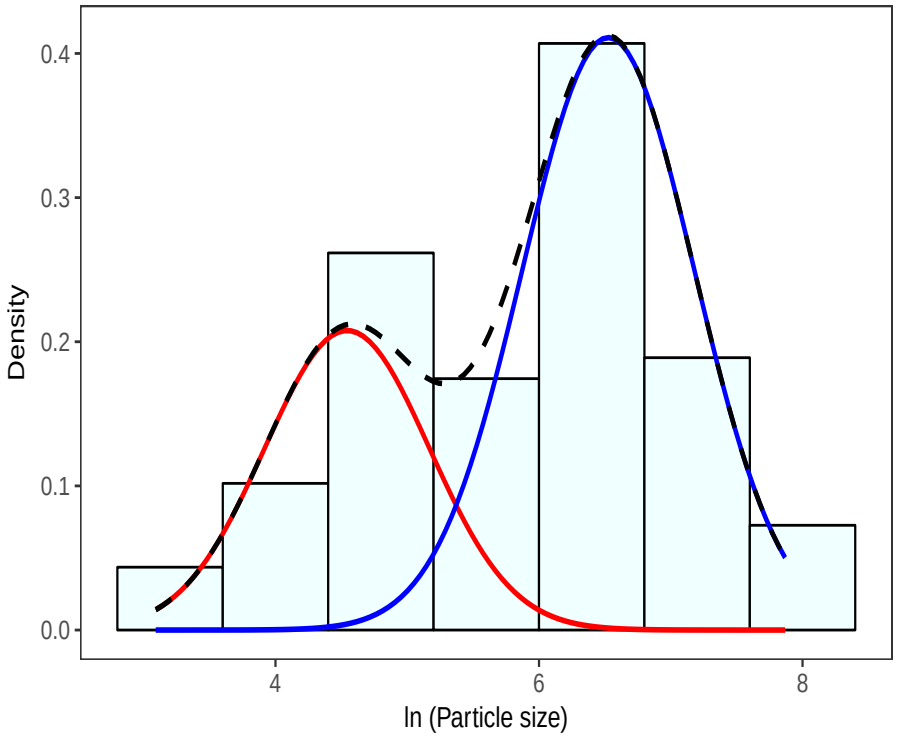

FIGURE 3.9: Fitted bimodal normal curve for the particle distribution in FRAG SERIES 6F test [55].

1. FRAG SERIES 6F test: The logged particle size distribution data from the FRAG SERIES test [48] was fitted normally as shown in Fig. 3.9 (solid lines in red and blue) with a logarithmic particle size in micrometers in the X-axis. The mixture of the two curves gives a bimodal normal fit represented in black dotted line. Thus, the bimodal mixture probability density distribution f for the particle diameter D (in mm) is represented by:

$$\begin{aligned} f(lnD) =& 0.33 \frac{1}{0.63\sqrt{2\pi}} \exp\left[-\frac{(lnD-4.54)^2}{2(0.63)^2}\right] \\ &+ 0.67 \frac{1}{0.65\sqrt{2\pi}} \exp\left[-\frac{(lnD-6.53)^2}{2(0.65)^2}\right] \end{aligned} \tag{3.4}$$

With this fitting, μ_1 and μ_2 for the two peaks are deduced to be 4.54 and 6.53 respectively and their corresponding σ_1 and σ_2 as 0.63 and 0.65 respectively. The median particle size was thus obtained as 0.09 mm and 0.69 mm, with a weight factor λ_1, λ_2 as 33% and 67% respectively.

2. FARO-TERMOS test: The particle size distribution with sub-cooled sodium is observed in FARO-TERMOS test [17]. The normal fitting of its distribution is shown in Fig. 3.10. Likewise, the bimodal

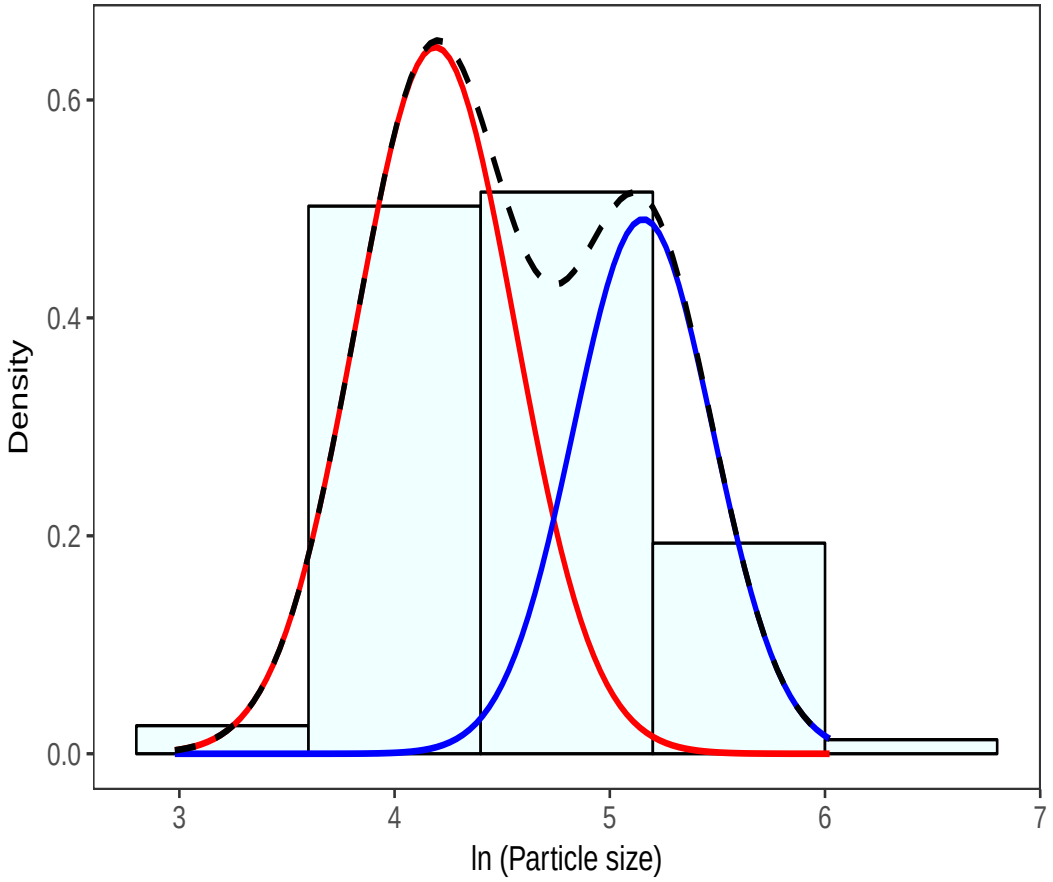

FIGURE 3.10: Fitted bimodal normal curve for the particle distribution in FARO-TERMOS test [55].

mixture probability density distribution for this test is computed to be:

$$\begin{aligned} f(lnD) =& 0.60 \frac{1}{0.37\sqrt{2\pi}} \exp\left[-\frac{(lnD-4.19)^2}{2(0.37)^2}\right] \\ &+ 0.40 \frac{1}{0.32\sqrt{2\pi}} \exp\left[-\frac{(lnD-5.16)^2}{2(0.32)^2}\right] \end{aligned} \tag{3.5}$$

With this fitting, μ_1 and μ_2 for the two peaks are deduced to be 4.19 and 5.16 respectively and their corresponding σ_1 and σ_2 are 0.37 and 0.32 respectively. The median particle size was thus computed to be 0.07 mm and 0.17 mm, with a weight factor of 60% and 40% respectively. Hence, it was observed that the range of particle size is way smaller than the FRAG SERIES experiment with warm sodium.

3. ANL T6 test: To observe the particle size distribution of metal melt (U-Zr) with relatively warm sodium, the ANL T6 test was considered [53]. Upon fitting the log data of particle size normally, the fitted curve was observed to be lying in a bit higher range of particle size. The distribution curve is shown in Fig. 3.11. The bimodal mixture probability density distribution for this case is as follows:

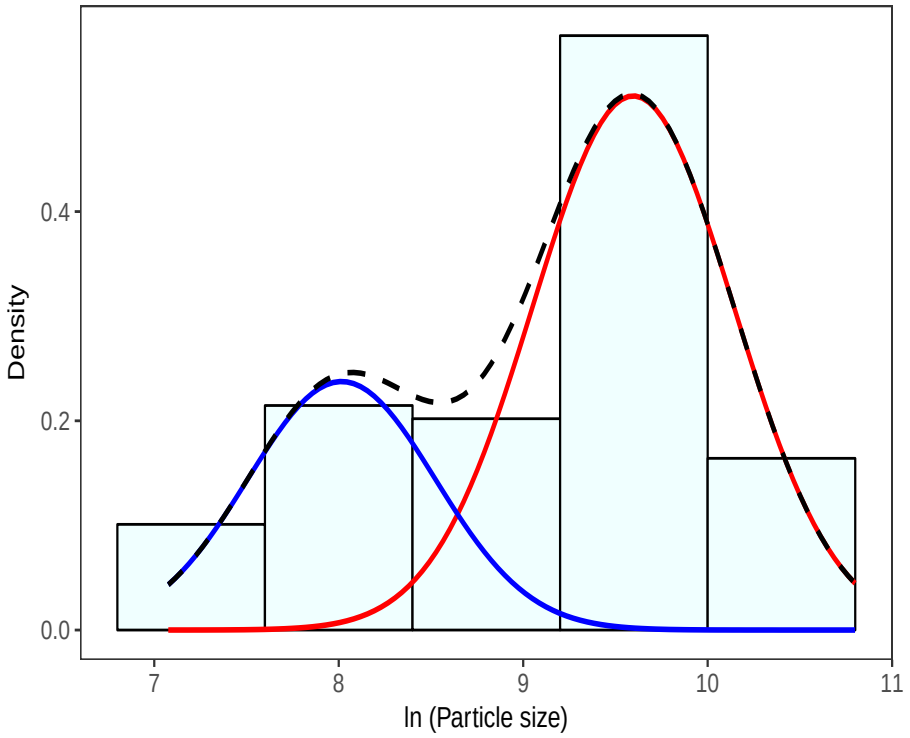

FIGURE 3.11: Fitted bimodal normal curve for the particle distribution in ANL T6 test [55].

$$\begin{aligned} f(lnD) =& 0.70 \frac{1}{0.54\sqrt{2\pi}} \exp\left[-\frac{(lnD-9.60)^2}{2(0.54)^2}\right] \\ &+ 0.30 \frac{1}{0.51\sqrt{2\pi}} \exp\left[-\frac{(lnD-8.02)^2}{2(0.51)^2}\right] \end{aligned} \tag{3.6}$$

With this fitting, μ_1 and μ_2 for the two peaks are deduced to be 9.60 and 8.02 respectively and their corresponding σ_1 and σ_2 as 0.54 and 0.51 respectively. The median particle size for this test fit was computed to be 14.76 mm and 3.04 mm, with their respective weight factor of 70% and 30%.

4. BETULLA-1-09 test: This test was considered to assess the distribution of metal melt with sub-cooled sodium. The normal fitting of the logged data is shown in Fig. 3.12. The bimodal mixture probability density distribution for this test is computed out to be:

$$\begin{aligned} f(lnD) =& 0.13 \frac{1}{0.36\sqrt{2\pi}} \exp\left[-\frac{(lnD-3.81)^2}{2(0.36)^2}\right] \\ &+ 0.87 \frac{1}{0.81\sqrt{2\pi}} \exp\left[-\frac{(lnD-6.48)^2}{2(0.81)^2}\right] \end{aligned} \tag{3.7}$$

For this fit, μ_1 and μ_2 for the two peaks are deduced to be 3.81 and 6.48 respectively and their corresponding σ_1 and σ_2 as 0.36 and 0.81 respectively. The median particle size for this test fit was computed to be 0.05 mm and 0.65 mm, with their respective weight factor of 13% and 87%.

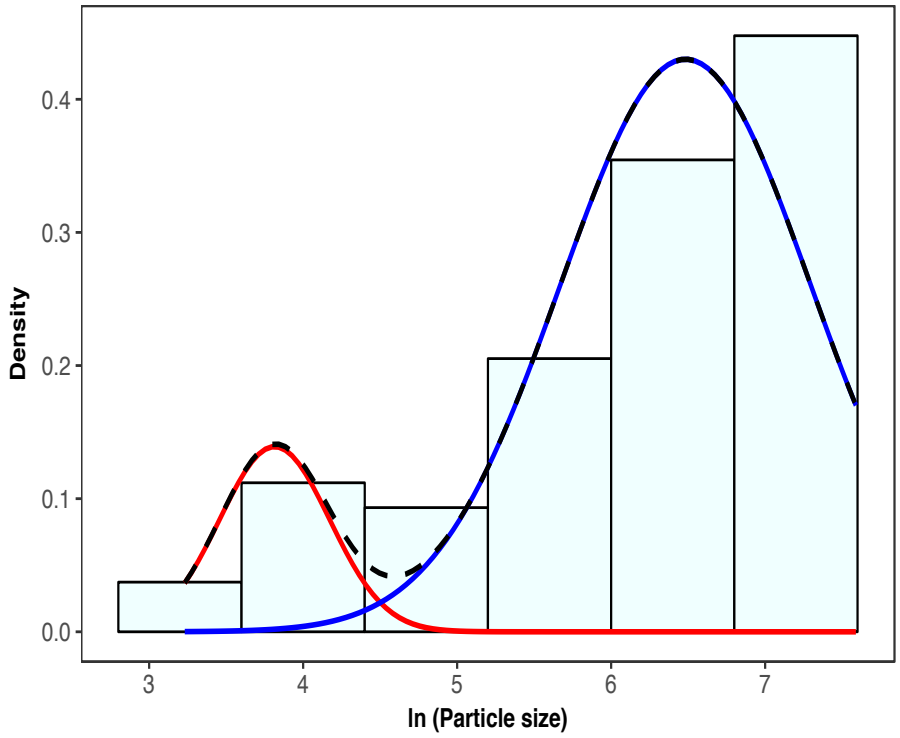

FIGURE 3.12: Fitted bimodal normal curve for the particle distribution in BETULLA-1-09 test [55].

These median diameter values, calculated for all these distributions are in agreement with the experimental results. It was observed that the oxide and metal melt show different behaviors with different temperature of sodium. To summarize, oxide particles have been found to be in the range of 0.01 to 0.7 mm while with metal melt it highly depends on the type of melt. The ANL T6 test with (U-Zr) metal has been observed to produce relatively bigger size than the oxide (FRAG SERIES 6F) and SS test and it will thus be easier to detect these particles with the X-Ray system.

3.5. Summary

In this chapter, the existing experiments of interest were reviewed and analyzed to characterize the shape and size of the particles formed during an FCI. A synthesis table is introduced summarizing the observations in Table 3.1. This will now enable the choice of characteristic configurations to be analyzed with the X-Ray imaging system.

Qualification of phantoms/models representing the fragmented corium in sodium and the choice of phantom materials beforehand requires preliminary simulations of expected images and the choice of phantom materials. The modelling is based on the CEA in-house code MODHERATO, can simulate the expected radiographies, qualitatively comparable to the images obtained by a real imaging system. Thus, the next chapter will be dealing

with the simulations of the expected images by the MODHERATO code and designing phantoms to be used for experimentation with radioscopy, taking into account the particle size analysis performed here.

TABLE 3.1: Summary of the FCI experiments considered in this chapter to analyze the size of the corium fragments formed.

Nature	**Temperature of Na** (T_{Na})	**Considered experiment**	**Median Diameter** $D_1(mm)$	σ_1	**Median Diameter** $D_2(mm)$	σ_2
Oxide Fuel	Warmer (690°C)	FRAG SERIES 6F Test	0.09	0.63	0.69	0.65
Oxide Fuel	Highly sub-cooled 400°C	FARO-TERMOS Test	0.07	0.37	0.17	0.32
Metallic Fuel (U-Zr)	Warmer (600°C)	ANL-T6 Test	3.04	0.51	14.76	0.54
Metallic Fuel (SS)	Highly sub-cooled (400°C)	BETULLA-1-09 Test	0.05	0.36	0.65	0.81

Chapter 4

Modelling of the X-Ray radioscopy system and phantom designing

> *To dissimulate is to pretend not to have what one has. To simulate is to feign to have what one doesn't have.*
>
> Jean Baudrillard

The characteristic shape and size of corium fragments formed in a corium-sodium interaction (CSI) has been reviewed in detail in the previous chapter. This idea we have of the fragment shape and size will help in designing models which would represent the three-phase mixture formed during a CSI. But whether or not the imaging system could visualize the corium fragments of size as small as 0.01 mm, is in itself a question. Thus, in the first step, it was decided to simulate these corium fragments with a CEA in-house radiography and tomography support software called MODHERATO, **MO**delling **D**etectors for **H**igh **E**nergies **RA**diography and **TO**mography [42]. The fragments which qualify to be seen by the imaging system could then be used in the second step to design phantoms. Phantoms are the 3-D representations of corium fragments in sodium using simulant materials having similar attenuation properties as corium and sodium.

We shall now be discussing the first part, i.e., the simulation principle of the software MODHERATO and the simulations carried out using this software in this work.

4.1. About MODHERATO and its simulation principle

MODHERATO is a radiography and tomography support software developed for high-energy imaging applications. This software then helps designing new equipments, looking for the best measurement conditions for a given problem and obtaining precisions about the contrast, the resolution and the detection limits for a given object [42].

The simulation itself can be divided into two main steps. The first step is to calculate the attenuation of the X-Ray beam passing through the object and reaching the detector. The following inputs must be defined for the first step:

1. **X-Ray source:** the angular and the energy distribution of the source must be described using an MCNP (Monte Carlo N-Particle transport code) computation. The calculation is done once for a given LINAC and can be used directly;
2. **Object:** the description of the 3D objects coming in the path between the source and the detector is required. For instance, a description of the design of the test section, the corium, liquid sodium, and sodium vapor needs to be done. This involves defining their dimensions, material and density;
3. **Interaction cross-sections:** tabulated data for photon-matter interaction cross-sections should be included;
4. **Magnification factor:** the distance between the source, the object and the detector must be specified.

The attenuation calculation of the software is based on the Beer Lambert's law of attenuation where the flux intensity $I_0(y,z)$ incident from the source in the direction of point (y,z) gets attenuated to $I(y,z)$ flux incident on the point (y,z) on the detector screen according to the relation:

$$I(y,z) = I_0(y,z)\exp(\sum_m(-\mu_m x_m)) \tag{4.1}$$

where for each material m on the way from the source to the detector, μ_m is the linear attenuation coefficient of the interacting material, and x_m is the thickness crossed by the X-Ray.

Thus, after the first step, we get the X-Ray flux arriving on the detector screen. The second step of the simulation computes the detector response together with the camera coupling. This step requires defining:

1. **Scintillator detector:** The scintillator material and thickness together with an MCNP calculation of the detection efficiency ε, and the mean energy deposited by the X-Ray photon as a function of its energy, as well as the associated dispersion ("swank noise");
2. **The scintillation yield:** The fraction of incident photon energy converted into visible light;
3. **The de-magnification factor:** Phosphor screen dimensions over camera sensor dimensions);
4. **Camera characteristics:** Electronic yield, readout noise, numerical conversion, etc.

The detected X-Ray flux is randomly sampled in a Poissonian law around the mean value $\varepsilon \cdot I$ to account for the statistical noise. It is then converted into visible photon flux, then into electron flux also randomly sampled in a Poissonian law around the mean value, then into a digital signal in ADCU (Analogue to Digital Conversion Units). The simulated signal noise, in addition to the statistical fluctuation of X-photons and visible photons counting, accounts for the swank and readout noise sources [42].

The simulation also accounts for the source spot-size and the detector response FWHM (Full Width at Half Maxima) for a point-source, resulting in image blur.

The code has been recently upgraded to include the scattered photon flux to the attenuated direct flux I, thereby obtaining good agreement between the simulated images and the images obtained from the experiments [42].

4.2. Simulating corium particles

This section details the application of MODHERATO in obtaining preliminary results of expected images of the corium fragments having sizes predicted from the statistical analysis in the previous chapter. MODHERATO allows understanding the performance of the X-Ray imaging system in detecting corium particulates in terms of resolution, detectability, contrast precision, etc. The simulation involves defining a virtual 3-D object or phantom placed between an X-Ray source and a detector describing its dimensions, material density, and composition as explained in the previous section. Understanding the quality of the simulated radiographies will thus help to complete the interaction zone designs.

Initial simulations were performed to obtain the detection limit for the PLINIUS-2-FR configuration [42]. The detection limit is the lowest quantity of a substance that can be distinguished from its background (a chosen value) with a stated confidence level. 3-D models of fragmented corium in reactor coolant with similar attenuation properties (phantoms), were used to investigate the criterion of object detectability, i.e., the detection limit. A similar simulation has been performed for the KROTOS facility to study corium-water interaction [37]. The phantoms utilized in the KROTOS facility were used to calculate the detection limit for the PLINIUS-2-FR configuration. This phantom is comprised of several steel balls (representing corium fragments) of dimension ranging from 1 mm to 30 mm, fixed inside a polyethylene plate (representing water). This phantom was simulated with MODHERATO in the PLINIUS-2-FR X-Ray imaging configuration (presented in chapter 2) ,i.e., with a 15 MeV source, in order to estimate the detection limit of this system. The simulated radiography of the phantom is shown in Fig. 4.1(b).

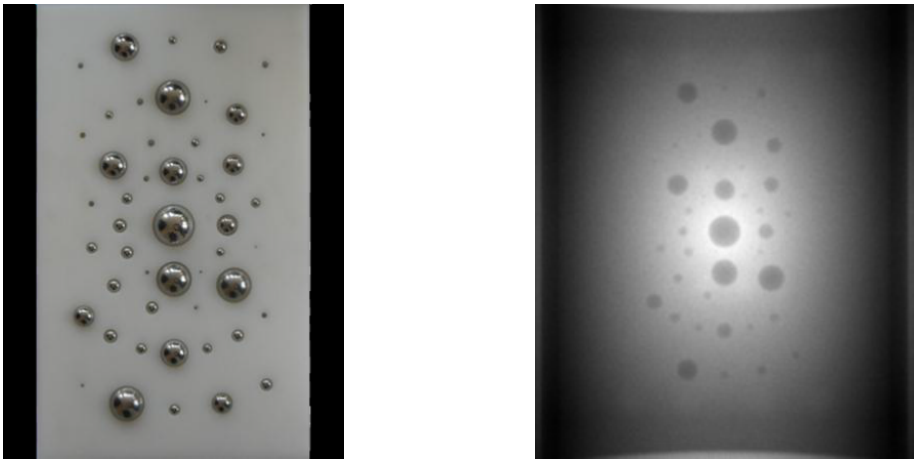

(a) **KROTOS phantom.** (b) **MODHERATO image.**

FIGURE 4.1: Phantom of polyethylene with steel balls manufactured for radioscopy test on KROTOS and its simulated image with MODHERATO.

The image is observed to have an inhomogeneity in the intensity, for instance, the images are brighter at the center while darker at the periphery. This could be very clearly observed in a full flux image shown in Fig. 4.2, an image simulated without any phantom between the X-Ray source and the detector screen. This inhomogeneity in the intensity in these images is due to the fact that the X-Ray source utilized is not monochromatic (as said in Chapter 2); its energy varies spatially and is maximum at the center and gradually decreases moving away from the center. Hence, in order to remove this inhomogeneity and obtain a contrast image we subtract the raw MODHERATO image of Fig. 4.1(b) from the full flux image shown in Fig. 4.2. We thus, obtain a contrast image as shown in Fig. 4.3(a).

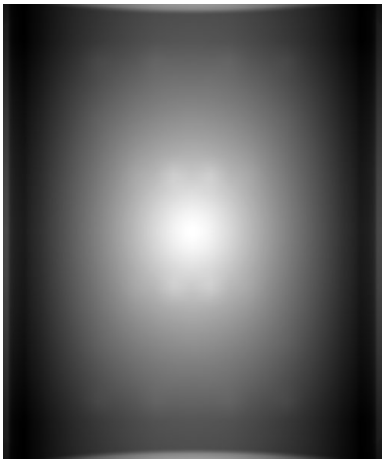

FIGURE 4.2: Full flux image without any particle as simulated by MODHERATO.

Signal to noise ratio (S/N) is a measure that compares the level of the obtained signal at the desired location to the level of background noise in the raw image (in an unprocessed image) [65]. However, a contrast to noise ratio estimation can help in comparing the quality of the balls in different regions. The contrast to noise ratio (C/N) is a measure of the image quality based on the contrast rather than the raw signal, i.e., it is similar to S/N but subtracts off a term before calculating the ratio [65]. Thus, from the contrast image shown in Fig. 4.3(a), C/N is estimated by dividing the contrast variation along the centerline horizontal axis of the image by noise. It is depicted in Fig. 4.3(b). A contrast of more than five times the background noise level (any variation in the signal apart from the signal being monitored), i.e., 5σ has been set to define the detection limit of this simulation. The particle size corresponding to this order of contrast to noise ratio is around 5 mm, and this defines the detection limit of corium particles. Also it must be noted that the highest central peak corresponding to a steel ball of size 30 mm has a width greater than 30 mm. This provides us data for further works on uncertainity estimation.

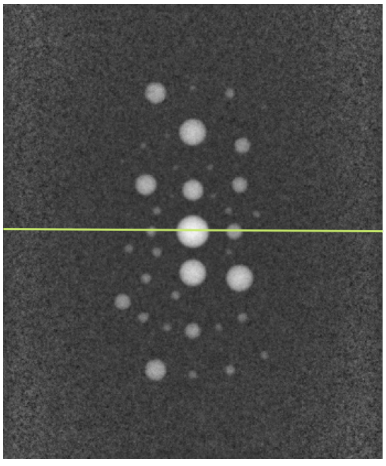

(a) **Contrast Image.**

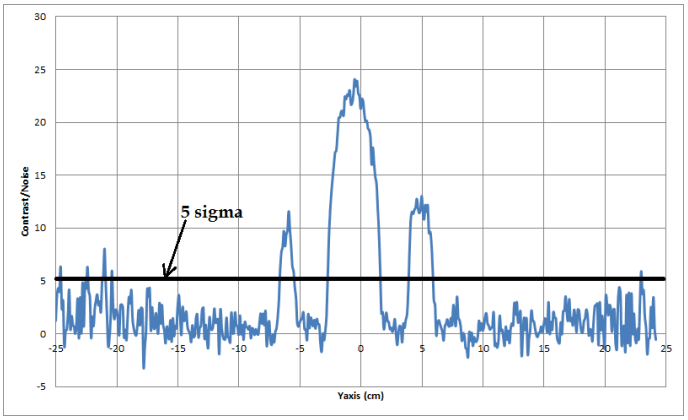

(b) **Contrast to Noise ratio variation along horizontal centerline.**

FIGURE 4.3: Contrast to noise ratio variation to determine the detection limit.

As discussed in the previous section, the analysis of the past corium-sodium experiments provides an estimate of the oxide particle size, i.e, $\sim 0\,01$ to $0.7\,\mathrm{mm}$ and SS particle size in the range 0.05 to $0.65\,\mathrm{mm}$ resulting from the interaction. This size is considerably smaller than the detection limit of the X-Ray imaging system as estimated by MODHERATO. Thus, it was opted to simulate clouds of particles (a group of small fragments) instead of detecting particle by particle. Anyhow, it must be considered that if 1l of corium (~ 8 kg) is fragmented in 0.1 mm particle, then there would be about 10^9 particles, so that even if the detection system would have a sufficient resolution, it would be meaningless to detect and analyze each individual particle as done in KIWI where only a few tens of particles are present. These clouds of particles were simulated in the PLINIUS-2-FR X-Ray imaging configuration with 15 MeV X-Ray beam projected on the PLINIUS-2-FR test section containing sodium coolant and the cloud of particles. The size of the cloud of particles was chosen to be slightly greater than the detection limit of MODHERATO, i.e. 5.5 mm. The volume of such a cloud will be considerably larger than the volume of individual corium particles of size $\sim$0.01 to 0.7mm. Thus, to simulate a cloud of particles (a group of small fragments), each cloud consists of a mixture of corium in sodium in different proportions. In this study, clouds of 5.5 and 10 mm will be simulated with corium mass fraction varying from 50 to 100% in the mixture and the rest being liquid sodium.

The simulated images of clouds of particles of size 5.5 and 10 mm with corium mass fraction varying from 50 to 100% in the mixture are shown in Fig. 4.4(a) and 4.4(b) respectively. It consists of cubic and spherical clouds placed at a distance of roughly 3 cm and 4 cm from the center. Also, a cylindrical cloud of corium jet of diameter 1 cm and length 4 cm is simulated and can be seen at the top in both Fig. 4.4(a) and 4.4(b).

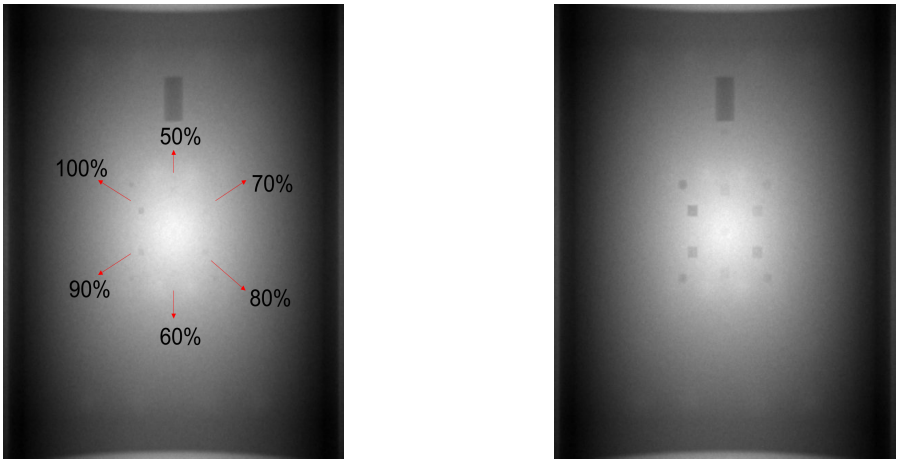

(a) **Cloud of size 5.5 cm.** (b) **Cloud of size 10 cm.**

FIGURE 4.4: Unprocessed MODHERATO simulated images of the clouds of size 5.5 mm and 10 mm with different proportions of corium in sodium.

The contrast to noise ratio (C/N) for each of the clouds of size 5.5 mm with corium mass fraction varying from

50% to 100% and with the corresponding density of the mixture is shown in Table 4.1. The 5.5 mm clouds with 80% or more of corium have a C/N greater than 5σ which is the detection limit. Thus 5.5 mm clouds with 80% or more of corium are observed to be detectable in 4.4(a). Likewise, the contrast to noise ratio for clouds of particle of size 10 mm is shown in Table 4.2. It was observed that the 10 mm clouds with 60% or more of corium are detectable in 4.4(b).

Mass fraction of corium in corium-sodium mixture	50%	60%	70%	80%	90%	100%
Density of the mixture $(\mathrm{g/cm^3})$	2.51	3.16	4.03	5.23	7.03	10.0
C/N ratio	3.9	4.5	4.9	5.6	6.75	9.8

TABLE 4.1: C/N ratio for clouds of particles of size 5.5 mm.

Mass fraction of corium in corium-sodium mixture	50%	60%	70%	80%	90%	100%
Density of the mixture $(\mathrm{g/cm^3})$	2.51	3.16	4.03	5.23	7.03	10.0
C/N ratio	4.5	5	6.75	8.75	11.6	15.4

TABLE 4.2: C/N ratio for clouds of particles of size 10 mm.

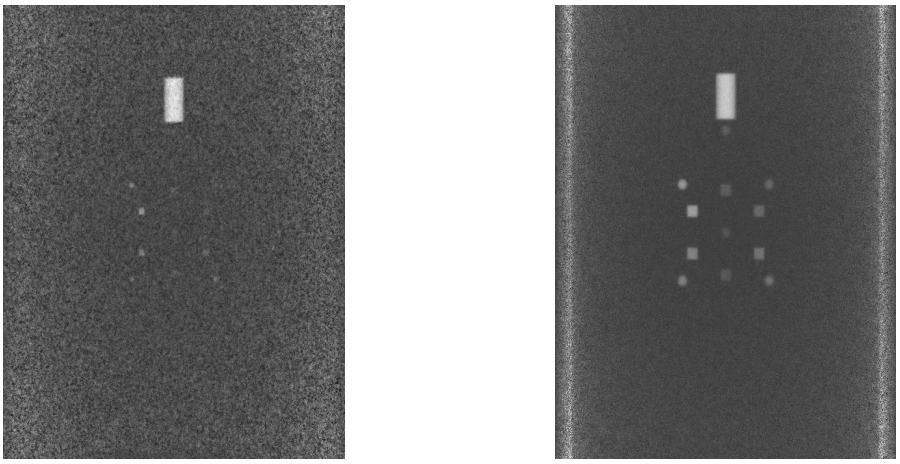

(a) **Contrast image of the cloud of size 5.5 cm.** (b) **Contrast image of the cloud of size 10 cm.**

FIGURE 4.5: Contrast image of the clouds of size 5.5 mm and 10 mm.

The variation of contrast of the clouds of size 5.5 mm and 10 mm, using ImageJ tool [66] is shown in Fig. 4.5(a) and 4.5(b) respectively. The contrast image gives a better picture of both 5.5 mm and 10 mm clouds. It appears that while less dense clouds have much lower contrast to noise ratios, it remains possible to visualize them. Therefore, it can be concluded that the limit of contrast of more than five times the background noise level is just

a conservative estimate of the lower detection limit. It is expected that the development of an advanced image processing and analysis tool, would help to detect these particles more efficiently.

The simulation was then extended to the large scale tests planned in the future PLINIUS-2-FR facility, where about 50 kg of corium is expected to be injected into sodium. For simplicity, a spherical cloud of 45 kg of corium in sodium was simulated as shown in Fig. 4.6(a). This cloud was simulated with a variation of density from the center (the densest being 100% of corium) to the peripheries (the least being 40% of corium in sodium). The contrast image of this simulation using ImageJ tool is shown in Fig. 4.6(b). The contrast to noise ratio of this image is comfortably above the detection limit, i.e., 13 for the least dense cloud, which is good enough to be clearly detectable. Furthermore, with a higher mass of corium in the cloud, the detectability improves as shown in Tables 4.1 and 4.2.

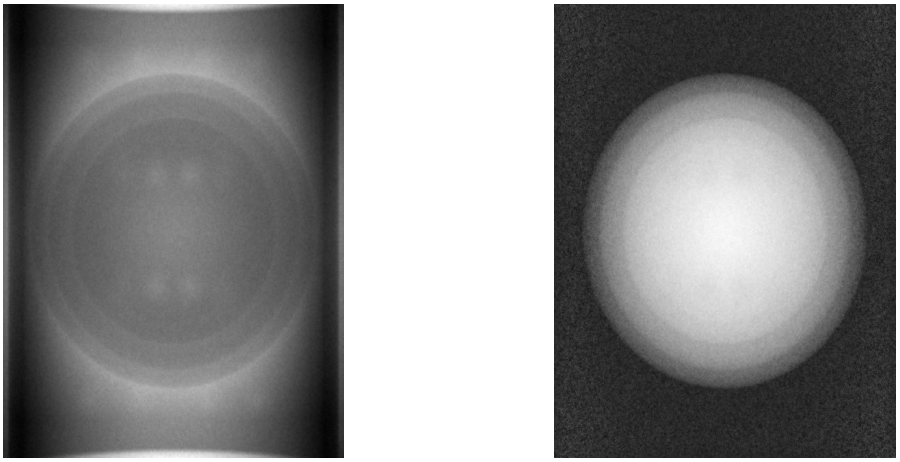

(a) **MODHERATO simulated image of the cloud of 45 kg corium.** (b) **Contrast image of the cloud of 45 kg corium.**

FIGURE 4.6: Simulated image and contrast image of the clouds of 45 kg of corium.

4.3. Simulating clouds of corium fragments

It should be noted that the simulations carried out in the previous section to simulate clouds of particles, were a homogenous mixture of corium in sodium. However, in real experiments, a cloud of individual particles will be formed. Thus a simulation of numerous individual corium fragments of ⌀0.5 mm stacked together in a cubical box of size 5 mm (the detection limit as calculated by MODHERATO) as shown in Fig. 4.7 was important to be performed.

Consequently, simulating 1000 individual corium fragments of ⌀0.5 mm packed closely in a cloud of size 5 mm we obtain the image shown in Fig. 4.8(a). The cloud is better visible in the contrast image (in red) shown in

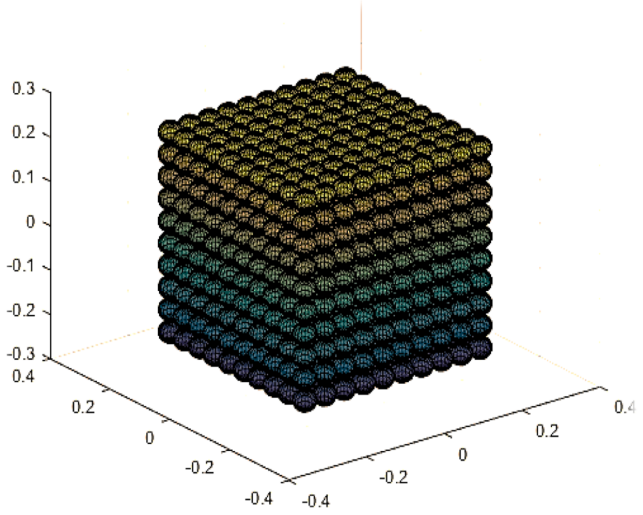

FIGURE 4.7: A pictorial representation of corium fragments stacked together in a cubical cloud.

Fig. 4.8(b) corresponding to the raw unprocessed image. The contrast to noise ratio of this cloud, with several

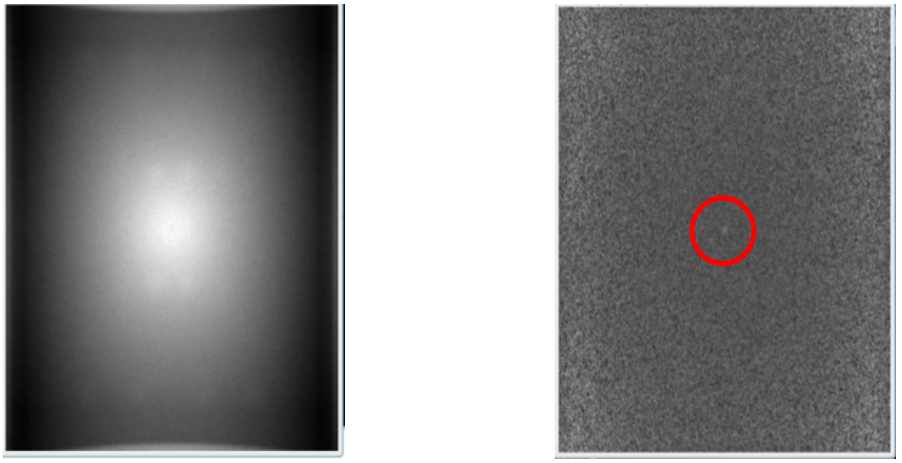

(a) **Simulated image.** (b) **Contrast image.**

FIGURE 4.8: Simulated image and contrast image of a cloud having 1000 corium fragments of ⌀0.5 mm.

corium fragments packed together in a cube (thus having a packing fraction of 52%), is 5.4. Whereas the C/N of homogenous density cloud with corium fraction 50% is 3.9. Since the C/Ns in both homogeneous and individual particles cloud is roughly the same. Thus, the clouds of particles can also be represented by homogenously density cloud.

It is crucial to indicate here that, the 1000 corium fragments being present in a small cubical cloud of size 5 mm will pose a challenge in tracking individual particles, as there will be several particles in one pixel. Thus, these particles will be indeed monitored as a cloud of particles.

4.4. Simulating vapor bubbles and liquid sodium

As discussed before, the interaction between corium and sodium leads to a 3 phase mixture one of these phases being vapor in the form of bubble and/or pockets. We then need to simulate vapor and verify its detectability. Assuming the temperature of sodium vapor to be around 1200 K, the density of the sodium vapor corresponding to this temperature is $0.394 \times 10^{-3}\,\mathrm{g/cm^3}$ [67]. The simulation of sodium vapor bubble with MODHERATO could be carried out by simulating a sodium vapor bubble of size 4 cm in sodium coolant and comparing with the simulation of a polyethylene ping pong ball of size 4 cm which was also used by Grishchenko. [46] to simulate steam. The simulations produce images as shown in Fig. 4.9. Upon simulating a polyethylene ball of size 4 cm and of thickness 0.4 mm we obtain the images shown in Fig. 4.10

(a) **Simulated image of sodium vapor bubble.**

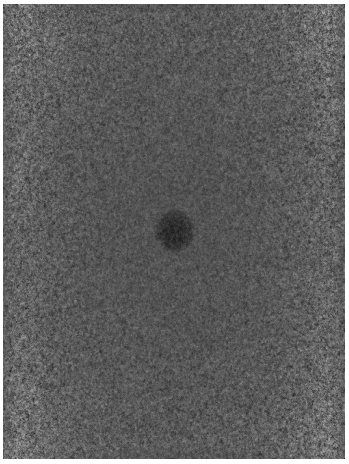

(b) **Contrast image of sodium vapor bubble.**

FIGURE 4.9: Simulated image and contrast image of sodium vapor bubble of size 4 cm.

(a) **Simulated image of ping pong ball.**

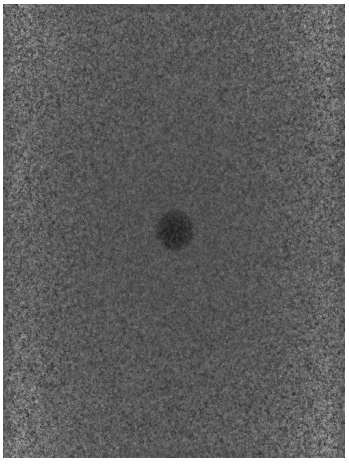

(b) **Contrast image of ping pong ball.**

FIGURE 4.10: Simulated image and contrast image of ping pong ball of size 4 cm.

Comparing the C/N ratio in each of the case we observe that both sodium vapor bubble and polyethylene pingpong balls exhibit the same C/N of roughly 5.6. Thus, we can say that sodium vapor bubble can be simulated by using polyethylene ping pong balls in our experiments.

4.5. Choice of materials for designing of phantoms

Phantoms cannot be constructed using materials with which we will perform experiments in the PLINIUS-2-FR facility. This is due to several reasons. One of them is the active nature of materials like uranium dioxide and also the restrictive use of sodium for safety reasons. Thus, we require the use of solid inactive materials which could play a role of corium, liquid sodium, and sodium vapor in terms of image analysis.

The choice of materials is highly dependent on their interaction properties with X-Rays, i.e., how the X-Rays are absorbed or scattered when they pass through the medium. These are together quantified by the attenuation parameter of the material. The degree of attenuation depends on the atomic number and physical density of the material, and the energy of the X-Rays. However, at high energy, the attenuation of X-Rays depends primarily on the density of the medium traversed as the mass attenuation coefficient reduces to very small values. We would, therefore, chose inactive materials for the phantoms whose density is as close as possible to that of the materials planned to be used in the future PLINIUS-2 facility.

So, the list of materials chosen for the production of the phantoms is presented below:
Material A: Corium fuel must be replaced by an inactive material of density close to $8\,\mathrm{g/cm^3}$. We chose to employ steel as it is easy to machine and has a density of $8.05\,\mathrm{g/cm^3}$ at room temperature. Both the corium fragments and corium jet were chosen to be represented by balls and rod, respectively, made of steel. **Material B:** Sodium coolant which has a density of $0.745\,\mathrm{g/cm^3}$ at saturation temperatures must be replaced by solid material of similar density. The requirement of solid material as a replacement of sodium will be depicted in the phantom designs in the next section. Low density ($0.75\,\mathrm{g/cm^3}$) polyethylene could not be used to fabricate phantoms with a good definition of edges. So, it was chosen to be represented by high-density polyethylene (HDPE) of density $0.95\,\mathrm{g/cm^3}$. The difference in the densities was adjusted while defining the dimensions of the phantoms, in such a way that the net mass thickness of the HDPE column was roughly the same as that of the sodium column planned in the PLINIUS-2 facility. The sole dependency of attenuation on the mass thickness can be guaranteed from the similar mass attenuation coefficients of corium with steel and sodium with polyethylene as presented in the Table 4.3

TABLE 4.3: Comparison of mass attenuation coefficients of material in CSI with its simulant material.

Mass attenuation coefficient (cm^2/g)	
Material in CSI	**Simulant material**
Corium Approx. 3.842E-02 (for 50% UO_2 – 50% SS)	Steel 2.991E-02
Sodium 2.319E-02	Polyethylene 2.383E-02

Material C: Sodium vapor having a density of $0.394 \times 10^{-3}\,\mathrm{g}/\mathrm{cm}^3$ was chosen to be represented by void (air). These can also be represented with plastic ping-pong balls which are voided in the center, depending on the configuration we want to observe. **Material D:** The partitions used in some of the designs to separate the "phases" (which will be explained in detail in the next section) will be made of polycarbonate of thickness $0.2\,\mathrm{mm}$. This material, because of its very low density ($1.2\,\mathrm{g}/\mathrm{cm}^3$) and very low thickness, will have a negligible effect on the attenuation of an X-Ray beam. These simulant materials chosen are summarized in Table 4.4

TABLE 4.4: Chosen simulant materials for designing phantoms.

Material type	**Material in a CSI**	**Simulant material**
A	Corium	Steel
B	Sodium (liq.)	Polyethylene
C	Sodium vapor	Void (Air)
D	Partitions	Polycarbonate

4.6. Proposed physical phantoms representing FCI phenomenon

The simulation with the code MODHERATO and the understanding developed on the phenomenology of corium-sodium interaction lead us to the second step, i.e., the designing of phantoms that are representative of certain CSI. These phantoms will be used to experimentally evaluate the performance of the X-Ray imaging system on a CSI medium. The phantom designs proposed to represent corium fragmentation in sodium are categorized into three categories:

1. **Premixing Phantom: Representing a premixing state**

This phantom is a representative of coherent corium jet in the middle of a fragmented area. The coherent corium jet is represented by a steel rod of diameter 20 mm corresponding to one of the ejection diameters planned in the PLINIUS-2-FR facility. The corium fragments are simulated with the help of steel balls. Although the fragments formed in a corium-sodium interaction are of the sub-millimetric size, the detection and difficulties in processing very small diameter steel balls is a problem. Therefore, balls of ⌀4mm have been considered. The residual volume between the steel balls causes a decrease in the mean density of the medium as in a cloud of corium particles. These balls will be distributed in the concentric cylinders of the

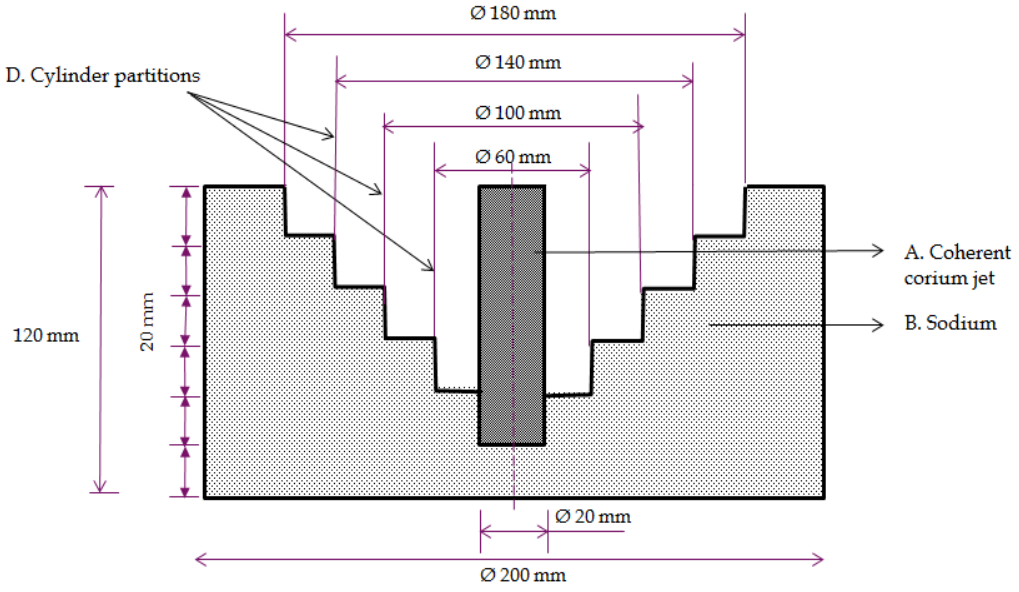

FIGURE 4.11: Geometry of the premixing phantom.

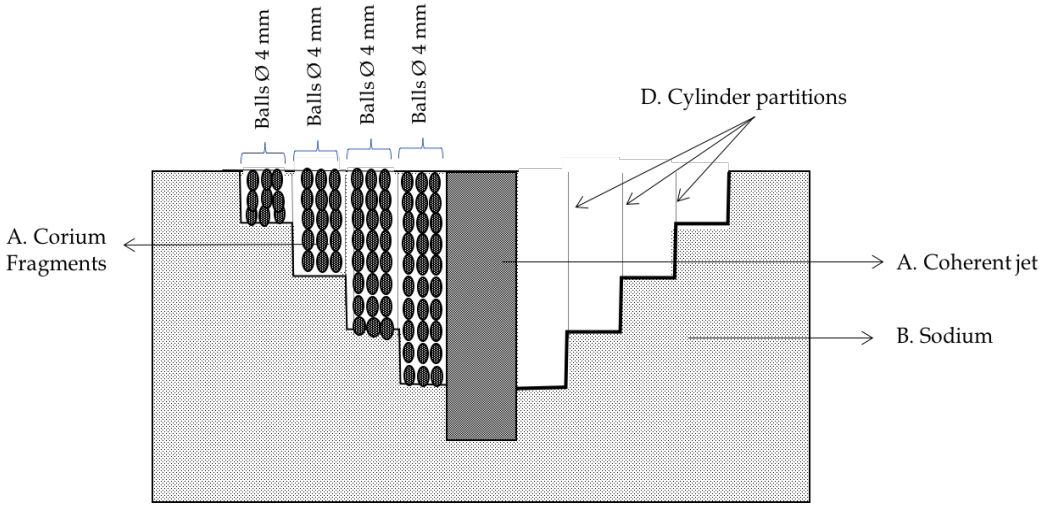

FIGURE 4.12: Premixing phantom filled with balls of varying diameter.

phantom. Each zone will have a given diameter of balls or may be a mixture of diameters. In the zone, the steel balls can also be mixed with hollow plastic balls representing sodium vapor voids.

The geometry of this phantom is shown in Fig 4.11. The sodium column is represented by a polyethylene cylinder with four concentric hollowed out cylinders. In the center-most hollow cylinder, a cylindrical rod of material A representing the coherent corium jet is fixed. Each of the concentric cylinders is separated by a material D of thickness $0.2\,\mathrm{mm}$ (partition). The steel balls of diameter 4 mm are filled in the hollow spaces as shown in Fig 4.12.

2. **Vapor phantom: Model for the vapor film around the coherent jet**

This phantom is designed to represent the vapor film which might be formed around the coherent jet of corium when it is injected into sodium.

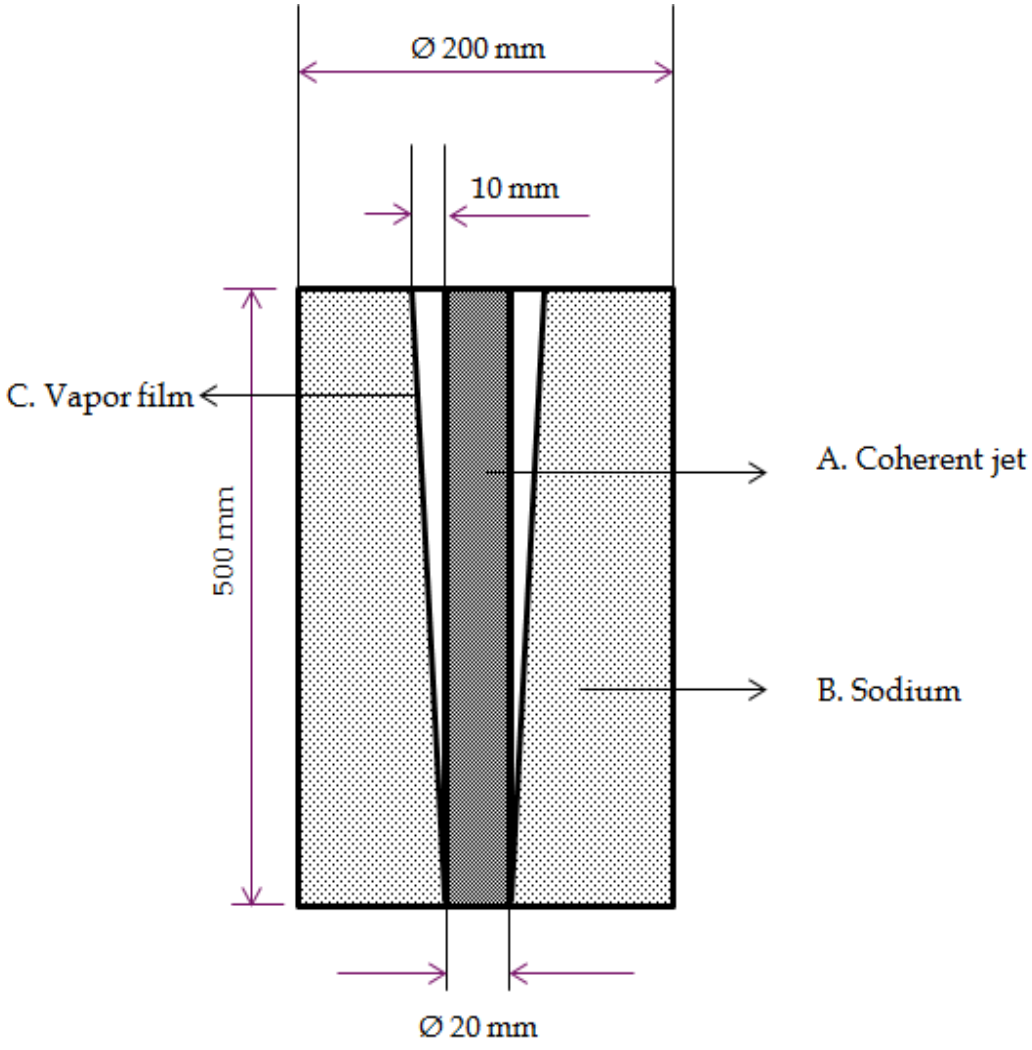

FIGURE 4.13: Geometry of the vapor phantom.

In this phantom, material A is used for the coherent jet, i.e., a steel rod of diameter $20\,\mathrm{mm}$, material B, i.e., polyethylene plastic is a representative of liquid sodium. The geometry of this phantom is depicted by Fig. 4.13. The vapor film is represented by an air gap between materials A and B. This is the reason why solid materials are required to replace sodium.

To evaluate the performance of the imaging system for the sodium vapor film, the phantom is designed in such a way that the thickness of the air gap representing the vapor film varies progressively around the steel rod. This is achieved by fabricating a cone in the inside of part B to obtain a varying thickness of the air gap between material A and B.

3. **Dynamic phantom: Dynamic model**

The objective of this phantom is to model the relative motion between the clouds of corium particles, so as observe how the overlapping clouds appear and thus trying to segment them. This phantom would also be essential for velocity estimation of the clouds of particles.

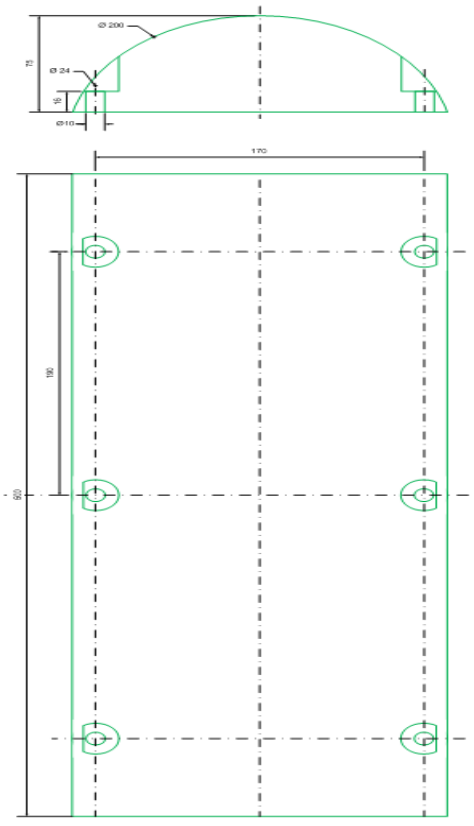

(a) **Geometric design of half cylinders of Dynamic phantom.**

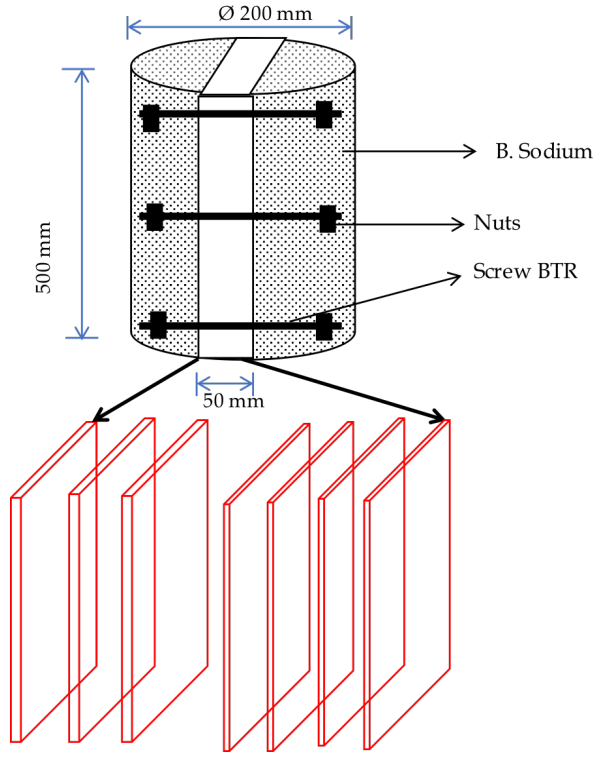

(b) **Pictorial representation of Dynamic phantom.**

FIGURE 4.14: Dynamic phantom geometry.

This phantom is composed of two identical HDPE cylindrical halves with a reach through window ($50\,\mathrm{cm} \times 160\,\mathrm{cm} \times 500\,\mathrm{cm}$) and connected to each other via rods, nuts, and bolts as shown in Fig. 4.14(b). The geometry of the cylindrical halves is illustrated in Fig. 4.14(a). The reach through window consists of 7 HDPE plates of $0.5\,\mathrm{cm}$ or $1\,\mathrm{cm}$ thickness, and of length 500 mm and breadth 160 mm stacked together as illustrated by Fig. 4.14(b). These plates represent different cross-sections of the 3-D space and can also be slid upwards or downwards to evaluate the performance of the X-ray imaging system on the relative motion between different cross-sections. All the 7 plates are pierced as shown in Fig. 4.15. Out of the 7 plates, 3 alternate plates are to be filled with several steel balls and hollow plastic balls representing a cloud of particles and voids. The remaining 4 plates will act as voids, representing vapor bubbles in sodium.

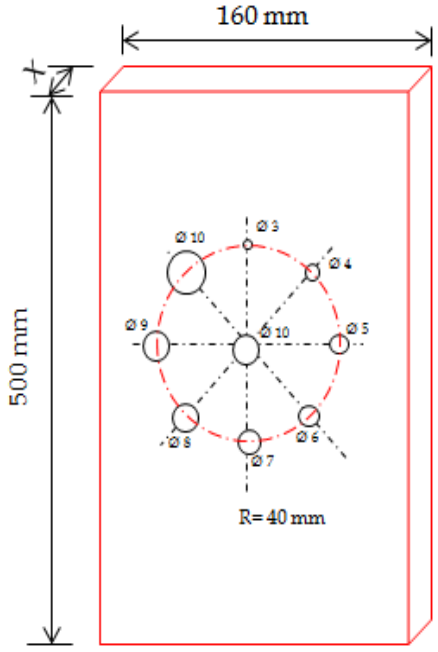

FIGURE 4.15: Geometry of HDPE plates where X= 0.5 cm for 3 plates and X= 1 cm for 4 plates.

4.7. Simulation of the PLINIUS-2-FR test section at the KROTOS facility

The PLINIUS-2-FR test section, due to its large sodium column and the substantial thermal shielding, holds a significant role in the attenuation of the X-Ray beam. Since the facility is still under conception, experiments were planned to be conducted at the KROTOS facility by simulating the PLINIUS-2-FR geometric and physical

conditions. Similar attenuation, as expected in the PLINIUS-2-FR test section, can be achieved by substituting a material which has an equivalent mass thickness of $115\,\mathrm{g/cm^2}$ of the PLINIUS-2-FR test section. Steel plates which have the appropriate density ($8\,\mathrm{g/cm^3}$) were planned to be used. It was computed that steel plates of thickness $14.5\,\mathrm{cm}$ could serve the purpose and would produce the same attenuation as the PLINIUS-2-FR facility. Instead of designing 1 steel plate of thickness 14.5 cm which would be huge and heavy, it was decided to use 3 plates each of thickness $4\,\mathrm{cm}$, $5\,\mathrm{cm}$ and $5.5\,\mathrm{cm}$, respectively.

The KROTOS aluminum alloy pressure vessel could not be avoided while performing experiments. Since it has a very low mass thickness of $2.81\,\mathrm{g/cm^2}$, it was approximated of producing a negligible attenuation. Thus, the PLINIUS-2-FR test section was simulated with the help of 3 steel plates of thickness $4\,\mathrm{cm}$, $5\,\mathrm{cm}$ and $5.5\,\mathrm{cm}$ respectively, placed in front of the KROTOS pressure vessel.

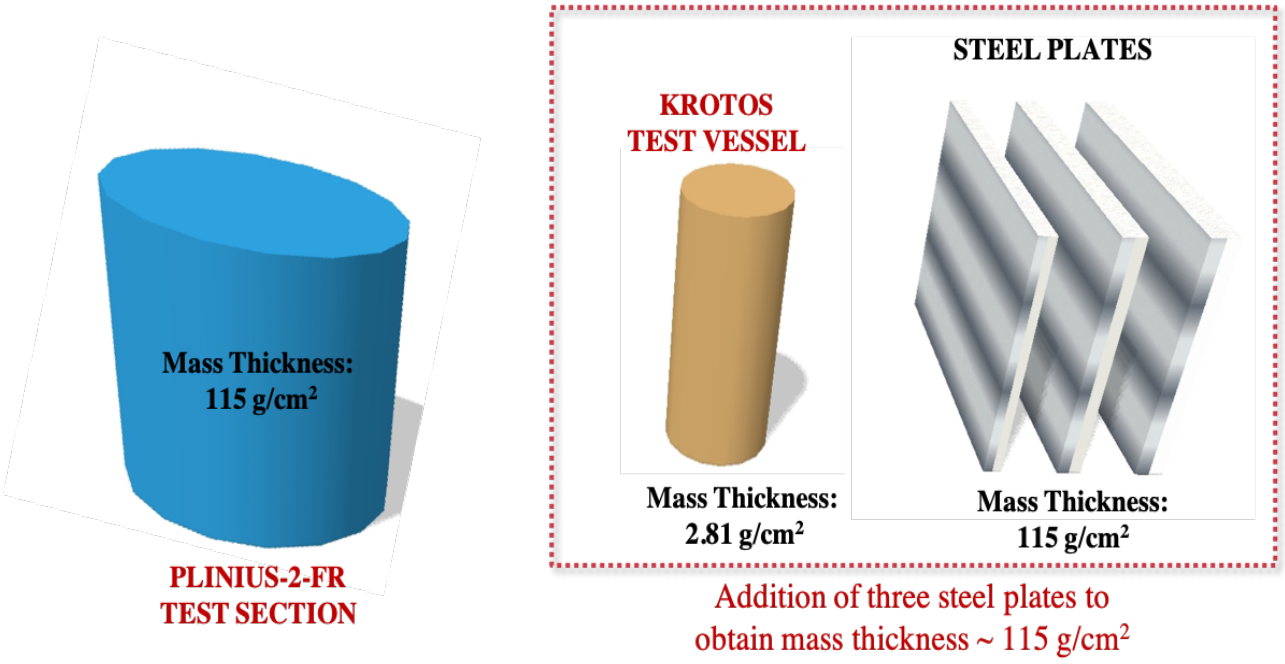

FIGURE 4.16: Simulating PLINIUS-2-FR test at KROTOS facility.

Now, since at the KROTOS facility, the imaging system is different from that at the PLINIUS-2-FR facility, the image signal obtained at the camera will be different. As simulated by MODHERATO, for the KROTOS facility, with a $9\,\mathrm{MeV}$ source, projected on the steel plates of total thickness $14.5\,\mathrm{cm}$, recorded by the camera was observed to be of very low quality as shown in purple in Fig. 4.17, in comparison to the recorded at the camera in the PLINIUS-2-FR facility with a $15\,\mathrm{MeV}$ source, projected on the PLINIUS-2-FR test section, shown in yellow. The peak signal anticipated at the PLINIUS-2 facility is higher than that of the KROTOS facility by a factor(R) of approximately 39.

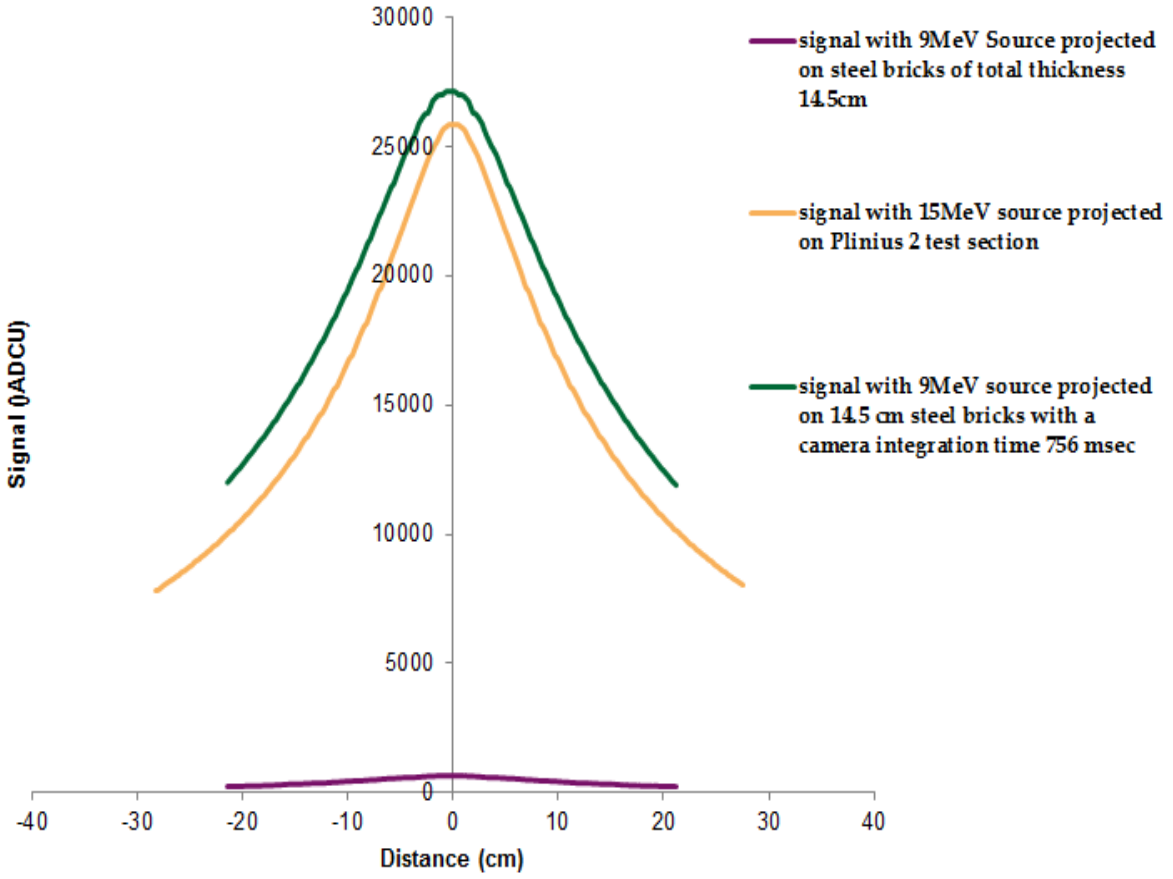

FIGURE 4.17: Comparison of signals recorded by the camera at the KROTOS facility and at the PLINIUS-2-FR facility (as simulated by MODHERATO).

Therefore, to compensate the reduction in source strength with the 9 MeV source and augment the signal by a factor of R, the camera acquisition time had to be increased by a factor of R, thereby integrating the signal over R LINAC pulses each of time duration t= 20 ms. This can be better understood with reference to Fig 4.18. If the camera integration time is less than one pulse duration of 20 msec, it integrates on one pulse, but if the camera integration time is more than one pulse duration, it integrates the signal over several LINAC pulses. Thus, the camera acquisition time to obtain R times more signal corresponds to 756 msec. Upon increasing the acquisition time of the camera, the signal quality improved as shown by green in Fig. 4.17 which is in agreement with the signal quality at the PLINIUS-2 facility. Similarly, the camera integration time was calculated for the other configurations as well, i.e without any plate, with one steel plate of thickness 4 cm, with two steel plates of thickness 9 cm in total. The integration times corresponding to each of the configurations are enlisted in Table 4.5. The configuration without any shield is named as S0. Configuration, where the experiments were performed placing steel plate of thickness 4 cm, is termed as S1. The configuration S2 corresponds to S1 plus a

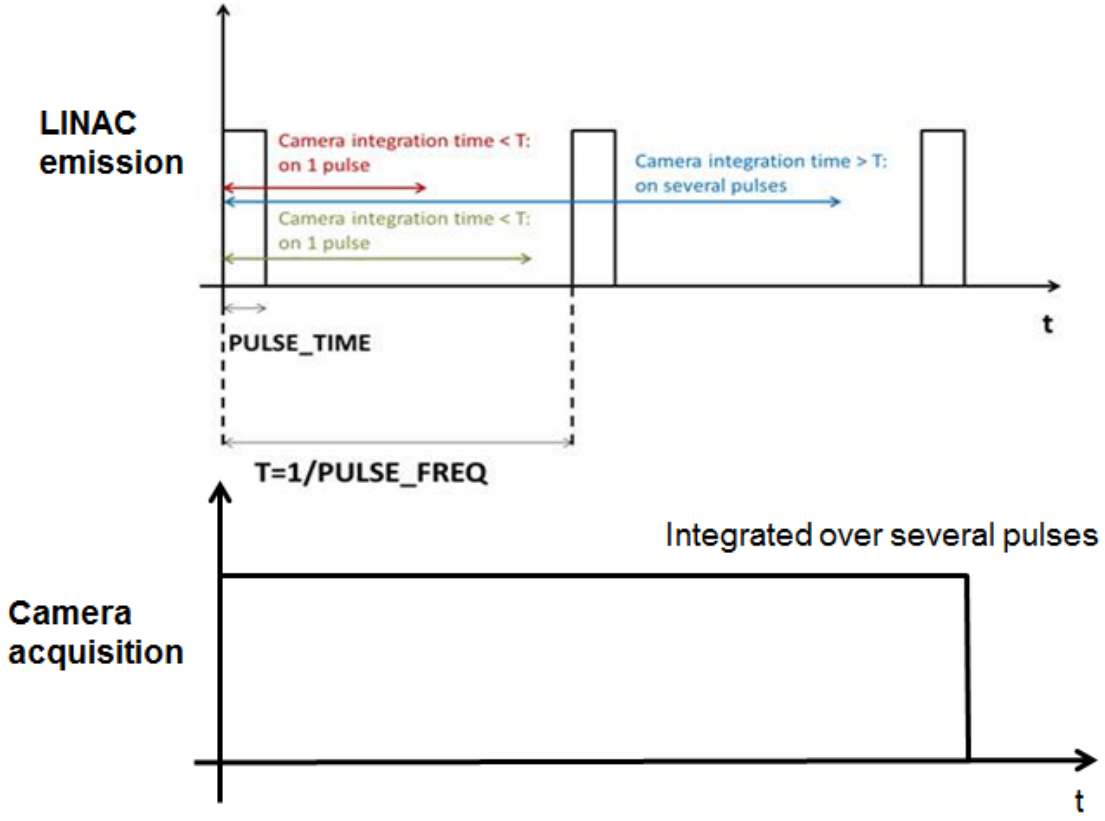

FIGURE 4.18: LINAC and camera synchronization.

steel thickness of 5 cm, i.e., a total thickness of 9 cm. Likewise, S3 corresponds to S2 plus a steel thickness of 4.5 cm, i.e., a total thickness of 14.5 cm.

Hence, by using steel plates and improving the camera acquisition time, the PLINIUS-2 image acquisition system could be simulated at the KROTOS facility to obtain a similar quality of output signal in spite of the diminished X-Ray source signal strength.

4.8. Modeling the phantoms with MODHERATO

The phantom designs are first simulated with MODHERATO to assess the performance of the imaging system.

The premixing phantom is simulated first in the KROTOS configuration as explained in the previous section, i.e., with three steel plates of total thickness $14.5\,\mathrm{cm}$ and an improved integration time of $756\,\mathrm{ms}$. Upon simulating with MODHERATO, it was observed that the image obtained is very noisy as shown in Fig. 4.19(a). This could be due to a bug in the noise calculation of the code. Simulating the phantom without the noise subroutine,

Configuration	Thickness of steel plate	Camera Integration time (msec)
S0	without any plate	4
S1	with a steel plate of thickness (4 cm)	60
S2	with two steel plates of thickness (4 cm + 5 cm= 9 cm)	225
S3	with all three steel plates of thickness: (4 cm + 5 cm + 4.5 cm= 14.5 cm)	756

TABLE 4.5: Integration time required to achieve comparable image quality at different steel shielding configurations.

generated the image shown in Fig. 4.19(b). This image clearly identifies the plastic and void regions accurately. The more precise configuration of the phantom with each ring filled with steel balls was too computationally demanding for the MODHERATO code to converge.

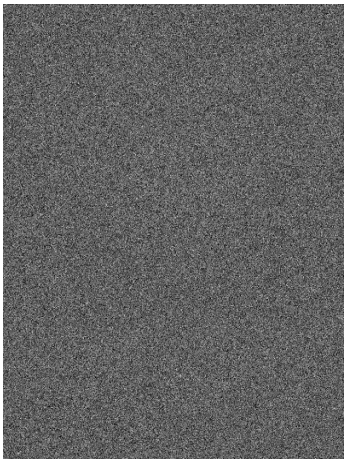

(a) **Premixing phantom in KROTOS configuration with noise simulation.**

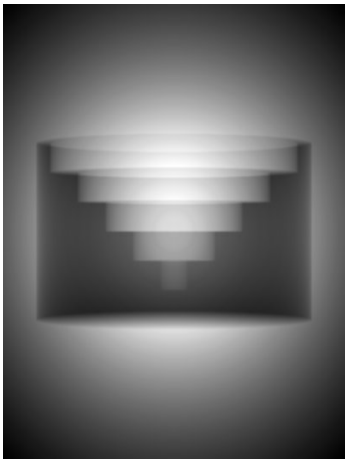

(b) **Premixing phantom in KROTOS configuration without noise simulation.**

FIGURE 4.19: MODHERATO simulated images of the phantom in KROTOS configuration.

In order to compare with the results expected at the PLINIUS-2-FR facility, the phantom designs were also simulated with the PLINIUS-2-FR X-ray imaging configuration. The image obtained is shown in Fig. 4.20.

The centerline signal profiles of the simulation obtained in the KROTOS configuration, shown in orange in Fig. 4.21 with the simulation obtained in the PLINIUS-2-FR configuration in blue were compared. It was observed that the signals demonstrate good agreement between the two configurations.

Assuming that the signal profiles obtained with MODHERATO code are in agreement with the experimental images, it can be approximated that the quality of the signal obtained while using the phantoms at the KROTOS facility will be similar to the one expected in the PLINIUS-2-FR facility.

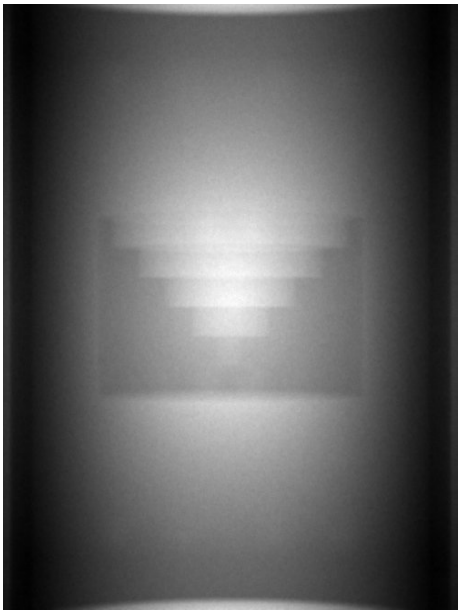

FIGURE 4.20: Premixing phantom simulated in PLINIUS-2 configuation.

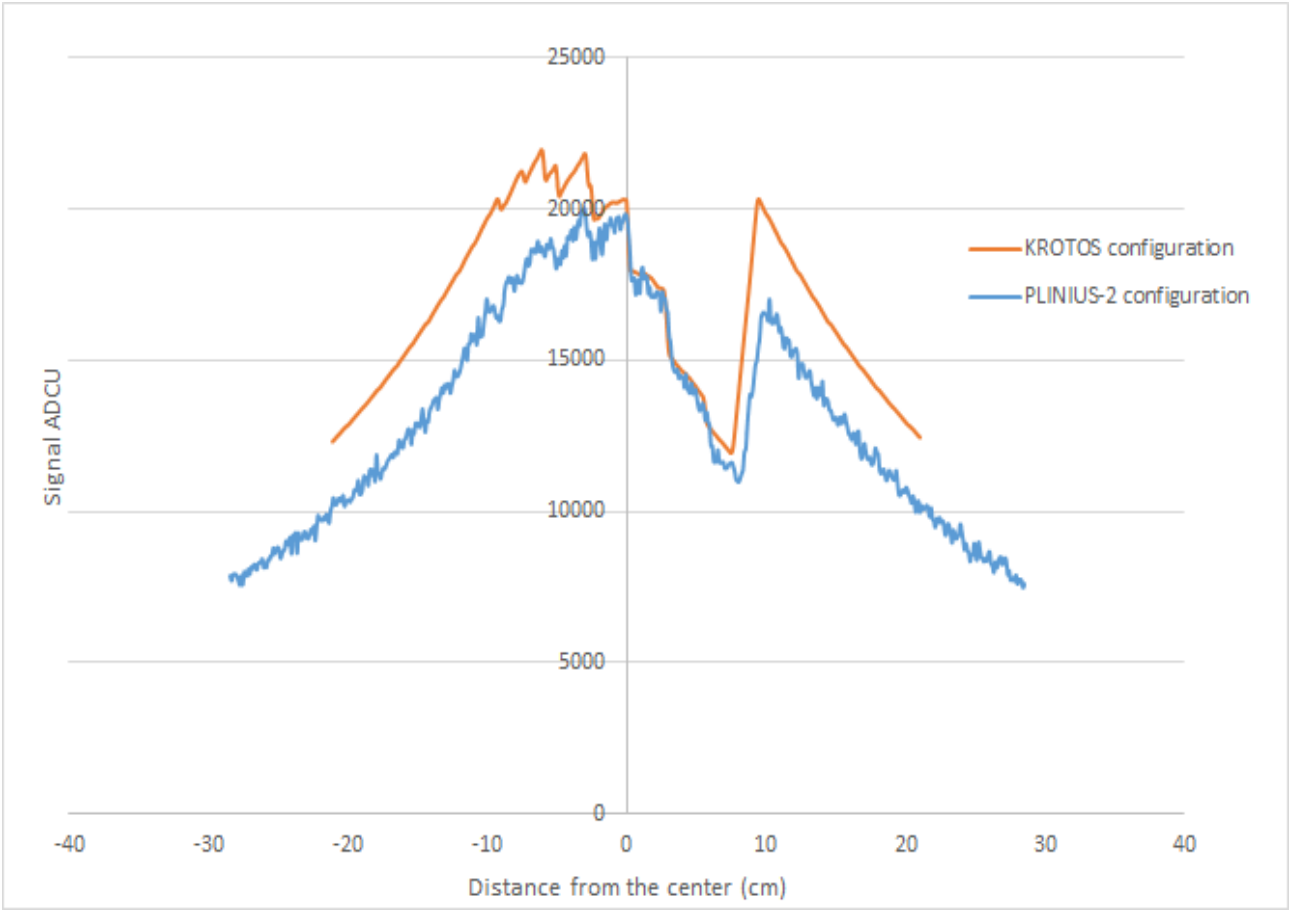

FIGURE 4.21: ADCU centerline signal obtained by simulating premixing phantom with MODHERATO.

The other phantoms were not simulated with MODHERATO assuming to obtain similar results.

4.9. Need to perform experiments

MODHERATO simulations of the premixing phantom in the KROTOS configuration were conducted. It was observed that the simulations produced noisy results when the noise calculations were included in the MODHERATO calculations and were difficult to interpret. The results without involving noise calculations, though clear, are not realistic of experimental X-Ray imaging data where some noise would be expected. Also, with the steel plates placed in front of the KROTOS test section, there would be some added abnormalities which might not have been taken into consideration in the code calculations.

MODHERATO gave us a hint of the kind of images to expect, the experiments in the KROTOS test section will allow us to verify these trends.

4.10. Summary

This chapter was dedicated to the designing of phantoms which represent the three-phase mixture formed during a CSI. In the first step of this work, corium fragments, liquid sodium, and sodium vapor were simulated with the MODHERATO code. Based on the simulation and the knowledge of a CSI phenomenology, three phantoms were designed in the second step. Simulant materials were chosen for each of the three phases present in a CSI, steel representing corium, polyethylene representing sodium and void (air) representing sodium vapor. The phantom designs were simulated with the KROTOS facility conditions and with modified conditions representing the PLINIUS-2-FR facility.

With the conditions idealized in this chapter and with manufactured phantoms, we now move to the experimental part of our work in the next chapter. Here, we will discuss the instruments and the procedure adopted to perform radiography on the phantoms. Each of the experimental instrument will be explained in detail. The results obtained from the radiography will also be summarized.

Chapter 5

Radiographic experiments with the designed phantoms

> *"See now the power of truth; the same experiment which at first glance seemed to show one thing, when more carefully examined, assures us of the contrary."*
>
> Galileo Galilei

It has been demonstrated in the previous chapter, how one can simulate an experiment representing corium-sodium interaction phase configuration in the PLINIUS-2-FR facility using, MODHERATO. The performance of the high energy X-Ray imaging system to obtain resolved images of the designed phantoms was also studied. It was necessary to confirm and refine the results obtained from MODHERATO by conducting experiments with fabricated phantoms. Following these experiments, it will be possible to investigate if the design of the facility PLINIUS-2-FR allows good detection and also optimize the X-Ray imaging system to detect at best the corium-sodium interaction medium. Also, the experiments will allow obtaining images representing the three-phase mixture of corium, liquid sodium and vapor sodium. These images could be later analyzed to visualize the three phases formed in the interaction. This will be discussed in detail in Chapter

6. The present chapter explains the experimental procedure and the chosen configurations to conduct several experiments using the designed phantoms.

5.1. Description of the experimental set-up

As mentioned in the previous chapter, the experiments were decided to be performed at the KROTOS facility utilizing its X-Ray imaging system. The experimental implementation of this system for our case was based on the parameters quantified during the simulation phase with MODHERATO in the previous chapter. The parameters included the configuration information and best suited operating conditions. These values have been adapted to the KROTOS X-Ray imaging system.

In this section, we will discuss the elements of the experiment and the operating conditions of these instruments which helped in the best outcome of the experimental results.

5.1.1 X-Ray source

The X-Ray source used is a Mini Linatron, operated at $9\,\mathrm{MeV}$, emitting impulses at $50\,\mathrm{Hz}$ with $4\,\mu\mathrm{s}$ pulse time. The device could not be tested for firing frequency other than $50\,\mathrm{Hz}$ due to its limited firing capabilities. The spot diameter of this machine is $3.4\,\mathrm{mm}$. The X-Ray radiation then passes through the lead collimator which reduces the image noise by suppressing a significant amount of scattered radiation. The simulations carried out with MODHERATO, succeeded in qualifying this X-Ray imaging system for performing the experiments as already discussed in the previous chapter.

5.1.2 Replicating the PLINIUS-2-FR test section

The thick PLINIUS-2-FR test section could be simulated with the help of steel plates like explained in the previous chapter. The mass thickness of the future PLINIUS-2-FR test section is expected to be around $115\,\mathrm{g/cm^2}$, due to the large sodium column and the thermal shielding. So, in order to have similar attenuation as expected in the PLINIUS-2-FR test section, three steel plates were used, each of thickness $4\,\mathrm{cm}$, $5\,\mathrm{cm}$ and $5.5\,\mathrm{cm}$, which, when assembled in series, have the equivalent mass thickness (defined in the previous chapter) of the PLINIUS-2-FR test section. The three steel plates depicted in Fig. 5.1 will be placed together in front of the KROTOS pressure vessel.

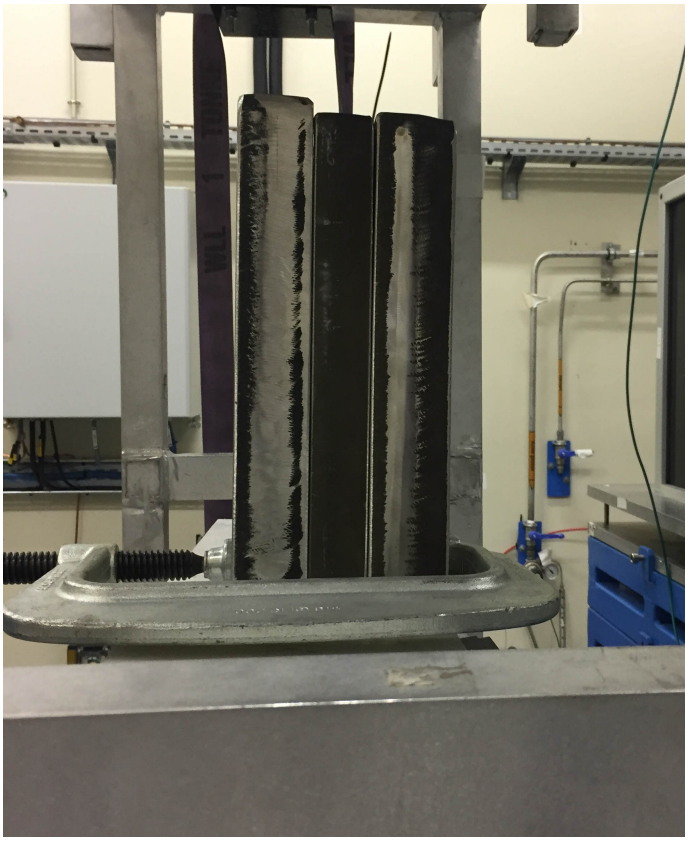

FIGURE 5.1: Steel plates for PLINIUS-2-FR facility realization.

5.1.3 Phantoms

The phantoms have been fabricated using plastic material with densities comparable to liquid sodium. Since at high energy, the attenuation depends mainly on the density of the material crossed, we thus compare only the densities of the material with that of sodium. To simulate a corium jet, we make use of a steel rod and for corium fragments, steel balls have been used. Three phantoms namely, **premixing phantom**, **vapor phantom** and **dynamic phantom** were fabricated with the help of 3D printing machines, by a French company, "AMGC".

Fabricated premixing phantom

The fabricated premixing phantom, shown in Fig. 5.2 has 4 concentric rings separated by cylindrical separations made of plastic (representing liquid sodium).

The center of the phantom is to be filled with a steel rod of diameter, 2 cm, representing a coherent jet of corium as shown in Fig. 5.3. The four concentric rings were filled with steel balls of diameter $4\,\mathrm{mm}$, shown in Fig. 5.4. The packing fraction of these steel balls was measured using the displacement method by measuring the volume

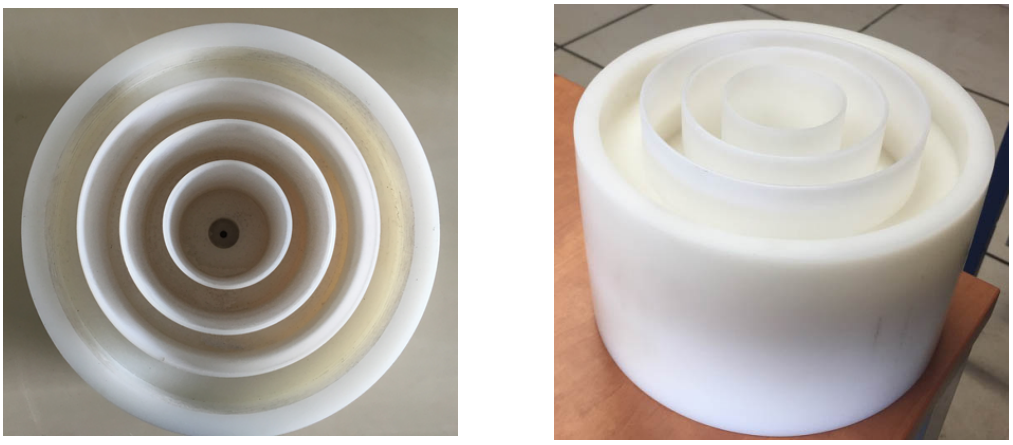

(a) **Top-view of premixing phantom.** (b) **Side-view of premixing phantom.**

FIGURE 5.2: Fabricated premixing phantom.

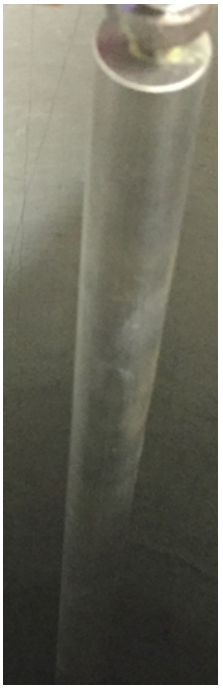

FIGURE 5.3: Steel rod representing coherent jet of corium.

displaced by the balls in water with respect to the volume occupied. The packing fraction of these steel balls was measured to be $52\,\%$. Steel balls having a density of 8 g/ml packed together with a packing fraction of 52% would represent a closely packed cloud of corium particles. However, this might not be the case in reality. To represent a loosely packed cloud of corium particles, i.e. a cloud having a lower density, Hafnia powder (HfO_2) was brought to use. A sample of the hafnia powder is shown in Fig 5.5. The density of used hafnia powder was estimated to be $2.2\,\mathrm{g/ml}$ in comparison to a density of $9.7\,\mathrm{g/ml}$ of hafnia powder in the solid state, thus indicating a 77% void fraction in the powder. The granulometry of hafnia powder was found to be such that 50% of the particles had a diameter less than 0.16 μm and 95% of them, less than 0.51 μm. Thus, the median

(a) **Steel balls used in the experiment to represent corium fragments.**

(b) **Size of the steel balls.**

FIGURE 5.4: Steel balls representing corium fragments.

diameter is close to that of expected particles during FCI.

FIGURE 5.5: Hafnia powder representing less dense cloud of corium particles.

Fabricated vapor phantom

The fabricated vapor phantom is designed to represent a vapor film of varying thickness around a coherent jet of corium. This is shown in Fig. 5.6 with a picture from the narrow hole side and one from a wider hole side. The hole size varies progressively along the length of the cylinder. A symmetric cylindrical rod shown in Fig. 5.3 is inserted in the phantom such that the gap between the steel rod and the phantom represents the vapor film. It should be noted that the phantom was made from four cylindrical columns instead of just one entire cylindrical

column of length 50 cm due to limitations of fabrication. These columns were assembled and stacked together one over the other to form one complete cylinder.

(a) **View from the narrow hole side .** (b) **View from wider hole side .**

FIGURE 5.6: Fabricated vapor phantom.

Fabricated dynamic phantom

As it has been discussed in chapter 4, a phantom was designed the overlapping behavior and the relative motion between clouds of corium particles. The fabricated half cylinders and plates are shown in Fig 5.7(a). However, due to delays in its manufacture, the experiments could not be conducted with this phantom within the time lapse of this research. Experiments with this phantom will be performed in the near future.

5.1.4 Detector Screen

The x-rays after attenuating from the phantoms are detected using scintillators as described in Chapter 2. The detector used in our case is composed of Tantalum (0.5 mm) and GADOX (1.4 mm). A picture of the detector screen is shown in Fig. 5.8.

5.1.5 ANDOR camera

The images formed on the rear side of the scintillator screen were filmed with a scientific-CMOS camera from ANDOR Zyla. This camera offers a large field of view, a high resolution of 2.6 megapixel and is well designed

(a) **Half cylinders of dynamic phantom.**

(b) **One of the plates to be used in the dynamic phantom.**

FIGURE 5.7: Fabricated components of the dynamic phantom.

FIGURE 5.8: 2D scintillator detector at the KROTOS facility with a screen size 80 x 60 cm^2 [40].

for research usage. This camera offers a 100 fps frame rate and ultra-low noise performance in a light, compact design. Thanks to a 45° mirror, the camera is placed at right angle to the axis of the X-Ray source and protected by a series of lead screens in order to avoid direct exposure and to minimize scattered radiation falling onto the camera. This is exhibited in Fig 5.9.

(a) **Configuration of camera on the rear side of detector screen.**

(b) **Camera placed at right angle to the axis of X-Ray.**

FIGURE 5.9: Camera configuration.

The following operating conditions have been implemented in the camera to film the experiment:

1. **Pixel Grouping:** All acquisitions have been carried out without any grouping of pixels, thus allowing a good resolution.

2. **Integration time:** As discussed in the previous chapter, additional attenuation due to the use of steel plates for the realization of the PLINIUS-2-FR test section, has led us to increase the acquisition time of the cameras and thus to integrate the signal over several pulses of LINATRON.

3. **Single or sequence acquisition mode:** In this series of experiments, a sequence mode is used which allows continuous acquisition of 100 images.

5.1.6 Camera-accelerator synchronization

The camera and the Mini-Linatron firing sequence are synchronized in such a way that there is no time lag between the firing trigger and the camera integration trigger. However, as far as camera integration is concerned, it takes place over several pulses of the accelerator. As already mentioned in Chapter 4, this is done in order to compensate for loss of signal of a 9 MeV source projected on the steel plates.

5.2. Configuration description

The elements of the experimental set-up are combined together to obtain the imaging chain. This imaging chain is then applied to the phantoms to obtain radiography images. Here, the geometric assembly of the imaging system and the configurations for each experiment are detailed.

5.2.1 Geometric set-up of the imaging system

The geometry of the imaging system is depicted in Fig 5.10. The source-center distance of the object is referred to as **FO** and the source-detector distance as **FD**. The magnification ratio used in the simulations carried out in Chapter 4 was 1.38. Thus, to have the same magnification ratio, following FO and FD distances have been implemented: FO: 227 cm and FD: 314 cm.

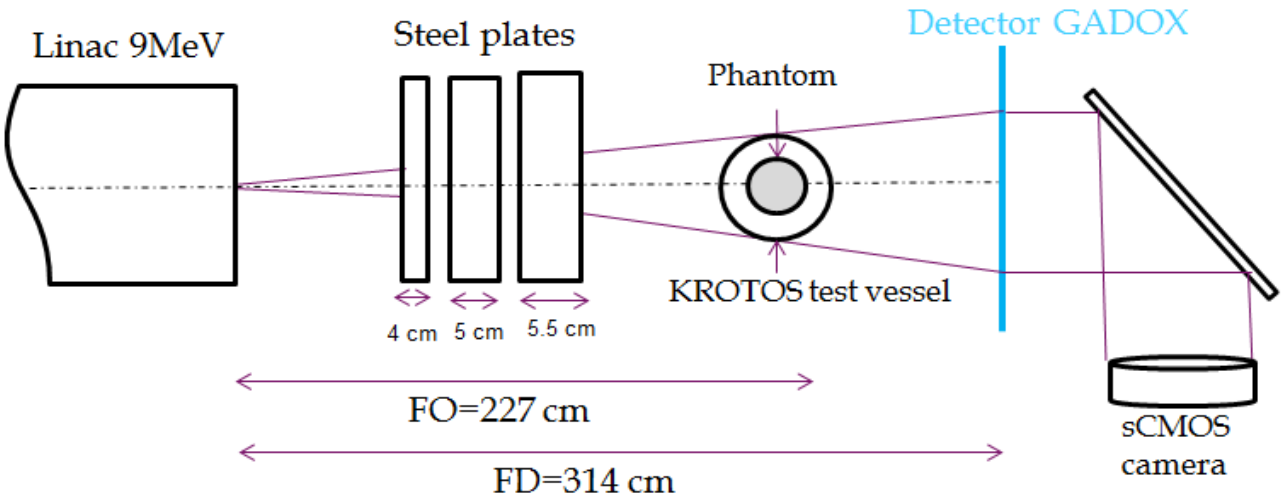

FIGURE 5.10: Schematic of the X-Ray imaging device.

5.2.2 Steel shields and integration time

This section summarizes the different configurations implemented in the series of tests. Experiments are performed to see the variation in attenuation with increasing shielding thickness. So, four acquisitions have been carried out for each type of phantom and have been represented in Fig. 5.11:

1. **Without any plate:** Configuration S0
2. **With a steel plate of thickness 4 cm:** Configuration S1

3. **With 2 steel plates of thickness 4 cm + 5 cm = 9 cm:** Configuration S2

4. **With 3 steel plates of thickness 4 cm + 5 cm + 5.5 cm = 14.5 cm:** Configuration S3 (equivalent to PLINIUS-2-FR configuration)

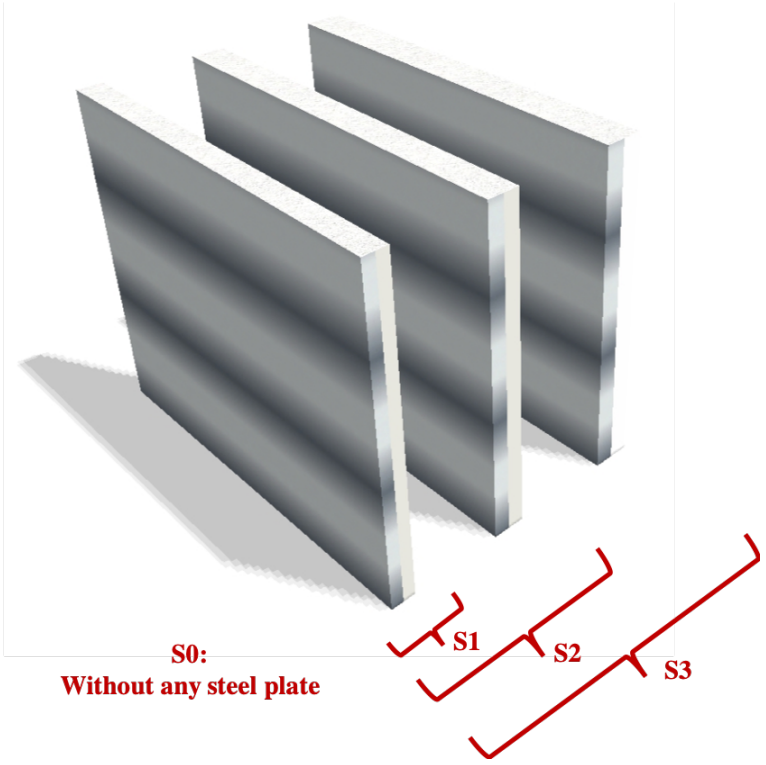

FIGURE 5.11: Shielding configurations implemented in the tests.

The corresponding integration time to obtain a signal comparable to the one without any steel shields was calculated in the previous chapter for all the configurations S0, S1, S2 and S3. Experiments were then performed for these four configurations with their respective integration time calculated in Chapter 4.

5.2.3 Number of accelerator pulses

The accelerator pulses are synchronized to the camera and the acquisition of the images is done over several accelerator pulses. Thus, homogeneity in the signal is maintained from one image to another. This can be understood with the help of Fig. 5.12. The frequency of the X-Ray flash being constant at $50\,\mathrm{Hz}$, the time duration of a single pulse of X-Ray is $20\,\mathrm{msec}$. Integrating over $4\,\mathrm{msec}$, $60\,\mathrm{msec}$, $225\,\mathrm{msec}$ and $756\,\mathrm{msec}$, we see that we integrate over, 1, 3, 11 and around 38 pulses for the S0, S1, S2 and S3 configurations, respectively. The firing period is set to be the same as the integration period.

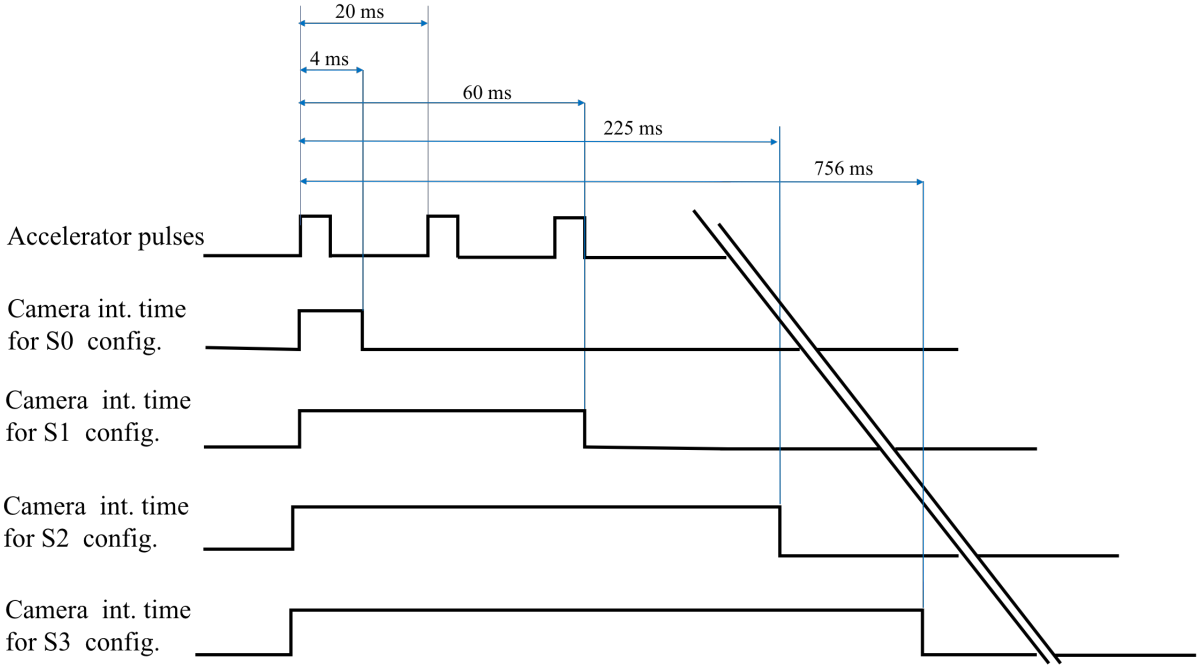

FIGURE 5.12: Accelerator camera synchronization.

5.3. Images obtained from the radiography

Performing the experiments on the phantoms allowed obtaining radiography images of the phantoms. The experimental procedure adopted to perform radiography on the phantoms is detailed in Appendix B. Three sets of experiments were performed in total: premixing phantom with steel balls, premixing phantom with hafnia powder and a last one with the vapor phantom. This has been summarised in Figure. 5.13. The images obtained from these experiments are presented in this section.

5.3.1 Premixing phantom with steel balls

Empty premixing phantom

As mentioned in the procedure of the experiment in Appendix B, 100 images were taken with each of the four configurations S0, S1, S2, and S3. It was then, necessary to perform a quick evaluation of the raw images obtained from the CMOS camera. An initial version of the image processing and analysis tool was ready at this point, that was capable of making average projections and adjusting the contrast (basic enhancement of the image). The add-on features in this image processing and analysis code were added at a later stage after we conducted the experiments and used the experimental image as a base to guide the development of the software.

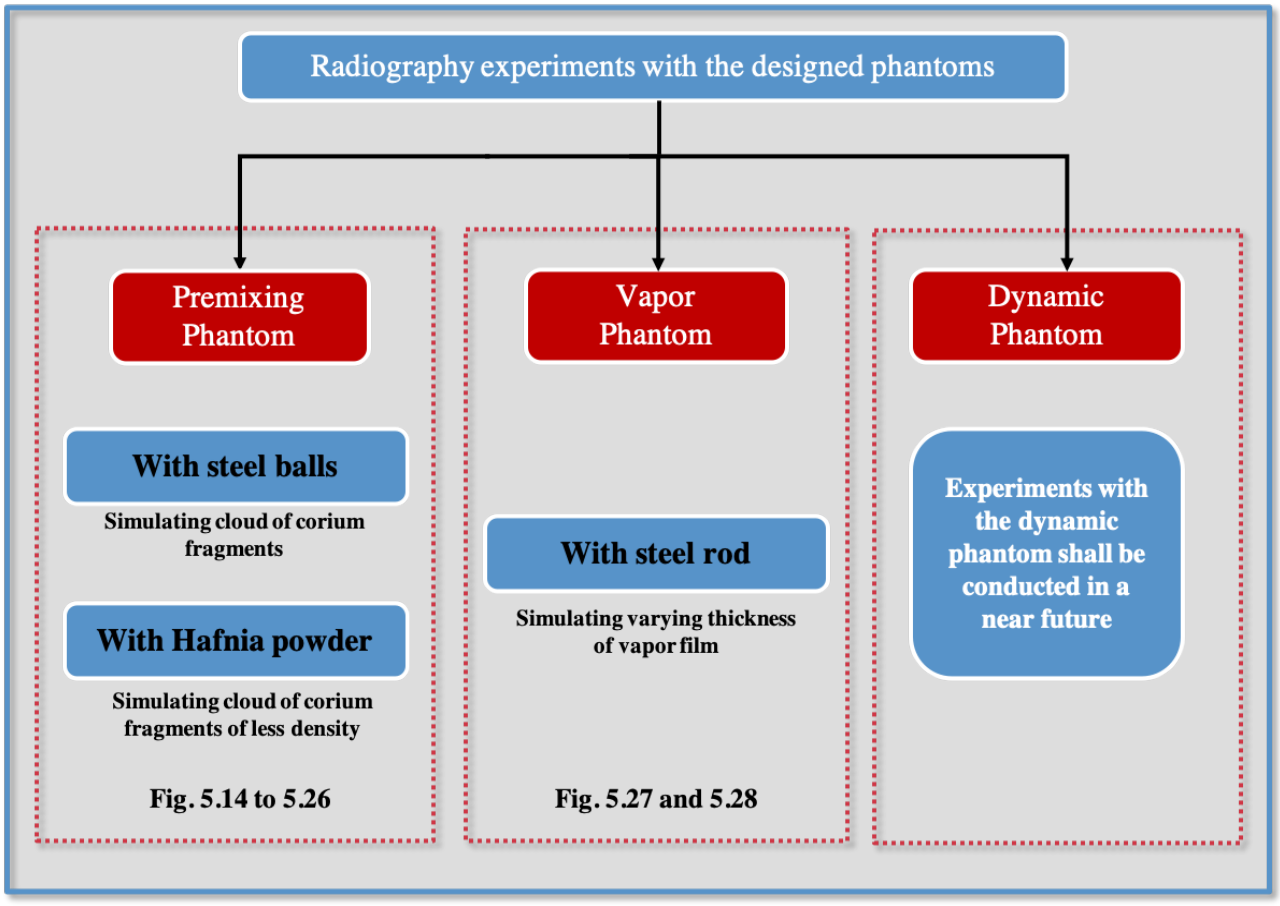

FIGURE 5.13: Sketch of the X-Ray radiography experiment with the designed phantom.

This feature along with the add on features will be discussed in detail in the next chapter. Averaged projection of these 100 images as 1 image for each configuration was made using an initial version of the image processing and analysis tool. The averaged raw images are shown in Fig. 5.14.

Figure 5.15 is the enhanced image (merely changing the contrast) obtained using the initial image processing and analysis code. The idea behind doing this analysis at this point was to verify if we are able to visualize the S3 configuration without any difficulty. This S3 configuration was performed with the maximum shielding and hence, the intensity of the X-Rays falling on the phantom was minimum. As we can see in Fig. 5.15 the image obtained in the S3 configuration after the enhancement is well resolved. This concluded that instead of doing all four configurations we could skip an intermediate configuration depending on the importance of a visualizing a particular region of interest. However, it was made sure that the images were captured in the S0 configuration (with the highest X-Ray intensity) and the S3 configuration (with the lowest X-Ray intensity) to have a better understanding of the two extremes.

Hereafter, we will only present the enhanced images directly for the configurations tested.

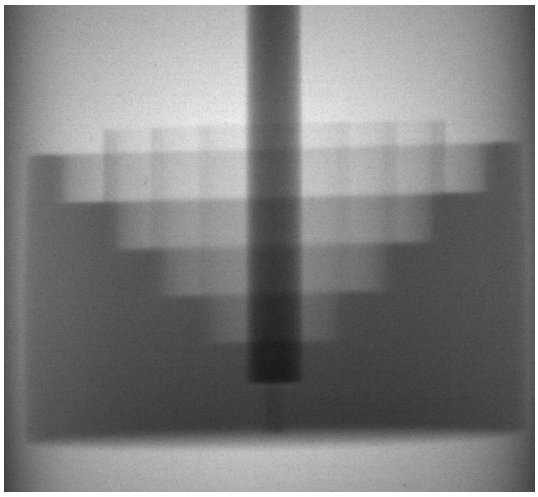

(a) **S0 configuration.**

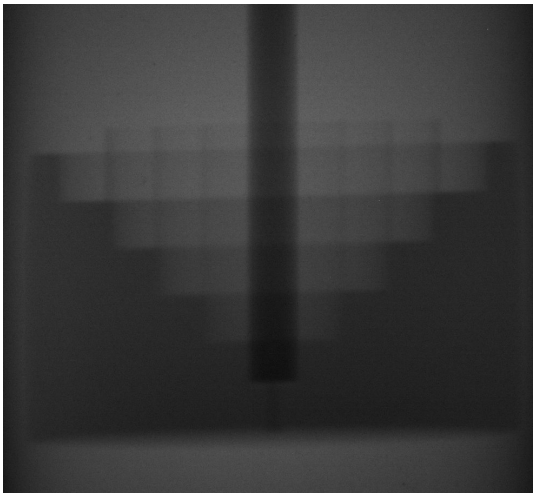

(b) **S1 configuration.**

(c) **S2 configuration.**

(d) **S3 configuration.**

FIGURE 5.14: Images of the empty premixing phantom.

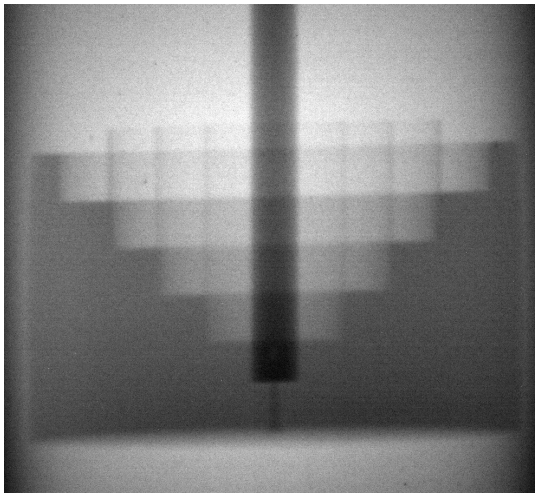

(a) **S2 configuration.**

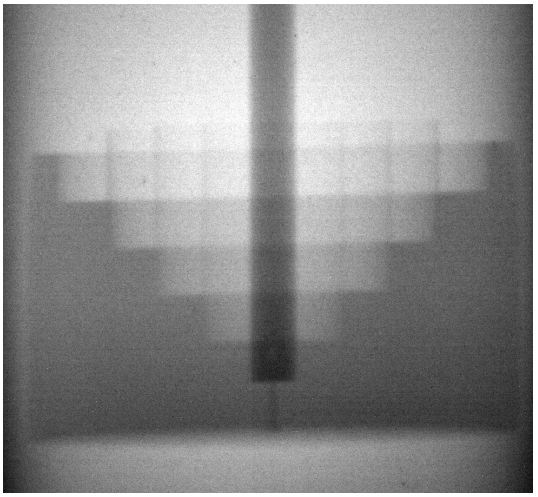

(b) **S3 configuration.**

FIGURE 5.15: Enhanced image of the empty phantom.

Premixing phantom with first ring filled

As discussed before, in this case only three configurations S0, S2 and S3 were tested in this series. The projected image in the 3 configurations is shown in Fig 5.16.

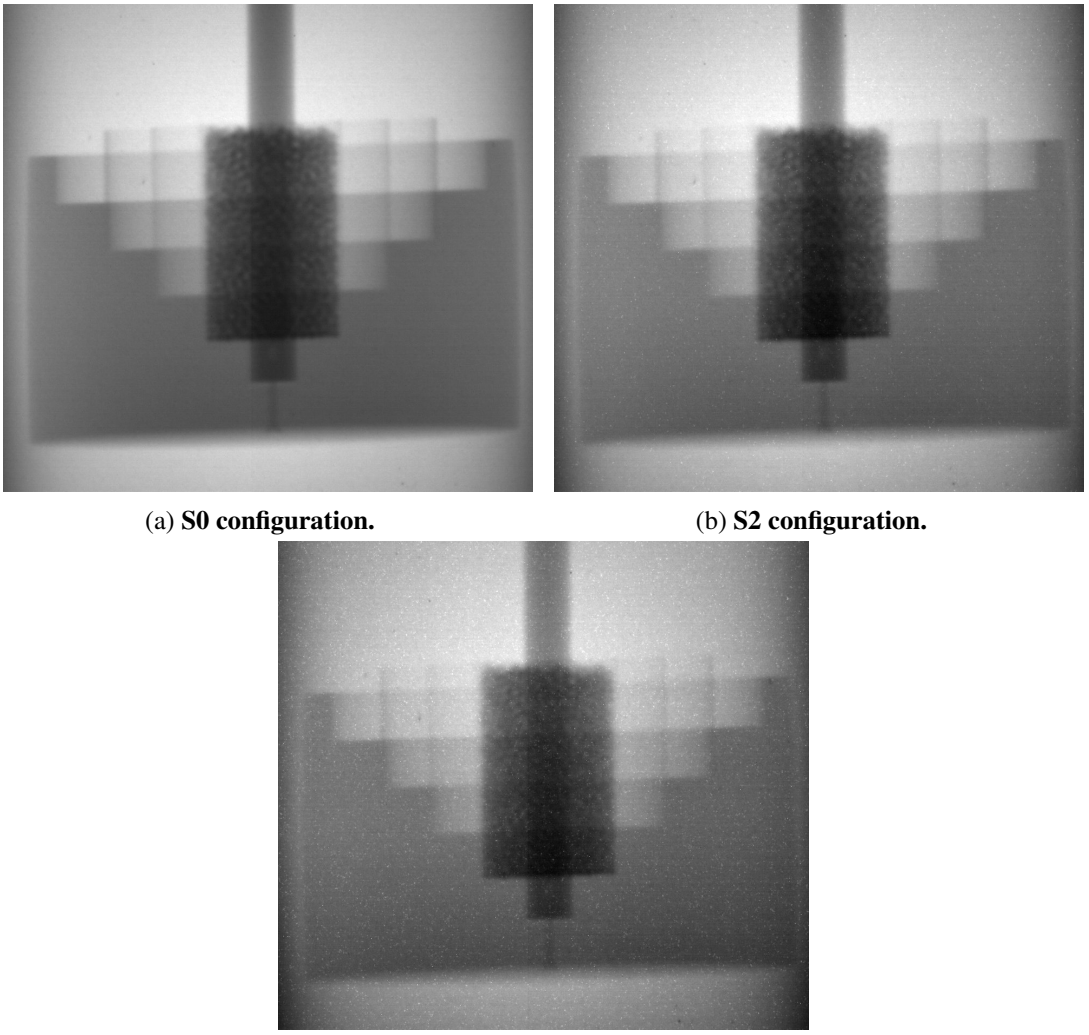

(a) **S0 configuration.** (b) **S2 configuration.**

(c) **S3 configuration.**

FIGURE 5.16: Image of the premixing phantom with its first ring filled with steel balls.

Premixing phantom with first two rings filled

Phantom with its 2 rings filled with steel balls was captured with the radiography in the 2 configurations S0 and S3. The projected images of the 100 images are shown in Fig. 5.17.

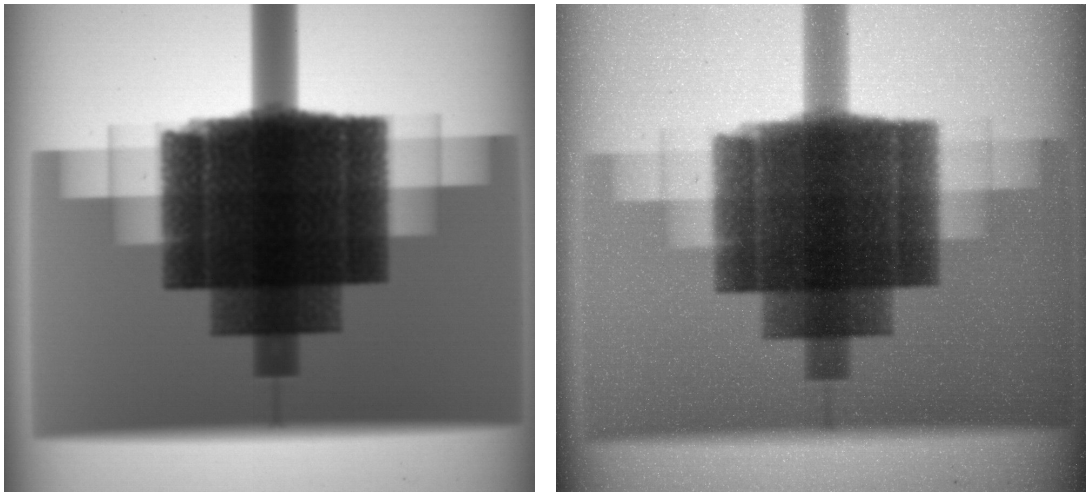

(a) **S0 configuration.** (b) **S3 configuration.**

FIGURE 5.17: Image of the premixing phantom with its first two rings filled with steel balls.

Premixing phantom with first three rings filled

Phantom with its first three rings filled with steel balls was captured with the radiography in just S3 configuration. The projected images of the 100 images are shown in Fig. 5.18.

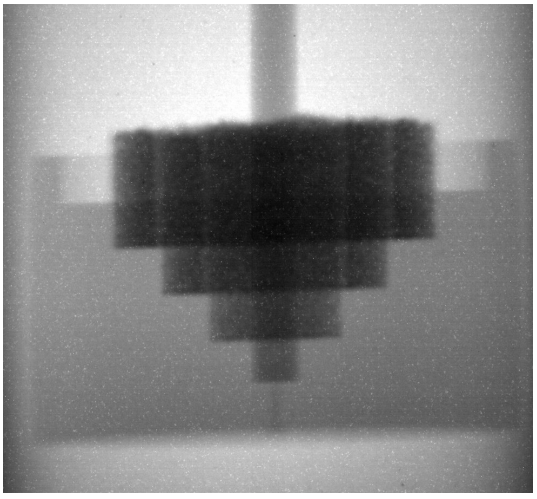

FIGURE 5.18: Images of the premixing phantom in S3 configuration with its first three rings filled with steel balls.

Premixing phantom with all 4 rings filled

As mentioned in the previous section 100 images were taken with each of the four configurations S0, S1, S2, and S3. Projection of these 100 images as 1 image for each configuration is shown in the Fig. 5.19.

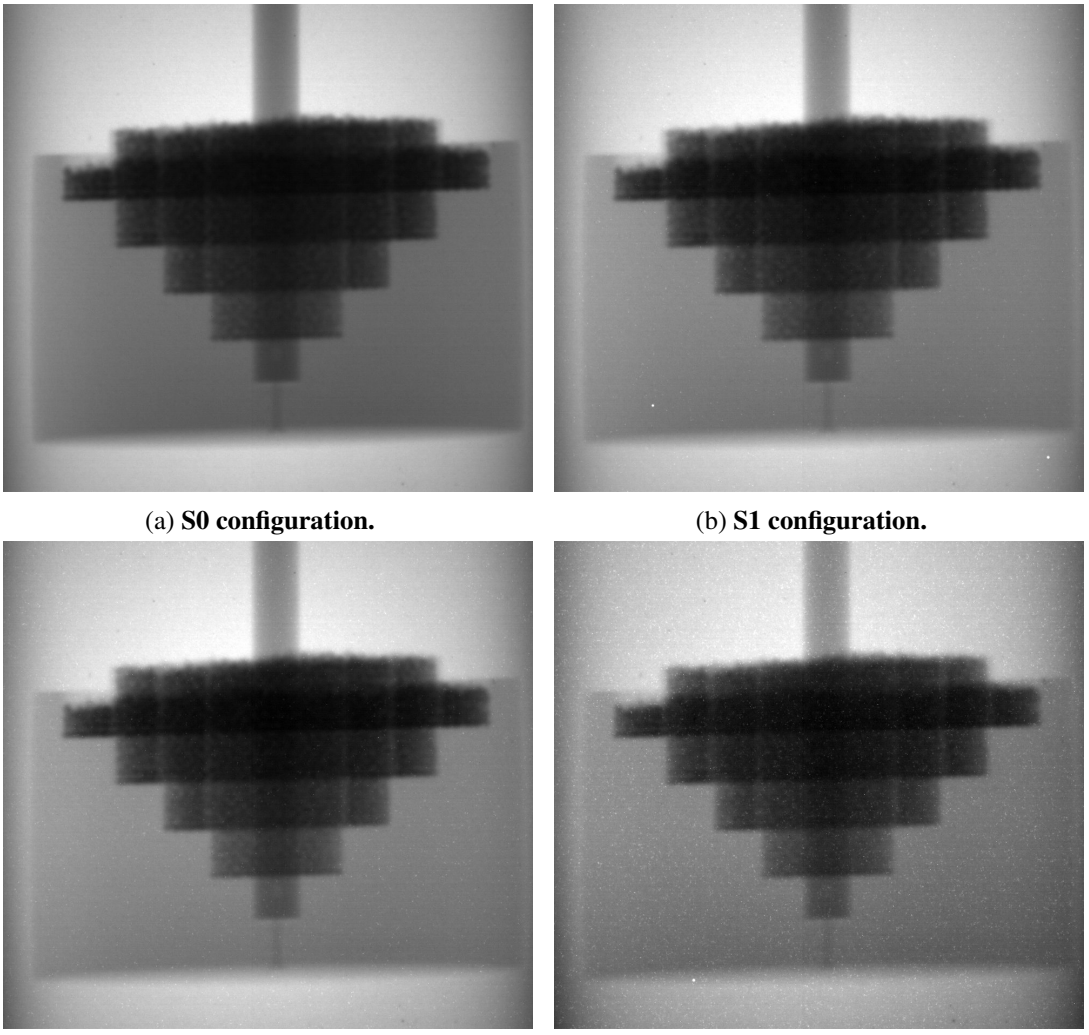

(a) **S0 configuration.** (b) **S1 configuration.**

(c) **S2 configuration.** (d) **S3 configuration.**

FIGURE 5.19: Images of premixing phantom in all 4 configuration and with its all four rings filled with steel balls .

5.3.2 Premixing phantom filled with fine hafnia powder

In this series of experiments, the premixing phantom was filled with hafnia powder. The density of hafnia powder is estimated to be $2.2\,\mathrm{g/cm^3}$. With this low-density powder, we wish to observe how a lightly dense cloud behaves with radiography.

Empty premixing phantom (with no hafnia powder)

Like the test carried out with steel balls, here also tests are initially performed with the empty phantom. 100 images on each of the configurations S0, S1, S2, and S3 were taken. The projected averaged images obtained are shown in Fig. 5.20.

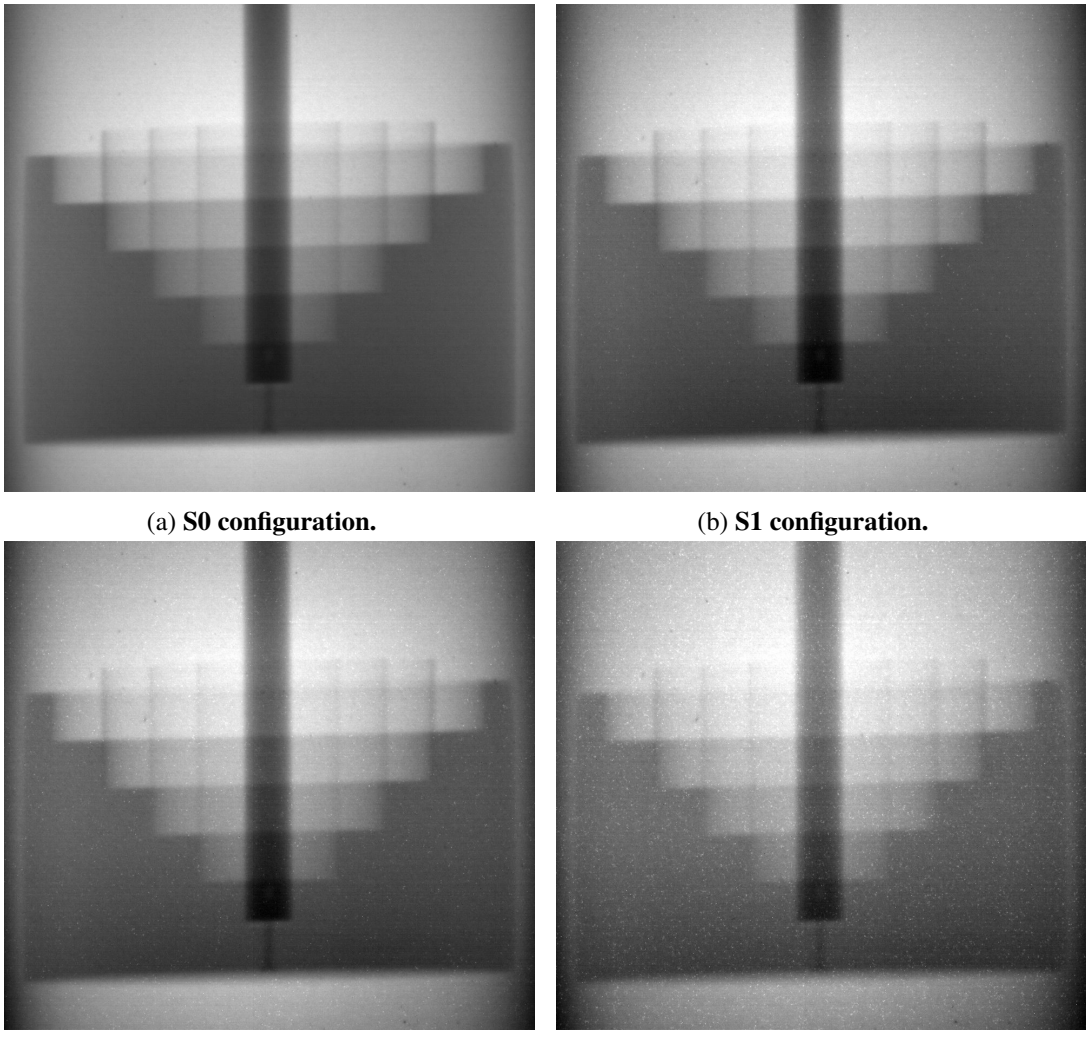

(a) **S0 configuration.** (b) **S1 configuration.**

(c) **S2 configuration.** (d) **S3 configuration.**

FIGURE 5.20: Images of the empty phantom.

Premixing phantom with first ring filled

On filling the first ring of the phantom with hafnia powder, the averaged images of the 100 images taken on the phantom is shown in Fig. 5.21. All the configurations S0, S1, S2 and S3 were tested for this case.

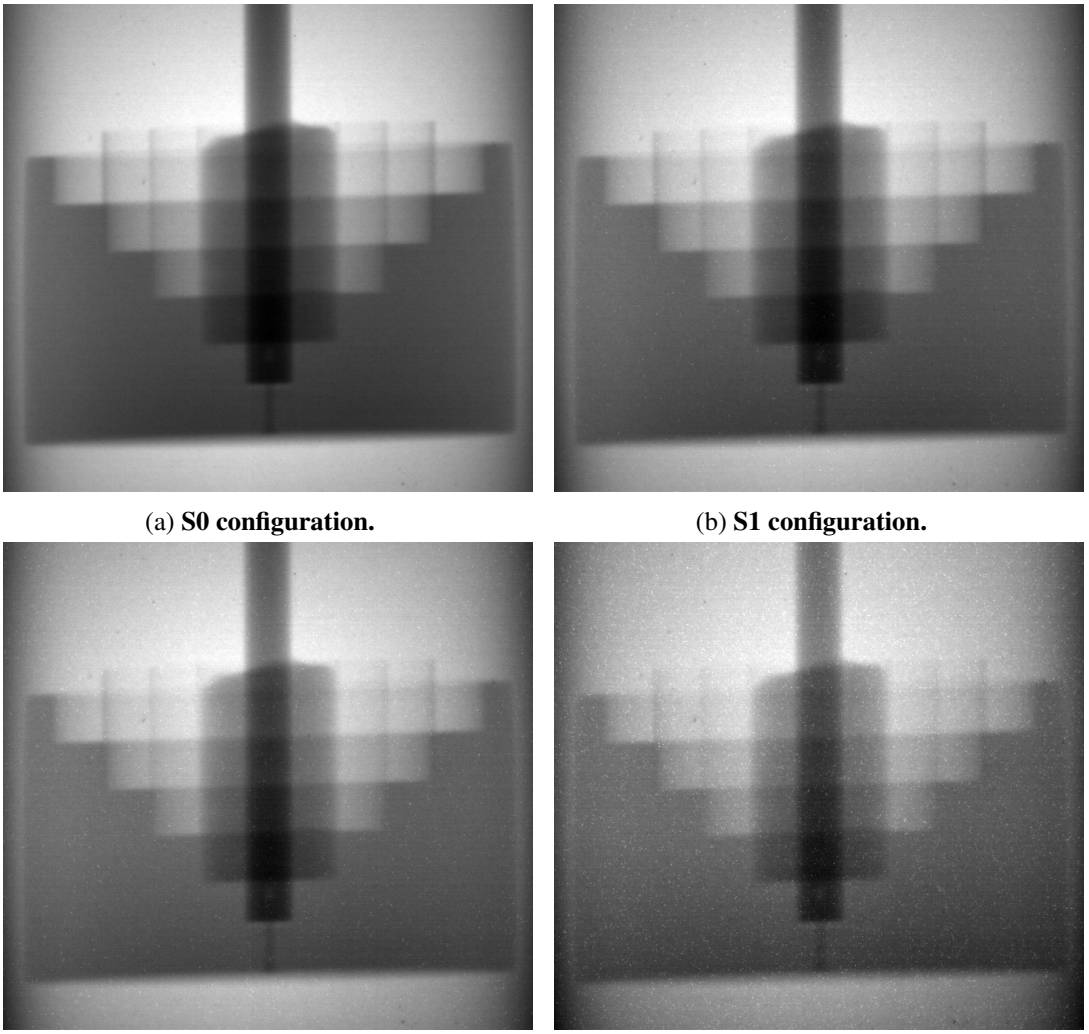

(a) **S0 configuration.** (b) **S1 configuration.**

(c) **S2 configuration.** (d) **S3 configuration.**

FIGURE 5.21: Images of the premixing phantom in all 4 configuration with its first ring filled.

Premixing phantom with its first two rings filled

The next radiography was performed on the phantom with the two innermost rings filled with hafnia powder. Three configurations S0, S1 and S3 were tested and the results are shown in Fig. 5.22.

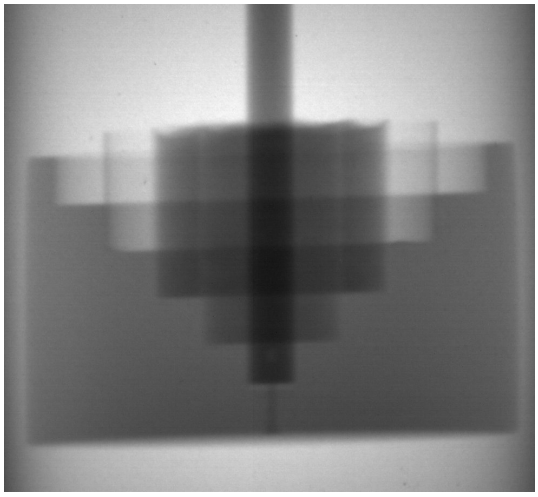

(a) **S0 configuration.**

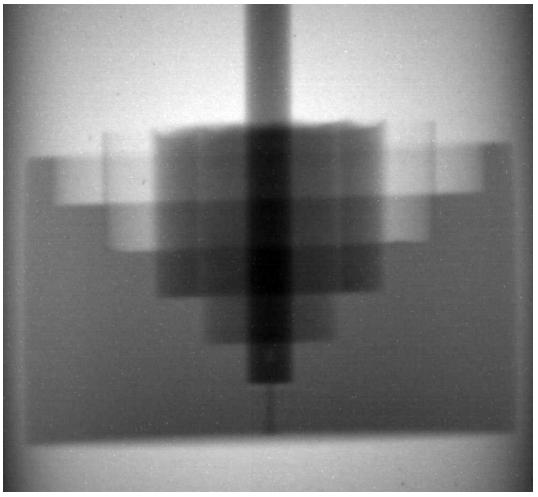

(b) **S1 configuration.**

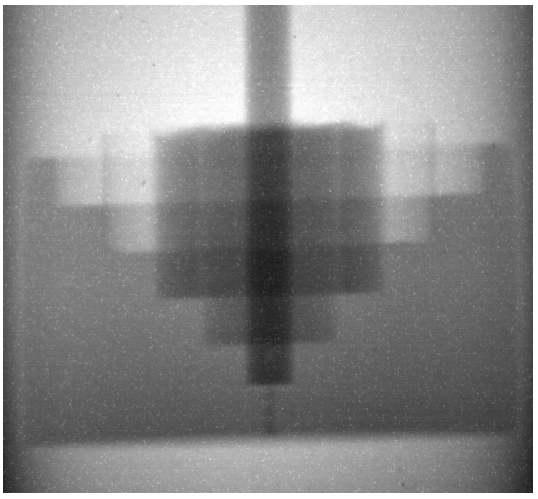

(c) **S3 configuration.**

FIGURE 5.22: Images of the premixing phantom in S0, S1 and S3 configuration with its first and second ring filled.

Premixing phantom with its first three rings filled

In this series, hafnia powder was filled in the third ring of the phantom and radiography was performed in all the four configurations S0, S1, S2 and S3. The averaged projections of 100 images taken for each configuration is shown in Fig. 5.23

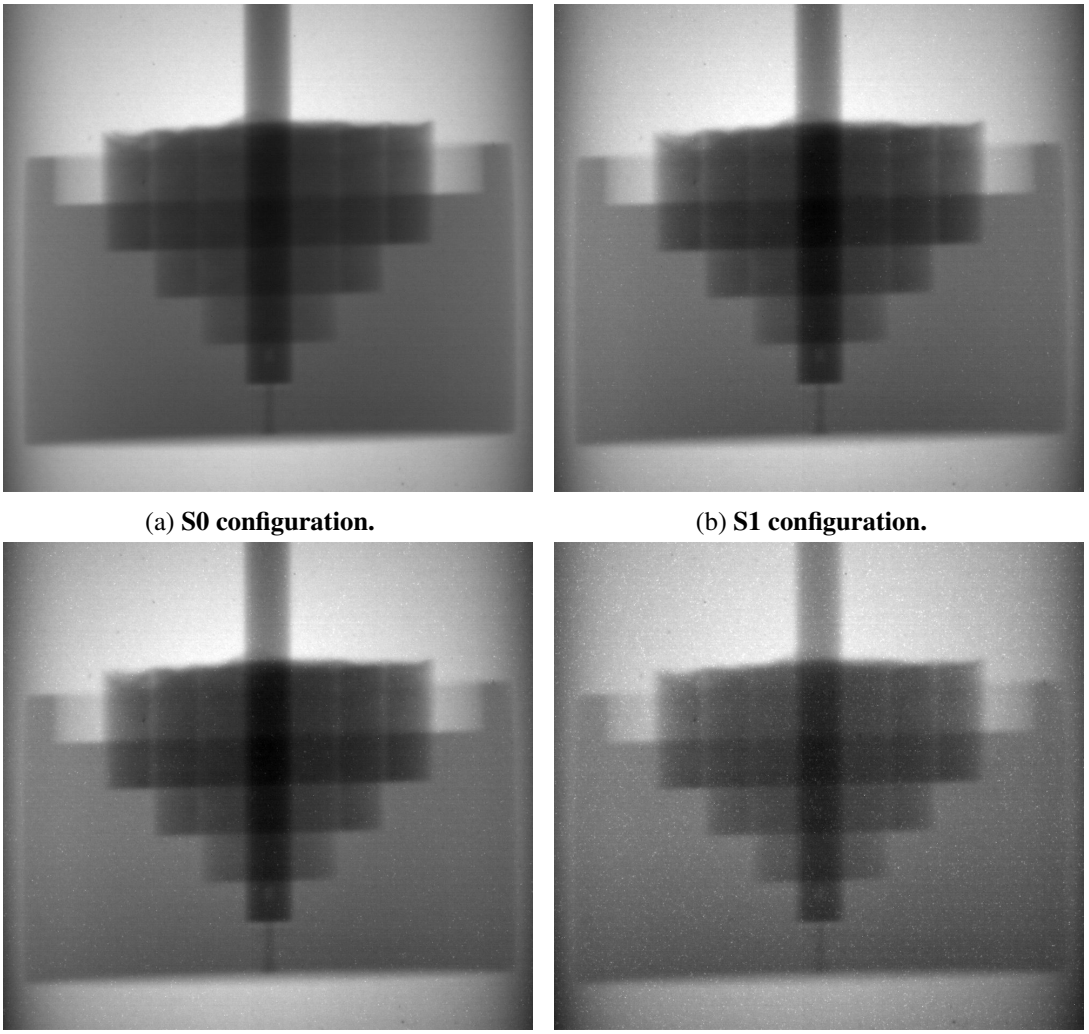

(a) **S0 configuration.** (b) **S1 configuration.**

(c) **S2 configuration.** (d) **S3 configuration.**

FIGURE 5.23: Images of the premixing phantom in all 4 configuration with its first three rings filled.

Premixing phantom with four rings filled

Finally, the final ring was also filled with hafnia powder. Radiography was performed with all four configurations S0, S1, S2 and S3. The results obtained are shown in Fig. 5.24.

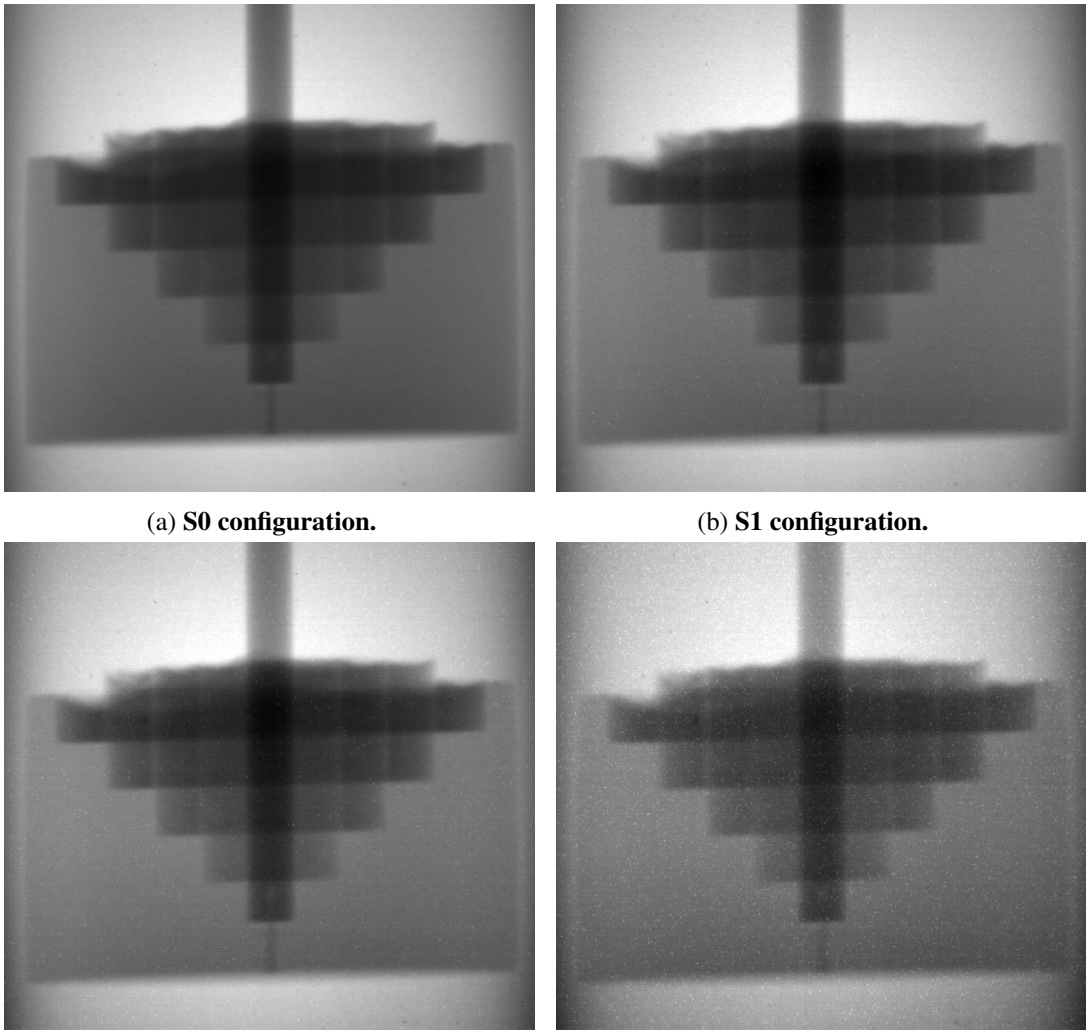

(a) **S0 configuration.** (b) **S1 configuration.**

(c) **S2 configuration.** (d) **S3 configuration.**

FIGURE 5.24: Images of the premixing phantom in all 4 configuration with its all four rings filled.

Steel rod alone

The images obtained by filming just the steel rod without any phantom and in all four configurations is shown in Fig 5.25.

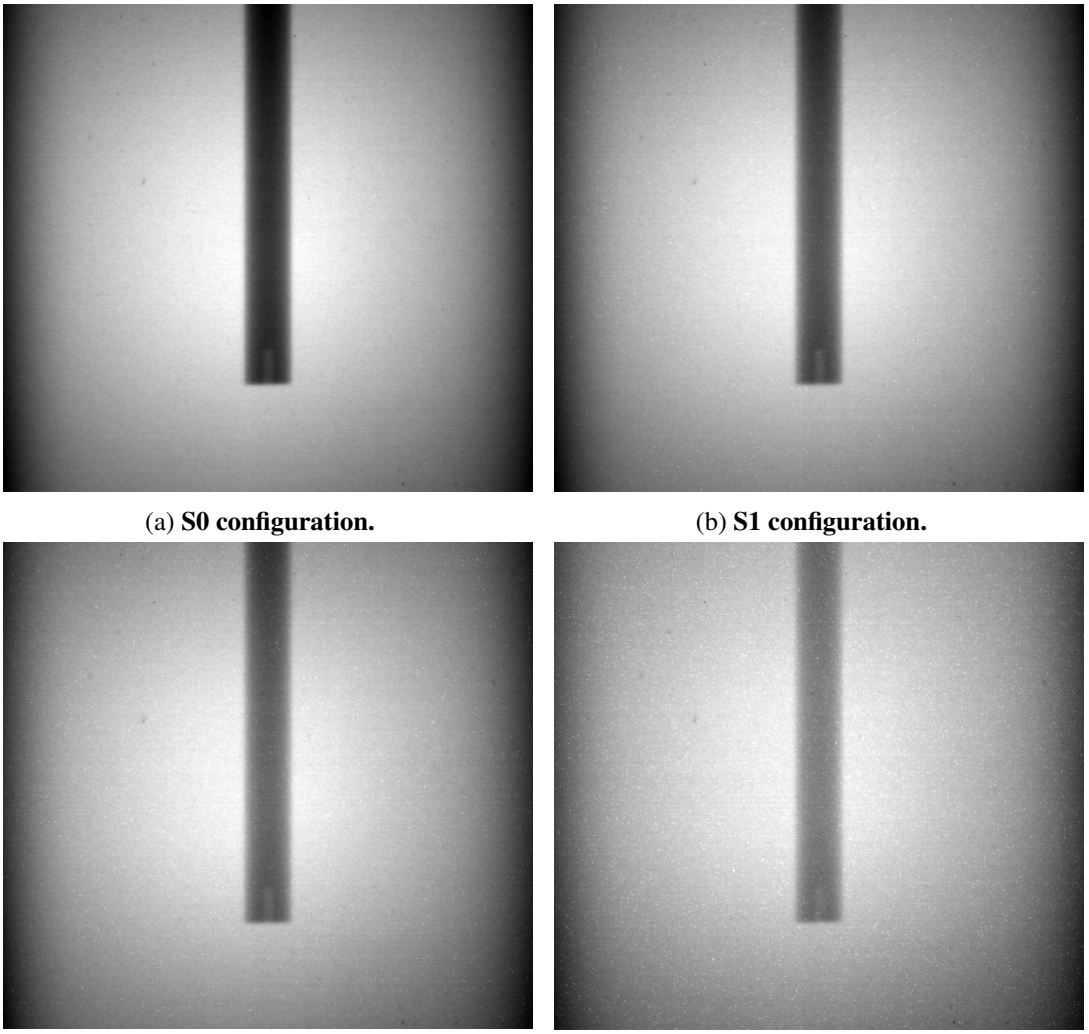

(a) **S0 configuration.** (b) **S1 configuration.**

(c) **S2 configuration.** (d) **S3 configuration.**

FIGURE 5.25: Images of the steel rod (without any phantom) in all 4 configurations.

5.3.3 Vapor phantom

Vapor phantom, a plastic cylindrical phantom with a steel rod passing through its center and progressively varying with height air gap between the steel rod and the plastic column, was filmed next. Projections with and without steel rod were taken.

With steel rod

As said in the experimental procedure in Appendix B, the long height of 50 cm of the phantom does not permit the steel plates to cover the entire length in the radiography images. In fact, it just covers the lowermost three columns of the plastic. The images obtained from radiography on this phantom are shown in Fig. 5.26. The horizontal white lines indicate the gaps between the three columns of the phantom.

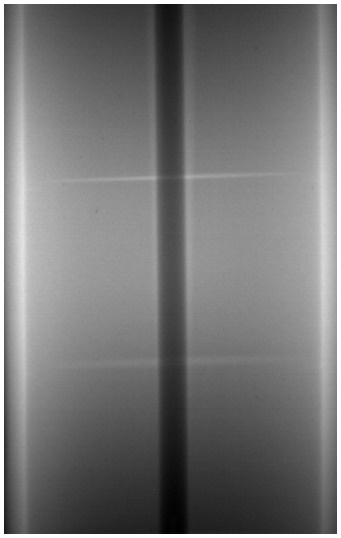

(a) **S0 configuration.**

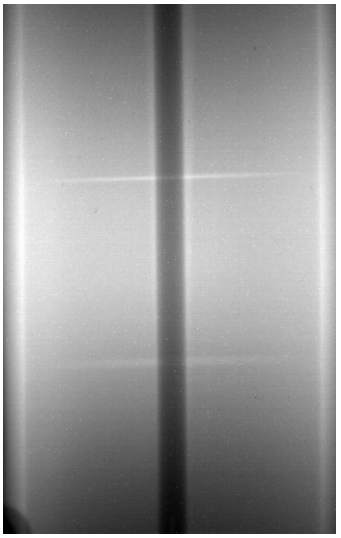

(b) **S1 configuration.**

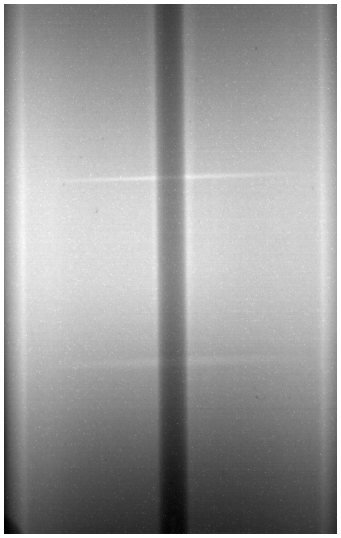

(c) **S2 configuration.**

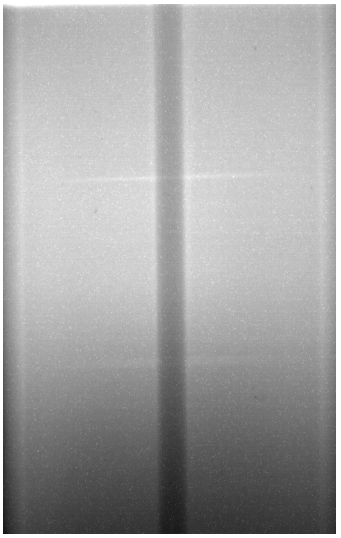

(d) **S3 configuration.**

FIGURE 5.26: Images of vapor phantom with steel rod in all 4 configurations.

Without steel rod

The steel rod has been removed for this series of radiography and is the "vapor" filmed for all four configurations as shown in Fig 5.27

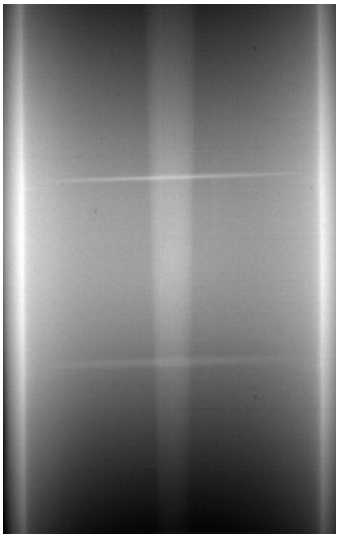

(a) **S0 configuration.**

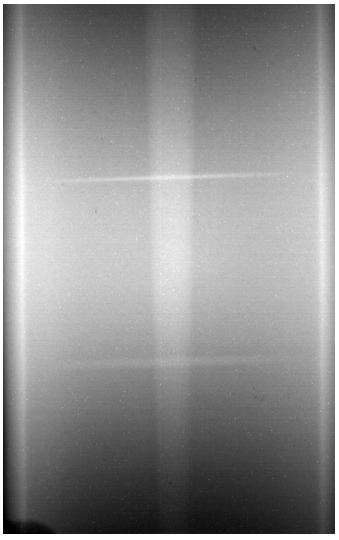

(b) **S1 configuration.**

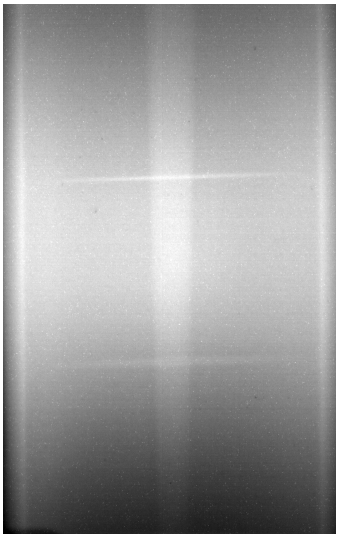

(c) **S2 configuration.**

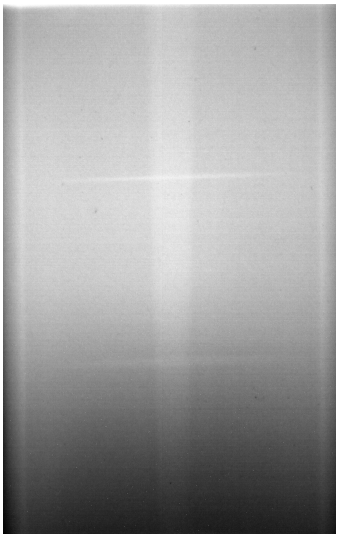

(d) **S3 configuration.**

FIGURE 5.27: Images of vapor phantom without the steel rod in all 4 configurations.

5.4. Observations

The following observations were made from the acquisitions carried out with the phantoms:

1. The dense cloud of particles represented by steel balls inserted in premixing phantom was observed to have a distinct contrast from the void and the plastic.

2. With the insertion of steel balls in every ring, comparing Fig. 5.16, 5.17, 5.18 and 5.19, a variation in contrast of the inner part of the phantom was observed with naked eyes indicating an increase in attenuation due to the increasing number of balls.

3. The enhanced acquisitions in the four configurations S0, S1, S2 and S3 are of roughly the same quality in

each test. Only the white noise was observed to increase with an increase in the shielding, i.e. moving from S0 to S3 configuration. This was due to the fact that the scattered radiation falling directly on the camera screen increases due to an increase in the scattered radiation arising from the increased steel thickness. This causes saturation of those pixels and thus a generation of white noise.

4. The X-Ray imaging facility was able to distinguish clouds of corium particles, whether represented by discrete steel balls or hafnia powder, from the coolant and vapor test materials even under the most intensive shielding configuration at 14.5 cm of steel plates.

5. For Vapor phantom which was designed to test the vapor film, detection was also successful. Though very thin air gap at the bottom was not detected very well, the air gap became noticeable in the upper part, where it is thicker.

6. The X-Ray imaging system was also successful in distinguishing the vapor film represented by an air gap, from the other two phases i.e. corium represented by steel and sodium represented by polyethylene.

Thus, it was concluded that all the phantoms in different configurations were successfully able to be detected with the X-Ray imaging system.

5.5. Summary

In this chapter, several acquisitions are carried out with the KROTOS X-Ray imaging system. Premixing phantom, made of plastic and filled with steel balls which act as corium fragments in sodium, testifies that a dense cloud of corium could be visualized by radiography. A less dense cloud is tested with hafnia powder and also qualifies to be visualized by radiography. The PLINIUS-2-FR facility is simulated with the KROTOS experimental set-up and with the help of three steel plates of thickness 4 cm, 5 cm and 5.5 cm respectively which lead to a total 14.5 cm thickness representative of the PLINIUS-2-FR insulation walls. Radiography is performed step by step without any steel plates, with one plate, with two plates, and with all the three plates for all the phantoms increasing the acquisition time of the camera accordingly. The images obtained are enhanced and observed to have a good contrast which is easily seen with naked eyes. The contrasts of the images are satisfactory even in the S3 configuration where all the steel plates are kept even if the images get a bit noisier. These are promising results for the designing of the PLINIUS-2-FR X-Ray imaging system. These images will be used as a base for the development of an image processing and analysis software. In this aim, it was of major interest to rely on images representing a medium with precisely known features.

The next chapter will focus on the development of the image processing and analysis software to achieve our final goal of detecting and decomposing corium, liquid sodium and sodium vapor from these images.

Chapter 6

Development of an image processing and analysis software to study corium-sodium interaction

> *People usually compare the computer to the head of the human being. I would say that hardware is the bone of the head, the skull. The semiconductor is the brain within the head. The software is the wisdom. And data is the knowledge.*
>
> Masayoshi Son

The radiographical experiments on the designed phantoms produced raw images as shown in previous chapters. These images need to be analyzed in order to understand the FCI mechanisms involving three phases. However, in general, processing and analysis of the images obtained during an FCI in sodium is a challenging task. This chapter deals with the work carried out during this Ph.D. to perform analysis of the experimental images and the developed image processing and analysis tool.

6.1. Need for the development of a new software

Several efforts have been made in the past to develop an image processing tool to visualize a fuel coolant interaction. Some preliminary but significant work has been carried out in different research laboratories worldwide. Simultaneous high-speed acquisition of X-Ray radiography and photography system (SHARP) and its image processing algorithm was developed in the Micro-Interactions Steam Explosion Experiments (MISTEE) facility at KTH, Sweden [68]. The analysis of the processed data by the SHARP system, provided quantitative information on the dynamics of the vapor bubble and melt droplets, thus, revealing the underpinning mechanisms of the vapor explosion phenomenon [69]. A technique was developed to depict FCI phenomena using real-time radiography in an opaque medium (woods metal injected in water) at IGCAR, India. An algorithm for image enhancement of the raw X-Ray images (obtained from the experiment) was developed. The attributes of FCI process, including jet breakup length, jet front axial displacement, and vapor phase displacement, could be calculated from the processed images [28]. Another image processing technique was developed to measure about ten thousand fragment diameters precisely in a liquid-liquid flow [70] in Japan. At CEA Cadrache, the images obtained from the KROTOS experiments, were analyzed using the software KIWI (Krotos Imaging software for Water Interactions) designed for image processing, analysis phase identification for corium-water interaction as explained in Chapter 2 [46].

All the above research demonstrates the importance of an image processing algorithm in determining features of a Fuel-Coolant Interaction, for instance, the dynamics of vapor bubbles and pockets and melt droplets, the jet breakup length, fragmentation mechanism and the fragment velocity.

CEA already has an in-house image processing tool called KIWI, which was designed for corium-water interactions and had inherent limitations to study FCI in sodium. KIWI software is capable of resolving and detecting corium fragments of size greater than $3\,\mathrm{mm}$ [46]. However, in the case of corium-sodium interaction, the particles formed are of a size smaller than $1\,\mathrm{mm}$ and are decided to be detected as a group of particles in the form of clouds for which KIWI is not designed. Due to the unavailability of any other comprehensive software to perform analysis of the images obtained in the previous chapter, it was necessary to develop a new image processing and analysis software. This new software should fulfill some basic capabilities to carry out image analysis to study FCI in sodium. This software should enable us to characterize the three-phase flow in the mixture composed of corium particle clouds, liquid sodium and sodium vapor. It is required to have potentials to determine size, shape, velocity and other important features of corium particle clouds.

Before moving towards the structure of the developed code and the methodologies involved, it is essential to introduce some basic concepts behind image processing. The next section covers an introduction and some prerequisites, basic concepts and terminology in image processing.

6.2. Basic concepts and terminology in image processing

This section defines the most frequently used terms in this chapter. For more detailed explanation, readers can refer to the literature [71, 72, 73].

What is an Image?

An image is a 2D representation of an object, person or a scene captured by an optical device like a camera, a mirror or a lens. It is one of the many projections possible of a 3D object or a scene.

What is a Digital Image?

A digital image is a representation of a 2D image using a finite number of points referred to as picture elements or *pixels*. Each pixel has one or more numerical values representing its intensity. In the case of monochrome (grayscale) images (which will be defined below), only one numerical value is required to represent the intensity of one pixel. While for color images, three values are required, representing the amount of red (R), green (G) and blue (B) composing the colors.

Digital image representation

A digital image can be represented by a 2D matrix of real numbers. Matrices for monochrome images of size $(M \times N)$ may be designated by a function $f(x, y)$, where x is the row number $(x = 0, ..., M-1)$ and y is the column number $(y = 0, ..., N-1)$.

$$f(x,y) = \begin{bmatrix} f(0,0) & f(0,1) & f(0,2) & \dots & f(0,N-1) \\ f(1,0) & f(1,1) & f(1,2) & \dots & f(1,N-1) \\ \vdots & \vdots & \vdots & \ddots & \vdots \\ f(M-1,0) & f(M-1,1) & f(M-1,2) & \dots & f(M-1,N-1) \end{bmatrix} \tag{6.1}$$

The value of the function at a given pixel coordinate (x_0, y_0) denoted by $f(x_0, y_0)$, represents the intensity or gray level of the image at that pixel [71]. The range of pixel intensities in an image depends on the data type in the image. For example, it varies from 0.0 (black) to 1.0 (white) for double data type and 0 (black) to 255 (white) for uint8 (unsigned integer, 8 bits) and 0 (black) to 65,535 (white) for uint16 (unsigned integer, 16 bits) data types.

Binary (1-bit) Images

Binary images are encoded as 2D arrays where pixels can have only 1-bit, i.e., either intensity 0 or 1. 0 represents "black" and 1 represents "white". This is often used to represent classification results.

Gray-level/ Grayscale/ Monochrome Images

These are also represented with the help of 2D arrays of pixels, but with 8 or 16 bits per pixel (bpp). Thus, the pixel value of 0 corresponds to "black" and a pixel value of 255 (in case of 8 bpp) or of 65,635 (in case of 16 bpp) corresponds to "white" and the intermediate values indicate varying shades of gray. As an example, let us consider one of the images from our experiments shown in Fig. 6.1, a 16 bit grayscale image in this case. The small 9×9 pixel region in the image as depicted in Fig. 6.1, demonstrate that the brighter pixels correspond to larger values and darker pixels correspond to lower values.

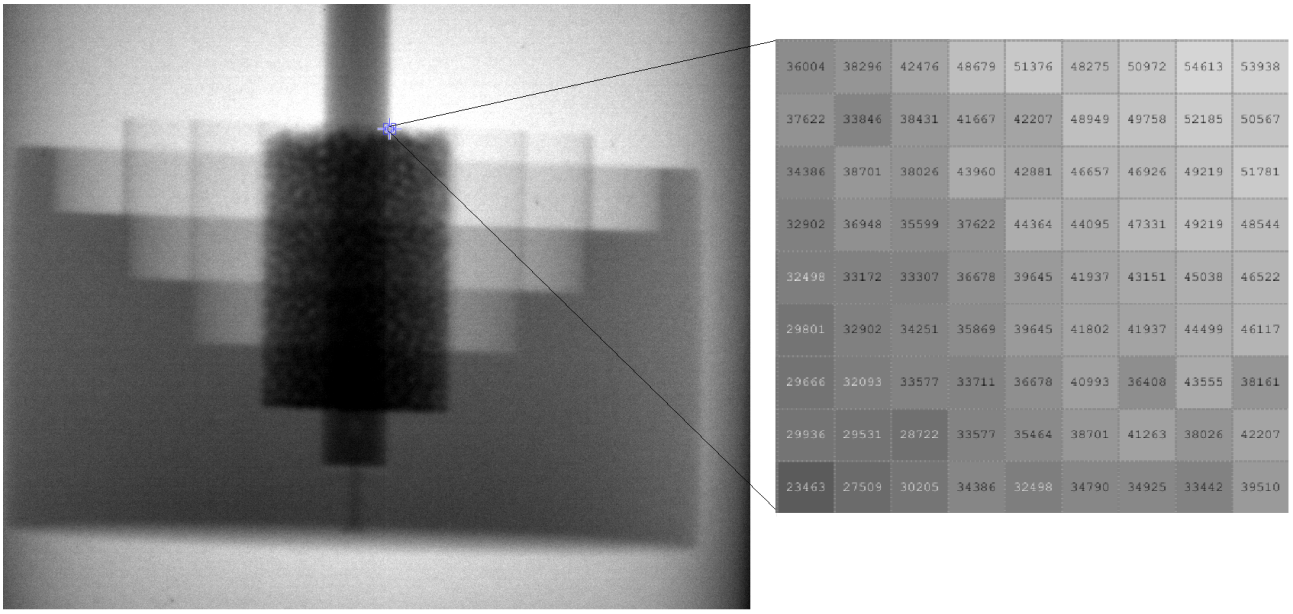

FIGURE 6.1: A grayscale image and the pixel value in a 9×9 neighborhood [71].

Color images (24-bit RGB)

A color image can be represented using three 2D arrays of the same size, one for each color channel: red (R), green (G) and blue (B). Each color array contains an 8-bit value which represents the amount of red, green or blue at that point in a [0,255] scale.

Raw images

This is the image format as collected from the imaging device. For example, the images obtained from the experiments are raw images with **.dat** extension, encoded with non-readable symbols.

Digital Image Processing

It is defined as the science of modifying digital images by applying certain designed mathematical operations in the form of algorithms. Such algorithms may include removal of background noise or artifacts, but always render a new digital image with the same spatial and intensity resolution. [73]. Other image processing techniques will be described as and when they are brought to use.

Image Analysis

This is a mathematical operation that transforms the image into the desired information. Often a mathematical data reduction is involved.

In the following section, the development of PICSEL software will be described with its application on the images obtained from radiography experiments.

6.3. The PICSEL software and its structure

PICSEL (**P**LINIUS-2 **I**mage processing for **C**orium **S**odium **E**xperimental **L**ibrary), is a code written in MATLAB (MATrix LABoratory) [74], a multiplatform, data analysis, prototyping, and visualization tool with built-in support for matrices and matrix operations, rich graphics capabilities, and a friendly programming language and development environment [71, 72]. MATLAB's basic data type is the matrix (or array). MATLAB does not require dimensioning, that is, memory allocation prior to actual usage. All data are considered to be

matrices of some sort. Single values are considered by MATLAB to be 1×1 matrices. This built-in support for matrices will ease the processing of digital images which are also stored in the form of matrices. Apart from these benefits, MATLAB offers programmers the ability to edit and interact with the main functions and their parameters, which leads to valuable time savings in the software development cycle. Also, it has an extensive built-in support for image processing operations, encapsulated in the Image Processing Toolbox. This toolbox provides a comprehensive set of specialized functions for image processing, analysis, visualization, and algorithm development. The user can perform image segmentation, image enhancement, noise reduction, geometric transformations, image registration, and 3D image processing, the techniques that will be discussed hereunder. For all the above reasons, MATLAB was the software chosen for the development of PICSEL. The code has been implemented using MATLAB ver. R2015b, it has a graphical user interface and can be executed on Mac, UNIX and Windows platforms within MATLAB environment.

Developing a software to carry out processing and analysis of video files, requires a prerequisite study and analysis of the raw images obtained from the experiment. The flaws in the images will govern the technique required for processing and analysis.

6.3.1 Considering Artifacts

Artifacts found

The camera sensors are extremely sensitive to X-Rays. If the X-Ray photons interact with the sensor arrays in the camera with its initial energy, it might result in an abnormally high intensity at that pixel. This appears in the form of "white spots" on the image as shown in Fig. 6.2.

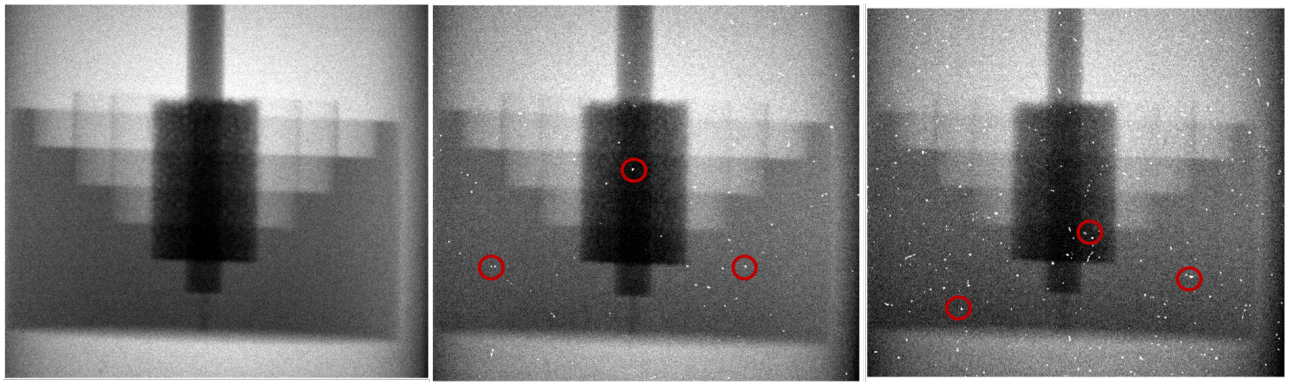

FIGURE 6.2: Spark artifacts at increasing X-Ray shielding from left to right. Left: in S0 configuration, Middle: in S2 configuration, Right: in S3 configuration.

Thus, an optically coupled high energy system using a CMOS camera must be protected to avoid photons interacting with the camera sensors. In our experiments, the camera was protected by a 100 mm thick lead protection to reduce the amount of direct radiation falling on the camera. Even with this protection, it was impossible to eliminate all the white spots. These are supposedly coming from the scattered radiation from the scintillator screen itself and also the mechanical frame which supports the screen. Also, the images in the configuration S0, S1 and S3 were observed to be increasingly corrupted by white spots with each configuration as demonstrated in Fig. 6.2. This could be due to the increased scattering radiation with increasing steel shielding.

White spots present in the images may potentially affect the qualitative and quantitative exploitation of the images. These need to be processed and removed from the images.

Correcting Artefacts

In this section, we will show how individual digital images are processed (each image of the 100 images) to produce averaged images (average of the 100 images we performed) for each case. The following approach was applied to process the images:

- Median filtering each image: for each image, a kernel big enough to include the biggest white spot is applied to filter the initial image (due to the big size of the white spots, the applied kernel is 11×11 pixel).
- An average of the 100 median filtered images produces the averaged images.

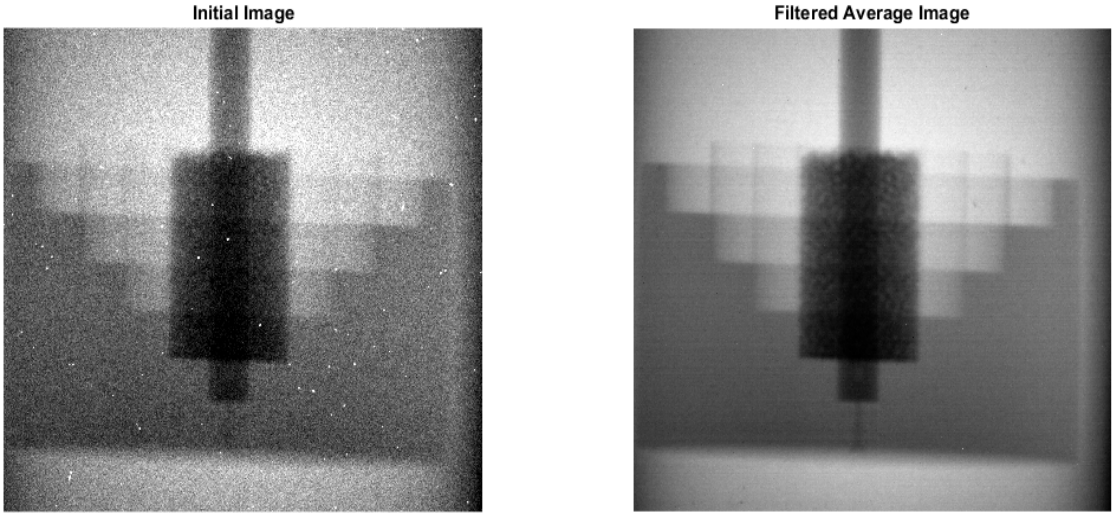

FIGURE 6.3: White spots filtering using median filter.

Figure 6.3 depicts an initial image and its filtered average image. The median filtering technique is successful in removing the white spots from the initial image. These treatments are very simple and their objective was only

to be able to treat the images as per the requirements. For the final software, more treatments will have to be defined in order to treat each frame of the video according to the artefacts observed in the video.

6.3.2 Detection of clouds of particles

Acquisitions to judge the detectability of clouds of corium particles was carried out using the premixing phantom defined in Chapter 4. This phantom includes cylindrical columns filled with steel balls or hafnia powder representing clouds of corium particles.

Processing

The variation in the intensity values (grey levels) along a line segment in an image is called intensity profiles. The intensity profiles along the horizontal lines of one of the resulting radiography, are shown in Fig. 6.4. These raw acquisitions, referred as I_{avg}, are found to have a strong non-uniformity along the profile of sodium. These have their origins from:

- the emission spectrum: X-Ray flux being larger at the center of the image than at the edges.
- the effect of tapering due to the geometry of the phantom.

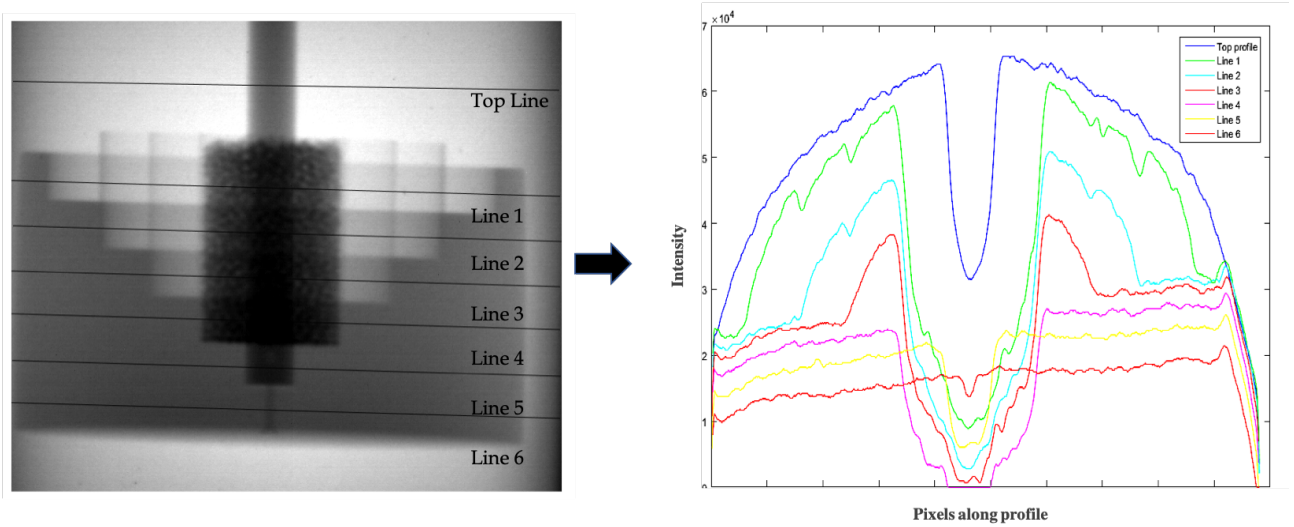

FIGURE 6.4: Raw Image intensity profile.

The predominant effect is due to the emission spectrum of the X-Rays. We, therefore, made full flux acquisitions without any phantom to acquire a "full flux image". These full flux images are obtained under the conditions identical to those with the phantom (geometry, configuration, camera parameters, synchronization with the X-Ray

beam). A sequence of 100 images was captured to ensure a comprehensive characterization of the background associated noise. After processing these images individually to remove any white spots, these can be averaged (as described in the previous section) to constitute the full flux image (I_{ff}). The I_{ff} and I_{avg} images are also corrupted by dark noise/obscurity. Dark Noise/Obscurity is a noise that arises from the small electric currents building-up in the camera, even when unexposed. This is caused by thermally excited electrons in the camera [75]. In our case, obscurity is corrected by subtracting a dark image, i.e. an image taken without any X-Rays. In this case also, a sequence of 100 images is taken to compute the average obscure image I_{obs} by following the procedure described in the previous section. Thus, the corrected full flux $I_{ff,cor}$ and average $I_{avg,cor}$ images can be computed as:

$$I_{ff,cor} = I_{ff} - I_{obs} \tag{6.2}$$

$$I_{avg,cor} = I_{avg} - I_{obs} \tag{6.3}$$

To correct the non-uniformities in the image, it needs to be flat field corrected. This is done by dividing the corrected full flux image by the corrected average image [75]. The attenuated image I_{att} is thereafter, computed by taking a log of this value, i.e. :

$$I_{att} = \ln \frac{I_{ff} - I_{obs}}{I_{avg} - I_{obs}} \tag{6.4}$$

Thus, this process reduced the effect of the emission spectrum and made the image much more "flat" as illustrated in Fig. 6.5. On the left is the processed image obtained from the correction of emission spectrum effect and on the right is the graph depicting attenuation intensity profiles along the horizontal line segments. The image clearly depicts that the intensity is the brightest at the center of the cloud, indicating the highest attenuation value at the center. This is complemented by the corresponding attenuation intensity profiles in the graph. It is observed that in all the profiles, the attenuation is the maximum at the center while it reduces moving away from the center. However, the variation that still remains in the graph is due to the tapering effect of the phantom. Comparing the profiles of Line 2, 3, 4, 5 and 6 with the profile of Line 1, it is clear that the attenuation intensity at the sides (i.e., in the sodium region) increases moving from Line 1 to Line 6. This is due to the increasing thickness of the sodium region and thus increasing attenuation. This is the tapering effect and can be corrected

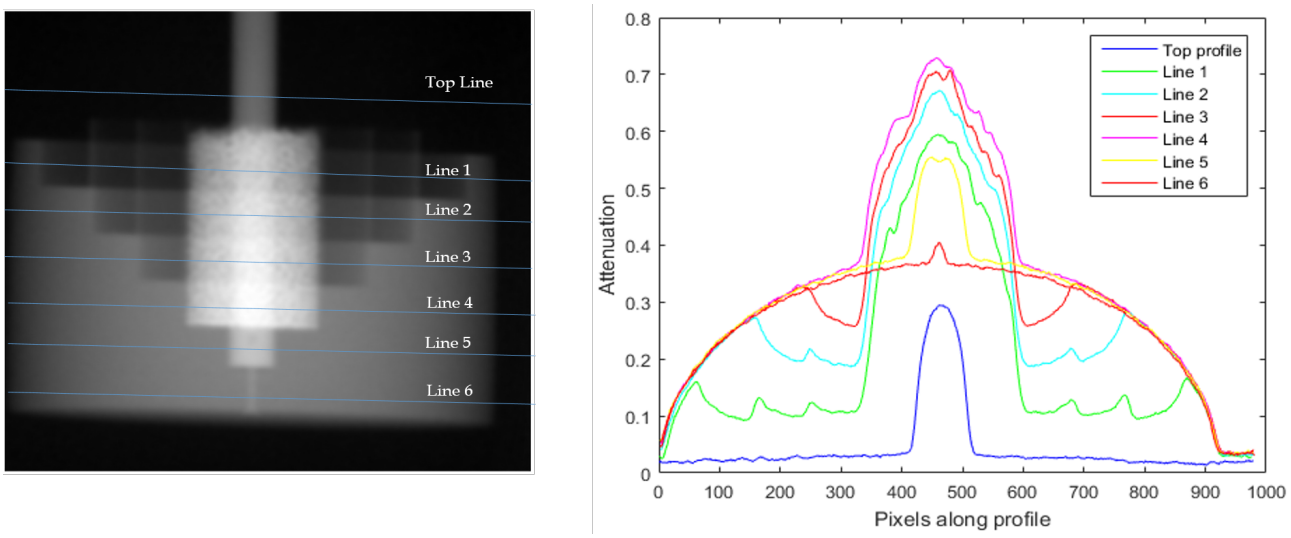

FIGURE 6.5: Processed image and its attenuation intensity profiles obtained by correcting the effect due to emission spectrum.

with the help of an image of the empty phantom that is taken without changing the position of the model on the measuring bench. In principle, there should be an image with a full cylinder representing sodium and the correction should be made with such a phantom. However, such an image was impossible in our case because of the construction of phantom: it would have been necessary to have a full cylindrical phantom representing the liquid sodium entirely. An image of the vapor phantom (except the jet) could have been used, but we chose not to due to dissimilarity in the measuring bench position while making acquisitions of vapor phantom. Thus, the image of the empty phantom (only containing the steel rods and the separation cylinders) was chosen. A series of 100 images of the empty phantom (as well as the full flux image and the obscurity image) were processed to remove white spots and then averaged, followed by the dark noise removal and the flat field correction, to constitute the initial image I_{ini}. This image is shown in Fig. 6.6.

The tapering effect can be corrected by dividing the flat field corrected image of the phantom with the cloud by the initial image of the empty phantom. Thus the final attenuated image incorporating the emission spectrum correction and the tapering effect correction can be computed as follows:

$$I_{att} = \ln \frac{\frac{I_{ff} - I_{obs}}{I_{avg} - I_{obs}}}{I_{ini}} \tag{6.5}$$

The entire procedure thus made it possible to reduce the effect of the emission spectrum and also the effect of tapering geometry of the phantom to result in an attenuation image of the cloud of corium particles as shown in Fig 6.7. The values of this image are representative of the attenuation μl (from the Beer Lambert's law) of each

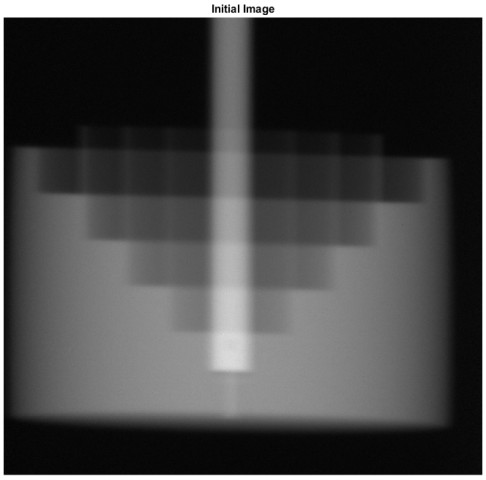

FIGURE 6.6: Initial image of the empty phantom I_{ini}.

photon from source to pixel trajectory. The two peaks correspond to the attenuation of a tangent ray passing at the edges of the coherent jet. This is due to the maximum thickness of the cloud traversed by the X-Ray through that point. A sudden dip in the attenuation at the center of the image is due to a decrease in the radial thickness of the cloud when the initial image of the phantom with coherent jet, is removed from the image of the phantom with cloud and coherent jet.

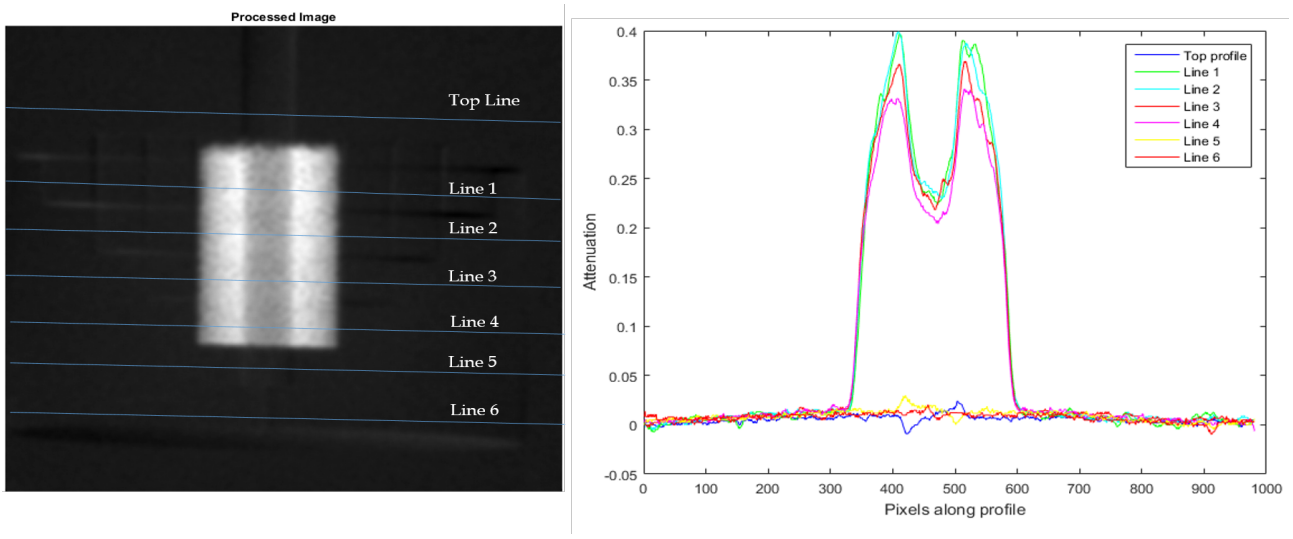

FIGURE 6.7: Processed image (with tapering effect correction) of premixing phantom filled with steel balls in ring 1 and its attenuation intensity profiles.

Following this computation, the spatial non-uniformity in the profiles is essentially reduced to zero, the only variation from noise remains. Thus, it should be remembered that on the final system also, i.e. while conducting the experiments, an initial image should be taken at the beginning of the experiment: test section containing only liquid sodium.

The four configurations S0, S1, S2 and S3, result in similar contrast of images, except the fact that the number of white spots increased with each configuration. This has already been discussed in the previous chapter. The white spots in the images can be corrected by following the procedure mentioned in section to obtain very similar images for all the configurations. Following this, only one of the four configurations in each case was processed.

Radiography with the 2nd ring filled with steel balls was also corrected for dark noise and tapering effect to obtain the image shown in Fig. 6.8. Similarly, for the Ring 3 and ring 4 filled phantoms the profiles are shown in

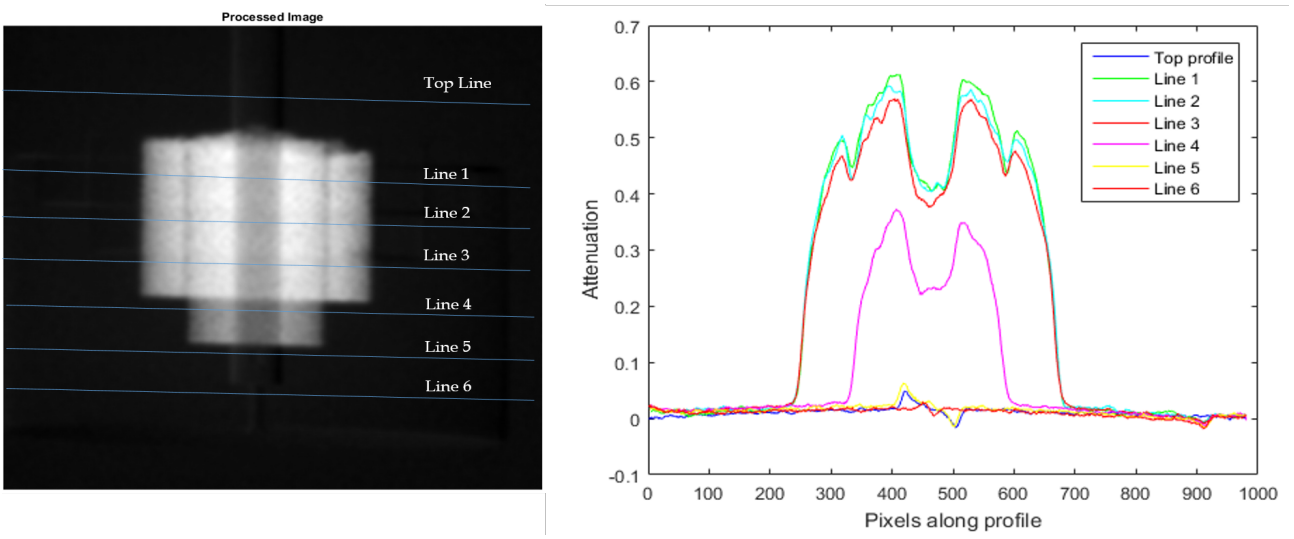

FIGURE 6.8: Processed image (with tapering effect correction) of premixing phantom filled with steel balls in the ring 1 and 2 and its attenuation intensity profiles.

Fig. 6.9 and 6.10 respectively.

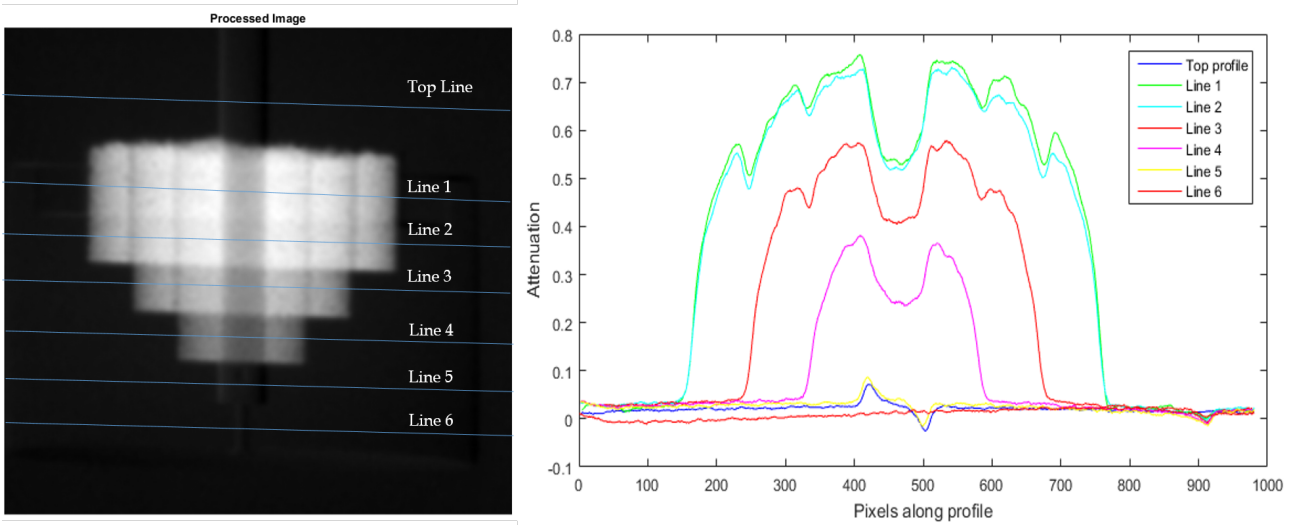

FIGURE 6.9: Processed image (with tapering effect correction) of premixing phantom filled with steel balls in all ring 1, 2 and 3 and its attenuation intensity profiles.

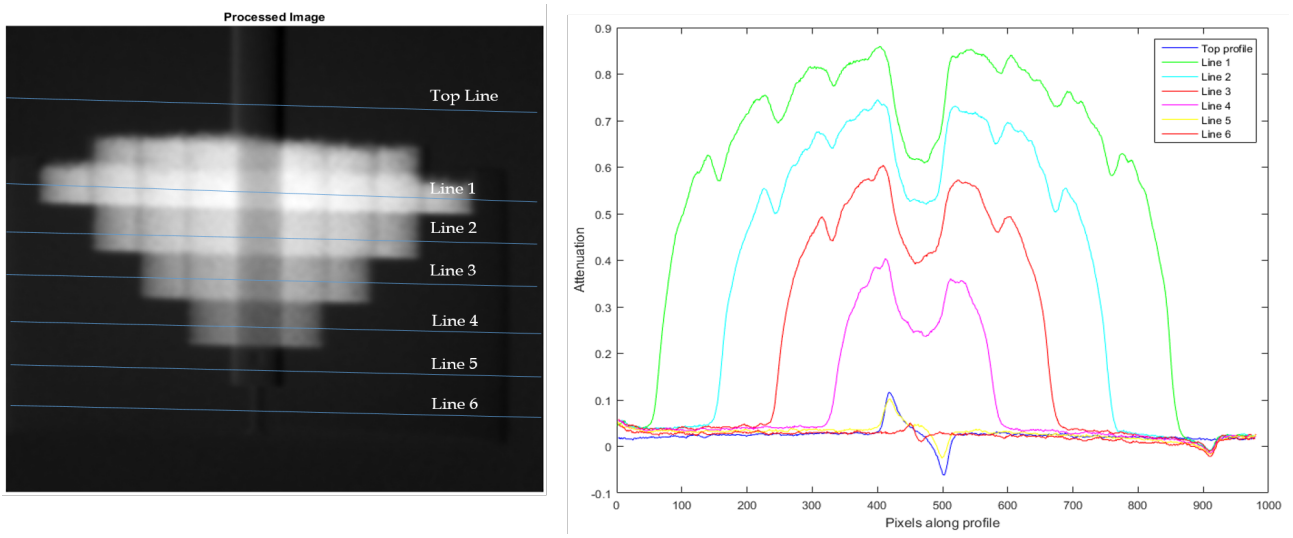

FIGURE 6.10: Processed image (with tapering effect correction) of premixing phantom filled with steel balls in all the rings and its attenuation intensity profiles.

Radiography images of phantom filled with hafnia powder representing less dense clouds of corium particles were also processed. The procedure followed is the same as described in section 6.3.1, i.e., by median filtering, followed by the dark noise correction and flat field correction and dividing by initial image. The processed images of the premixing phantom with its first ring filled with hafnia powder together with its plot profiles are shown in Fig 6.11. Subsequently, the processed images of the phantom with its two rings, three rings and all four rings filled with hafnia powder with their plot profiles are presented in Fig 6.12, 6.13 and 6.14.

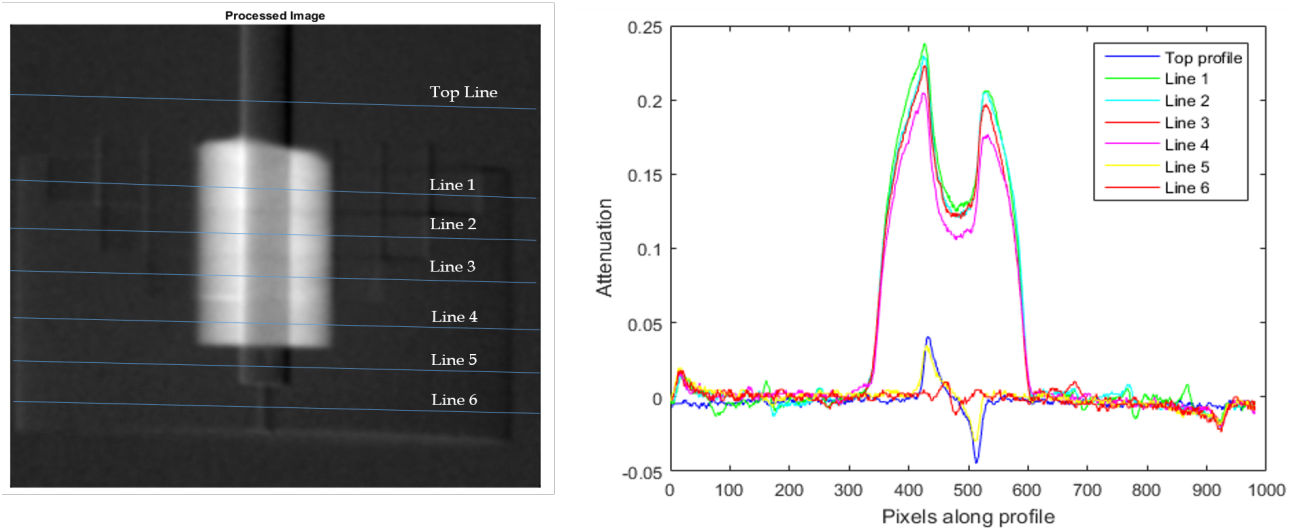

FIGURE 6.11: Processed image (with tapering effect correction) of premixing phantom filled with hafnia powder in ring 1 and its attenuation intensity profiles.

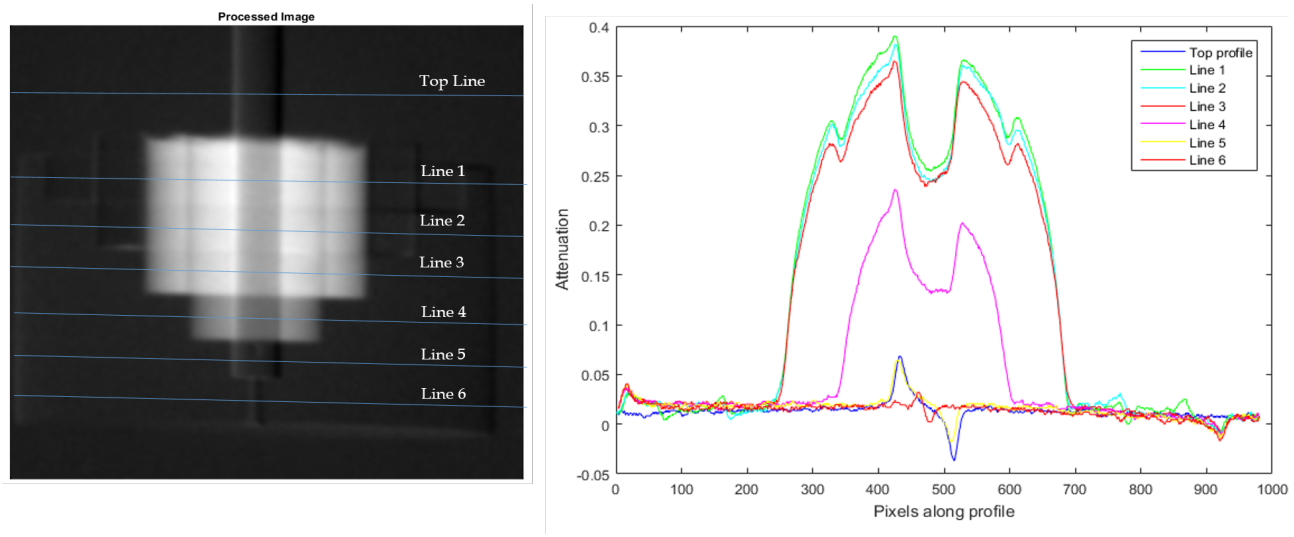

FIGURE 6.12: Processed image (with tapering effect correction) of premixing phantom filled with hafnia powder in ring 1 and 2 and its attenuation intensity profiles.

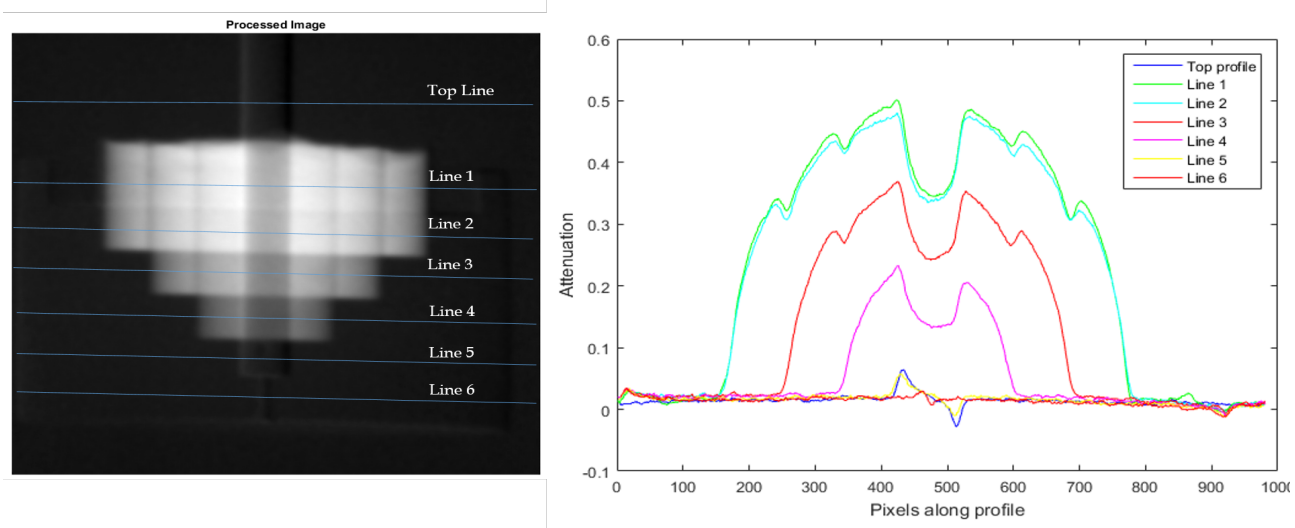

FIGURE 6.13: Processed image (with tapering effect correction) of premixing phantom filled with hafnia powder in ring 1, 2 and 3 and its profile plots.

Analysis

The analysis on the cloud of corium particles is carried out by computing its contrast to noise (C/N) defined already in Chapter 4 which will confirm its detectability. This ratio is determined according to the criterion given in Fig. 6.15. It is defined as the ratio between the signal of corium $level_{cor}$ from the level of sodium $level_{sod}$ which is denoted as "a", to the sodium noise denoted as σ_{sod}. The sodium noise estimation is described in the next section in detail.

The profiles across the corium cloud, i.e. Line 1, Line 2, line 3 and Line 4 in all the processed figures can be

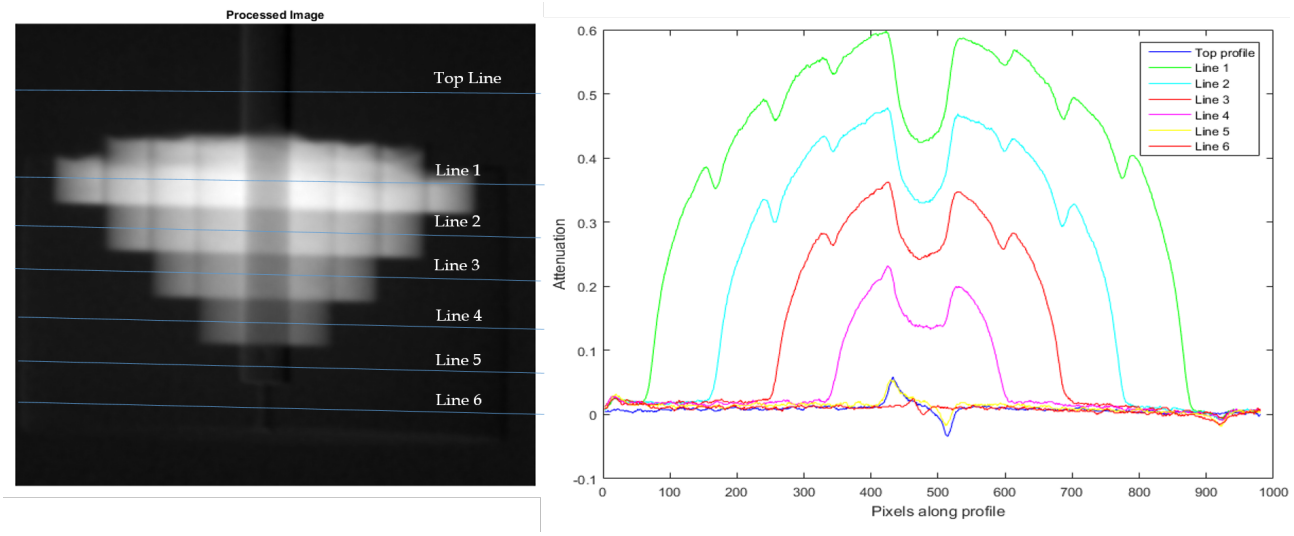

FIGURE 6.14: Processed image (with tapering effect correction) of premixing phantom filled with hafnia powder in all its rings and its profile plots.

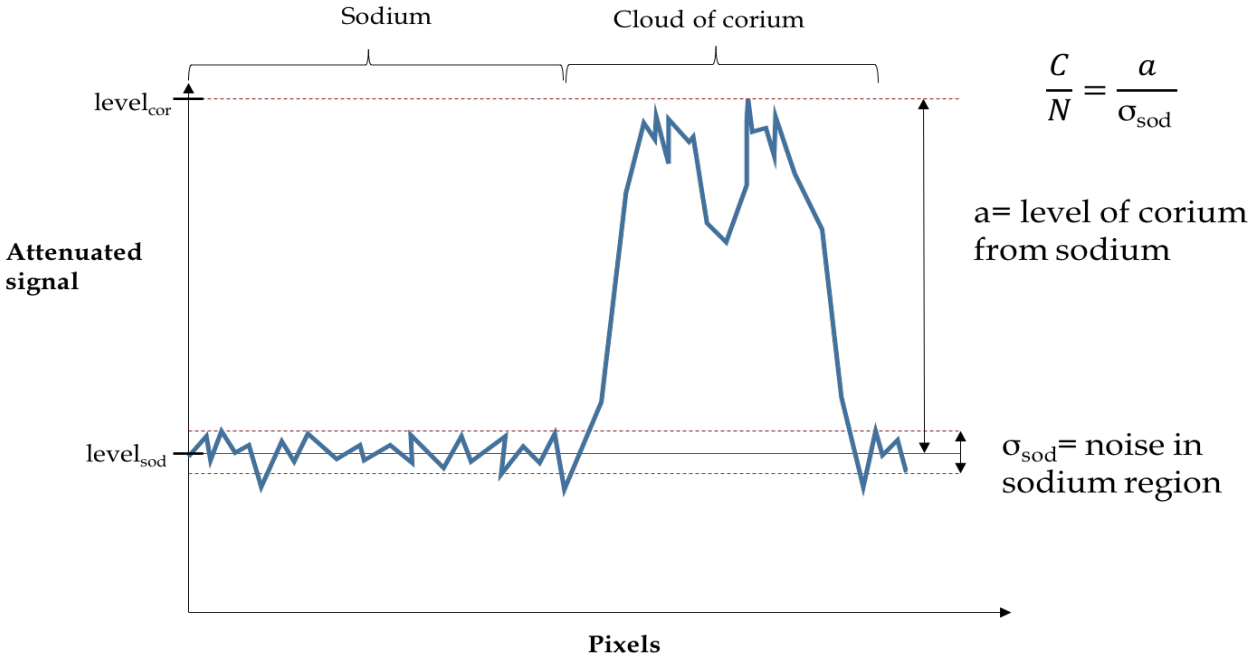

FIGURE 6.15: Defining C/N ratio.

averaged to compute the average profile for Ring 1 filled phantom. This makes it possible to overcome the noise which can locally substantially deform a profile produced on the single line. Similarly, for Ring 2 filled phantoms, profiles across Line 1, Line 2 and Line 3 will be averaged to compute the C/N ratio across Ring 2 and Line 4 will give the C/N ratio across Ring 1. Similarly, when Ring 3 is also filled, the C/N ratio in Ring 3 is computed by averaging intensity profiles across Line 1 and 2 and intensity across Ring 2 is computed from intensity profiles across Line 3 and for Ring 1 from Line 4. Likewise, for Ring 4, the C/N ratios are computed

for each line.

Thus C/N ratio of the 4 dense clouds of corium and the 4 lightly dense clouds is to be computed. Tables 6.1 and 6.2 detail the C/N ratios for each of the 4 dense clouds represented by steel balls and the 4 light clouds of particles represented by hafnia powder.

TABLE 6.1: C/N ratios for denser cloud of corium particles represented by steel balls.

Rings filled		**Ring 1**	**Ring 2**	**Ring 3**	**Ring 4**
Only 1	level_{sod}	0.0196	-	-	-
	level_{cor}	0.387	-	-	-
	a	0.367	-	-	-
	σ_{sod}	0.011	-	-	-
	C/N	32.745	-	-	-
1+2	level_{sod}	0.030	0.030	-	-
	level_{cor}	0.373	0.588	-	-
	a	0.343	0.559	-	-
	σ_{sod}	0.012	0.0116	-	-
	C/N	29.683	48.355	-	-
1+2+3	level_{sod}	0.047	0.0446	0.047	-
	level_{cor}	0.380	0.577	0.740	-
	a	0.335	0.532	0.696	-
	σ_{sod}	0.014	0.0144	0.014	-
	C/N	23.210	36.870	48.222	-
1+2+3+4	level_{sod}	0.064	0.064	0.064	0.064
	level_{cor}	0.403	0.604	0.745	0.859
	a	0.339	0.540	0.680	0.794
	σ_{sod}	0.029	0.02	0.029	0.029
	C/N	11.803	18.801	23.7	27.677

TABLE 6.2: C/N ratios for less dense cloud of corium particles represented by hafnia powder.

Rings filled		Ring 1	Ring 2	Ring 3	Ring 4
Only 1	level_{sod}	0.0196	-	-	-
	level_{cor}	0.233	-	-	-
	a	0.214	-	-	-
	σ_{sod}	0.011	-	-	-
	C/N	19.048	-	-	-
1+2	level_{sod}	0.057	0.057	-	-
	level_{cor}	0.236	0.378	-	-
	a	0.18	0.320	-	-
	σ_{sod}	0.008	0.008	-	-
	C/N	22.136	39.586	-	-
1+2+3	level_{sod}	0.047	0.047	0.046	-
	level_{cor}	0.233	0.37	0.49	-
	a	0.187	0.323	0.46	-
	σ_{sod}	0.006	0.006	0.006	-
	C/N	28.665	49.600	38.570	-
1+2+3+4	level_{sod}	0.0335	0.0335	0.0335	0.0335
	level_{cor}	0.232	0.363	0.479	0.598
	a	0.199	0.33	0.445	0.564
	σ_{sod}	0.007	0.007	0.007	0.007
	C/N	29.418	48.823	66.014	83.666

These results lead us to the following remarks:

- Large (much larger than 1) C/N ratio for the dense and light cloud clearly demonstrates that it is possible to detect the particles of corium as clouds of particles.
- It is observed that a cloud of particles having a lower density, as represented by hafnia powder, has a lower C/N in comparison to the dense cloud of particles represented with the help of steel balls. This makes it difficult to detect lighter clouds of particles.

- The C/N ratio also varies as the radial extension of the cloud is changed. Generally, increasing the size of the cloud (the number of rings) improves the C/N ratio.
- The thickness of the cloud could be determined from the attenuation intensity graph, for instance, Fig. 6.13, 6.14 representing μl knowing the mass attenuation coefficient and the density of the cloud.

Noise Estimation

Three different sources of noise were investigated in the images [75]: read-out noise, dark noise/obscurity and photon noise. Read-out noise arises from the due to fluctuations in the output signal caused by thermal effects in the read-out electronics of the camera. Dark noise/obscurity as already explained arises from the small current build-up on the sensor array of the camera over time. Photon noise arises from the particulate nature of light and can be seen as the variation of a number of photons arriving on the detector which takes into account the fluctuations from the source. This can be described by Poisson statistics and is thus given by square root mean of the number of photons,

$$\sigma_{ph} = \sqrt{N} \tag{6.6}$$

The read-out and the dark noise being directly related to the effects of camera sensors, were measured from the dark images, i.e., images acquired without X-Rays. The subtraction of dark noise σ_{obs} as carried out in Eq. 6.3 increases the noise in the corrected image $\sigma_{avg,cor}$ according to

$$\sigma^2_{avg,cor} = \sigma^2_{avg} + \sigma^2_{obs} \tag{6.7}$$

However, since the measurement was recorded over long exposure times and high X-Ray flux (due to more photons for 100 images), the noise level in the real image will be much higher than in the dark image where there is an absence of X-Ray flux. And therefore, the increase in noise is negligible.

The flat field correction by dividing the image with a flat field image as carried out in Eq. 6.4 results in an increase in the relative noise (since the two noises are decorrelated) according to

$$\sigma^2_{att} = \sigma^2_{avg} + \sigma^2_{ff} \tag{6.8}$$

Also, since the two images have the same relative noise, the noise level in the corrected image will increase by a factor of $\sqrt{2}$. Similarly for the initial image, the noise level will increase by $\sqrt{2}$. Therefore, introducing the

tapering correction noise level will increase by a factor 2.

We measure the noise in the corrected images on the left and right side of the corium cloud. For example in the case of ring one filled, the noise is measured in box red and box green separately of the Fig. 6.16. The calculation is carried out separately for all of the four cases of the experiments, i.e. with, one ring filled, with two rings filled, with three rings filled and with four rings filled each for dense cloud (with steel balls) or lighter cloud (with hafnia powder)

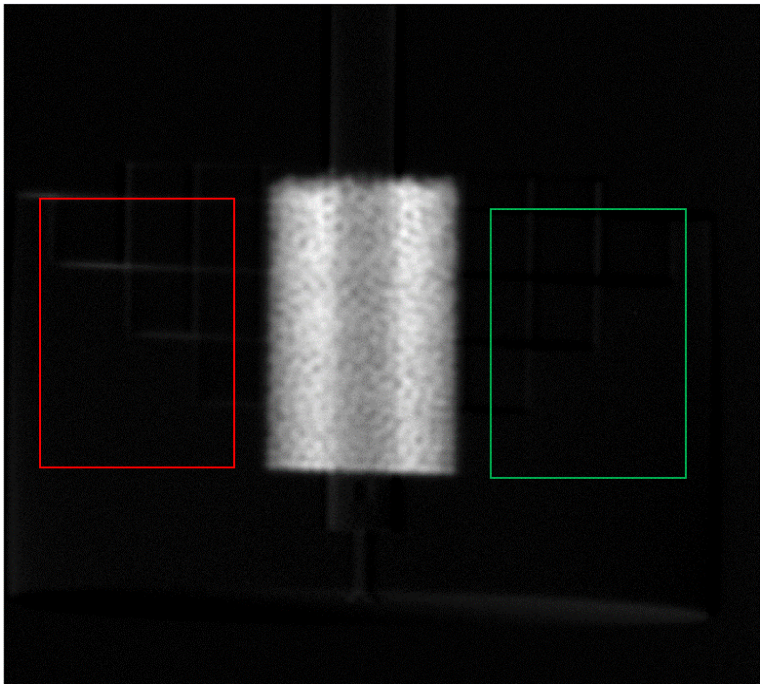

FIGURE 6.16: Areas of noise estimation.

6.3.3 Vapor film

Acquisitions to determine the detectability of the vapor film was carried out using the vapor phantom. This phantom presents a vapor film with a varying thickness ranging from 0 to 1 cm. This range of thickness was chosen to predict the limit of detection of the vapor film. In practice, all acquisitions have been made in the lower part of the phantom, for a film thickness of less than 7.5 mm.

Like in the phantom with fragments, the images obtained with this phantom were also observed to have white spots. Median filtering was applied on all the raw images and was later averaged to obtain the averaged image. The images were then flat field corrected to obtain the attenuated image shown in Fig. 6.17. The tapering effect was not implemented in the processing of this phantom. As already said, in principle, there should be an image with a full cylinder representing liquid sodium and the tapering correction should be made with such a phantom.

However, for this phantom, there is an image of the phantom without the steel rod, but this image cannot be used for tapering correction since it would not preserve the vapor film attenuation properties, which is the point of our analysis.

FIGURE 6.17: Processed image of the phantom with vapor film.

The detectability of the vapor film could be judged by determining its contrast to noise ratio. Intensity profiles along different lengths of the phantom are shown in Fig. 6.18. The small dips on both sides of the bell shape in all the profiles represent the attenuation in the vapor film, i.e. "a" in the calculation of the C/N ratio.

$$\frac{C}{N} = \frac{a}{\sigma_{sod}} \tag{6.9}$$

The C/N ratio is computed on both the areas of the vapor film, on the left and right side. Since the tapering effect could not be corrected, the noise is estimated in the region as close as possible to the vapor film. It is calculated on both the left and right side of the vapor film and is recorded.

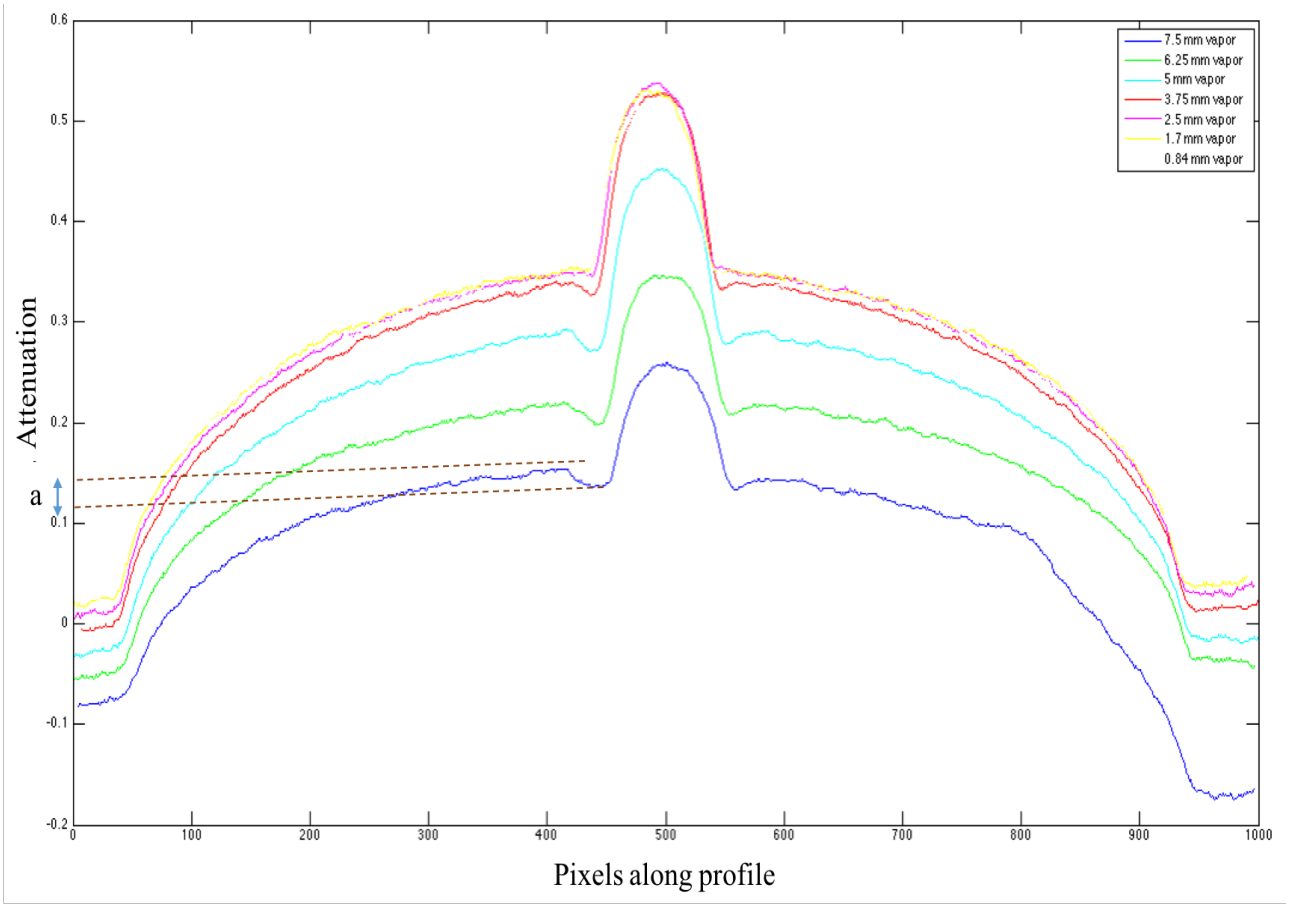

FIGURE 6.18: Intensity profiles across various thickness of vapor film.

Following this, the C/N ratio of the vapor film is estimated at different points of the phantom and are reported in Table 6.3.

TABLE 6.3: C/N ratio for the vapor film.

Thickness of vapor film	Side	Left	Right
7.5 mm	level_{sod}	0.153	0.143
	level_{vap}	0.136	0.133
	a	0.018	0.010
	σ_{sod}	0.003	0.003
	C/N	5.746	2.715
6.25 mm	level_{sod}	0.220	0.219
	level_{vap}	0.197	0.207
	a	0.023	0.012

Continued on next page

Table 6.3 – continued from previous page

Thickness of vapor film	Side	Left	Right
	σ_{sod}	0.005	0.005
	C/N	4.304	2.418
5 mm	level_{sod}	0.293	0.290
	level_{vap}	0.271	0.277
	a	0.023	0.013
	σ_{sod}	0.004	0.004
	C/N	5.929	3.173
3.75 mm	level_{sod}	0.343	0.34
	level_{vap}	0.325	0.331
	a	0.018	0.009
	σ_{sod}	0.003	0.003
	C/N	4.994	3.083
2.5 mm	level_{sod}	0.350	0.351
	level_{vap}	0.344	0.345
	a	0.006	0.005
	σ_{sod}	0.003	0.003
	C/N	2.455	1.770
1.7 mm	level_{sod}	0.355	0.351
	level_{vap}	0.348	0.348
	a	0.007	0.003
	σ_{sod}	0.002	0.002
	C/N	2.698	1.107
0.84 mm	level_{sod}	0.341	0.344
	level_{vap}	0.347	0.345
	a	-0.006	-0.001
	σ_{sod}	0.003	0.003
	C/N	-1.712	-0.354

The variations in C/N ratio between the left and right of the vapor film come from the difference in flux between

each side. These computations suggest that the vapor film can be detected up to a thickness of the order of 1.7 mm, but very faint below 3.75 mm. However, in a corium-sodium interaction, a film of very unstable nature is expected. There is a lack of experimental evidence that states the thickness of expected vapor film. Thus, knowledge on the vapor film formation is required which could later instigate more investigation on the detection limit of vapor film.

6.4. Sequence of image processing in the PICSEL software

Image processing is not a one-step process. Most algorithms developed to carry out measurements in multi-phase flows follow sequential processing scheme [28, 69, 70, 76]. The main steps and how they can be implemented in our case are described below:

Acquisition is the first step of processing. This includes reading raw data frames of the video.

The *pre-processing* step aims at improving the quality of the frames of the video. Image enhancement techniques to enhance/adjust the contrast and brightness of the frames of the video to interpret the video. Noise removal filtering techniques are one of the pre-processing technique which will reduce the noise in the images. Background subtraction to separate the foreground objects from the background as described in section 1.3.2 is another possible algorithm to be employed in the pre-processing step.

The *segmentation* block is responsible for partitioning an image into its significant components. The purpose of this technique is to simplify the representation of an image to an image which will be easier to analyze and interpret. The image segmentation algorithm is mostly based on the two basic properties of an image intensity value - discontinuity and similarity. These will be discussed in the next section. In our particular case segmentation will be performed for the extraction of two phases: (1) Corium-cloud extraction (2) Vapor extraction, thus, attaining qualitative analysis of the images.

The *quantitative analysis* block consists of algorithms responsible for calculating important features. In our case, typical features include estimating size, velocity and density of the cloud of particles.

These steps of analysis can be described by the block diagram shown in Fig. 6.19

It should be noted that presently, PICSEL is capable of treating 2D images only. However, plans are there to perform 3D reconstruction of the images as this would help to estimate the corium and vapor surface area and volume. A technique involving the method of rolling sphere could be used as a preliminary approach to

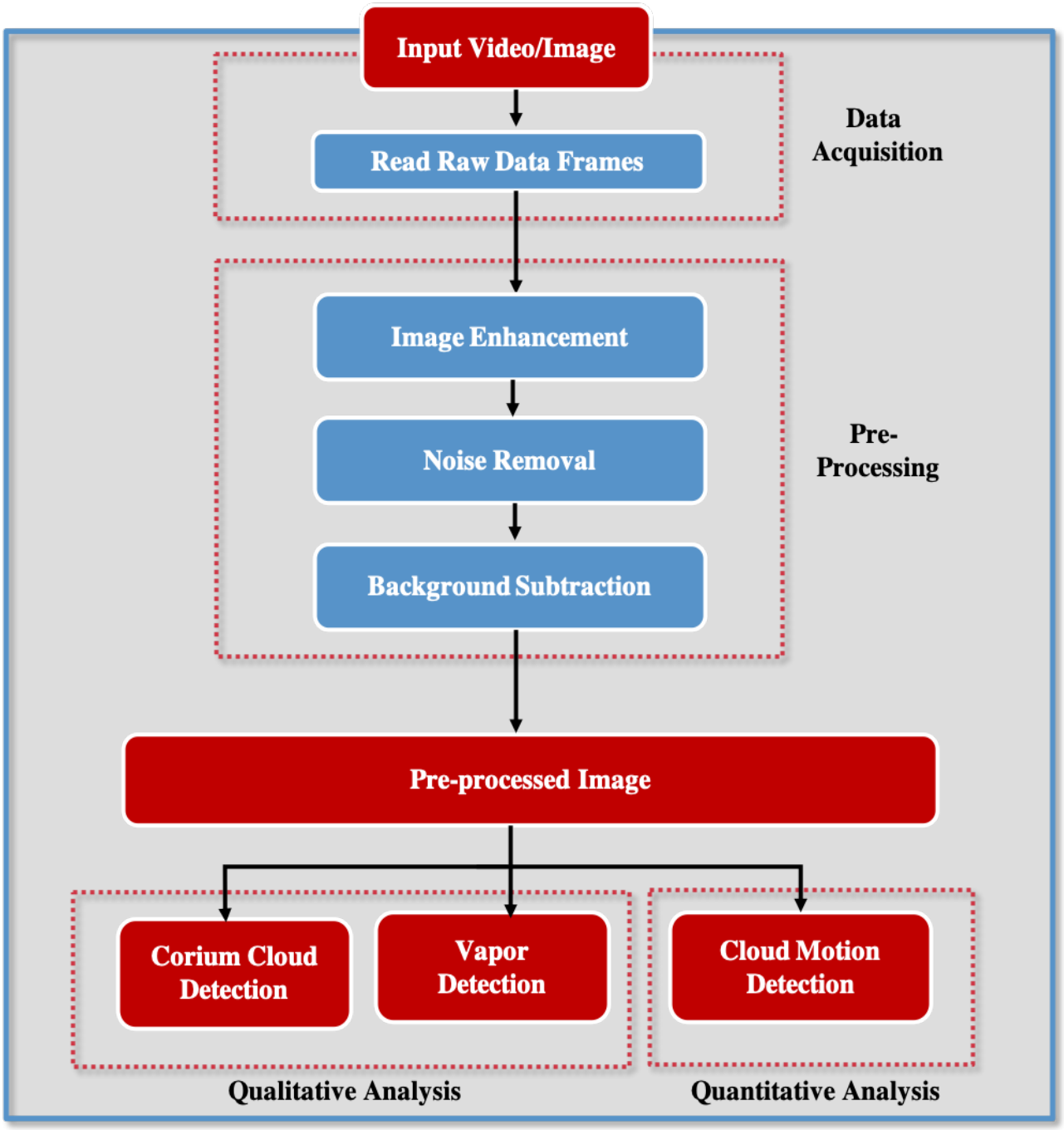

FIGURE 6.19: Block diagram demonstrating the steps implemented in the image processing algorithm.

performing this task. However, unlike the case of corium-water interaction where the rolling sphere method generally works and the results are promising [46], in the present tool PICSEL, which analyzes corium-sodium interaction its efficiency is questionable. Reason being, the particle size formed in the corium-sodium interaction is small enough to be detected as individual particles and therefore reconstruction of clouds of particles is done as an approximation. The choice of visualizing particles as clouds sets a substantial limitation to formulate an algorithm for 3D reconstruction. This would be a subject of future research in this domain.

6.5. Description of techniques used

The techniques implemented at each step in the software depend on the image quality and the information that is required to be extracted. In this section, several techniques will be applied to the experimental images and compared to see which technique best suits our requirements.

6.5.1 Acquisition

Reading raw data

This is the first step of the software. This involves reading the raw frames of the video and also the dark noise and the full flux images.

6.5.2 Pre-processing

The pre-processing procedure used to interpret the images obtained from the experiment has already been discussed in the early part of this chapter. The same procedure could be applied to video files of a test assuming the quality of the video file will be similar to the experimental images.

Enhancement

The raw images acquired from the experiments had a poor contrast as already mentioned in Chapter 5. It was impossible to differentiate the three phases in the phantom from the raw data. Thus, in order to interpret the images, they needed to be enhanced using intensity transformation techniques, for example, the negative transformation, contrast-stretching, gamma transformation techniques, log transformation and histogram equalization [72]. All these techniques will be applied to the raw images selecting the one that improves best the image quality.

Negative transformation computes the negative of the input image. Gamma transformation is a technique that maps the intensity values in the grayscale image to new desired values. With Gamma Transformations, one can scale the grayscale components either to brighten the intensity (when gamma is less than one) or darken the intensity (when gamma is greater than one). The gamma transformation function is expressed mathematically by

$$s = c \cdot r^{\gamma} \tag{6.10}$$

where r is the pixel value of the original image, and s is the resulting pixel value, c is a scaling constant and γ is a positive value either less than one or greater than one. Histogram equalization is about modifying the intensity values of all the pixels in the image such that the histogram is "flattened". The idea behind Histogram Equalization is to try to evenly distribute the occurrence of pixel intensities so that the entire range of intensities is used more fully. We are trying to give each pixel intensity equal opportunity; thus, equalization. Log transformation technique is used to compress or expand the dynamic range of pixel values in an image. More often, it is used to increase the detail (or contrast) of lower intensity values. It can be mathematically described by:

$$s = c \cdot log(1 + r) \tag{6.11}$$

Contrast stretching is a technique which expands a narrow range of input intensity levels to a wide (stretched) range of output levels. All the intensity values are linearly spread out between this range. It would lead to an image with higher contrast. Fig. 6.20 depicts an original image obtained from the experiment and the enhanced images obtained using negative, gamma transformation, histogram equalization, log transformation and contrast stretching.

Comparing the enhanced images in Fig. 6.20 it is clear that contrast stretching is most effective in improving the contrast of the images while preserving all the information. Thus, this technique is applied to all the frames of the video.

Noise Removal

Noise removal is important and a pre-requisite for image segmentation. After obtaining good contrast images, it was observed that the images had a lot of noise in the form of white spots. The removal of white spots could be attained by applying the median filter as mentioned before. A kernel big enough to include the biggest spot is applied to filter all the frame of the video (a kernel of 11×11 pixel is commonly applied).

Background removal

To revise the readers, in order to remove the inhomogeneity of the image background from the image I_{avg}, we need to divide the images from full flux image to get I_1 and then divide the image from its background image I_2. Full flux image I_{ff} is obtained by capturing the emission spectrum of the X-Ray system in the absence of the test facility. Background image I_{bkg} can be obtained by taking a blank image before the ejection of corium

(a) **Original image.**

(b) **Negative transformation.**

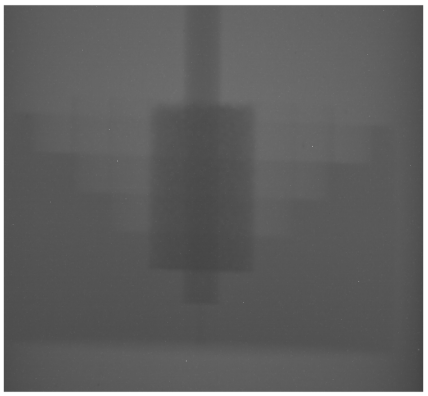

(c) **Gamma transformation with γ=0.75.**

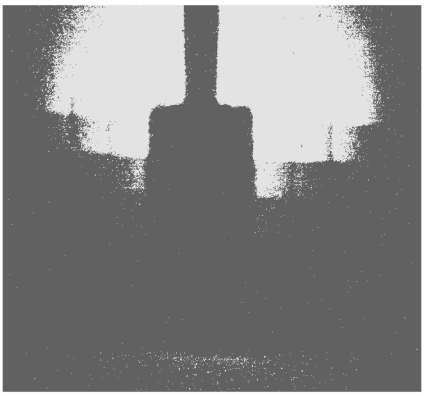

(d) **Histogram Equalization.**

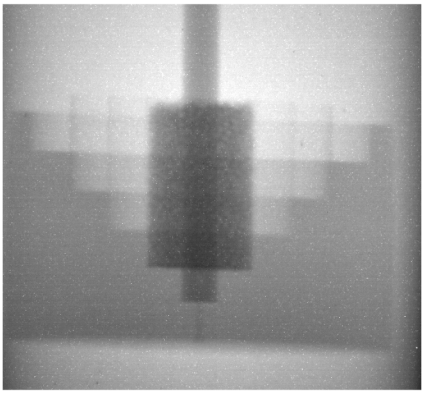

(e) **Log Transformation.**

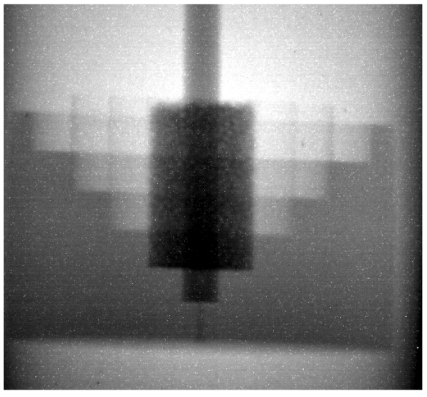

(f) **Contrast Stretching.**

FIGURE 6.20: Effect of various enhancement techniques on the original image.

into sodium, i.e. the sodium system alone. Also, obscurity correction I_{obs} has to be implemented in each of the images. As already discussed before, the processing is done according to the following equations:

$$I_1 = \frac{I_{ff} - I_{obs}}{I_{avg} - I_{obs}} \tag{6.12}$$

$$I_2 = \frac{I_{ff} - I_{obs}}{I_{bkg} - I_{obs}} \tag{6.13}$$

$$I_{proc} = \ln \frac{I_1}{I_2} \tag{6.14}$$

This procedure is applied to all the frames of the video to obtain attenuation images.

6.5.3 Segmentation/Qualitative analysis

This step aims at decomposing the image to extract the three phases in the image: corium, sodium vapor and liquid sodium. The analysis starts by first extracting corium particle cloud, followed by the extraction of sodium vapor.

Cloud detection

The detection of corium particles can be achieved by testing segmentation techniques. The thresholding technique is one of the image segmentation technique that can be used to separate the corium cloud from vapor and liquid. This technique is based on the selection of a gray level inquisitively from the histogram of the image [77]. This grey level will serve as a threshold to distinguish the corium cloud from the rest of the images. This produces a binary image representing the corium cloud as shown in Fig. 6.21.

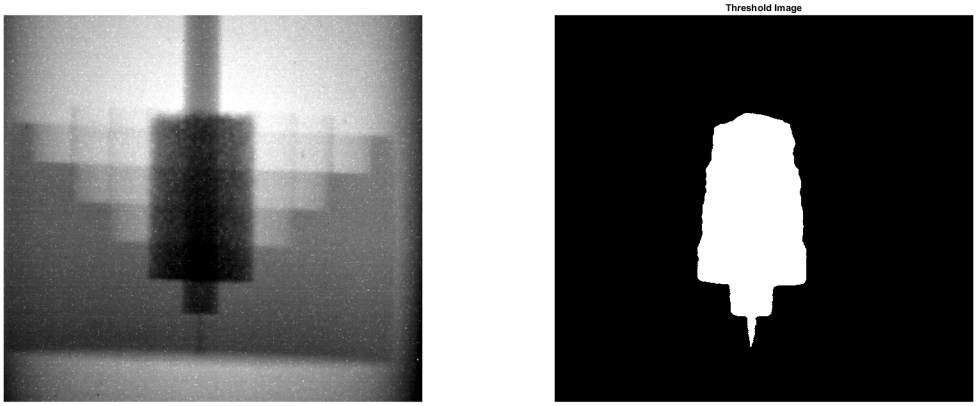

(a) **Original image.** (b) **Thresholded binary image.**

FIGURE 6.21: Example of image thresholding.

These initial attempts to threshold the image globally to extract the cloud of corium were not very successful. It fails to detect the cloud at the top edges. This is due to the fact that the cloud is superimposed by a certain amount of vapor which reduces its intensity significantly at those edges and mistakes it for liquid sodium. This example clearly demonstrates that the intensity of the corium cloud is not necessarily below that of sodium. Global thresholding thus fails to extract corium.

Edge detection is another segmentation technique that detects meaningful discontinuities in the intensity values. An edge is a boundary between two regions with relatively distinct gray level properties [78]. They are measured in terms of first-order derivative and second order derivative along the intensity profile. These gradients are often computed with the help of convolution masks. There are many edge detection techniques that are frequently used in image segmentation like Sobel edge detection, Prewitt Edge detection, Canny Edge detection and Roberts Edge detection. These techniques use different convolution masks on the images and are compared in [79] and available in MATLAB. Interested readers can refer to a book explaining these techniques in detail [71]. It was observed that the Canny edge detection algorithm produced the best results as depicted in Fig 6.22.

FIGURE 6.22: Example of edge detection algorithm.

Vapor detection

The intensity gradient at the boundary of liquid sodium and sodium vapor is not significant. Therefore, edge detection techniques fail to detect vapor efficiently. Whereas the Otsu thresholding technique when applied on the image, gives a result as shown in Fig. 6.23. There are uncertainties associated with the estimation from Otsu thresholding as well. However, this uncertainty is supposed to come with all the technique as the superposition of void with sodium or corium, might alter its intensity.

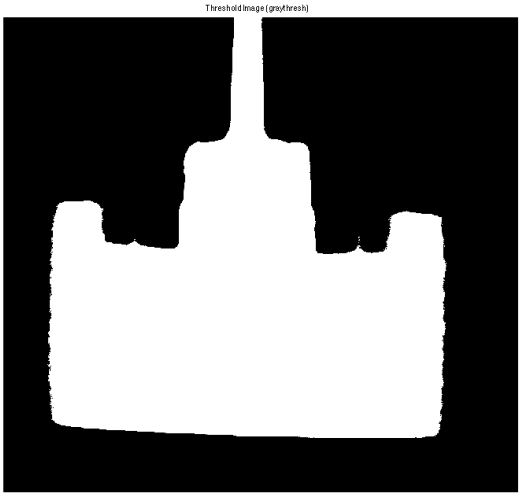

FIGURE 6.23: Application of Otsu thresholding technique for vapor distribution estimation.

6.5.4 Quantitative analysis

Quantitative analysis is directed towards determining the size, velocity and other important features of the corium particle clouds. The data obtained will help in characterizing the three-phase flow in the mixture composed of molten corium, liquid sodium and sodium vapor.

6.5.5 Corium cloud motion detection

Cross-correlation technique is frequently used for the measurement of particle velocity in particle image velocimetry (PIV) techniques [80, 81, 82, 83]. PIV is an effective instantaneous and non-intrusive technique for the measurement of velocity fields in fluid mechanics research [83]. Like in PIV, the motion of the corium cloud could also be measured using a cross-correlation technique that was decided to be adapted to our case in order to estimate the cloud motion.

Cross-correlation technique is based on the block matching algorithm. This algorithm selects a block/template in the initial frame and searches a sub-region in the target frame as shown in Fig. 6.24. It searches the entire sub-region and selects the block where the normalized cross-correlation (NCC) has a maximum value. Normalized cross-correlation closely follows the following formula [85]:

$$\gamma(u,v) = \frac{\sum_{x,y}[f(x,y) - \overline{f}_{(u,v)}][t(x-u,y-v) - \overline{t}]}{\left[\sum_{x,y}\left[f(x,y) - \overline{f}_{(u,v)}\right]^2 \sum_{x,y}[t(x-u,y-v) - \overline{t}]\right]^{0.5}} \tag{6.15}$$

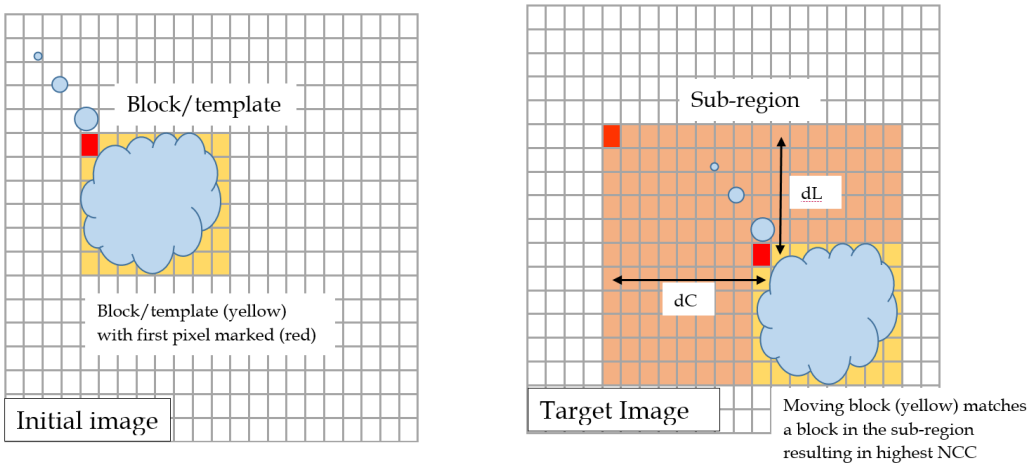

(a) **Initial image.** (b) **Target image.**

FIGURE 6.24: Scheme of block matching [84].

where $f_(x, y)$ is the sub-region of the target image, $\bar{t}$ is the mean of the template in the initial frame and $f_{u,v}$ is the mean of $f(x, y)$ in the region under the template. The displacement of the block from initial frame to the target frame, is then converted from the image domain to the spatial domain thus estimating the distance moved by the cloud. Finally, the cloud displacements within the spatial domain are then divided by the time separation between the consecutive frames, i.e. velocity = displacement/Δt, to provide the velocity field.

This technique could not be tested on the phantoms as they are static. For this, a real-time test conducted at the KROTOS facility under the Euro-Chinese project ALISA was chosen. This corium-water interaction test was carried out to study the effect of a reduced water pool depth on the interaction between prototypic corium and water. This test experienced a vapor explosion followed by a second premixing phase which was found to be more akin to corium-sodium interaction. Therefore, this test was chosen to validate the corium cloud motion detection algorithm which will be discussed in the next chapter.

6.6. Conclusion

The interpretation of the experimental results confirmed the feasibility of monitoring corium-sodium interaction with the help of high energy X-ray imaging system. The corium particle cloud was found to have a good contrast to noise ratio making it detectable. The attenuation signal from the processed images could not quantify density and the attenuation thickness both, as there will be two unknowns. Thus the vapor fraction and the corium fraction could not be estimated in the cloud. The detectability limit of the vapor film is of the order of 1.7 mm.

This limitation comes from the photonic noise which decreases its C/N ratio. On the final experiments, it will thus be necessary to optimize the photonic signal.

The image processing software PICSEL was developed to characterize the three-phase flow involved in corium-sodium interaction. It was able to process the 2D images and to extract corium clouds and vapor separately. PICSEL was made capable of tracking clouds of corium and estimation of their velocities. The software will be validated on the KROTOS-ALISA test as described in the next chapter.

Chapter 7

Application and first validation of the image processing tool PICSEL

> *Doubt the conventional wisdom unless you can verify it with reason and experiment.*
>
> Steve Albini

The developed software PICSEL, for the processing and analysis of the images obtained during corium-sodium interaction experiments, has been discussed in the previous chapter. This software is capable of qualitatively characterizing the three-phases formed during a corium-sodium interaction in terms of spatial distribution. The experiments conducted on phantoms helped the development of the PICSEL software. However, it was essential to use PICSEL on any real corium-sodium interaction test, to verify and validate its capabilities. This sort of validation would provide better confidence in the software and would also depict its limitations.

Due to the unavailability of X-Ray images for a corium-sodium interaction, images from the KROTOS-ALISA test, a test between corium-water was chosen to use for this preliminary validation. This test though being

on corium-water, shows many similar behavioral characteristics to a corium-sodium interaction, since a first explosion leads to the formation of sub-millimetric particle clouds followed by a second coherent corium flow, a jet and a particle cloud would then be obtained simultaneously.

This test [45] was conducted at the KROTOS facility within the Euro-Chinese project framework: ALISA (**A**ccess to **L**arge **I**nfrastructure for **S**evere **A**ccidents) [86].

This chapter deals with the validation of the PICSEL software on the KROTOS-ALISA test, starting with a description of the test setup, data acquired and finally the processing and analysis of the X-Ray images obtained during this experiment.

7.1. KROTOS-ALISA test and data acquisition

The idea behind the ALISA project is to work collaboratively on large scale experimental facilities available in Europe and China. The KROTOS facility has already been introduced in detail in Chapter 2. The KROTOS-ALISA test for water, carried out at the CEA for the Hong Kong City University, is presented in detail in Appendix C. The X-Ray imaging system of the KROTOS facility helped record the three stages of the interaction, i.e, premixing phase, explosion phase and the second premixing phase. In this final phase, premixing jet coexists with fine particles produced by explosion, as expected in corium-sodium interaction. The three stages of the interaction were recorded in the form of a video which lasted 90-seconds. A brief description of the video is given below:

- **Duration:** 90 seconds
- **Bits per pixel**: 24 bpp
- **Frame rate:** 100 frames per second
- **Size of each frame:** 640 x 209 pixels
- **Video format:** RGB24

Processing and analysis of this video will be explained in the next section.

7.2. Application of PICSEL to KROTOS-ALISA test

As mentioned in the previous chapter, PICSEL analysis the video following three steps. First, data acquisition is performed where the raw input video or image is read and stored in the form of data frames. Following this step, a pre-processing of the data frames is carried out which comprises the image enhancement, noise removal and background subtraction. Once the pre-processed image is obtained a qualitative analysis of the data frames are carried out (corium cloud detection and vapor detection). This will be discussed in the present section.

7.2.1 Data acquisition

The input video was first read by the PICSEL software and stored in the form of data frames. It was observed that there were around 9000 data frames in the 90 second video (i.e. a frame rate of 100 frames per second). A visual inspection of the video reveals that corium release starts after 3.1 seconds and the first premixing occurs between 3.11 and 3.55 seconds. The explosion occurs at 3.56 seconds followed by the second premixing at 4.25 second.

7.2.2 Pre-processing

The image pre-processing step involves image enhancement, noise removal and background removal.

- **Image enhancement:** The image enhancement of the data frames was not necessary in this case as the images obtained were of sufficiently good quality.
- **Noise removal:** There were no observed white spots or any other type of noise in the KROTOS-ALISA video. This could be attributed to the fact that the images were acquired with a short acquisition time due to the thin KROTOS test section walls (compared to the foreseen PLINIUS-2-FR wall). This short camera acquisition time did not allow the pixels to saturate from the scattered radiation falling directly on the camera matrix. The noise removal step was thus skipped and was not necessary for this test.
- **Background subtraction:** The background subtraction is performed to remove the in-homogeneity arising from the emission spectrum of the X-Ray flux and the tapering effect of the geometry of the facility. Due to the unavailability of the obscurity image, the in-homogeneity arising from the emission spectrum could not be corrected. Only the tapering effect could be corrected in this case. Background removal process (correcting only the tapering effect) is easier to perform on the frames depicting the premixing

phase, i.e. before the explosion phase. It is done simply by dividing the frames by an initial frame in which no corium has come into the picture yet, i.e. a frame recorded before the start of the corium injection (reference frame). However, background removal becomes difficult for the frames depicting the explosion and those after the explosion. This is due to the motion induced in the whole vessel after the explosion resulting in the translation of the test-section in the frames (which will be referred to as translated frames). This effect was due to the peculiar system used to reduce the pool depth without changing the water surface altitude (and thus the jet velocity at the start of its interaction with water). It will be corrected in subsequent shallow water tests in KROTOS.

Using the translated frames as it is for background removal will give unreliable results. Thus, it becomes of utmost importance to first align back the translated frames and then perform background removal. This will be discussed in the next section.

7.2.3 Image alignment algorithm for video stabilization purposes

The image alignment algorithm is applied in two steps: firstly, the motion of the translated frames is estimated using the block matching algorithm technique explained in the previous chapter. The second step is the stabilization/aligning of the frames by taking into account the motion. The global motion estimation of the entire frame cannot be adapted to our case due to its robustness issues with concerning illumination changes (arising from the explosion) and moving objects (entry of corium into the picture) as explained in the article [87]. So, in order to see the motion from one frame to another, we select six screw segments: (Screw 1-6) in the reference frame and observe their corresponding matching segments in the translated frame using the normalized cross-correlation technique. To reduce the computation time, instead of tracking them in the entire translated image, these are tracked in small sub-regions. These are illustrated in Fig. 7.1 where one of the translated frames after the explosion is shown on the right with the six selected regions (Reg 1-6).

Normalized cross-correlation (NCCR) of the screw template and sub-region is computed. The maximum value in the NCCR matrix indicates where the images are best correlated. Thus, a surface plot of calculated NCCR is plotted in which the peak represents the best matching position. An example of a surface plot of calculated NCCR of Screw 1 in the reference frame and Reg 1 in a translated frame is shown in Fig. 7.2.

The coordinates of the peak are determined. Following which, the offset of the screws in the X (towards the right) and Y-direction (downwards) is calculated. Similarly, translation for all the six screws is calculated both in

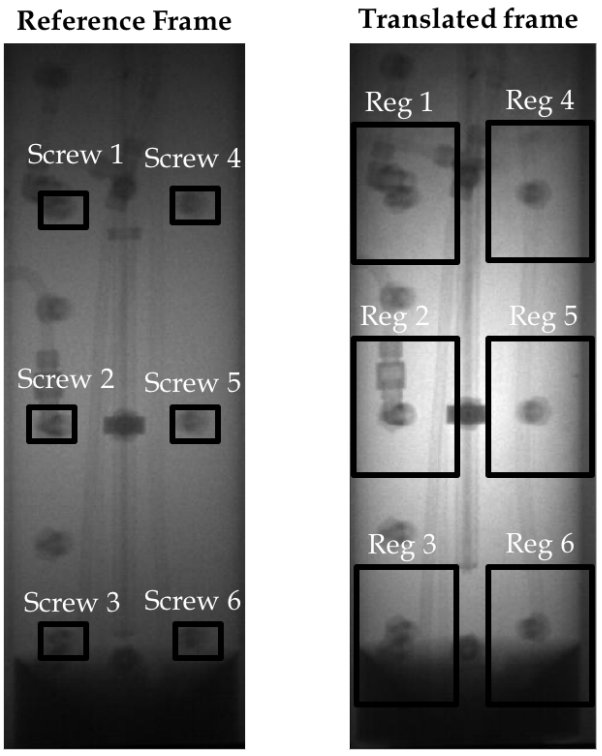

FIGURE 7.1: Screws in the reference frame are tracked in corresponding sub-regions of the translated frames.

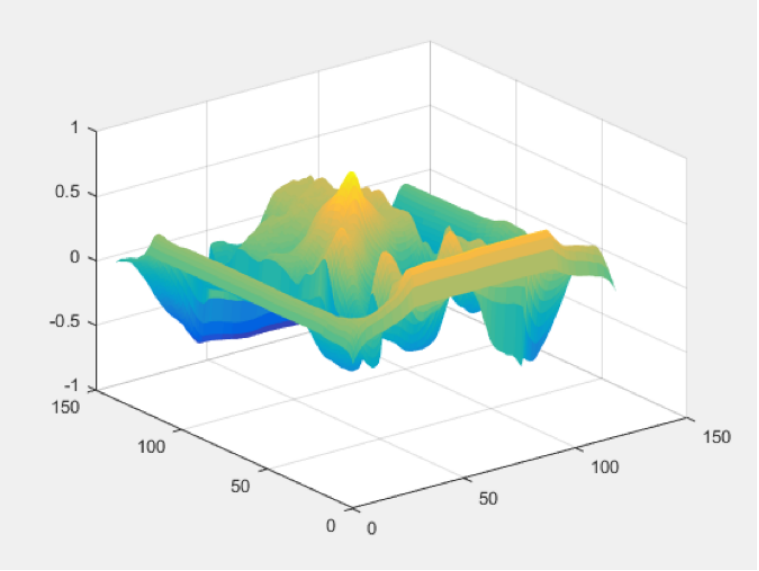

FIGURE 7.2: Surface plot of the Normalized Cross-Correlation between screw 1 in the reference frame and sub-region 1 in the translated frame.

X and Y-direction. It is chosen to consider that the average of the translation that occurred in the six screws will represent the translation of the entire frame. A plot of the pixels translated in the X-direction by the vibrating test-section with respect to the time is shown in Fig. 7.3. The graph clearly shows that after the explosion at 3.56 seconds, the test-section translates by -4 pixels, i.e., 4 pixels to the left and keeps oscillating between 3 and 4

pixels. Since each pixel corresponds to 1.04 mm distance at the position of the test section, the translation of the facility is computed to be oscillating between 3.12 to 4.16 mm. After 9 seconds it comes to rest at 4 pixels to the left of the original reference frame, i.e. 4.16 mm to the left.

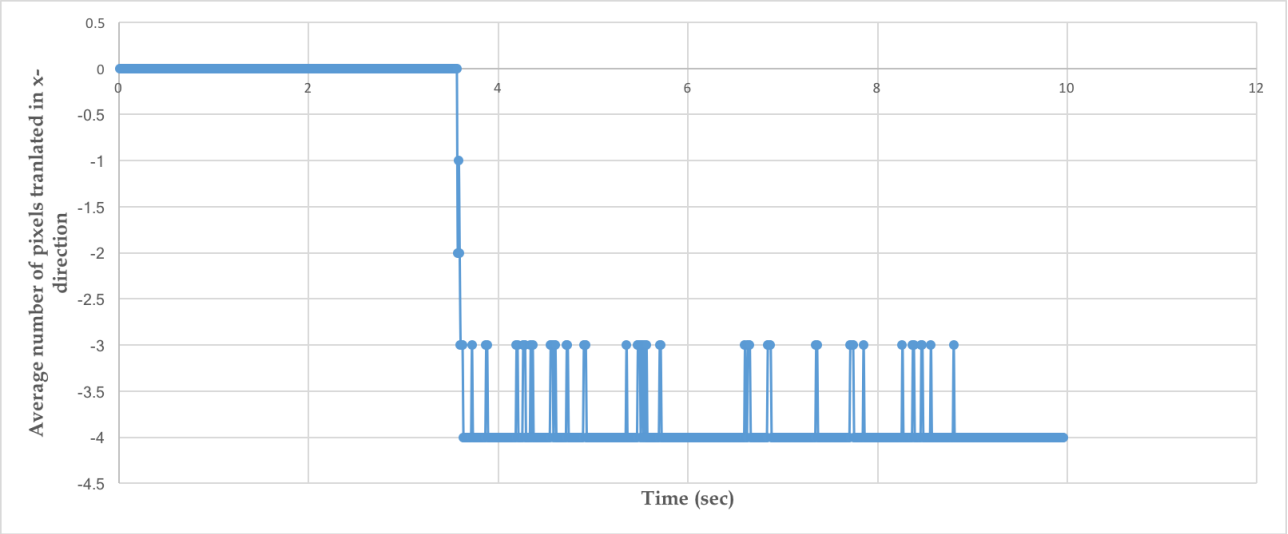

FIGURE 7.3: Number of pixels translated by the vibrating KROTOS test-section in X-direction with time.

Similarly, a plot of the pixels translated in Y-direction by the vibrating test section with time is shown in Fig. 7.4. The facility translates from +2 to -9 pixels, i.e., 2 pixels (2.08 mm) downwards, then 9 pixels (9.36 mm) upwards, and so on, until it comes to rest at the same height as before the explosion. Thus, as a whole the test-section

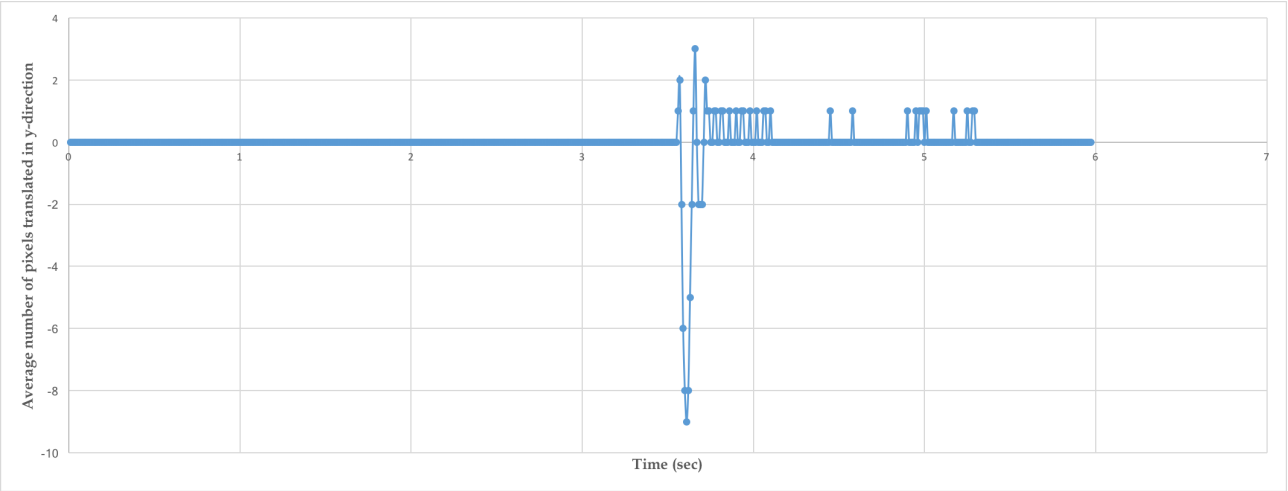

FIGURE 7.4: Number of pixels translated by the vibrating KROTOS test-section in X-direction with time.

oscillated downwards and upwards by a distance as high as approximately 1 cm but came to rest eventually at its initial axial position, drifted by 4.16 mm to the left.

The second step consists of registering/aligning back the images. This is done according to the translation estimated for each translated frame in the previous step. The frames are aligned back to compose a new video which will be referred to as the registered video from here on.

Background subtraction is then carried out on the registered video. A comparison of background removal on an unregistered frame and its corresponding registered frame is shown in Fig. 7.5. It is clear that on the unregistered

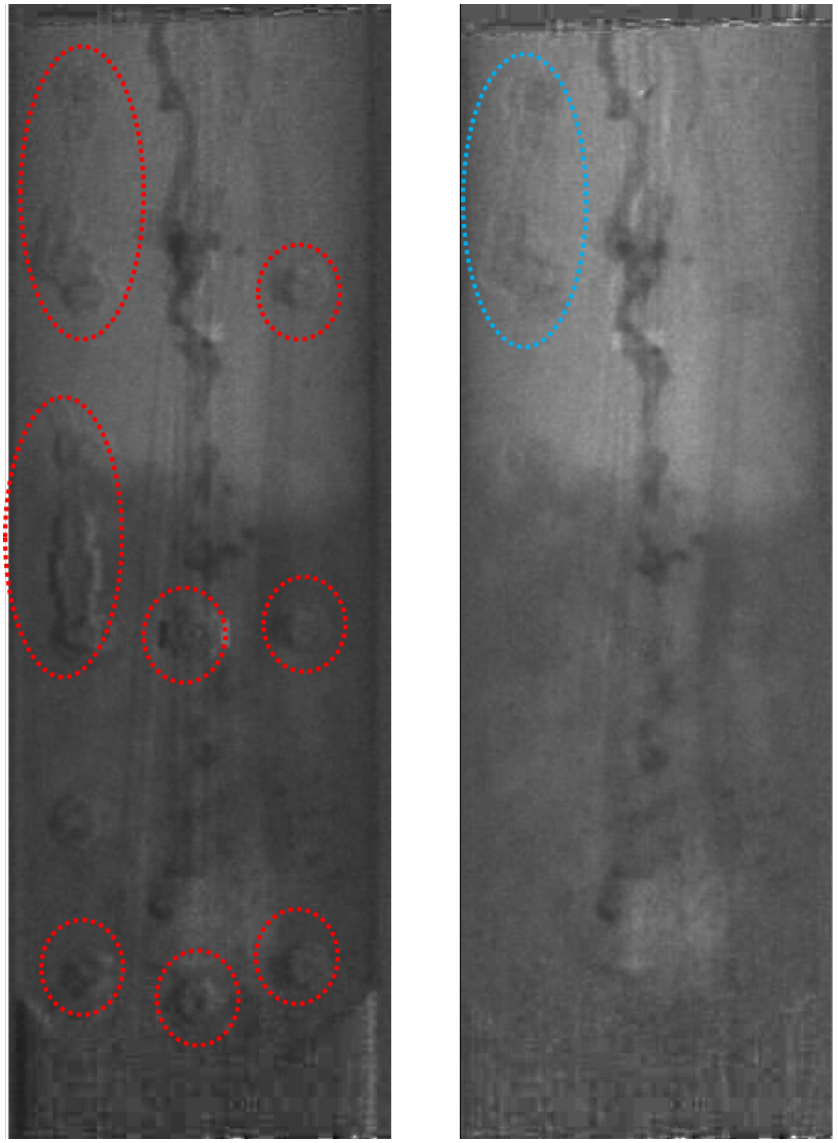

FIGURE 7.5: Example of background subtraction on (left): unregistered frame and (right): registered frame.

frame on the left, background removal is not efficient enough to remove the background instrumentation encircled in red. The grays in the red circles could be mistaken for corium by the code PICSEL in later stages of processing. It is very important to effectively remove the instrumentation to only keep the three phases of interest in the picture after processing, i.e. corium, water and steam as shown in the registered frame on the right. Only the

instrument region marked in blue is not efficiently removed. In the registered frame, we can clearly see that majorly three types of gray levels are present representing corium, water and steam. This demonstrates the importance of the image alignment in the first place, to efficiently remove the background from the frames.

7.2.4 Qualitative analysis

We focus now on decomposing the frames in order to extract corium and vapor fractions from the processed images.

- **Corium cloud detection:** The first step is to extract corium for which we make use of the edge detection technique as explained in the previous chapter. A result of the application of the Canny edge detection technique, mentioned in Chapter 6, on a premixing frame is illustrated in Fig 7.6. The image on the left is the processed image of a frame from the first premixing phase and the image on the right is the result of the application of the Canny edge detection on the processed frame. It is clear that the edge detection technique is able to extract the edges of the corium jet. However, the edge detection technique could not resolve the cloud of corium fragments. Improvements in this domain are thus necessary to visualize the corium cloud edges, as the Canny edge detection technique cannot successfully track the edges of the fine corium fragments. As mentioned before, detecting fine fragments as a cloud (instead of individual particles) posses a big challenge in the application of a variety of known image processing algorithms. However, as an initial approach, a superpixel segmentation technique as explained in [88] has been tried to implement in the PICSEL and is a subject of further improvement in PICSEL. This superpixel technique when implemented is expected to visualize clouds of corium particles.

- **Vapor detection:** The visualization of vapor formed during the corium-water interaction is carried out using the Otsu thresholding technique [89]. This technique automatically calculates an optimum threshold which would separate from the rest of the image. This technique was applied to the X-Ray image obtained during the first premixing stage and has been shown in Fig. 7.7. The image on the left is the pre-processed image and on the right is the image obtained using Otsu thresholding technique which is a binary image with white regions representing void and the black region representing corium and water.

  Otsu thresholding technique was also applied on data frames before and after the explosion. This has been shown in Fig. 7.8. On the left, is the thresholded image of premixing before the explosion. While the image on the right shows the image obtained by applying thresholding on a frame after the explosion,

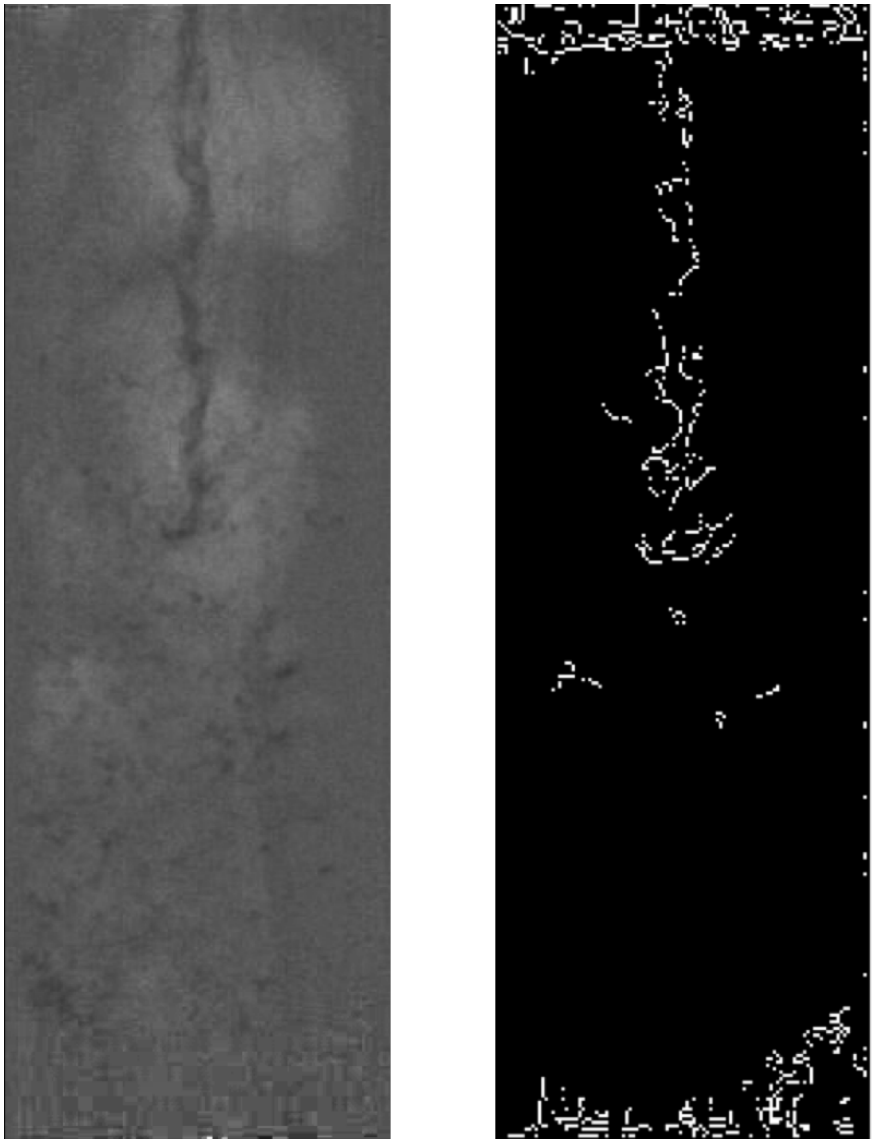

FIGURE 7.6: Application of the Canny edge detection to extract the corium jet outline. (left): Processed image of the first premixing stage; (right): Application of the Canny edge detection technique on the processed image.

depicting the second premixing phase. The image on the right shows void detected in the entire upper half indicating that after the explosion half of the sodium has been splashed out and the sodium level now remains half of the original height for the second part of the test.

Thus, all the techniques implemented in the PICSEL software were able to qualitatively characterize the three phases in the images successfully. In the next section, we will present a quantitative analysis of the images obtained from the test.

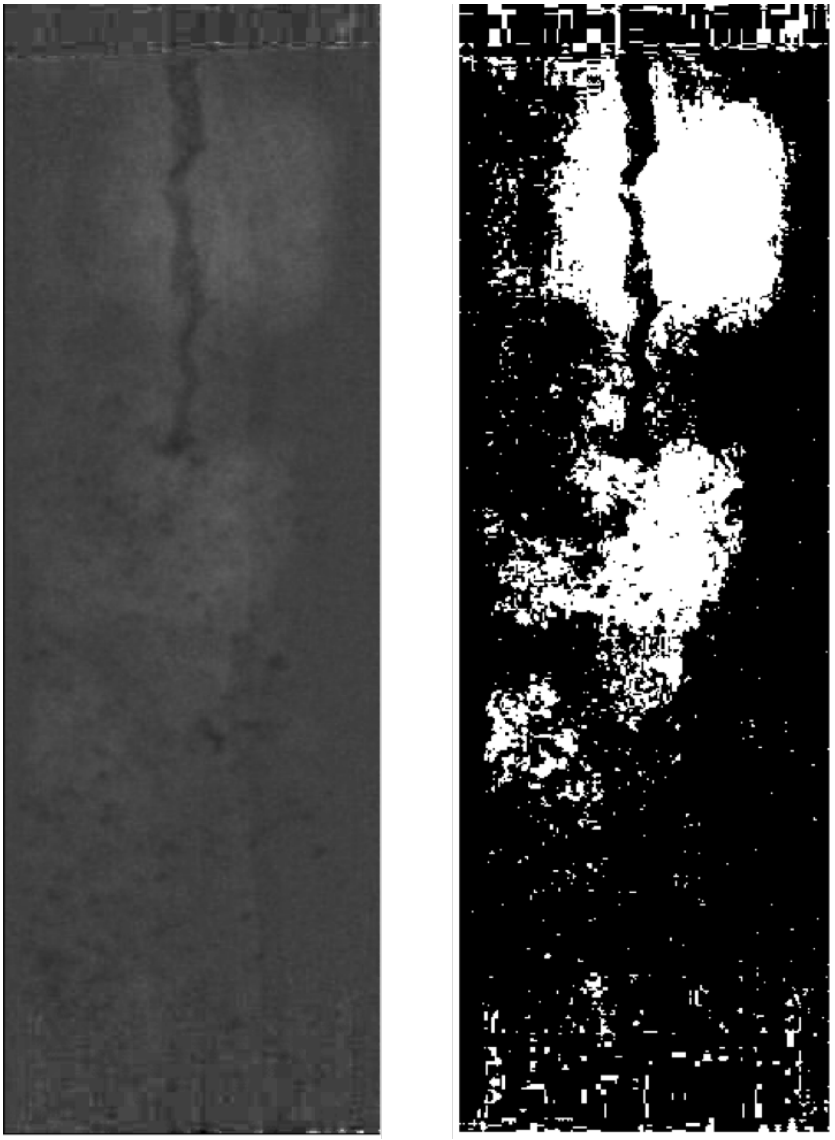

FIGURE 7.7: An example of the application of the Otsu thresholding technique to extract void fraction; (left): processed premixing image; (right): Thresholded image.

7.3. Quantitative analysis

The Particle Image Velocimetry (PIV) technique already introduced in Chapter 6 has been implemented in the PICSEL software to perform the quantitative analysis. The verification and validation of its capabilities to estimate the corium fragment velocities were carried out on the KROTOS-ALISA test.

The PIV algorithm could be best verified for its velocity estimation, at the point of entry of corium jet in the water pool. As stated in the article [45], corium is injected in the water pool from a free fall distance of 492 mm [45]. The instantaneous velocity of the corium jet front, at the point of entry, is thus estimated to be around 3.52 m/s. The application of PIV from the PICSEL software to estimate the motion of the corium jet front is shown in

FIGURE 7.8: Otsu thresholding application; (left): image from the first premixing before explosion; (right): second premixing image after explosion .

Fig. 7.9. The corium jet front to be detected in the first frame is shown in a black rectangle (top left of the figure), the sub-region where the corium jet is to be tracked in the subsequent frame is shown in black rectangle (top right). The normalized cross-correlation is thus calculated between the two regions and the maximum is shown marked in black rectangle (bottom left of Fig. 7.9. This indicates the best matching position of the corium jet front in the subsequent frame. The offset is thus calculated between the corium jet front in the first frame and its best matching position in the subsequent frame calculated in the previous step. The calculated offset of the corium jet front between the two frames and the time difference between them help to calculate the instantaneous velocity of the corium jet front. Thus, the PIV technique computes its instantaneous velocity to be 3.63 m/s. The estimated velocity from PIV is in agreement with the experimentally estimated velocity [45]. This is the first

qualification of the PIV algorithm for velocity calculation.

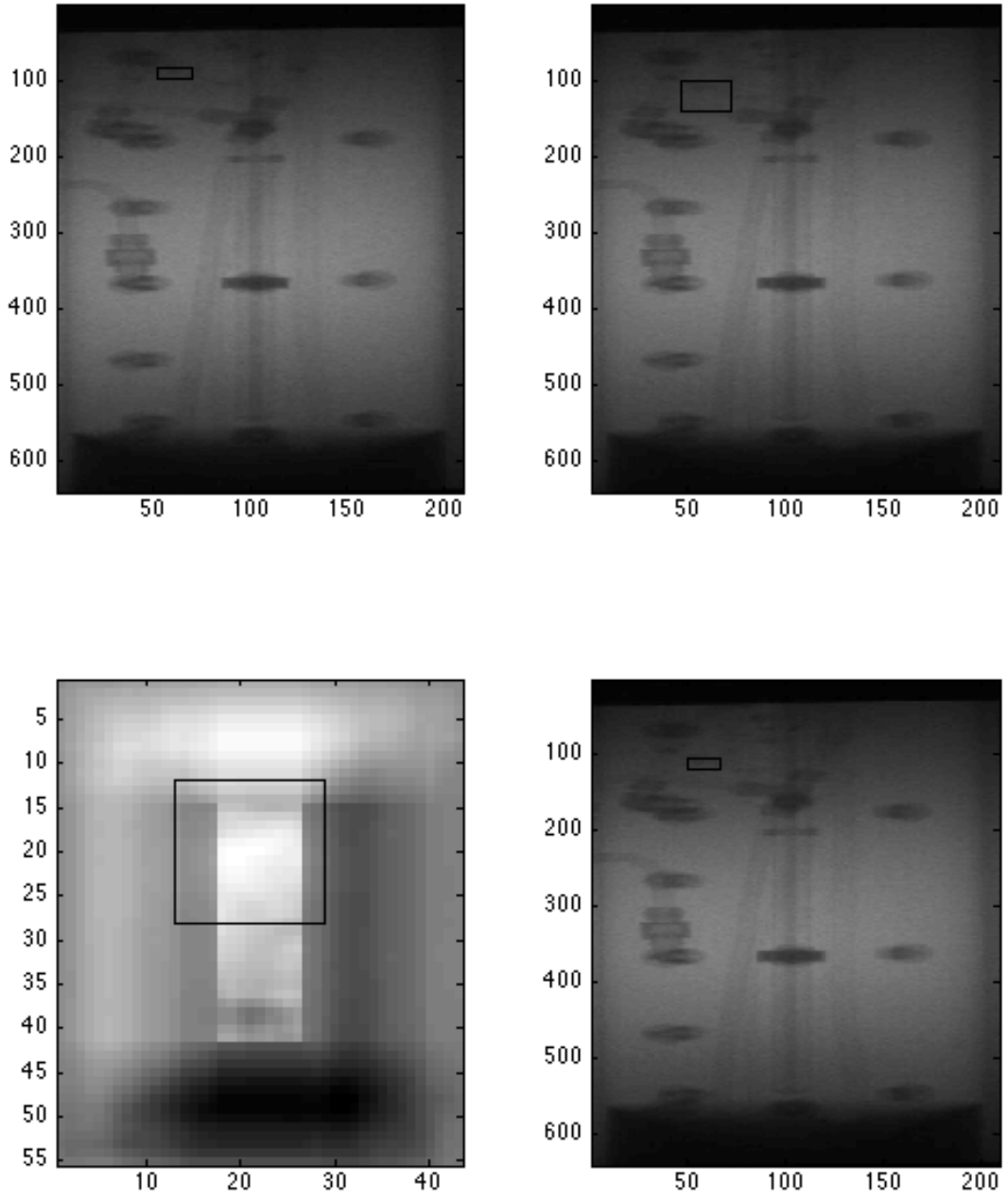

FIGURE 7.9: Tracking the motion of corium jet front. (top left): the block of corium jet front to be tracked; (top right): the region where the corium fragments needs to be tracked in the subsequent frame; (bottom left): normalized cross-correlation of the two regions; (bottom right): the tracked corium jet front in the subsequent frame.

In the later premixing phase, the instantaneous velocity reduces to around 3.2 m/s. It should be noted that the

velocity at any point of time is dependent on various governing factors, like the position of the cloud, the choice of the region of the cloud, and the fragmentation rate of the corium jet, and also the stage of the interaction (premixing/explosion). In the second premixing phase, when the pool depth was reduced due to the explosion, the velocity of the cloud from the corium jet was found to be 4.1 m/s. This was due to the lower water depth encountered by the falling jet and also because of the increase in the free fall distance.

It is foreseen to extend PICSEL to three dimensions, to provide the quantitative data like the corium and void volume fractions, necessary to the validation of a corium-sodium simulation software.

7.4. General remarks about the PICSEL software

In this chapter, the operationality of the PICSEL software was verified by its application on the KROTOS-ALISA test. The different techniques implemented in the PICSEL software including the background removal and the image alignment algorithm were applied on the frames of the X-Ray video to process the images. A cross-correlation technique was applied to align back the vibrating frames of the video and thus facilitating the background removal. Among the other techniques of the PICSEL software, the edge detection and the thresholding techniques were used to analyze the frames, qualitatively by extracting the different phases and then showing their estimated 2D extension. Edge detection was able to extract the corium outline and Otsu thresholding technique was able to binarize the image to locate the vapor phase. The PIV technique was also verified for the corium jet velocity evaluation by comparing its estimation with the experimental value at the point of corium jet injection into the water pool. The results obtained were in fair agreement with the literature stated value. This gave a first validation of the PIV technique implemented in the PICSEL software. To conclude, the whole process of video analysis using the PICSEL software produced promising results and provided a base for its extension to 3D.

Overall it can be concluded that PICSEL was able to successfully demonstrate its capabilities to process and analyze the three-phases molten fuel, liquid coolant and coolant vapor. Further validation is required on test with corium-sodium interaction to have confidence in its capabilities and its application to a broader scale.

Conclusions

The research developed in this Ph.D. is related to the safety of nuclear reactors, where a better understanding of the Fuel Coolant Interaction (FCI) phenomenology and its associated risks are necessary to establish mitigation and post-accident management strategies. However, FCI in Sodium-cooled Fast Reactors (SFRs) called corium-sodium interaction, lacks a good state of knowledge and remains to be studied. The primary objective of this thesis was to develop an experimental means with which the evolution of a corium-sodium interaction could be better visualized and thus studied. Due to the constraints related to experimental set-ups, one of the means of visualizing such an interaction is X-Ray radiography. Thus, the objective of this research is the development of an X-Ray radiography system for detecting and locating the three phases involved in a corium-sodium interaction. Such a system must include an image processing software to analyze and characterize the three phases of the mixture (corium, liquid sodium, and sodium vapor) in terms of location, spatial extension and volume fraction.

PLINIUS-2, the future large mass experimental platform of CEA Cadarache is under conception. Thus, conducting a real experiment between corium and sodium and testing an X-Ray imaging system for this platform was not possible at this time. Nevertheless, the existing corium-water facility of the CEA Cadarache called KROTOS could be used to carry out visualization experiments by simulating a three-phase mixture and thus propose an X-ray imaging system for the PLINIUS-2 facility.

The present work started with a bibliographic study to review the current state of knowledge on the phenomenology of the corium-sodium interaction. This was also compared with the phenomenology of corium-water

interaction. For corium-sodium interaction, past experiments had shown that molten material was always heavily fragmented but that some change in the phenomena occurred when sodium was close to saturation and that behaviors were more similar to corium-water interaction in terms of pressure rise time and energy release. Note that we cannot quantify "close". Subsequently, the existing experiments of interest involving prototypical materials were investigated in terms of shape and size of the corium particles formed in corium-sodium interaction. In almost all of the experiments, it was found that the particle size distribution follows a bimodal curve that we interpret as a sign of a two-step fragmentation process. Experimental prototypic corium being usually composed of uranium dioxide and/or stainless steel (SS), and the behavior of interaction varying with the levels of sub-cooling of sodium, the study of past experimental results to characterize the shape and size of corium particles has been split up into four categories: oxide fuel interaction with highly sub-cooled sodium and lightly sub-cooled sodium separately, and metallic component interaction with the highly sub-cooled and lightly sub-cooled sodium, respectively. Statistical analysis was carried out on the post-test debris bed particles. It was concluded from the analysis that most of the oxidic debris are observed to have angular fractured shapes with a median particle size relatively small in highly sub-cooled sodium (with a sub-cooling of $483°C$) ranging between 0.07 mm and 0.17 mm, in comparison to relatively bigger median particle size ranging between 0.09 mm and 0.69 mm in relatively warmer sodium (with a sub-cooling of $193°C$). While with metal melt, the size distribution seems to depend on the type of melt. U-Zr metal melt is observed to produce debris with a median particle size ranging between 3.04 mm to 14.76 mm whereas a SS melt is observed to produce smoother debris of median particle size ranging between 0.05 mm and 0.65 mm. The results from this statistical analysis are found to be in agreement with the qualitative observations reported in the literature.

Prior to conducting an experiment with particles of this size, it was necessary to verify the detectability of such fine corium fragments by an X-Ray imaging system with the help of simulations. These corium fragments are then modeled with the CEA in-house tool MODHERATO, a tool designed to simulate the whole X-Ray imaging system and produce the expected images. However, since individual corium particles are smaller than the detection limit of 5 mm of the system as estimated with MODHERATO for our X-Ray imaging system, it was chosen to detect clouds of particles instead of individual particles. These clouds of particles are represented as containing a given mass fractions of corium, liquid sodium and sodium vapor. A cloud of particles amassing 45 kg of corium (to simulate the mass range expected in the future experiments of PLINIUS-2-FR facility) is also simulated and the contrast to noise ratio is sufficient for the cloud to be visible. MODHERATO gave us better confidence in the ability of our X-Ray imaging system to detect the anticipated corium fragments.

With the help of bibliographic study and the MODHERATO simulations, 3D phantoms (mock-ups) representing the three-phase medium formed during corium-sodium interaction were designed and manufactured. Simulant materials were chosen for each of the three phases on the basis of their attenuation properties, thus mimicking their respective phase densities. Corium was simulated using steel, liquid sodium using polyethylene and sodium vapor by void. Three phantoms were designed to carry out the experiments: the premixing phantom, the vapor phantom and the dynamic phantom. The premixing phantom representing a premixing state of a corium-sodium interaction, the vapor phantom to simulate a vapor film around a coherent jet of corium, and dynamic phantom to model the relative motion between the clouds of corium particles. The experiments on the phantoms were simulated and designed in advance, using MODHERATO to evaluate the performance of the X-Ray imaging system taking into account the future, PLINIUS-2-FR facility geometry.

Experimental radiographies were then carried out on the phantoms to obtain images depicting the three phases formed in the interaction. Several configurations were tested in the existing KROTOS facility, by reproducing the PLINIUS-2-FR vessel thickness by adding steel plates. Premixing phantom, made of plastic and filled with steel balls which acts as corium fragments in liquid sodium, testifies that a dense cloud of sodium with a packing fraction of 53% could be visualized by radiography. A less dense cloud was mimicked with hafnia powder with a packing fraction of 23%, and was also visualized with radiography. The vapor phantom designed to test the detection of vapor film formed around the coherent jet of corium when injected in sodium is also radiographed.

To analyze these raw images, a new software was developed, capable of locating the phases in 2D images. This comprehensive image processing software called PICSEL was based on the MATLAB ver. R2015b with a built-in support for image processing operations, encapsulated in the Image Processing Toolbox. Several techniques including noise removal, background removal, enhancement and also qualitative analysis using the edge detection and image enhancement techniques, were incorporated in the PICSEL software. Our algorithm was also capable of tracking clouds of corium and estimate their velocities using a normalized cross-correlation technique based on the block matching algorithm. The interpretation of the experimental results using the PICSEL software confirmed the feasibility of monitoring corium-sodium interaction with the help of high energy X-ray imaging system. The corium particle cloud with particle volume fraction as low as 23% was found to have a satisfactory signal to noise ratio making it easily detectable. The vapor film was found to be detectable up to a thickness of the order of 1.7 mm, but very faint below 3.75 mm. Consequently, the software was deemed successful in qualitatively decomposing the image into its three phases corium cloud, void and sodium.

Finally, the PICSEL software was applied to the X-Ray images recorded during the Euro-Chinese experiment

'ALISA' in the KROTOS facility and the results obtained are very promising. The cloud tracking technique was tested on the vibrating frames of the video and was used to align back the frames and thus to stabilize the video. Techniques like background removal, edge detection and thresholding were then verified to be successful too. The Particle Image Velocimetry algorithm to estimate the instantaneous velocity of clouds was also tested on the KROTOS-ALISA test. This algorithm was verified for its velocity evaluation at the point of entry of the corium jet front in water. It was found to be in agreement with the experimental velocity. The 2D image processing software PICSEL developed to visualize the three-phase flow in corium-sodium interaction was thus able to process the images and to extract corium clouds and void separately.

In summary, the PICSEL software is able to perform a 2D X-Ray video processing and analysis of an experiment conducted between corium and sodium. However, the work remains incomplete, in view of improving the code for corium cloud detection using better techniques. For instance, a technique of superpixel segmentation which would group the pixels together into superpixels based on the edge detection and thereafter threshold the image to extract the clouds with varying densities. An implementation of this technique could produce significant cloud segmentation. Indeed, PICSEL also needs to be extended to 3D processing, before being fully operational and useful to the calculation codes. A PICSEL-3D tool will be beneficial to CEA and the nuclear community for analyzing images from an upcoming experiment to obtain quantitative estimations of the three-phase volume fractions. PICSEL-3D. In particular, PICSEL will be useful in the longer term for processing the images of the tests conducted in the forthcoming PLINIUS-2 facility.

Future work and perspectives

Thesis has been conducted in two steps, the experimental part where experiments with phantoms have been conducted at the KROTOS facility whereas on the other side the 2D image processing software PICSEL has been developed. Both the steps could not be dealt completely and work needs to be done in both the domains. As a result of this, a brief perspective is presented to extend the work carried out in the Ph.D. to improve the understanding of corium-sodium interaction.

Experimental development

The experimental approach adopted in this thesis by performing experiments with the phantoms had its own limitations. The calibration tests with the phantoms could be improved with the help of full cylindrical phantoms representing entirely sodium. Also, experiments by mixing the steel balls with plastic balls (beads like) representing vapor phase, to address the issue of visualizing clouds of different densities are of interest to us and could be performed in the near future. In addition to that, a study of unequal packing fractions in a cloud region, could be a more realistic scenario and thus needs to be studied by performing experiments with the phantoms having varying packing fractions. Experiments with the dynamic phantom designed in the framework of this Ph.D. representing a dynamic state of interaction, could not be carried out due to limited research time-frame. This test, when carried out, would extend the idea of cloud, to a more realistic dynamic moving cloud and thus will facilitate the improvement of the calibration of PICSEL.

Besides the representative tests mentioned above, it is deemed necessary to conduct more FCI experiments with oxide fuel and sodium, as well as with stainless steel and sodium. More importantly, assisting these tests with an X-Ray imaging system are required to be conducted so as to have improved experimental knowledge about corium-sodium interaction. For example, very recently, experiments have been performed in collaboration with JAEA (Japan) at their test facility called MELT with aluminium melt (a simulant of stainless steel) and sodium. The interaction is also filmed with an X-Ray imaging system. This test when thoroughly analyzed, will allow us to simultaneously visualize the interaction and have better insights about the interaction phenomenology and qualitative three-phase distribution. More experiments like these would help us to have a better understanding of the interaction mechanism and would improve the knowledge that will have to be implemented into the SCONE.

Software development

CEA is developing a software called SCONE for the numerical modeling of corium-sodium interaction. The future works proposed above like conducting more experiments and analyzing the experiments with PICSEL, extended to 3D will give us more quantitative data for the development of SCONE. When fully mature, SCONE software will be able to precisely simulate the interaction mechanism between corium and sodium before conducting an actual experiment. This would thus help in designing future experiments with confidence in the extrapolation of the simulations to reactor FCI scenarios.

Significant work has been done in the development of software PICSEL, which vows to analyze the radiographic images obtained from corium-sodium interaction. However, this code still needs improvements in many fields. The first step would be to implement the super pixel segmentation technique for detecting clouds of corium particles more precisely. Once the 2D qualitative analysis is completed, its extension to 3D analysis to obtain quantitative data such as the three-phase volume fractions. As of now, the PICSEL tool has been only partly validated with KROTOS-ALISA. A kind of validation, after extending PICSEL to 3D would also be required. If possible, the experiment at the Japanese facility MELT, can be used to validate PICSEL. As at the time of writing, PLINIUS-2 platform is only at the design stage, time is still available to improve this image processing tool in order to achieve good operability when PLINIUS-2 first FCI experiments are carried out in order to provide useful data for the development of SCONE modeling code.

References

[1] F. Bertrand et al. “Status of severe accident studies at the end of the conceptual design of ASTRID: Feedback on mitigation features”. In: *Nuclear Engineering and Design* 326 (Jan. 2018), pp. 55–64. ISSN: 0029-5493. DOI: 10.1016/j.nucengdes.2017.10.019 (cit. on p. 2).

[2] J. Papin. “Behavior of fast reactor fuel during transient and accident conditions”. In: *Elsevier Ltd.* (2012) (cit. on p. 3).

[3] *Council Directive 2014/87/Euratom of 8 July 2014 amending Directive 2009/71/Euratom establishing a Community framework for the nuclear safety of nuclear installations*. en. July 2014 (cit. on p. 3).

[4] M. Zabiégo and C. Fochesato. “The SCONE software for corium-sodium interaction”. In: *26th International Conference Nuclear Energy for New Europe*. Bled, Slovenia, Sept. 2017 (cit. on p. 5).

[5] G. Berthoud, H. Jacobs, and B. Knowles. *Large scale fuel-sodium inetarctions: synthesis of european programs*. English. Fast Reactor Coordinating Committee/ Safety Working Group, WAC(94)-D375). 1994 (cit. on pp. 6, 8, 9, 11, 12, 22).

[6] M. L. Corradini, B. J. Kim, and M. D. Oh. “Vapor explosions in light water reactors: A review of theory and modeling”. In: *Progress in Nuclear Energy* 22.1 (Jan. 1988), pp. 1–117. ISSN: 0149-1970. DOI: 10.1016/0149-1970(88)90004-2 (cit. on pp. 6, 7, 60).

[7] L. Caldarola. “Current Status of Knowledge of Molten Fuel/Sodium Thermal Interactions”. de. In: (1974) (cit. on p. 6).

[8] M. J. Bird, P. Naylor, and R. B. Tattersall. “Experimental studies of thermal interactions between thermite generated molten fuel and sodium”. en. In: *Proceedings of the L.M.F.B.R. safety topical meeting* (1982) (cit. on p. 6).

[9] G. Berthoud. “Vapor Explosions”. In: *Annual Review of Fluid Mechanics* 32.1 (2000), pp. 573–611. DOI: 10.1146/annurev.fluid.32.1.573 (cit. on p. 7).

[10] M. Zabiégo and C. Fochesato. “Corium-sodium interaction: the development of the SCONE software”. In: *17th International Topical Meeting on Nuclear Reactor Thermal Hydraulics (NURETH 17)*. Xi’an, China, 2017 (cit. on pp. 8, 9, 15, 58).

[11] P. Piluso. *Status Report on Ex-Vessel Steam Explosion (EVSE)*. Tech. rep. NEA/CSNI/R(2017)15. OECD/CSNI, 2017, p. 25 (cit. on pp. 9, 37).

[12] A. Le Belguet. “Etude de l’ébullition en film du sodium autour d’une sphère à haute température”. PhD thesis. France: Thèse de l’Université de Grenoble, 2013 (cit. on p. 9).

[13] G. Berthoud, A. Le Belguet, and M. Zabiégo. “The Farahat sodium natural convection film boiling experiment revisited”. In: *Experimental Thermal and Fluid Science* 91 (Feb. 2018), pp. 117–125. ISSN: 0894-1777. DOI: 10.1016/j.expthermflusci.2017.10.015 (cit. on pp. 9, 15).

[14] R. Meignen, S. Picchi, J. Lamome, B. Raverdy, S. Castrillon Escobar, and G. Ortega Nicaise. “The challenge of modeling fuel–coolant interaction: Part I – Premixing”. In: *Nuclear Engineering and Design* 280 (2014), pp. 511–527. DOI: 10.1016/j.nucengdes.2014.08.029 (cit. on p. 9).

[15] R. Meignen, B. Raverdy, S. Picchi, and J. Lamome. “The challenge of modeling fuel–coolant interaction: Part II – Steam explosion”. In: *Nuclear Engineering and Design* 280 (2014), pp. 528–541. DOI: 10.1016/j.nucengdes.2014.08.028 (cit. on p. 9).

[16] L. DOP. *An Experimental Study of Scaling in Molten Fuel and Sodium Interactions,(SUS Series Final Report)*. Tech. rep. AEEW-R2325-June. 1988 (cit. on p. 11).

[17] D. Magallon, H. Hohmann, and H. Schins. “Pouring of 100-kg-Scale Molten UO2 into Sodium”. In: *Nuclear Technology* 98.1 (Apr. 1992), pp. 79–90. ISSN: 0029-5450. DOI: 10.13182/NT92-A34652 (cit. on pp. 11, 20, 21, 49, 55, 56, 63).

[18] F. Huber, A. Kaiser, and D. Wilhelm. “Results on the behavior of thermie melt injected into sodium”. In: *14th Meeting of the Liquid Metal Boiling Working Group*. ENEA Brasimone, Italy, Apr. 1991 (cit. on pp. 11, 21).

[19] H. Schins and F. S. Gunnerson. “Boiling and fragmentation behaviour during fuel-sodium interactions”. In: *Nuclear Engineering and Design* 91.3 (Feb. 1986), pp. 221–235. ISSN: 0029-5493. DOI: 10.1016/0029-5493(86)90077-4 (cit. on pp. 11, 23, 47, 52, 54, 57, 58).

[20] V Bouyer, N Cassiaut-Louis, P Fouquart, and P Piluso. “Plinius Prototypic Corium Experimental Platform”. en. In: (2015), p. 14 (cit. on pp. 12, 36).

[21] C. Journeau et al. “Corium-Sodium and Corium-Water Fuel-Coolant-Interaction Experimental Programs for the PLINIUS2 Prototypic Corium Platform”. In: *Nuclear Technology* 205.1-2 (Jan. 2019), pp. 239–247. ISSN: 0029-5450. DOI: 10.1080/00295450.2018.1479580 (cit. on pp. 13, 14, 39, 41).

[22] F. Bertrand, N. Marie, G. Prulhière, J. Lecerf, and J. M. Seiler. “Comparison of the behaviour of two core designs for ASTRID in case of severe accidents”. In: *Nuclear Engineering and Design* 297 (Feb. 2016), pp. 327–342. ISSN: 0029-5493. DOI: 10.1016/j.nucengdes.2015.04.020 (cit. on p. 15).

[23] K.-I. Matsuba, M. Isozaki, K. Kamiyama, and Y. Tobita. “Distance for fragmentation of a simulated molten-core material discharged into a sodium pool”. In: *Journal of Nuclear Science and Technology* 53.5 (May 2016), pp. 707–712. ISSN: 0022-3131. DOI: 10.1080/00223131.2015.1113897 (cit. on pp. 15, 27, 28, 49).

[24] I Huhtiniemi, D Magallon, and H Hohmann. “Results of recent KROTOS FCI tests: alumina versus corium melts”. In: *Nuclear Engineering and Design* 189.1 (May 1999), pp. 379–389. ISSN: 0029-5493. DOI: 10.1016/S0029-5493(98)00269-6 (cit. on pp. 22, 26, 49).

[25] H. Holtbecker, H. Schins, E. Jorzik, and K. Klein. *Sodium-fuel interaction: dropping experiments and subassembly test*. en. Tech. rep. EUR–5854. Commission of the European Communities, 1978 (cit. on pp. 24, 51, 52, 54).

[26] T. Y. Chu, A. G. Beattie, W. D. Drotning, and D. A. Powers. *Medium-scale melt-sodium fragmentation experiments*. en. Tech. rep. SAND–79-0126C. Sandia Labs., 1979 (cit. on pp. 24, 53, 55).

[27] S. K. Das et al. “Post-accident heat removal: Numerical and experimental simulation”. In: *Nuclear Engineering and Design* 265 (Dec. 2013), pp. 1246–1254. ISSN: 0029-5493. DOI: 10.1016/j.nucengdes.2013.09.032 (cit. on p. 25).

[28] A. K. Acharya, A. K. Sharma, C. S.S. S. Avinash, S. K. Das, L. Gnanadhas, B. K. Nashine, and P. Selvaraj. “Investigation of molten fuel coolant interaction phenomena using real time X-ray imaging of simulated woods metal-water system”. In: *Nuclear Engineering and Technology* 49.7 (Oct. 2017), pp. 1442–1450. ISSN: 1738-5733. DOI: 10.1016/j.net.2017.07.003 (cit. on pp. 26, 118, 139).

[29] S. T. Tukhvatulin. “National Nuclear Center of the Republic of Kazakhstan”. English. In: (2001) (cit. on p. 26).

[30] K.-i. Matsuba, K. Kamiyama, J.-i. Toyooka, Y. Tobita, V. A. Zuyev, A. A. Kolodeshnikov, and Y. S. Vassiliev. “Experimental discussion on fragmentation mechanism of molten oxide discharged into a sodium pool”. en. In: *Mechanical Engineering Journal* 3.3 (2016), pp. 15–00595–15–00595. ISSN: 2187-9745. DOI: 10.1299/mej.15-00595 (cit. on pp. 26, 49).

[31] Y. Zagorulko, V. G. Zmurin, A. Volov, Y. Kovaliov, and K. Matveev. “Energy transformation in the processes of thermal interaction between corium and sodium”. In: *11th Meeting of the International Association for Hydraulic research (IAHR) Working Group)*. Russia, July 2004 (cit. on p. 27).

[32] K.-i. Matsuba, M. Isozaki, K. Kamiyama, Y. Tobita, and T. Suzuki. “Fundamental experiment on the distance for fragmentation of molten core material during core disruptive accidents in sodium-cooled fast reactors”. English. In: *International Electronic Journal of Nuclear Safety and Simulation* 4.4 (2014), pp. 272–277. ISSN: ISSN 2185-0577 (cit. on p. 27).

[33] R. C. Hansson, T. N. Dinh, and L. T. Manickam. “A study of the effect of binary oxide materials in a single droplet vapor explosion”. In: *Nuclear Engineering and Design*. SI:NURETH-14 264 (Nov. 2013), pp. 168–175. ISSN: 0029-5493. DOI: 10.1016/j.nucengdes.2013.02.017 (cit. on pp. 27–29).

[34] L. Manickam, S. Bechta, and W. Ma. “On the fragmentation characteristics of melt jets quenched in water”. In: *International Journal of Multiphase Flow* 91 (May 2017), pp. 262–275. ISSN: 0301-9322. DOI: 10.1016/j.ijmultiphaseflow.2017.02.005 (cit. on pp. 28, 30, 50).

[35] V. Tyrpekl, P. Piluso, S. Bakardjieva, and O. Dugne. “Material Effect in the Nuclear Fuel–Coolant Interaction: Analyses of Prototypic Melt Fragmentation and Solidification in the KROTOS Facility”. In: *Nuclear Technology* 186.2 (May 2014), pp. 229–240. ISSN: 0029-5450. DOI: 10.13182/NT13-63 (cit. on pp. 30, 50).

[36] S.-W. Hong, P. Piluso, and M. Leskovar. “Status of the OECD-SERENA Project for the Resolution of Ex-vessel Steam Explosion Risks”. en. In: (), p. 10 (cit. on pp. 30, 37).

[37] C. Brayer, P Piluso, N. Cassiaut-Louis, and D. Grishchenko. “Application of X-Ray radioscopy for investigations of the 3-phase-mixture resulting from the fragmentation of a high temperature molten material jet in water”. In: *8th International Conference on Multiphase Flow*. Jeju, Korea, May 2013 (cit. on pp. 31, 32, 35, 37–40, 72).

[38] M. Zabiego, C. Brayer, D. Grishchenko, J. Dajon, P. Fouquart, Y. Bullado, F. Compagnon, C. Patricia, J. Haquet, and P. Piluso. “The KROTOS KFC and SERENA/KS1 tests: experimental results and MC3D calculations”. en. In: *ResearchGate* () (cit. on p. 32).

[39] G. F. Knoll. *Radiation Detection and Measurement, 4th Edition*. en-us (cit. on pp. 32, 33).

[40] N. Estre, D. Eck, J. Pettier, E. Payan, C. Roure, and E. Simon. “High-energy X-ray imaging applied to non destructive characterization of large nuclear waste drums”. In: *2013 3rd International Conference on Advancements in Nuclear Instrumentation, Measurement Methods and their Applications (ANIMMA)*. June 2013, pp. 1–6. DOI: 10.1109/ANIMMA.2013.6727987 (cit. on pp. 36, 97).

[41] *Gadolinium oxysulfide*. en. Page Version ID: 792380097. July 2017 (cit. on p. 36).

[42] L. Berge et al. “Fast High-Energy X-Ray Imaging for Severe Accidents Experiments on the Future PLINIUS-2 Platform”. In: *IEEE Transactions on Nuclear Science* 65.9 (Sept. 2018), pp. 2573–2581. ISSN: 0018-9499. DOI: 10.1109/TNS.2018.2847460 (cit. on pp. 36, 42, 69–72).

[43] *(2) (PDF) Integrating cross-correlation and relaxation algorithms for particle tracking velocimetry*. en (cit. on p. 36).

[44] *Zyla 5.5 sCMOS - Andor*. en (cit. on p. 36).

[45] N. Cassiaut-Louis, C. Brayer, N. Chikhi, P. Fouquart, P. Piluso, C. G. Journeau, W. Zhou, and Y. Liao. “Experiments linked to Fuel Coolant Interaction within the Euro-Chinese Project ALISA”. In: Sept. 2017 (cit. on pp. 37, 150, 158, 159, 195, 196).

[46] D. Grishchenko. “X-ray measurements of the premixing phase: Analysis with KIWI software.” In: *Proc. OECD/NEA SERENA Seminar. 2012* (cit. on pp. 38, 78, 118, 140).

[47] S. Saito, Y. Abe, and K. Koyama. “Flow transition criteria of a liquid jet into a liquid pool”. In: *Nuclear Engineering and Design* 315 (2017), pp. 128 –143. ISSN: 0029-5493. DOI: https://doi.org/10.1016/j.nucengdes.2017.02.011 (cit. on p. 49).

[48] T. Y. Chu. *Fragmentation of molten core material by sodium*. en. Tech. rep. SAND–82-0300C. Sandia National Labs., 1982 (cit. on pp. 49, 51, 53, 55, 58, 62, 63).

[49] T. R. Johnson, J. R. Pavlik, and L. J. Baker. *Postaccident Heat Removal: Large-Scale Molten-Fuel-Sodium Interaction Experiments*. English. Tech. rep. ANL–75-12. Argonne National Lab., Argonne, IL (United States), Feb. 1975. DOI: 10.2172/4228270 (cit. on pp. 50, 51).

[50] D. Armstrong, F. Testa, and D. J. Raridon. *Interaction of sodium with molten UO2 and stainless steel using dropping mode of contact*. Tech. rep. Report ANL-7890. 1971 (cit. on p. 50).

[51] R. Henry. *Large scale vapor explosions*. Tech. rep. CONF-740401 - P2. Baverly Hills, Apr. 1974 (cit. on pp. 50–52).

[52] T. R. Johnson, L. J. Baker, and J. R. Pavlik. “Large-scale molten fuel–sodium interaction experiments”. en. In: (1974) (cit. on pp. 51, 53).

[53] J. D. Gabor, R. T. Purviance, R. W. Aeschlimann, and B. W. Spencer. “Breakup and quench of molten metal fuel in sodium”. In: *Proceedings of the ANS "Safety of next generation power reactors" meeting*. Seattle, USA: Argonne National Lab., 1988 (cit. on pp. 56, 57, 64).

[54] R. C. Asher. *The injection of liquid sodium into stainless steel: a report of further experiments NaSS/4, NaSS/5, NaSS/6*. Tech. rep. Bournemouth UK, Apr. 1979 (cit. on p. 57).

[55] S. Singh, N. Cassiaut-Louis, C. Journeau, M. Zabiégo, N. Estre, and L. Tamagno. “Modelling of X-Ray Radioscopy for Phase Topology Estimation During Corium Sodium Interaction”. In: American Society of Mechanical Engineers, July 2018, V009T16A084–V009T16A084. DOI: 10.1115/ICONE26-82400 (cit. on pp. 59, 63–66).

[56] C. C. Chu, J. J. Sienicki, B. W. Spencer, W. Frid, and G. Löwenhielm. “Ex-vessel melt-coolant interactions in deep water pool: studies and accident management for Swedish BWRs”. In: *Nuclear Engineering and Design* 155.1 (Apr. 1995), pp. 159–213. ISSN: 0029-5493. DOI: 10.1016/0029-5493(94)00874-X (cit. on p. 59).

[57] G. Pohlner, Z. Vujic, M. Bürger, and G. Lohnert. “Simulation of melt jet breakup and debris bed formation in water pools with IKEJET/IKEMIX”. In: *Nuclear Engineering and Design*. Festschrift Edition Celebrating the 70th Birthday of Prof. Bal Raj Sehgal: Invited papers on - Core melt accidents in LWRs State of the art of "COOLABILITY OF POROUS DEBRIS" 236.19 (Oct. 2006), pp. 2026–2048. ISSN: 0029-5493. DOI: 10.1016/j.nucengdes.2006.03.037 (cit. on p. 60).

[58] J Namiech, G Berthoud, and N Coutris. “Fragmentation of a molten corium jet falling into water”. In: *Nuclear Engineering and Design* 229.2 (Apr. 2004), pp. 265–287. ISSN: 0029-5493. DOI: 10.1016/j.nucengdes.2004.01.004 (cit. on p. 60).

[59] E. De Malmazet. “Etude de la fragmentation de gouttes chaudes en ébullition en film dans un écoulement d’eau”. PhD thesis. Thèse de l’Institut Polytechnique de Grenoble, France, 2009 (cit. on p. 60).

[60] A. W. Cronenberg, T. C. Chawla, and H. K. Fauske. “A thermal stress mechanism for the fragmentation of molten UO2 upon contact with sodium coolant”. In: *Nuclear Engineering and Design* 30.3 (Sept. 1974), pp. 434–443. ISSN: 0029-5493. DOI: 10.1016/0029-5493(74)90228-3 (cit. on p. 61).

[61] G. Berthoud and W. H. Newman. “A description of a fuel-coolant thermal interaction model with application in the interpretation of experimental results”. In: *Nuclear Engineering and Design* 82.2 (Oct. 1984), pp. 381–391. ISSN: 0029-5493. DOI: 10.1016/0029-5493(84)90223-1 (cit. on p. 61).

[62] M. Pilch and C. A. Erdman. “Use of breakup time data and velocity history data to predict the maximum size of stable fragments for acceleration-induced breakup of a liquid drop”. In: *International Journal of Multiphase Flow* 13.6 (Nov. 1987), pp. 741–757. ISSN: 0301-9322. DOI: 10.1016/0301-9322(87)90063-2 (cit. on p. 61).

[63] L. P. Hsiang and G. M. Faeth. “Drop deformation and breakup due to shock wave and steady disturbances”. In: *International Journal of Multiphase Flow* 21.4 (Aug. 1995), pp. 545–560. ISSN: 0301-9322. DOI: 10.1016/0301-9322(94)00095-2 (cit. on p. 62).

[64] T. Benaglia, D. Chauveau, D. R. Hunter, and D. Young. “**mixtools** : An *R* Package for Analyzing Finite Mixture Models”. en. In: *Journal of Statistical Software* 32.6 (2009). ISSN: 1548-7660. DOI: 10.18637/jss.v032.i06 (cit. on pp. 62, 181).

[65] M. Welvaert and Y. Rosseel. “On the Definition of Signal-To-Noise Ratio and Contrast-To-Noise Ratio for fMRI Data”. en. In: *PLOS ONE* 8.11 (Nov. 2013), e77089. ISSN: 1932-6203. DOI: 10.1371/journal.pone.0077089 (cit. on p. 73).

[66] C. A. Schneider, W. S. Rasband, and K. W. Eliceiri. “NIH Image to ImageJ: 25 years of image analysis”. In: *Nature Methods* 9 (June 2012), p. 671 (cit. on p. 75).

[67] J. K. Fink and L. Leibowitz. *Thermodynamic and transport properties of sodium liquid and vapor*. English. Tech. rep. ANL/RE-95/2. Argonne National Lab., IL (United States), Jan. 1994. DOI: 10.2172/94649 (cit. on p. 78).

[68] R. C. Hansson, H. S. Park, and T.-N. Dinh. “Simultaneous high speed digital cinematographic and X-ray radiographic imaging of a intense multi-fluid interaction with rapid phase changes”. In: *Experimental Thermal and Fluid Science* 33.4 (Apr. 2009), pp. 754–763. ISSN: 0894-1777. DOI: 10.1016/j.expthermflusci.2009.01.011 (cit. on p. 118).

[69] R. C. Hansson, H. S. Park, and T.-N. Dinh. “Dynamics and Preconditioning in a Single-Droplet Vapor Explosion”. In: *Nuclear Technology* 167.1 (July 2009), pp. 223–234. ISSN: 0029-5450. DOI: 10.13182/NT09-A8864 (cit. on pp. 118, 139).

[70] Y. Narushima, Y. Abe, A. Kaneko, T. Kanagawa, and H. Yoshida. “Development of Numerical Simulation for Jet Break Up Behavior in Complicated Structure of BWR Lower Plenum (7) Measurement of Fragment

Diameter by Image Processing Technique". In: (June 2016), V005T15A045. DOI: 10.1115/ICONE24-60623 (cit. on pp. 118, 139).

[71] O. Marques. *Practical Image and Video Processing Using MATLAB®: Marques/Practical Image Processing*. en. Hoboken, NJ, USA: John Wiley & Sons, Inc., Sept. 2011. ISBN: 978-1-118-09346-7 978-0-470-04815-3. DOI: 10.1002/9781118093467 (cit. on pp. 119–121, 145).

[72] R. C. Gonzalez, R. E. Woods, and S. L. Eddins. *Digital Image Processing Using MATLAB, 2nd ed.* en. Vol. Vol. 624. Pearson-Prentice-Hall Upper Saddle River, 2004 (cit. on pp. 119, 121, 141).

[73] P. Geladi and H. F. Grahn. "Multivariate Image Analysis". en. In: *Encyclopedia of Analytical Chemistry*. American Cancer Society, Sept. 2006. ISBN: 978-0-470-02731-8. DOI: 10.1002/9780470027318.a8106 (cit. on pp. 119, 121).

[74] *MATLAB version 8.5.0.197613 (R2015b)*. Natick, Massachusetts: The Mathworks, Inc., 2015 (cit. on p. 121).

[75] J. Larsson. "X-Ray Deyector Characterization- a comparison of scintillators". Master of Science Thesis. Stockolm, Sweden 2013: KTH – Royal Institute of Technology, June 2013 (cit. on pp. 125, 134).

[76] R. Lindken and W. Merzkirch. "A novel PIV technique for measurements in multiphase flows and its application to two-phase bubbly flows". en. In: *Experiments in Fluids* 33.6 (Dec. 2002), pp. 814–825. ISSN: 1432-1114. DOI: 10.1007/s00348-002-0500-1 (cit. on p. 139).

[77] S. N and V. S. "Image Segmentation By Using Thresholding Techniques For Medical Images". en. In: *Computer Science & Engineering: An International Journal* 6.1 (Feb. 2016), pp. 1–13. ISSN: 2231329X, 22313583. DOI: 10.5121/cseij.2016.6101 (cit. on p. 144).

[78] *SLR Magic25mm T0.95 HyperPrime Cine III Lens (MFT Mount)* (cit. on p. 145).

[79] J. Kaur, S. Agrawal, and R. Vig. "A Comparative Analysis of Thresholding and Edge Detection Segmentation Techniques". en. In: *International Journal of Computer Applications* 39.15 (Feb. 2012), pp. 29–34. ISSN: 09758887. DOI: 10.5120/4898-7432 (cit. on p. 145).

[80] K. Jambunathan, X. Y. Ju, B. N. Dobbins, and S. Ashforth-Frost. "An improved cross correlation technique for particle image velocimetry". en. In: *Measurement Science and Technology* 6.5 (May 1995), pp. 507–514. ISSN: 0957-0233. DOI: 10.1088/0957-0233/6/5/012 (cit. on p. 146).

[81] *CS425 Lab: Image Processing Toolbox and Histograms* (cit. on p. 146).

[82] D. Dabiri. "Cross-Correlation Digital Particle Image Velocimetry – A Review". en. In: (), p. 54 (cit. on p. 146).

[83] W. Wenguo, F. Weicheng, L. Guangxuan, and Q. Jun. "An improved cross-correlation method for (digital) particle image velocimetry". en. In: *Acta Mechanica Sinica* 17.4 (Nov. 2001), pp. 332–339. ISSN: 0567-7718, 1614-3116. DOI: 10.1007/BF02487460 (cit. on p. 146).

[84] K. Zakšek, M. Hort, J. Zaletelj, and B. Langmann. "Monitoring volcanic ash cloud top height through simultaneous retrieval of optical data from polar orbiting and geostationary satellites". English. In: *Atmospheric Chemistry and Physics* 13.5 (Mar. 2013), pp. 2589–2606. ISSN: 1680-7316. DOI: https://doi.org/10.5194/acp-13-2589-2013 (cit. on p. 147).

[85] J. P. Lewis. "Fast Normalized Cross-Correlation". en. In: (), p. 7 (cit. on p. 146).

[86] A. Miassoedov, N. Cassiaut-Louis, Y. Liao, and P. Chen. "ALISA Project: Access to Large Infrastructures for severe accidents in Europe and China". In: *Proc. NUTHOS-12, 12th International Tropical Meeting on Nuclear Thermal Hydraulics, Operation, Safety*. Oct. 2018 (cit. on p. 150).

[87] G. Puglisi and S. Battiato. "A Robust Image Alignment Algorithm for Video Stabilization Purposes". en. In: *IEEE Transactions on Circuits and Systems for Video Technology* 21.10 (), pp. 1390–1400. ISSN: 1051-8215 (cit. on p. 152).

[88] K. Jeya, C. Vinola, and D. Joy Winnie Wise. "Superpixel segmentation based automatic cloud detection". In: *International Journal of Advances in Engineering Research* 11.I (Jan. 2016) (cit. on p. 156).

[89] N. Otsu. "A Threshold Selection Method from Gray-Level Histograms". In: *2EEE TRANSACTIONS ON SYSTREMS, MAN, AND CYBERNETICS,* SMC-9.No. 1 (Jan. 1979) (cit. on p. 156).

Publications and oral presentations

Publications:

1. **S. Singh**, N. Cassiaut-Louis, C. Journeau, M. Zabiego, N. Estre, L. Tamagno, "Review of the three phase distribution of corium-sodium interaction and modelling of X-ray radiosocopy system of the future PLINIUS-2-FR facility", **Journal of Nuclear Engineering and Radiation Science, 2019 (In progress).**

2. Berge, L., Estre, N., Tisseur, D., Payan, E., Eck, D., Bouyer, V., Cassiaut-Louis, N. , Journeau, C. , Le Tellier, R. , **Singh, S.** and Pluyette, E., "Fast high-energy X-ray imaging for Severe Accidents experiments on the future PLINIUS-2 platform", **IEEE Transactions on Nuclear Science, 65(9), 2573-2581 (2018)**

3. C. Journeau, L. Aufore, L. Berge, C. Brayer, N. Cassiaut-Louis, N. Estre, F. Payot, P. Piluso, J. Prele, **S. Singh**, M. Zabiego, E. Pluyette, F. Serre, B. Teisseire, "“ Corium-Sodium and Corium-Water Fuel-Coolant-Interaction Experimental Programs for the PLINIUS2 Prototypic Corium Platform", **Nuclear Technology 205.1-2 (2019): 239-247, January 2, 2019**

4. **S. Singh**, N. Cassiaut-Louis, C. Journeau, M. Zabiego, N. Estre, L. Tamagno, "Modelling of X-ray Radioscopy for Phase Topology Estimation during Corium Sodium Interaction", **26th International Conference on Nuclear Engineering, 2018, London, England.**

5. C. Journeau, L. Aufore, L. Berge, C. Brayer, N. Cassiaut-Louis, N. Estre, F. Payot, P. Piluso, J. Prele, **S. Singh**, and M. Zabiego, “Corium-Sodium and Corium-Water fuel-coolant-interaction experimental programs for the PLINIUS2 prototypic corium platform”, **17th International Topical Meeting on Nuclear Reactor Thermal Hydraulics (NURETH 17), Sept. 3-8, 2017, Xi’an, China.**

Oral presentations:

1. Oral presentation at the Café thesard, les Rendez vous scientifiques et techniques du DTN, CEA Cadarache France (2018).
2. Oral presentation at the 26th International Conference on Nuclear Engineering, 2018, London, England (2018).
3. Oral presentation at “Journée Scientifique”, CEA Cadarache, France (2016 and 2017).
4. Oral presentation at the “Journées des Ecole Doctoral”, University of Paris-Saclay, France (2016 and 2017).
5. Oral presentation at the CEA-JAEA Face-to-Face meeting F2F Meeting, CEA Cadarache, France (2017).
6. Poster presentation at the SAFEST workshop, KTH Stockholm, Sweden (2016).
7. Oral presentation at the CEA Cadarache-IGCAR Annual Meeting (Indo-French collaboration), CEA Cadarache, France (2016).

Appendix A

Code to carry out statistical analysis of the particle size distribution data

Following is the code written in R, that calculates the parameters of the fitting functions of the bimodal distribution. This code is written in the R language using the mixtools package [64]. The mixtools package contains a fitting function that fits a bimodal distribution to the given.

```
setwd("/path_to_the_working_directory")
# Import mixtools and ggplot2 package
library(mixtools)
library(ggplot2)

#############################################################################
############################## Input data set ###############################
# Choose a particular data set to perform the bimodal
#                                          operation by uncommenting it

# FRAG SERIES particle size data
#bin=c(20,100,200,500,800,1000,1200,1800,2200,2800)
#Particle <- c(runif(4,20,45),runif(9,45,120),
#              runif(15,120,140), runif(15,240,450),
#              runif(15,450,600),runif(10,600,900),
#              runif(10,900,1400), runif(8,1400,2800))
```

```
17
18 # FARO TERMOS particle size data
19 #bin=c(10,50,100,150,200,250,300,350,400,500)
20 #Particle <- c(runif(3.5,10,38),runif(8.5,38,50),
21 #               runif(45,50,100), runif(33,100,200),
22 #               runif(6,200,300), runif(2.8,300,500))
23
24 # ANL T6 particle size data
25 #bin=c(100,1000,5000,10000,15000,20000,50000)
26 #Particle <- c(runif(10,100,5000),runif(49,1000,15000),
27 #               runif(23.6,10000,20000), runif(17,15000,50000))
28
29 # BETULLA particle size data
30 bin=c(20,62,105,149,250,500,1000,2000)
31 Particle <- c(runif(7,20,62), runif(2,62,105),
32               runif(2,105,149), runif(6.5,149,250),
33                  runif(12.5,250,500), runif(17.5,500,1000),
34                  runif(21.5,1000,2000))
35 ##########################################################################
36
37 # Presently analyzing the BETULLA particle size data
38
39 # Taking log of the particle size
40 l_particle=log(Particle)
41
42 # Using mixmdl tool available in the mixtools package
43 mixmdl<- normalmixEM(l_particle,k=2)
44
45 plot_mix_comps <- function(x, mu, sigma, lam) {
46   lam * dnorm(x, mu, sigma)
47 }
48 plot_add <- function(x, mu_1, sigma_1,mu_2,sigma_2,lam_1,lam_2)
49             {(lam_1*dnorm(x, mu_1, sigma_1))+(lam_2*dnorm(x, mu_2, sigma_2))}
50
51
52 data.frame(x = mixmdl$x) %>%
53   ggplot() +
54   geom_histogram(aes(x, ..density..), binwidth =0.8, colour = "black",
55                  fill = "azure") +
56   stat_function(geom = "line", fun = plot_mix_comps,
57                 args = list(mixmdl$mu[1], mixmdl$sigma[1],
58                 lam = mixmdl$lambda[1]),
59                 colour = "red", lwd = 1.0,aes(colour = "Small particle")) +
60   stat_function(geom = "line", fun = plot_mix_comps,
61                 args = list(mixmdl$mu[2], mixmdl$sigma[2],
62                 lam = mixmdl$lambda[2]),
63                 colour = "blue", lwd = 1.0,aes(colour = "Big particle")) +
64   stat_function(geom = "line", fun = plot_add,
65                 args = list(mixmdl$mu[1], mixmdl$sigma[1],mixmdl$mu[2],
66                        mixmdl$sigma[2],mixmdl$lambda[1],mixmdl$lambda[2]),
67                 colour = "black", lwd = 1.0,lty=2)+theme_bw()+
```

```
68    scale_colour_manual(values = c("red", "blue"))+
69    xlab("ln (Particle size)")+ylab("Density")+
70    theme(panel.background = element_blank(),
71          axis.text=element_text(size=10),
72          axis.title=element_text(size=10,face="bold"),
73          panel.grid.minor = element_blank(),
74          panel.grid.major = element_blank(),
75          legend.position="top")
76
77 # Print the Bimodal fitting parameter to the output file
78 out<-capture.output(summary(mixmdl))
79 cat(out,file="betula_param.dat",sep="\n",append=TRUE)
```

./matlab_code/bimodal_fit_code_thesis.R.

1.2

Appendix B

Experimental procedure of the tests with the designed phantoms

This appendix presents the detailed procedure of the tests carried out at the KROTOS facility with the designed phantoms.

B.1. Procedure for the X-Ray radiography on the phantoms

Below will be discussed the procedure followed to perform radiography on phantoms. First, radiography is performed on premixing phantom filled with steel balls. The same premixing phantom geometry is then used with hafnia powder. Then radiography is performed on vapor phantom.

Initial setup

1. The configuration (source-scintillator-camera) parameters were recorded. It was assured that they were equal to what was planned for the tests for the:
    - Geometric set-up: with the focal distances FO: 227 cm and FD: 314 cm
    - X-Ray source setting with a firing frequency of 50 Hz with a $4\mu s$ pulse time

- Camera settings, integration time etc.

2. The scintillator detector screen was mounted in line with the X-Ray source.

3. The images formed on the rear side of the scintillator screen was filmed with a camera.

4. The camera and the X-Ray source firing sequence were synchronized in such a way that there is no time lag between the firing trigger and the camera integration trigger.

5. Certain important features of the phantom may be obscure due to the image noise. So, an obscurity acquisition using the chosen settings (ex. the camera integration time) for each configuration S0, S1, S2 and S3 without any phantom was taken. These images were acquired in sequence acquisition mode in great numbers, for instance 100 in our case. These images will be averaged to obtain the final obscure image.

Acquisition using Phantom-1 filled with steel balls

Empty phantom

6. Phantom-1, a cylindrical plastic column with cylindrical hollow concentric rings of different depths, each separated by plastic sheet, and having steel rod fixed in its innermost ring, was suspended with the help of a hook in the KROTOS test section. A view from the top of the test section is shown in Fig. B.1. The position of the phantoms was fixed to be in the center of the X-Ray beam. The distance from the position where the phantom was suspended to the test section was measured and used for further acquisitions (place a mark to make it easy to find the same position in subsequent acquisitions).

FIGURE B.1: Empty premixing phantom inserted in the KROTOS test section.

7. First acquisition was carried out without any shielding i.e. in the S0 configuration and setting an integration time of 4 ms, 100 images were captured.

8. Radiography was then carried out in the S1 configuration, by placing the first steel plate of thickness 4 cm in front of the KROTOS test facility in the center of the X-Ray beam. The integration time needed to be increased to 60 ms as fixed for the S1 configuration, 100 images were captured for this configuration as well.

9. Similarly acquisition was made in the S2 configuration by placing the second steel plate behind the first. The camera's integration time was increased to 225 ms as fixed in step 7 for S2 configuration. In each of the configurations and the ones to come 100 images were captured.

10. Finally, the S3 configuration was filmed, where the third plate was placed behind the two plates from the S1 and S2 configuration. Setting up the camera integration time to 756 ms, 100 images of camera were captured for this configuration too.

11. The phantom is taken out of the KROTOS test section.

First ring filled with steel balls

12. The phantom innermost first ring is filled with the 4 mm steel balls up to the rim of the plastic separation.

13. The phantom is again suspended like before in the KROTOS test section for radiography acquisition. A photograph is captured from the top as shown in Fig B.2. Care was taken to keep the position of the phantom identical to that in step 8.

FIGURE B.2: Premixing phantom with its first ring filled with steel balls.

14. The high image quality observed in the four shielding configurations using the empty phantom, enabled the number of preparatory experiments to be reduced. Thus, 100 images were captured for only S0, S2 and S3 configuration in this series.

    First and second ring filled with steel balls

15. The phantom was again removed from the KROTOS test section and its second ring was also filled with the steel balls.

16. It was suspended back again and shown in Fig. B.3 and acquisitions were made in the S0 and S3 configuration setting the corresponding camera integration time (100 images).

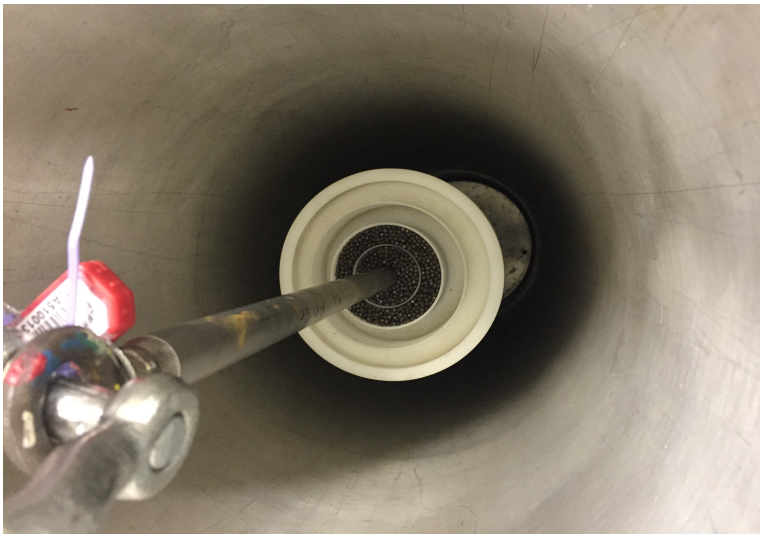

FIGURE B.3: Premixing phantom with its first and second ring filled with steel balls.

First 3 rings filled with steel balls

17. Subsequently, the three innermost rings of the phantom were filled and is shown in Fig. B.4 and acquisitions were made straight away in S3 configuration with its corresponding integration time (100 images).

    All 4 rings filled with steel balls

18. In this case all four rings of the phantom were filled with steel balls as shown in Fig. B.5 and the four configurations S0, S1, S2, S3 were tested and filmed using their corresponding integration time. Once again, 100 images were captured.

Image acquisition for Premixing phantom filled with hafnia powder

Empty phantom

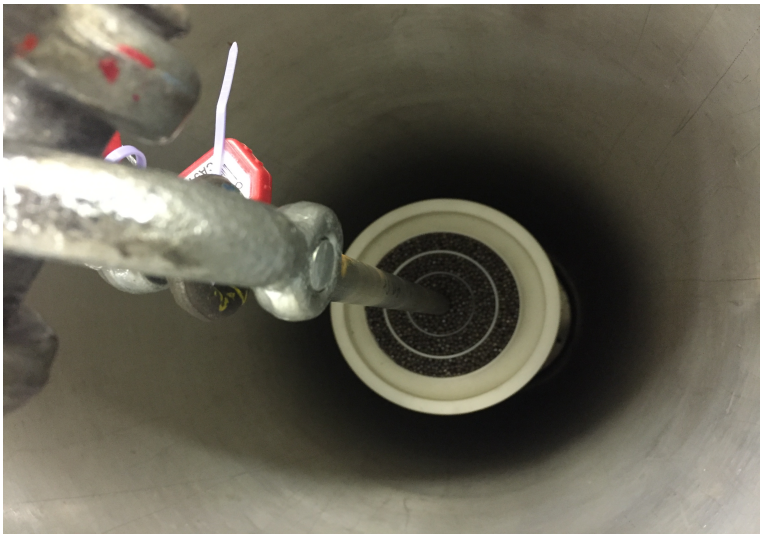

FIGURE B.4: Premixing phantom with its first 3 rings filled with steel balls.

FIGURE B.5: Premixing phantom with its all 4 rings filled with steel balls.

19. Just as for the tests using the steel balls, tests were initially carried out with an empty phantom.
20. The positioning of the phantom was maintained the same.
21. 100 images in the S0, S1, S2 and S3 configuration were made each with their respective integration time.

    First innermost ring filled with hafnia powder

22. In this series of experiments, the plastic phantom used is the same as before but instead of the steel balls, very fine Hafnia (HfO_2) powder was used.
23. Care was taken while putting the phantom back in the test section. Its position should be the same in all the configurations. Fig. B.6 shows the phantom from the top.

FIGURE B.6: Premixing phantom with its first ring filled with hafnia powder.

24. 100 images were captured in all four configurations S0, S1, S2 and S3.

    First and second innermost rings filled with hafnia powder

25. The next radiography was performed on the phantom with two innermost rings filled with hafnia powder shown in Fig. B.7.

FIGURE B.7: Premixing phantom with its first and second ring filled with hafnia powder.

26. Three configurations S0, S1 and S3 were tested.

    3 innermost rings filled with hafnia powder

27. In this series, hafnia powder was filled in the third ring of the phantom as shown in Fig. B.8 and radiography was performed in all the four configurations.

FIGURE B.8: Premixing phantom with its first three rings filled with hafnia powder.

All 4 rings filled with hafnia powder

28. Finally, the outermost ring was also filled with hafnia powder. Radiography was performed with all four configurations S0, S1, S2 and S3.

FIGURE B.9: Premixing phantom with its all 4 rings filled with hafnia powder.

With Steel rod alone

29. In this series, the steel rod alone without any plastic phantom was visualized as shown in Fig. B.10. The position of the rod was kept the same as in the above series.

30. Images of X-Ray were acquired on the steel rod without any steel plate and with the three steel plates introduced one by one in between the source and the phantom.

FIGURE B.10: Steel rod without any phantom.

Acquisition with vapor phantom (air gap around rod)

With steel rod

31. Phantom-2 is a plastic cylindrical phantom made from four columns of the plastic placed one over the other, with a steel rod passing through its center and progressively varying gap between the steel rod and the plastic column. It was kept in the center of the test section over a fixed barrel. The top view of the phantom is shown in Fig B.11.

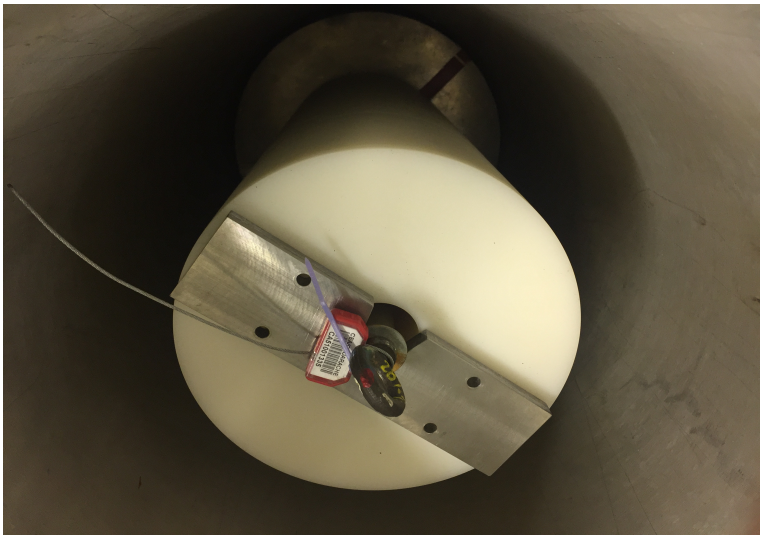

FIGURE B.11: vapor phantom with steel rod inserted.

32. The long height of $50\,\mathrm{cm}$ of the phantom does not permit the steel plates to cover the entire length in the radiography images. In fact, it just covers the lowermost three columns of the plastic. So, only a limited

view of the X-Ray radiography could be performed.

33. In this series, it was filmed in all four configurations S0, S1, S2 and S3 with 100 images in each configuration.

    Without steel rod

34. The steel rod was removed for this series of radiography, keeping the position of the phantom same as before. This is shown in Fig. B.12

FIGURE B.12: vapor phantom without steel rod.

35. This was the last acquisition and it was taken for all four configurations using their respective set camera integration time (100 images each).

36. After finishing all the acquisitions, the phantom and the barrel over which it was placed were removed from the test section.

37. The image files were collected in their raw format to carry out its image processing and analysis.

Appendix C

KROTOS-ALISA test

For completeness, and to support Chapter 7, a detailed experimental procedure of the KROTOS-ALISA test is presented, following reference [45].

C.1. KROTOS-ALISA test

The ALISA project aims at providing mutual access of large research infrastructures in the domain of severe accidents, to the European Union and the Chinese partners [45]. Within this framework, a Fuel-Coolant Interaction test was proposed by the Chinese partners to be performed at the KROTOS facility of CEA Cadarache, with a shallow water depth (645 mm) as shown in the setup of the ALISA experiment Fig. C.1. The aim of conducting such a test with a low water height (compared to other tests performed in KROTOS where the water depth is usually set to 1145 mm) was to study the effect of this reduced water pool depth on the corium-water interaction.

In this test, 5150 g of a prototypic corium mixture (80 wt% UO_2- 20 wt% ZrO_2) was heated up, melted and released into a water pool whose temperature was 60°C. When the corium jet reached a certain length, an external trigger was initiated to cause a steam explosion. This explosion splashed out almost 50% of the volume of water. The pressure induced by the explosion momentarily stopped the corium from entering the test section,

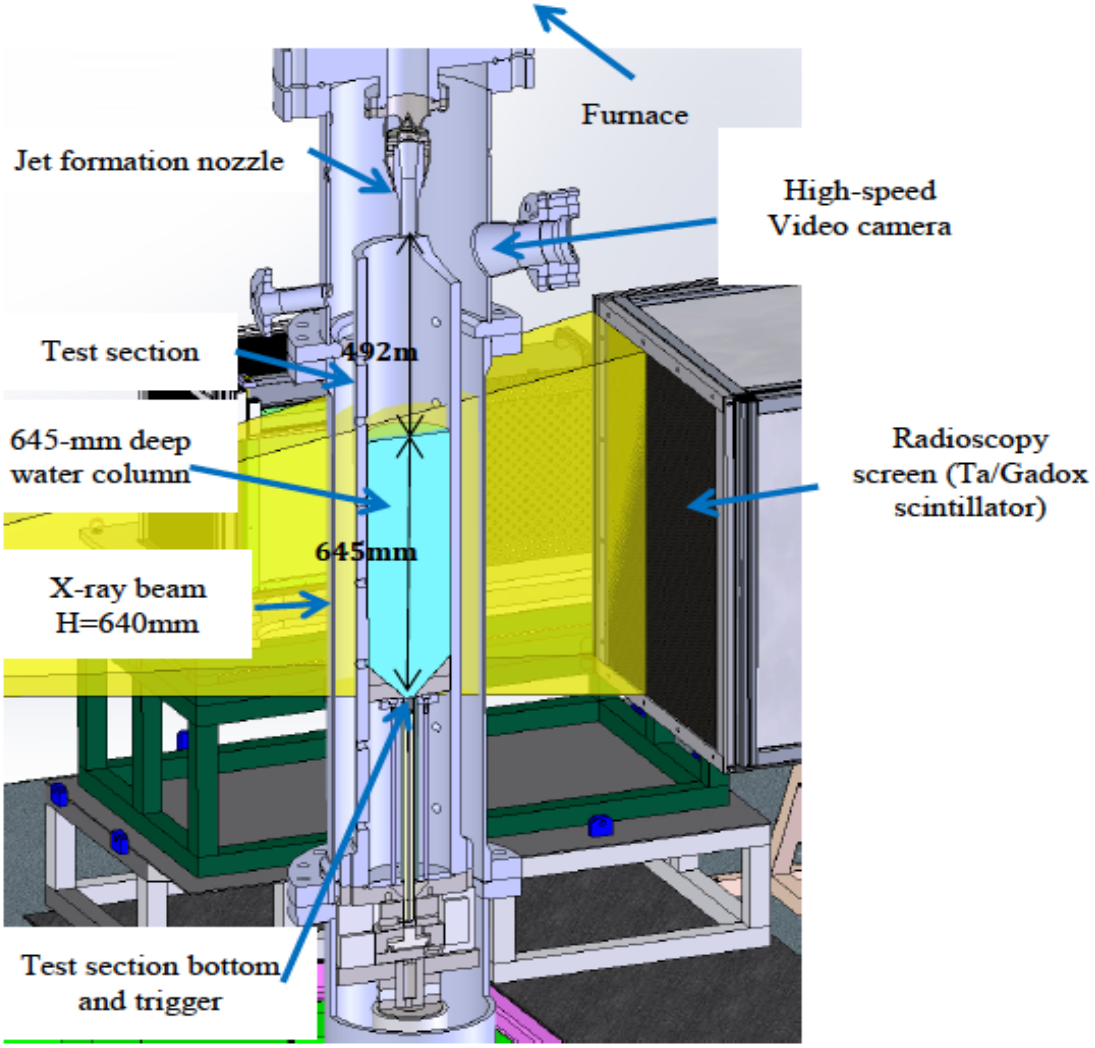

FIGURE C.1: ALISA experimental setup [45].

but the corium jet resumed later. The second time corium entered the pool, it faced only a smaller amount of water, thus reached the bottom of the test section without being totally fragmented. No spontaneous explosion occurred during this phase [45].

C.2. Reason behind using KROTOS-ALISA test for the validation of PICSEL

The entire phenomenon was believed to be occurring in three stages, a pre-mixing phase, an explosion phase and a second premixing phase with no explosion. An illustration of the phenomenon using the X-Ray images acquired, have been given in Fig. C.2. The background observed in all of the figures, includes various instrumentation devices of the test section like the thermocouples, pressure sensors, screws, etc. As it can be seen in Fig. C.2(a), the dark continuous jet of corium enters the pool of water from the top. In the Fig. C.2(b) one of the X-ray

images showing the first premixing phase is presented. The corium jet dissociates and fragments into corium particulates with a certain brighter vapor fraction visible in the image. This constitutes a premixing frame. Figure C.2(c) depicts the steam explosion phase, with two big vapor bubbles being generated and propagated from the bottom to the top. Due to the explosion, a significant amount of liquid water is splashed out of the test section. Figure C.2(d) shows the second premixing phase where the water pool depth has been reduced by more than 50 %. In this phase, clouds of corium particles generated by the explosion are observed to be formed and slowly translated towards the botttom.

Thus, in the second premixing phase, a presence of a flowing jet and clouds of corium particles was observed. This could be due to the fact that, the very fine fragments formed from the first explosion generate the kind of clouds expected in corium-sodium interaction. The KROTOS-ALISA experiment, though being a corium-water interaction test, exhibited a second premixing phase with particle clouds translating towards the bottom which may be similar to corium-sodium interaction.

After conducting the KROTOS-ALISA test the corium fragments (debris) were collected at the test section bottom. Debris of various sizes were found that can be categorized in three different size ranges: submillimeter range (fine debris of sub-millimeter range, medium-size (between millimeter and centimeter range) and large size debris of the order above 10 mm. An interesting phenomenon that was observed was that the debris found in the space between the test tube and test vessel. Here, fine sub-millimetric and larger millimetric debris were found. In addition, submillimetric size particles were also found in the debris bed. These fine fragments have been believed to undergo explosion and represent clouds of particles in the second premixing phase. However, this effect is still to be verified since our information were too preliminary to draw a precise conclusion.

For the above mentioned reasons, the X-Ray acquisition obtained after the second pre-mixing phase was decided to be processed using the software PICSEL for its preliminary validation.

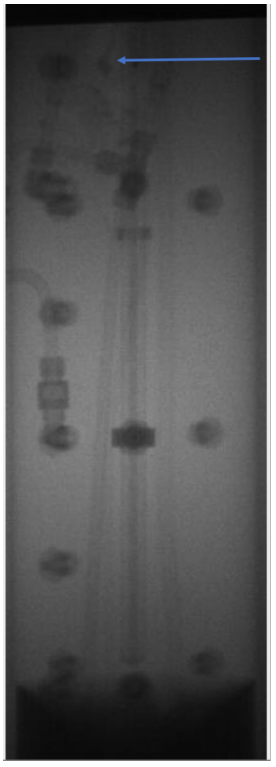

(a) **Corium jet entering water.**

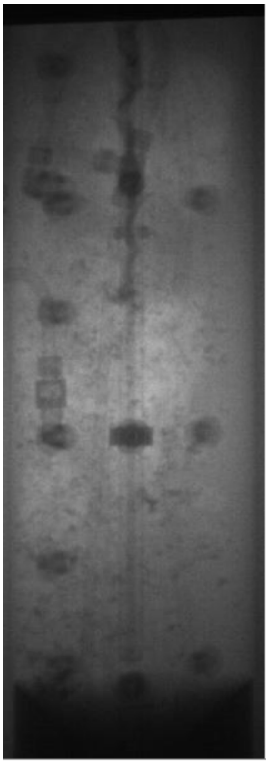

(b) **Premixing phase.**

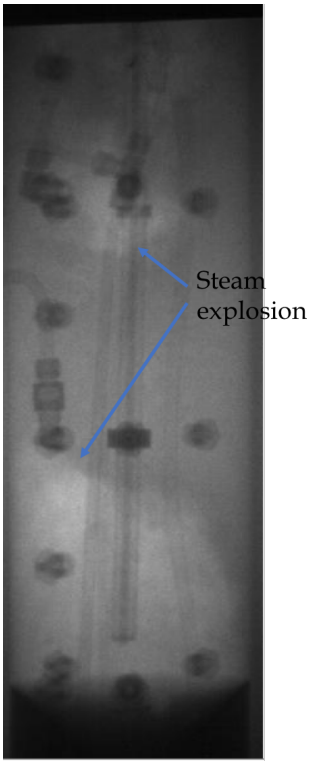

(c) **Explosion phase.**

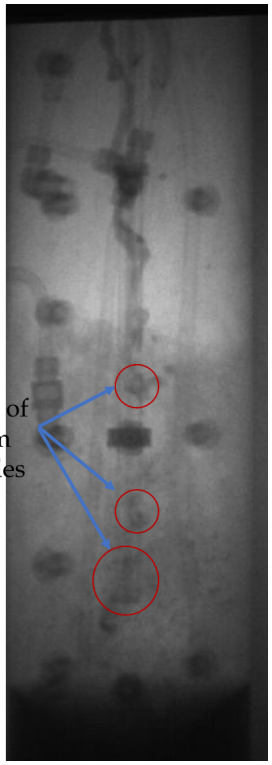

(d) **Second Pre-mixing.**

FIGURE C.2: X-Ray images of different phases of the ALISA test.

Appendix D

Résumé

Dans les réacteurs à neutrons rapides refroidis au sodium (RNR-Na), une défaillance dans le système de refroidissement du coeur ou de protection du réacteur peut conduire à un accident grave. Dans un tel scenario, les matériaux du coeur (combustible et acier) fondent pour former un mélange appelé corium susceptible d'interagir avec le réfrigérant (sodium). Une telle interaction (Fuel Coolant Interaction, FCI) peut générer des évènements énergétiques aptes à mettre en danger les structures du réacteur. La violence de l'explosion dépend essentiellement de l'état du mélange corium-sodium. Connaître les caractéristiques des trois phases en présence dans la zone d'interaction (corium, sodium liquide, vapeur de sodium) est donc crucial.

En raison de lacunes dans les connaissances de la physique de l'interaction, le CEA s'intéresse à la FCI d'un point de vue de la modélisation mais aussi d'un point de vue expérimental en concevant de nouveaux programmes. Pour la modélisation de la fragmentation du corium et des transferts de chaleur entre corium et sodium, le CEA s'est engagé dans le développement du logiciel SCONE, capable de décrire les écoulements 3D, multiphasiques et multiconstituants. Pour les aspects expérimentaux, la plateforme PLINIUS-2 est en cours de conception au CEA, l'objectif étant de réaliser des essais où interviennent des masses importantes de corium prototypique et du sodium dont la plage de température initiale pourra varier de la température moyenne de fonctionnement d'un RNR-Na ($\sim$ 400K) à la saturation. De plus, des essais à petite échelle sont aussi en cours de définition afin de comprendre les phénomènes fondamentaux tels que l'ébullition en film du sodium autour d'un fragment chaud

ou bien la fragmentation thermique et hydrodynamique de gouttes de corium dans du sodium. Les connaissances de base ainsi acquises sur l'interaction corium-sodium permettront de combler certaines des lacunes identifiées et seront capitalisées dans le logiciel SCONE. Les résultats des expériences à plus grande échelle permettrons une validation plus globale du logiciel avec, entre autres, la vérification que les modèles implémentés représentent correctement la physique de l'interaction.

Le présent travail se situe dans le cadre de la conception de la plateforme PLINIUS-2 et son objectif est de développer, pour cette installation, un système d'imagerie basée sur des radiographies X afin de visualiser et de mieux comprendre l'interaction corium-sodium. Un algorithme de post-traitement de ces images a aussi été écrit afin de les analyser, d'en déduire la répartition des trois phases dans le système et de contribuer ainsi à l'amélioration de la modélisation numérique.

Ce travail de thèse a été conduit en trois étapes. La première était consacrée à une étude bibliographique des expériences passées d'interaction corium-sodium dont la phénoménologie a été comparée à celle de l'interaction corium-eau. Une interaction corium-eau est en général décomposée en quatre étapes, la première étant l'étape de prémélange. Lorsque le corium (liquide dense, chaud, T $\sim$ 3000K) entre en contact avec l'eau (liquide plus volatile et plus froid, T $\sim$ 330K), il se fractionne en fragments assez grossiers dont la taille est comprise entre quelques millimètres et le centimètre. Les échanges de chaleur entre corium et eau conduisent à la vaporisation de l'eau et à la formation, autour des particules de corium, d'un film stable de vapeur. L'échelle de temps de l'étape de prémélange est de l'ordre de quelques secondes. Lors de l'étape suivante (déclenchement), un évènement extérieur ou, dans le cas expérimental, l'application d'un pulse de pression (trigger), provoque la déstabilisation des films de vapeur et la mise en contact brutale des gouttes de corium liquide avec l'eau liquide. Ces contacts liquide-liquide entraînent une fragmentation fine du corium, une augmentation soudaine de la surface d'échange entre les deux corps, une vaporisation intense de l'eau et la formation d'une onde de pression qui se propage dans le milieu et entraîne, de proche en proche, la déstabilisation des films de vapeur. C'est l'étape de propagation. Tout cela contribue à la mise en mouvement relatif des différentes phases en présence ce qui accroît le phénomène de fragmentation hydrodynamique des particules de corium. Le processus dans son ensemble conduit à la formation d'une "bulle de vapeur" dont la détente, souvent dénommée explosion, va impacter les structures environnantes voire menacer l'intégrité du réacteur.

Du fait des propriétés thermiques du sodium peu comparables à celles de l'eau, la phénoménologie de l'interaction corium-sodium et celle de l'interaction corium-eau comportent certaines différences. En effet, si en interaction corium-eau on peut clairement distinguer prémélange et explosion, la littérature montre que ce n'est plus tout à

fait le cas en interaction corium-sodium, surtout si le sodium est sous-refroidi. Les différentes étapes existent toujours mais les échelles de temps sont beaucoup plus courtes et l'étape de prémélange peut être extrêmement rapide. De plus, même si un film de vapeur de sodium se forme autour des fragments de corium, ce film est, par nature, beaucoup plus instable et se déstabilise spontanément comme l'ont montré les programmes expérimentaux passés où il n'est jamais fait mention d'un trigger externe. Ceci est d'autant plus vrai que le sodium est sous-refroidi.

En effet, les expériences du passé ont montré que la phénoménologie globale de l'interaction corium-sodium évoluait avec la température du sodium. Lorsque celui-ci s'approche de la saturation, le comportement se rapproche de celui observé en eau, en termes de temps de montée en pression (plus rapide) et d'énergie mécanique dégagée (plus grande). Précisons que nous ne savons pas encore quantifier "proche de la saturation". L'une des explications possibles de la différence des comportements pourrait être que, lorsque le sodium est froid ($\sim$ 400K), l'établissement d'un film de vapeur est rapidement bloqué par la solidification en surface des particules de corium. Ce gel va aussi freiner la fragmentation, limiter la surface d'échange corium-sodium et donc la production de vapeur ce qui mène à des évènements de relativement faible intensité (en termes d'amplitude et d'étalement dans le temps du pic de pression). De plus, il a été observé qu'une masse cohérente de corium ne pouvait pénétrer dans du sodium sous-refroidi. Elle se fragmente très rapidement et la vaporisation soudaine engendrée bloque l'écoulement de corium mais contribue aussi à réchauffer le sodium. L'écoulement de corium se fait par à-coups, donnant lieu à de multiples interactions de faible amplitude, jusqu'à ce que le sodium soit suffisamment chaud pour que l'on puisse parler d'un jet de corium qui se propage dans le milieu devenu diphasique. La configuration de l'interaction devient alors plus similaire à ce qui a été observé en eau.

La taille des débris obtenus constitue une différence supplémentaire entre l'interaction corium-sodium et l'interaction corium-eau. En effet, pour l'interaction corium-sodium, les expériences du passé ont montré que le matériau fondu subissait toujours une fragmentation très intense lors de son contact avec le sodium ce qui conduisait à des débris sub-millimétriques, que le dégagement d'énergie soit important ou pas c'est-à-dire qu'il y ait réelle explosion ou pas. En interaction corium-eau, des débris de cette gammes de tailles sont obtenus après la phase explosive.

Dans le présent travail, les expériences d'intérêt mettant en jeu des matériaux prototypiques ont ensuite été étudiées sous l'angle de la forme et de la taille des débris produits. Notre étude des résultats expérimentaux montre que, dans la plupart des cas, la distribution en taille des particules suit une courbe bimodale que nous interprétons comme un signe de l'existence d'au moins deux régimes de fragmentation. Nous pensons en effet

que la fragmentation hydrodynamique, essentiellement liée aux différences de vitesses entre les phases, et la fragmentation liée à solidification en surface des gouttes de corium entrent en jeu et donnent des tailles et des formes différentes de débris en fonction aussi de la composition du corium.

Dans la littérature, e corium prototypique expérimental est en générale composé de dioxyde d'uranium et/ou d'acier inoxydable (stainless steel, SS) ; le comportement de l'interaction évoluant avec le degré de sous-saturation du sodium, l'étude des particules générées lors des essais passés est scindée en quatre catégories : l'interaction d'oxydes ou de matériaux métalliques avec du sodium fortement sous-refroidi, l'interaction d'oxydes ou de matériaux métalliques avec du sodium moins fortement sous-refroidi. L'étude statistique a été réalisée à partir de l'analyse des débris issus des lits-de-débris post-test fournie par la littérature. Notre étude a ainsi montré que les débris d'oxydes, de formes majoritairement fracturées, présentaient un diamètre moyen (en masse) relativement petit en sodium fortement sous-refroidi (degré de sous-refroidissement de l'ordre de 480°C) avec des valeurs comprises entre 0.07 mm et 0.17 mm. Avec du sodium relativement plus chaud (degré de sous-saturation de l'ordre de 190°C), le diamètre moyen des particules varie entre 0.09 mm et 0.69 mm. Lorsque que du métal fondu est injecté dans du sodium liquide, la distribution en taille des particules semble plus dépendre de la nature du métal : un mélange U-Zr (non prototypique) conduit à des débris dont la taille moyenne est comprise entre 3.04 mm et 14.76 mm tandis que de l'acier inox produit des débris de forme plutôt arrondie et de surface lisse dont la taille varie entre 0.05 mm et 0.65 mm. Les résultats de cette analyse statistique sont en accord avec les observations expérimentales.

Dans une deuxième étape, la simulation du nuage de particules de corium suivie de la conception de fantômes (maquettes 3D) représentant les trois phases du milieu ont été réalisées. Nous avons tout d'abord vérifié la détectabilité par un système d'imagerie X des particules dont les tailles caractéristiques ont été estimées à l'étape précédente. Pour cela nous avons modélisé ces particules avec le logiciel CEA MODHERATO capable de simuler la chaîne complète d'imagerie X et de produire des images similaires à celles attendues lors des futurs essais. Ces simulations ont mis en évidence que nos particules de corium n'étaient pas détectable par la chaîne envisagée pour PLINIUS-2 pour lequel MODHERATO a montré un seuil de détectabilité autour de 5 mm. Nous avons donc choisi de chercher à détecter des nuages de particules plutôt que des particules individuelles. Ces nuages sont représentés comme composés d'une fraction massique donnée de corium, de sodium liquide et de vapeur de sodium. Afin de représenter les masses qui seront mises-en-jeu dans les futurs essais PLINIUS-2-FR, nous avons simulé un nuage comportant 45 kg de corium. Pour un tel nuage, le rapport contraste sur bruit est estimé suffisant pour que le nuage soit visible. MODHERATO nous a donc permis de gagner une relative

confiance dans les capacités de notre chaîne d'imagerie X à détecter les particules de corium attendues dans PLINIUS-2-FR. A partir de notre synthèse bibliographique et des simulations réalisées avec MODHERATO, des fantômes représentant les trois phases du milieu généré lors d'une interaction corium-sodium ont été conçus et fabriqués. Des matériaux simulants ont été sélectionnés pour représenter chacune des phases sur la base de leurs propriétés d'atténuation du rayonnement X, simulant ainsi leurs densités respectives. Nous avons ainsi choisi de représenter le corium par de l'acier, le sodium liquide par du polyéthylène et la vapeur de sodium par du vide (air). Trois fantômes ont été conçus pour être testés expérimentalement : un fantôme caractéristique d'un nuage de particules de corium, un fantôme mettant en jeu un film de vapeur et un fantôme dynamique destiné à étudier/détecter le mouvement relatif de deux nuages de particules. Les expériences étaient préparées en les simulant avec MODHERATO afin d'évaluer les performances de la chaîne d'imagerie X à notre disposition, modifiée pour prendre en compte les spécificités de la future chaîne PLINIUS-2.

La troisième étape de cette thèse était dédiée à la conduite des expériences avec les fantômes 3D et au développement du logiciel de traitement des images ainsi obtenues. Des radiographies des différents fantômes mis au point à l'étape précédente ont été réalisées dans différentes configurations en utilisant la chaîne de radioscopie X de l'installation KROTOS. Afin de simuler la géométrie de PLINIUS-2 (épaisseur des parois de l'enceinte en particulier), des plaques d'acier ont été placées entre la source X et l'enceinte KROTOS. Le fantôme prémélange, composé de billes d'acier représentant le corium (dans du sodium liquide) avec un taux de présence volumique de l'ordre de 53% a permis de montrer qu'un nuage dense de corium pouvait être visualisé. Un nuage de corium moins dense a aussi été simulé à l'aide de poudre d'hafnie. Ce nuage (fraction volumique de corium de l'ordre de 23%) a aussi pu être visualisé. Le fantôme représentant un film de vapeur autour d'un jet de corium a été radiographié et étudié nous permettant ainsi d'estimer une épaisseur limite de vapeur détectable.

Afin d'analyser les images brutes obtenues lors des radiographies des fantômes, un nouveau logiciel a été développé, capable de localiser les phases dans les images 2D. Ce logiciel d'analyse d'images (PICSEL) est basé le logiciel MATLAB ver. R2015b qui intègre la bibliothèque Image Processing Toolbox. Différentes techniques ont ainsi été mises en places dans PICSEL parmi lesquelles la réduction du bruit, l'extraction de l'arrière-plan, l'intensification du signal ainsi qu'un analyse qualitative utilisant la détection des frontières d'un milieu donné. Notre logiciel est ainsi capable de suivre des nuages de particules et d'estimer leur vitesse en utilisant une technique de corrélations croisées normalisée basée sur un algorithme de block-matching. L'interprétation de nos images expérimentales avec PICSEL a confirmé la faisabilité de l'observation d'un milieu représentatif de l'interaction corium-sodium avec un système d'imagerie X. Le nuage de corium de faible densité (poudre

d'hafnie) a montré un rapport contraste sur bruit satisfaisant ce qui le rend détectable. Le film de vapeur s'est lui aussi montré détectable jusqu'à une épaisseur de l'ordre de 1.7 mm, sa détectabilité décroissant cependant significativement en-dessous d'une épaisseur de 3.75 mm. Nous considérons donc que le logiciel PICSEL est capable d'extraire de manière qualitative, d'une image radiographique 2D, les trois phases qui composent le milieu.

Pour terminer, le logiciel PICSEL a été appliqué aux radiographies X enregistrées lors de l'essai d'interaction corium-eau ALISA, réalisé dans la section KROTOS, dans le cadre coopératif Europe-Chine. La technique de suivi de nuages a été utilisée pour stabiliser et aligner des images perturbées par les vibrations générées lors de l'interaction. Les techniques d'extraction de l'arrière plan et de reconnaissance des frontières ont donné des résultats satisfaisants. L'algorithme de vélocimétrie a été lui aussi testé sur l'essai KROTOS-ALISA. On a ainsi pu vérifier que l'évaluation de la vitesse au point d'entrée du jet de corium dans l'eau étant en bon accord avec la valeur expérimentale. Nous avons donc montré que le logiciel PICSEL d'analyse d'images 2D que nous avons développé pour observer les mélanges triphasiques de l'interaction corium-sodium était capable de localiser et séparer les phases de ce mélange. Enfin, même si le logiciel PICSEL est capable de traiter les images 2D issues d'une radioscopie X acquise lors d'une interaction corium-sodium, le travail reste incomplet et les techniques de détection du nuage de particules nécessitent des améliorations. Par exemple, l'implémentation de l'algorithme de segmentation en superpixels permettrait de produire une meilleure segmentation des nuages et de réduire ainsi les incertitudes sur leur détection.

Il sera aussi nécessaire d'étendre PICSEL à l'analyse 3D des images. Cet aspect est indispensable à une analyse quantitative et à une estimation des taux de présence volumique des différentes phases, en particulier pour les futurs essais PLINIUS-2. Ainsi, lors de cette thèse, un système d'imagerie X a été défini pour visualiser les interactions corium-sodium qui seront étudiées dans le cadre du programme d'essais PLINIUS-2-FR. Une analyse quantitative des images produites par ce système a aussi été réalisée avec le logiciel PICSEL que nous avons développé. PICSEL permet de caractériser l'évolution des trois phases qui composent le milieu, sa version 3D fournira, à terme, des données capitales pour la compréhension de la physique impliquée lors d'une interaction corium-sodium. Ces données seront utilisées pour la validation des outils numériques destinés aux études de sûreté des réacteurs à neutrons rapides refroidis au sodium.

université PARIS-SACLAY | ÉCOLE DOCTORALE PHENIICS

Titre: Radioscopie X pour les interactions corium-sodium lors d'un scénario d'accident grave

Mots clés: Réacteur à neutrons rapides à caloporteur sodium, Accidents graves nucléaires, Interaction corium-sodium, Radioscopie X, Traitment d'images

Résumé: En cas d'accident grave dans les réacteurs à neutrons rapides refroidis au sodium (RNR-Na), les matériaux du coeur (combustible et acier) fondent, pour former un mélange appelé corium. Ce corium est susceptible d'interagir avec le réfrigérant (sodium) ce qui peut générer des évènements énergétiques aptes à mettre en danger les structures du réacteur (FCI : Fuel Coolant Interaction). PLINIUS-2, la future plateforme expérimentale du CEA Cadarache, sera dédiée à l'étude de la phénoménologie de l'interaction corium-réfrigérant (eau et sodium) en mettant en jeu de grandes masses de matériaux. L'objectif du présent travail est de développer, pour cette installation, un système d'imagerie basée sur des radiographies X afin de visualiser et de mieux comprendre l'interaction corium-sodium. Un algorithme de post-traitement de ces images a aussi été écrit afin de les analyser et d'en déduire la répartition des trois phases (corium, sodium liquide et sodium vapeur) au cours de cette interaction.

Title: X-Ray diagnostics on corium-sodium interactions during a severe accident scenario

Keywords: Sodium-cooled Fast Reactors, Nuclear severe accidents, Corium-sodium interaction, X-Ray radiography, Image processing.

Abstract: In case of a severe accident in Sodium-cooled Fast Reactors (SFRs), core materials (fuel and steel) melt down generating a hot molten mixture called corium. This corium may interact with the coolant (liquid sodium), leading to Fuel Coolant Interaction (FCI) and can generate energetic events that can jeopardize the reactor structures. PLINIUS-2, the future large-mass experimental platform of CEA Cadarache, will be dedicated to experiments aiming at understanding the interaction phenomenology of prototypic corium with coolant (sodium and water). This Ph.D. research intends to develop a high-energy X-Ray imaging system for this facility, to simultaneously visualize and better understand the corium-sodium interaction. An image-processing algorithm is also developed to analyze the three-phase repartition (i.e., corium, liquid sodium, and sodium vapor) during this interaction.

Université Paris-Saclay
Espace Technologique / Immeuble Discovery
Route de l'Orme aux Merisiers RD 128 / 91190 Saint-Aubin, France